Facultad de Ciencias Físicas
Universidad Complutense de Madrid

Magnetism and spin dependent transport at interfaces between complex oxides

Cristina Visani

Tesis Doctoral dirigida por:

Prof. Jacobo Santamaría Sánchez-Barriga

Madrid, 2010

Facultad de Ciencias Físicas
Universidad Complutense de Madrid

Magnetism and spin dependent transport at interfaces between complex oxides

Cristina Visani

Tesis Doctoral dirigida por:

Prof. Jacobo Santamaría Sánchez-Barriga

Madrid, 2010

Resumen

Se resumen a continuación los resultados y las conclusiones principales de esta memoria. Hemos realizado un análisis de la interacción entre ferromagnetismo (F) y superconductividad (S) en heteroestructuras epitaxiales del superconductor de alta Tc $YBa_2Cu_3O_7$ (YBCO) y la manganita ferromagnetica $La_{0.7}Ca_{0.3}MnO_3$ (LCMO). Encontramos grandes valores de magnetorresistencias positivas en tricapas LCMO/YBCO/LCMO, que aparecen a lo largo de la transición superconductora, cuando la imanación de las capas LCMO está alineada antiparalela. Se trata de un comportamiento anómalo que en la literatura se ha dado en denominar "interruptor" superconductor inverso. El origen de este fenómeno es actualmente objeto de controvertido debate, en que el mecanismo por el que aumenta la ruptura de pares superconductoras debido a quasiparticulas polarizadas en espin se enfrenta al efecto de depresión de la superconductividad por el campo dipolar generado durante la inversión de la imanación. Para un mejor entendimiento del origen de esta magnetorresistencia hemos realizado experimentos en nuestras muestras utilizando distintas técnicas cuyos resultados se resumen en los siguientes puntos:

- Encontramos una magnetorresistencia positiva que muestra valores mucho más grandes que los observados en el GMR en superredes y heteroestructuras metálicas, en el que el efecto del campo dipolar se ha demostrado dominante.
- Hemos encontrado que la forma y la altura de los picos de magnetorresistencia no se modifican cuando la orientación relativa de la corriente y el campo magnético cambia de paralela a perpendicular. Más aun, observamos que el desplazamiento en temperatura de las curvas de resistencia es independiente de la corriente y del ritmo al que cambia el campo magnético. Estas observaciones descartan cualquier interpretación ya sea en términos de vórtices espontáneos o de magnetorresistencia anisótropa de las capas ferromagneticas.
- La comparación de tricapas y bicapas (que muestran magnetorresistencia negativa o ninguna magnetorresistencia dependiendo de las características de la interfase LCMO/YBCO) permite descartar el efecto de los campos dipolares asociados a la estructura de dominios del ferromagnetico como la causa del fenómeno de "interruptor" superconductor inverso (ISS).

- Medidas de magnetometría combinadas con medidas de resonancia ferromagnetica, y con reflectometría de neutrones polarizados, muestran que la anisotropía magnética es biaxial con el eje fácil a lo largo de las direcciones [110] de sustrato. La orientación del campo respecto al eje fácil muestra un marcado efecto sobre la superconductividad. Identificamos un "*plateau*" bien definido de la magnetorresistencia cuando el campo magnético tiene la dirección del eje fácil, mientras que para otras direcciones del campo lo que se observan picos. La magnetorresistencia sigue de cerca el intervalo de campo magnético en el que los momentos magnéticos de las capas de manganita esta alineados antiparalelamente. Las medidas de resistencia realizadas mientras se cambia de forma continua la dirección del campo aplicado en el plano, muestran que la respuesta está únicamente causada por el desalineamiento de la imanación en los dos electrodos de LCMO controlado por la anisotropía biaxial en el plano.
- Un efecto no reportado hasta ahora es que aparece un *plateau* de magnetorresistencia positiva para el alineamiento antiparalelo de las imanaciones de las capas ferromagneticas y un pico de magnetorresistencia negativa en el campo coercitivo. Esto evidencia la importancia de los efectos de scattering dependiente de espin en la interfase (en contraposición al efecto del campo dipolar) en el comportamiento magnetorresistivo de "interruptores" de espín basados en óxidos.
- Proponemos un modelo de scattering dependiente de espín de quasiparticulas polarizadas en el la interfase ferromagnético / superconductor. En este escenario, la dependencia de la magnetorresistencia con el espesor de la capa ferromagnetica resulta proporciona una estimación de la longitud de difusión de espin (de quasi partículas polarizadas) en YBCO de 13nm.
- Finalmente nuestras tricapas LCMO/YBCO/LCMO tienen efectivamente un comportamiento de *válvula de espin superconductora inversa que* da lugar a un efecto de memoria magnética sensible al ángulo; este concepto de memoria explota las ventajas del elemento de detección superconductor (baja disipación y rápida respuesta) y presenta peculiaridades que la diferencian de otras memorias basadas en GMR como son la posibilidad de "escribir" aplicando campos en distintas direcciones y de "leer" con campos realmente bajos (del orden de 10mT).

Estos resultados constituyen una evidencia directa del transporte dependiente de espin como origen del efecto de válvula de espin inversa en este sistema, y puede dar lugar al desarrollo de nuevos dispositivos de aplicaciones en espintrónica.

Agradecimientos

En primer lugar quisiera agradecerle a mi director de tesis, el profesor Jacobo Santamaría, por haberme transmitido su experiencia y sabiduría y por su confianza en mí a lo largo de estos años. También les agradezco mucho a todos los miembros del GFMC: Carlos, Alberto, Flavio, Zouhair, Fabian, Javier Tornos, Mirko y Javier Barriocanal por haber compartido conmigo momentos inolvidables de tiempo laboral y extra-laboral. Un agradecimiento general va al Departamento de Física Aplicada III y al de Física de Materiales por su colaboración en el desarrollo de mi formación doctoral y la preciosa ayuda en las cuestiones administrativas. Gracias también a Mar García Hernández, Norbert Nemes y Federico Mompean del Instituto de Ciencia de Materiales de Madrid, por su fundamental aportación a esta tesis y al personal del CAI de rayos-X de la Universidad Complutense, en particular Emilio Matesanz y Ignacio Carabias por su gran trabajo y paciencia. Quiero agradecerle a todos los que me ayudaron a llevar a cabo con éxito mi estancia en Estados Unidos: Suzanne te Velthuis (por haber sido mi guía fundamental en el campo de la espectroscopia de neutrones), Axel Hoffman del Argonne National Laboratory y Mike Fitzsimmons del Los Alamos National Laboratory. Gracias a la colaboración con Ferenc Simon y Titus Feher de la Universidad de Tecnología y Economía de Budapest esta tesis cuenta con resultados fundamentales en el campo de la espectroscopia de resonancia ferromagnetica. Gracias también a Sean Giblin, de Appleton Rutherford Laboratoty por haber compartido conmigo el duro trabajo del estudio del dicroísmo magnetico. Durante estos años he podido mejorar considerablemente mi formación gracias a la interacción con científicos de alto nivel como Tim Charlton y Ricardo López Antón del Rutherford Appleton Laboratory, Agnes Barthelemy y Manuel Bibes de La Unité Mixte de Physique CNRS/Thales y Allen Goldman de la Universidad de Minnesota. Finalmente unas gracias especiales a Javier Villegas por su confianza en mí y por su infinita paciencia.

Supplementary acknowledgments:

Thanks to Flexo for singing Queen together in the clean room (and many other places) convinced that nobody was hearing us.

Thanks to the six undergrads and one post-doc awarded to me by my senior professors; their pedantry, clumsiness and conceit addressed me towards a fearless and successful career of supervisor.

Thanks to Zharen and Torniquet who, from being pedant, clumsy and conceited, turned into colleagues and eventually good friends.

Thanks to Carlos for his illuminating pearls of wisdom (we are going to write a book which will start with the parable about eating the soup with a fork) and, of course, for the summer BBQ-pool parties in your chalet.

Thanks to Barriocanal for showing me that instrument scientist career is incompatible with social life.

Thanks to Matteo for making me discover the 80cents-Instant-Spicy Pork-Chinese noodles when I was writing this thesis; they saved my life.

Thanks to Skonny and La Rata for ruling the world.

Table of contents:

Chapter 1. Introduction

Chapter 2. Experimental Techniques

Chapter 3. Experiments

1. Introduction

1. 1. Motivation and Outline

Transition-metal oxides constitute a wide family of materials with interesting properties. Almost every possible solid state can be found: superconductivity, ferromagnetism, antiferromagnetism, metal phases, insulating phases, ferroelectricity and in particular these materials are good candidates for future applications in oxide electronics. This project is focused on the characterization of highly spin-polarized manganites $La_{0,7}Ca_{0,3}MnO_3$ (LCMO), high-T_C-superconductor (HTSC) $YBa_2Cu_3O_7$ (YBCO) and on the interplay between superconductivity and ferromagnetism in heterostructures of these two materials. Ferromagnetism and superconductivity are two distinct phenomena with antagonistic long-range order. While ferromagnetism tries to align spins, superconductivity is built upon coupled electrons with opposite spins, which implies both cannot coexist in the same region of a sample. Therefore artificial ferromagnet/superconductor structures seem to be a promising candidate to study experimentally this interplay. Recently many experiments and theoretical models have been focused on the realization of spintronic devices based on the spin selectivity that can take place at the F/S interfaces [1,2]. The experimental research of the interplay between magnetism and superconductivity started in the 60s with the pioneer work of Hauser et al. [3]. They show that an ordered magnetic metallic layer, deposited onto a thin superconducting layer, depresses the transition temperature much more efficiently than a non-magnetic layer. The understanding of this effect started with the theory of the proximity effect in normal metal/superconductor by De Gennes and Werthamer [4,5] in combination with the Abrikosov-Gor’kov [6] pair breaking effect, which accounts for the effect that antialigned spins try to align in the presence of an exchange field. Later Buzdin and collaborators [7,8] provided a different theoretical framework incorporating the quasi-classical theory of Eilenberger in the dirty limit using the Usadel equations. It is interesting that the magnetic coupling through a metallic non-magnetic spacer was studied so deeply theoretically and experimentally, but the coupling through a ternary and quaternary complex oxide is a recent invention. In this context the oxide superconductors and transition metal oxides present a fascinating alternative with new ingredients:

- the variety of oxides allows choosing materials with distinct properties but still with the same crystal structure (perovskite), a good chemical compatibility and similar lattice parameters which enables to grow heterostructures with limited interface disorder. This is an important feature of the oxide interfaces in contrast to the conventional metals which, in many cases, have tendencies to interfacial defects.
- the small coherence length of the new oxide superconductors in the *c*-axis direction of the crystal allows superconductivity to survive in thin films, what permits studying the F/S interplay at short distance from the interface.
- the high level of spin-polarization of the manganite conduction band creates an additional barrier for the Cooper pairs penetrating into the ferromagnetic material. This will depress the proximity effect.
- the *d*-wave symmetry of the order parameter in the high-temperature superconductors opens up the possibility to create polarized excitations along the nodes. These excitations can break the Cooper pairs or can transport the magnetic order over the superconducting gap.

This project is motivated by all these aspects and its purpose is to explore their basic effects in heterostructures combining the manganite LCMO and the high-temperature superconductor YBCO.
The project intends to cover the following objectives:

- possibility of producing samples which present magnetism and superconductivity simultaneously at nanometric thickness scale.
- explore the impact of the proximity effect in ferromagnets/superconductor bi- and trilayers combining a high-temperature superconductor and a transition metal oxide ferromagnet, investigating the effect of spin-polarized quasiparticles on the superconductor.

When a thin superconductor is brought in contact with an inhomogeneous ferromagnet, the cancellation of the exchange field over the coherent volume results in novel effects. Examples are domain wall superconductivity [13,14] or the F/S/F superconducting spin switch [15-17]. In the first case, oppositely directed magnetizations at both sides of a domain wall promote nucleation of superconductivity if the coherence length is larger than the width of the domain wall [13,14]. In the second case, antiferromagnetic alignment of the magnetizations of the F layers results in larger T_C values than does the ferromagnetic alignment, due to the averaging out of the exchange field over the coherent volume [15-17]. In recent years there has been an increasing interest in structures combining oxide ferromagnets and oxide superconductors [18-22]. In particular, the combination of high- T_C superconductors (HTS) and colossal magnetoresistance materials (CMR), gives rise to a number of new properties and behaviors, which considerably enrich the study of F/S interplay [23-24]. The unconventional pairing symmetry (*d*-wave) of the superconductor with an anisotropic gap exhibiting nodes in [110] directions, affords quasiparticles to be incorporated at zero energy cost. On the other hand, the highly spin polarized conduction band of the manganites will cause the suppression of Andreev reflection, and thus conventional proximity effect, at F/S interfaces. Thus *d*-wave superconductivity and half-metallicity will conspire to enhance the relative importance of phenomena originating at the transfer of (spin polarized) quasiparticles. Perovskite HTS and CMR materials, chosen with good lattice matching, can be grown epitaxially one on top of the other with atomically flat interfaces exhibiting no interdiffusion [25,26]. In spite of the well defined chemical interface structure the electronic and magnetic structure at the interface can be significantly more complex due to charge transfer or other interface processes [27]. In conventional F/S/F junctions the critical temperature may be modulated by the relative orientation of the magnetization in the two ferromagnetic layers. This T_C modulation results from a compensation of the exchange field over the coherent volume in the antiferromagnetic configuration if the thickness of the superconductor is comparable to the coherence length [15-17]. Since at the interface between a half-metal and a superconductor proximity effect is suppressed, [29] T_C is affected distinctly in F/S/F structures with highly spin polarized carriers.

Recent reports [28,30,31] have shown an inverse superconducting spin-switch (ISS) behavior in F/S/F structures with strong ferromagnets, where superconductivity is favored for parallel orientation of the adjacent magnetizations. Its origin is a subject of debate. Normal [17] and inverse [31,32] superconducting spin switches have been found by different groups in very similar Ni/Nb/Ni and Py/Nb/Py samples, highlighting the key role of the interface. Moreover, while some reports suggest an enhanced pair breaking by spin-polarized quasiparticles in the antiparallel configuration, others emphasize the effect of stray fields in depressing the superconductivity during the magnetization switching. [33,34] The enhanced (perpendicular) stray field at Bloch-type domain walls in ferromagnets with in-plane magnetization may depress superconductivity if the coherence length ξ_{GL} is smaller than the domain-wall thickness or even nucleate vortices if the stray field is larger than the lower critical field H_{c1} of the superconductor. [35] A detailed study of the domain structure of the ferromagnetic layers is thus of major importance. Magnetic anisotropy may depend on crystalline orientation and on thickness through the influence of strain, surface morphology, and roughness. [36-39] As the thickness of the manganite thin film is shown to be responsible for dramatic changes in the magnetic and metallic behavior of the ferromagnetic layer, it will be important to study the properties of manganite thin films when they form part of various LCMO/YBCO (F/S) heterostructures. The domain state of the ferromagnet can play a primary role in modulating the strength of the F/S interplay by the cancellation of the exchange field (nucleation of superconductivity) or by the depression of the pairing amplitude by the (dipolar) stray fields generated by domains or domain walls [33,34].

Outline

Chapter 1 is an overview of the most important properties of YBCO and LCMO respectively, focusing on those aspects which can help elucidating the nature of the F/S interplay in YBCO/LCMO heterostructures. Among them, the unconventional pairing mechanism of the YBCO and the magnetic anisotropy of the LCMO play an important role.

The state-of-the-art in the field of the interaction between ferromagnetism and superconductivity is reviewed, emphasizing the problem of the interface between complex oxides such as the high-T_C superconductor YBCO and the half-metallic manganite LCMO.

Chapter 2 describes the experimental techniques used to produce and characterize our samples giving particular importance to those (polarized neutron reflectivity and X-ray magnetic circular dichroism) which allow interface sensitive measurement of the magnetic state of the sample.

Chapter 3 is devoted to describe the experimental results:

- we perform a detailed analysis of the magnetic anisotropy of the LCMO both in thin films and LCMO/YBCO multilayers.
- we provide evidence for an inverse spin switch effect (ISS), with superconductivity favored when the F layers are parallel aligned, with an origin different from stray fields, in oxide based $La_{0.7}Ca_{0.3}MnO_3$ (LCMO) / $YBa_2Cu_3O_7$ (YBCO) / $La_{0.7}Ca_{0.3}MnO_3$ (LCMO) trilayers. This mechanism is determined exclusively by the magnetic alignment of the ferromagnetic layers and therefore has a spin dependent origin.
- we explore how the F/S interplay in F/S/F structures is modulated by the biaxial in-plane magnetic anisotropy of the ferromagnets. The angle between applied magnetic field and easy axis controls magnetization switching and determines the magnetic alignment of the ferromagnetic layers, altering the superconductivity of the S layer.
- we study the interplay between the domain structure of the ferromagnet and the superconductivity in F/S/F samples where one of the oxide F layers is substituted by Co.

Chapter 4 summarizes the main conclusions of this work.

1. 2. High-T_C superconductors: the $YBa_2Cu_3O_{7-\delta}$

The high temperature superconductor $YBa_2Cu_3O_7$ (YBCO) was discovered in 1987 by M. K. Wu *et al.* [40] as the first superconductor with a transition temperature above the boiling point of liquid nitrogen (77 K). Since then it became one of the most studied superconductors; nevertheless it still holds many secrets the most important of which is the origin of the pairing mechanism of the superconducting carriers. YBCO shares many characteristics with the other members of the vast family of HTS: it is a hole-doped type II superconductor; its properties are strongly dependent on the oxygen content resulting in a complex phase diagram (strange behavior is observed in the normal state of the underdoped compound); it presents a layered structure responsible of highly anisotropic properties; it shows unambiguous signature of *d*-wave pairing symmetry. Due its perovskite structure it can be successfully coupled to other complex oxides of primary importance like colossal magnetoresistance (CMR) manganites, allowing the researchers to study the interplay between superconductivity and magnetism as the manifestation of new, often unexpected, phenomena. Here we propose a survey of some of the most important characteristics of YBCO focusing on those required to study the exotic phenomena that take place when the superconducting order parameter competes with ferromagnetism in the same heterostructure. This case is effectively represented by YBCO/LCMO hybrids. The basic concept of superconductivity are reviewed in order to introduce the distinctive features of YBCO.

The discovery of superconductivity belongs to Kammerlingh Onnes who first observed this phenomenon in 1911 as a transition to a zero-resistance state in mercury at a critical temperature T_C. In 1932 Meissner observed another phenomenon related to superconductivity which is the perfect diamagnetism. The first theory that tried to give an interpretation to superconductivity was developed only in 1957 by Cooper, Schrieffer and Bardeen obtaining a great success, even though in 1986, with the discovery of high temperature superconductors (HTS), new hypothesis have been formulated which are still waiting for clarification.

The BCS theory

The first microscopical interpretation of superconductivity was given by the BCS (Bardeen, Cooper, Schrieffer) theory [41]. It is based on the assumption of a weak attractive interaction between electrons; this can be seen as the formation of a bound pair of electrons with the same moment and opposite spin (the *Cooper pair*) that makes the ground state of the electron gas unstable. The global mechanism is often described in a simplified picture of a conduction electron crossing the crystal lattice and attracting positive ions due to the Coulomb interaction. The consequent deformation in the local charge density establishes a more favorable energetic condition for other incoming electrons. So when a *second* electron absorbs the phonon, it will be effectively coupled with the *first* electron. For a sufficiently small Coulomb interaction and phonon frequency, the net energy contribution *is negative;* an attractive interaction between the electrons is possible even at a distance of several lattice parameters. The minimum size of the Cooper pair is defined as ξ_0, the coherence length. The many body system made by the entire set of Cooper pairs must be studied using an electron pair density of states instead of a single particle density of state. So from the study of the excited state spectrum, the minimum energy to break a pair and form two *quasi-particle excitations*, can be written as

$E_g=2\Delta(T)$ where Δ appears as a *gap*. At absolute zero $E_g(0)=2\Delta(0)=3.528kT_C$, while close to T_C we have [42]:

$$\frac{\Delta(T)}{\Delta(0)} \approx 1.74\left(1-\frac{T}{T_C}\right)^{\frac{1}{2}} \tag{1.1}$$

and the coherence length can be rewritten as:

$$\xi_0 = \frac{\hbar v_F}{\pi\Delta(0)} \tag{1.2}$$

Superconductors in a magnetic field I: the Meissner effect

Superconductors in a magnetic field display perfect diamagnetism. The so called Meissner effect [43] consists of the exclusion of the magnetic field lines from a bulk material in the superconducting state. Among others interesting effects (i.e. flux trapping from a superconducting cylinder) it shows the existence of a critical field H_C, above which the normal state can be recovered. This fact allows applying thermodynamics to superconductivity being H_C related to the difference in the free energy of the superconducting and normal state in zero-field by the following expression:

$$\frac{H_c^{\,2}(T)}{8\pi} = f_n(T) - f_s(T) \tag{1.3}$$

The difference $f_n(T)$-$f_s(T)$ (the condensation energy of the superconducting state) defines the overall energy change as the superconducting transition occurs. Experimentally the free energy change during the transition can be obtained by integrating the area under the magnetization curve from zero up to a certain field where superconductivity is destroyed. To introduce the effect of an external magnetic field and to explain superconductivity in a purely phenomenological way it was necessary to modify the conventional electrodynamics equations leading to the London equations for the electric and magnetic fields:

$$\begin{cases} \vec{E} = \dfrac{\partial}{\partial t}(\Lambda \vec{J}_s) \\ \vec{B} = -c\nabla \times (\Lambda \vec{J}_s) \end{cases} \qquad 1.4$$

$$\Lambda = \frac{m}{n_s e^2} = \frac{4\pi\lambda_L^2}{c^2} \qquad 1.5$$

with Λ as phenomenological parameter and n_s superconducting electron density. The first equation describes the acceleration given by the field on the superconducting electrons, the second one, combined with the Maxwell's equation, $\nabla \times (\vec{h}) = 4\pi\vec{J}/c$ implies that the magnetic field decays inside the superconductor as:

$$B(x) = B_0 \exp\left(-\frac{x}{\lambda_L}\right) \qquad 1.6$$

$$\lambda_L = \sqrt{\frac{m}{n_s e^2}} \qquad 1.7$$

over the distance λ_L, that is called the *London penetration depth*.

The London equations are commonly written in a more compact expression:

$$\vec{J}_s = \frac{n_s e^2 A}{mc} = -\frac{cA}{4\pi\lambda_L^{\;2}} \qquad 1.8$$

which is true only in the London gauge that is for $\Delta \cdot A = 0$, being A the vector potential. From the London equations, Pippard deduced that the spatial change of n_s must be controlled by a characteristic length estimated using as indetermination principle the fact that only those electrons with energy within kT_C from the Fermi level are determinant for the occurrence of superconductivity. Since they will have a moment $\Delta p \sim kT_C/v_F$, with v_F the Fermi velocity, this characteristic length can be determined by the relation $\Delta x \geq \frac{\hbar}{\Delta p}$ which yields to the definition of *coherence length* as:

$$\xi_0 = \frac{a\hbar v_F}{kT_c} \qquad 1.9$$

where a is a constant.

The Ginzburg –Landau theory

The GL theory [44] is a complementary phenomenological model focused more on the superconducting electrons than the underlying pairing mechanism. The formalism used by this model allows making consideration on the spatial variation of the superconducting electron density and how the superconducting phase varies under the application of sufficiently strong magnetic field. It first introduces a pseudo-wave function $\psi(r)$ and rewrites the free energy in the superconducting phase as an expansion of the form:

$$f = f_{n0} + \alpha|\psi|^2 + \frac{\beta}{2}|\psi|^4 + \frac{1}{2m^*}\left|\left(\frac{\hbar}{i}\nabla - \frac{e^*}{c}A\right)\psi\right|^2 + \frac{h^2}{8\pi} \qquad 1.10$$

where α and β are phenomenological parameters, A is the potential vector, m^* the effective electron mass and e^* the effective charge. Under this assumption, the free energy contains nonlinear terms corresponding to the effects of fields and currents strong enough to change the density of superconducting electrons. Minimization of the free energy yields to the differential equation:

$$\alpha\psi + \beta|\psi|^2\psi + \frac{1}{2m^*}\left(\frac{\hbar}{i}\nabla - \frac{e^*}{c}A\right)\psi^2 = 0 \qquad 1.11$$

which can be solved using the normalized wave function $f = \frac{\psi}{\psi_\infty}$; this yields to the following expression: $\frac{\hbar^2}{2m^*|\alpha|}\frac{d^2 f}{dx^2} + f - f^3 = 0$. In this way the variation of ψ is ruled by a characteristic length scale:

$$\xi_{GL} = \sqrt{\frac{\hbar^2}{2m^*|\alpha|}}\,. \qquad 1.12$$

By assuming a temperature dependence of α of the kind, $\alpha = \alpha_0(T - T_C)$ the coherence length ξ diverges while approaching the normal state. $\psi(r)$ behaves like an order parameter and $|\psi|^2$ assumes the role of the superconducting electron density n_s. In the presence of an external magnetic field an expression for the *penetration depth* can be derived:

$$\lambda = \sqrt{\frac{m^* c^2}{4\pi e^{*2}\,|\psi_0|^2}} \qquad 1.13$$

that is similar to the London's one if n_s *is* $4|\psi_0|^2$ (the density of superconducting electrons in zero magnetic field).

Superconductors in a magnetic field II: the vortex state

The strength of the GL theory resides in the way it approaches to the superconducting transition (as a thermodynamically second-order transition). Although it is purely phenomenological it can predict how the magnetic field is coupled to the system. An external magnetic field applied parallel to the surface of a superconductor will be excluded giving rise to the Meissner effect, until a certain value is reached; at that point the field start to penetrate the superconductor and convert some areas into a normal material (this is the mixed state) (see Fig. 1.1).

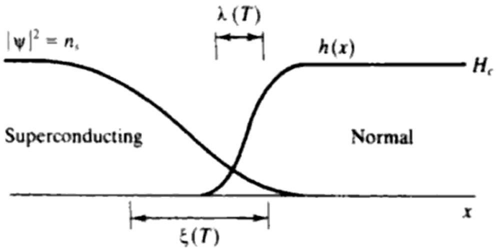

Fig. 1.1 : Interface between the superconducting and normal phases in the mixed state. [42]

How this is achieved is in many cases dependent on the geometry of the sample. But in many superconductors the mixed state has been shown to take place as flux penetration, with supercurrent circulating around a core of normal material but without Meissner effect and with no dependence on the geometry. The GL theory is useful to explain this phenomenon that was predicted by Abrikosov [45]. Two classes of superconductors can be distinguished: type I and type II. The criterion which separates these two classes is given by the ratio of the two fundamental lengths $k = \lambda(T)/\xi(T)$ called the Ginzburg-Landau parameter; the transition occurs at $k = 1/2$. For $k < 1/2$ the superconductor is of type I: the supercurrent decays exponentially in the bulk material according to the London penetration depth. In type-II superconductors $k > 1/2$ and the magnetic flux penetrates in the shape of vortices. Every vortex is a tridimensional structure containing a quantum of flux $\Phi_0 = hc/2e$ with a minimum size given by ξ. When k is large, the vortex state exists over a large field range. The vortex starts to nucleate at a field H_{C1} then the normal core increases until the field H_{C2} is reached (see Fig.1.2).

In the case of the conventional BCS pairing, spin-singlet Cooper pairs would be destroyed by an external magnetic field H which establishes a predominant orientation for electron spins. As a result, there exists the so-called paramagnetic Clogston–Chandrasekhar limit:

$$H_P^{BCS}(0) = \frac{2m^* c\Delta_0^{BCS}}{e\hbar\sqrt{2}} \qquad 1.14$$

for the upper critical field H_{c2} at T=0, considering the transition from the normal to the superconducting state as a first-order phase transition.

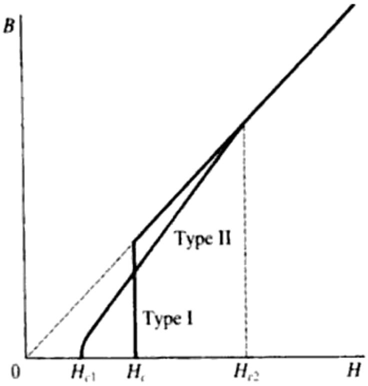

Fig.1.2 : Flux penetration behavior of type I and type II superconductors, with the same thermodynamic critical field H_C. $H_{c2} = \sqrt{2}kH_c$. [42]

The vortices interact with each other through the circulating currents around each vortex and form a lattice in equilibrium; the triangular array, with the lowest free energy is also known as the Abrikosov lattice (see Fig.1.3 left), after A. Abrikosov who first developed a theoretical prediction of vortices in type-II superconductors [45] . The currents reflect the symmetry of the electronic states and give rise to a complex evolution of vortex lattice structures with the applied field. In the right panel of Fig.1.3 the structure of a vortex is represented.

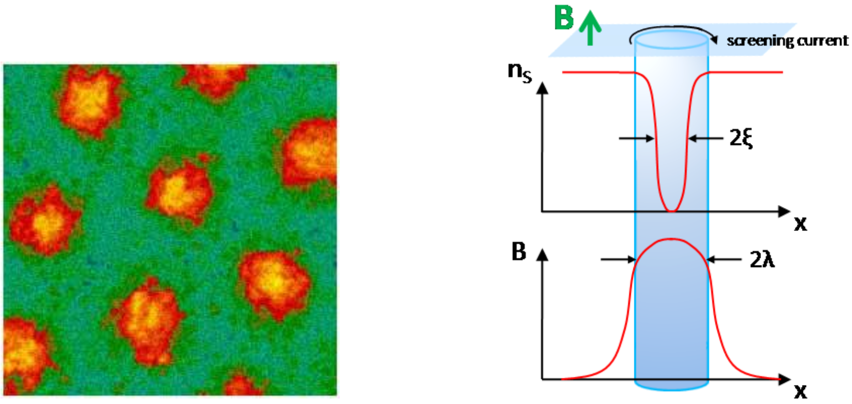

Fig.1.3 : (left) Image of a vortex lattice by scanning tunnel spectroscopy on MgB$_2$ [46]. (right) Structure of a vortex.

Although superconductors are usually categorized as being either type-I or type-II, it has been also reported the evidence for a superconducting phase that spans these categories, showing coexisting type-I and type-II behavior [47]. This new phase, found in a two-component MgB_2 single crystalline superconductor, has been called 1.5-type superconductivity and may be due to the presence of two nearly independent order parameters corresponding to the two electronic bands that carry the superconductivity, leading to novel effects related to the attraction of vortices.

The superconductivity research changed dramatically when the high T_C-cuprates superconductors with CuO_2-layers like $La_{2-x}Sr_xCuO_4$, $YBa_2Cu_3O_{7-\delta}$, $Tl_2Ba_2CaCu_2O_8$, etc., were discovered by Bednorz and Müller in 1986 [48], with transition temperature T_C ranging from 35K to 160K (under pressure in $HgBa_2CaCu_2O_{6+\delta}$). The carriers in the cuprates are strongly correlated. As a result one observes many unusual properties, non-Fermi liquid behavior, a rich phase diagram and antiferromagnetism. Superconductivity depends sensitively on hole-doping in the CuO_2 planes which allow identifying new phases of the vortex state, represented in Fig.1.4.

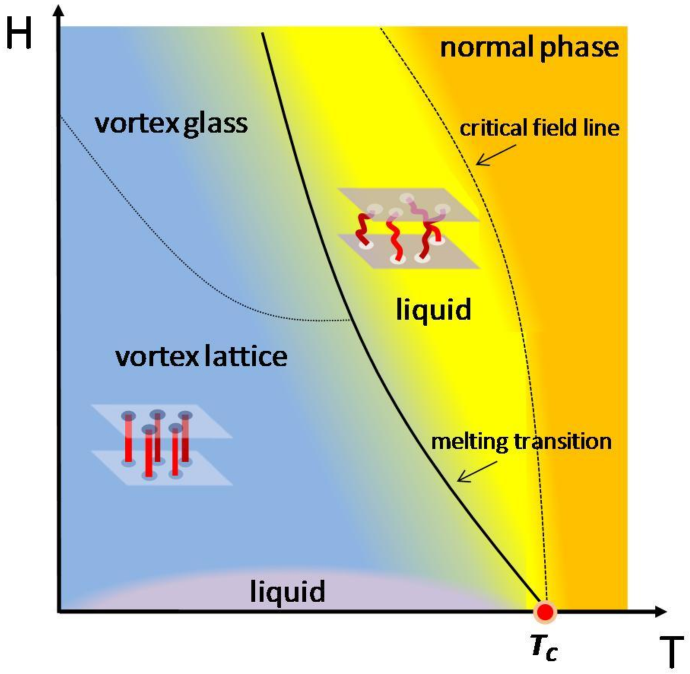

Fig.1.4: Schematic temperature-field phase diagram for a high-T_C cuprate superconductor for field applied perpendicular to the CuO_2 planes, adapted from [49].

In general the interaction between vortices and defects within the crystal structure determines most of the H-T phase diagram [49]. The solid phase, the Abrikosov lattice, is a highly ordered phase which takes place at sufficiently low temperature below T_C. Small-scale defects like oxygen vacancies or interstitial defects can act as pinning sources inducing a further change to the vortex glass phase. A first-order transition from the solid to the liquid phase occurs at a temperature T (depending on the applied field) close to T_C due to thermal fluctuations. The liquid phase is characterized by short-range interactions and the vortices are free to move.

YBCO Structure

As evidenced by the formula $YBa_2Cu_3O_{7-\delta}$, variation in the oxygen content ($0\leq\delta\leq1$) is possible. This has deep consequences on the structural, magnetic and transport properties of this material. In first approximation the crystal lattice can be described as a stack of three perovskite structures so the *c* axis will be about three times the *a* and *b* axis. For $\delta=0$ the structure is a defect orthorhombic perovskite, in which oxygen atoms play four different roles, as shown on Fig 1.5a. Two substructures can be defined to describe the properties of YBCO; Cu-O chains are given by Cu1 and O1 according to the figure, while Cu2, O2, O3 atoms are located in the so called Cu-O planes. This structure defines the high-temperature superconducting phase. For $\delta=1$ the structure, showed in Fig 1.5b, is tetragonal ($a=b$) and the oxygen on site O1 is missing. Increasing the oxygen content, the two equivalent O1 position near Cu1 are randomly occupied. Around $\delta=0.6$ and at room temperature oxygen atoms tend to form chains along the *b* axis causing the transition to the orthorhombic structure; in this case the lattice parameters are: $a=3.823$Å, $b=3.866$Å, $c=11.676$Å. The orthorhombic order is in itself divided into several phases characterized by different oxygen ordering; the Ortho-I and Ortho-II are the most well known. Ortho-I has identical oxygen chains along the *b* axis, i.e. every *b*-axis chain is occupied. In the Ortho-II phase *b*-axis chains occupied by oxygen atoms are alternated to unoccupied chains. As a consequence of its orthorhombic crystal symmetry, YBCO can often present twinned structure with twin boundaries running at 45^o with respect to the major axis in the *ab* plane. Twins are related by a nearly 90° rotation of the [100] and [010] lattice planes about the [001] axis across the interfaces.

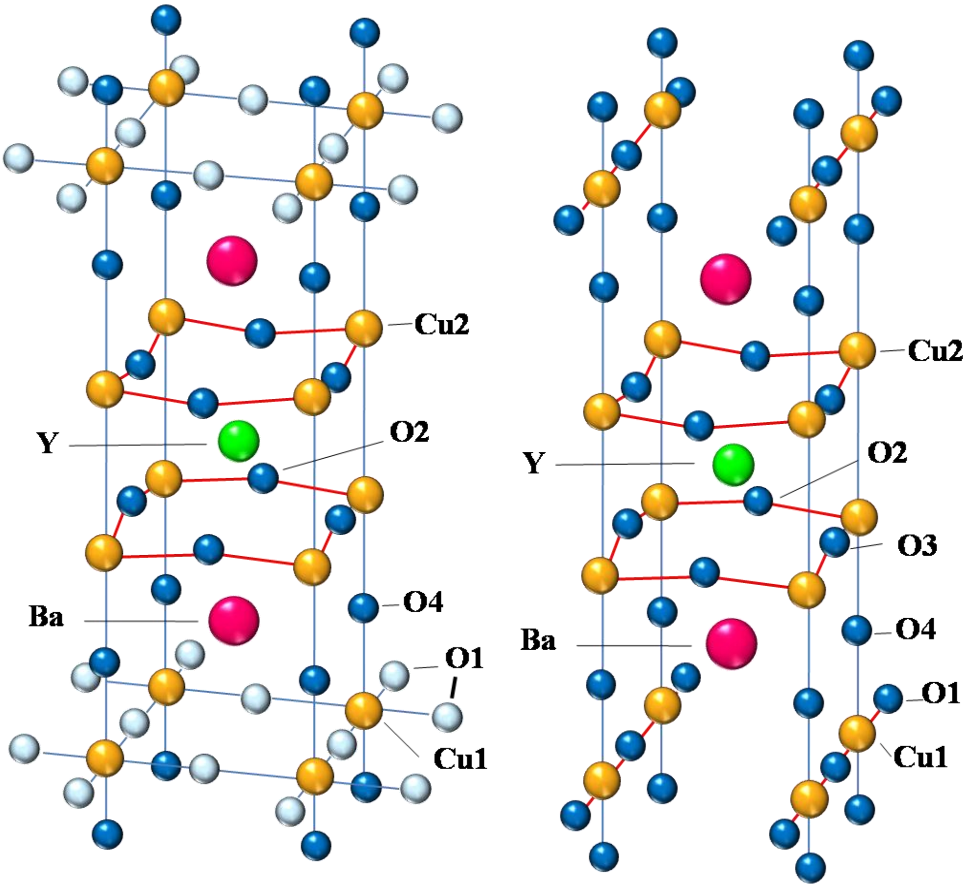

Fig 1.5: Image adapted from [50]. (a) Structure of $YBa_2Cu_3O_6$; oxygen atoms on sites denoted by light colored spheres are missing. $YBa_2Cu_3O_7$; the higher critical temperature is obtained by including a small fraction of oxygen vacancies in this structure.

Superconductivity of YBCO

Investigation of c-axis charge dynamics and transport has provided strong evidence for charge confinement on the CuO_2 plane. The CuO_2 sheets are separated from each other by ionic blocking layers. Although it has one conduction electron (or hole) per Cu site, each CuO_2 sheet is originally insulating because of the large electron correlation. That behavior is typical of the Mott-insulator state in which all the conduction electrons are tied to the atomic sites. The superconducting state emerges when holes from the blocking layers dope the CuO_2 layers in a way that alters the number of conduction electrons and triggers the Mott transition. Researchers believe that the strong antiferromagnetic correlation which originate in the Mott-insulating CuO_2 sheet, and persists into the metallic state, is most responsible for the mechanism of the high-T_C superconductivity. In the superconducting state large anisotropy in the penetration depth and the superconducting coherence length is observed.

Anisotropy of YBCO

Many phase-sensitive pairing symmetry experiments provided clear evidence for *d*-wave pair state in several cuprate superconductors [51], although it has been also argued that at very low temperature a transition between a full *d*-wave state ($d_{x^2-y^2}$) to a mixed state ($d_{x^2-y^2}+is$ or $d_{x^2-y^2}+id_{xy}$) can occur. The *d*-wave symmetry of the gap can be visualized by a cylindrical structure with lobes oriented along the *a* and *b* crystal axis and nodes, as showed in Fig 1.6 at right, where the gap is zero, at 45 degrees to the *a* or *b* direction ([110] direction). Using SQUID microscope images of a series of YBCO-Nb 2-junction rings, the position of the in-plane nodes in YBCO has been determined by the presence or absence of the half-flux quantum effect, showing that the gap has predominantly *d*-wave symmetry and confirming the small size, if any, of an imaginary component (id_{xy}, *is* or *ip*) to the gap [52]. On the other hand, non-phase sensitive techniques can be also used. In high-temperature copper-oxide superconductors, the gap seen in ARPES exhibits *d*-wave anisotropy in momentum space - smallest along nodal direction ((0, 0) - (π, π)) and largest near the anti-nodal point (π, 0).

The type II superconductors are characterized by the extreme values of *k*, for example k=100 for YBCO. The reason for this lies in the very small coherence length ξ and the large penetration depth λ in the cuprates. The structure of the vortex depends on the relative orientation of the magnetic field respectively to the crystal axes of the material. Therefore, we can define distinct length scales for a vortex in the mixed state. The radius of a vortex in the *ab*-plane is defined by ξ_{ab} and ξ_c if the vortex is orientated along the *c*-axes. The penetration length λ_{ab} and λ_c describes the currents circulating around a flux line in the directions *ab* and *c*, respectively. In the following table, the in plane and out of plane parameters are listed for YBCO at T=0K.

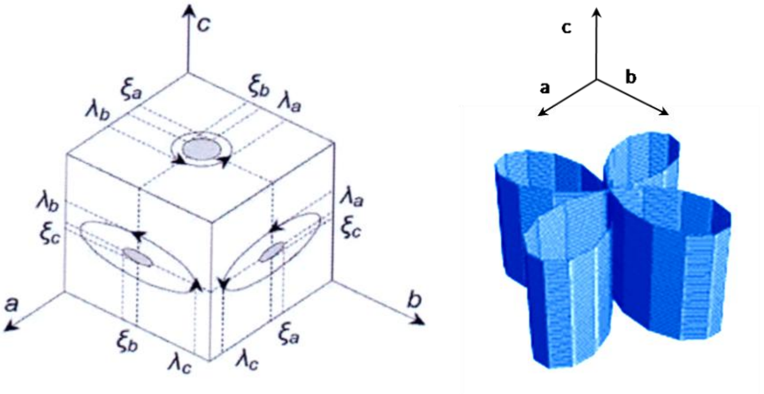

Fig 1.6 : (left) asymmetry of the vortex in YBCO. (right) diagram of the *d*-wave symmetry of the gap.

parameter	c	a,b
λ(nm)	890	135
ξ (nm)	0.24	1.6

Table 1.1 : Anisotropic coherence length ξ and penetration depth λ for in plane (*a*,*b*) and out-of plane (*c*) directions.

The phase diagram of YBCO

In the HTS context, the $La_{2-x}Sr_xCuO_4$ (LSCO) phase diagram is usually considered as the universal diagram for cuprates. A schematic temperature vs doping phase diagram of the YBCO is given in Fig.1.7, adapted from references [53,54]. When undoped, the copper-oxygen planes have an odd number of electrons. According to standard band theory (which works for most materials), it should have an unfilled band and thus be a metal. The parent compounds of the cuprates are not only not-metals, but are insulators with a very healthy gap. This is because the on-site repulsion U is very large. The large U per copper site prevents the electrons from tunneling from site to site, effectively leaving one valence electron per copper site. The material is insulating due to strong correlation effects. An effective antiferromagnetic interaction between the spins of the neighboring localized spins, which prefer to line up antiparallel to each other, is realized. The reason that the interaction is antiferromagnetic is that if the spins are aligned parallel to each other, the Pauli exclusion principle prohibits tunneling, be it virtual or real. This prohibition vitiates the possible lowering of kinetic energy due to localization. If the spins are antiferromagnetic aligned neighboring sites, then tunneling fluctuations and their concomitant energy reduction can and does occur. This is the reason why the half filled, or undoped, cuprates are antiferromagnetically ordered Mott insulators.

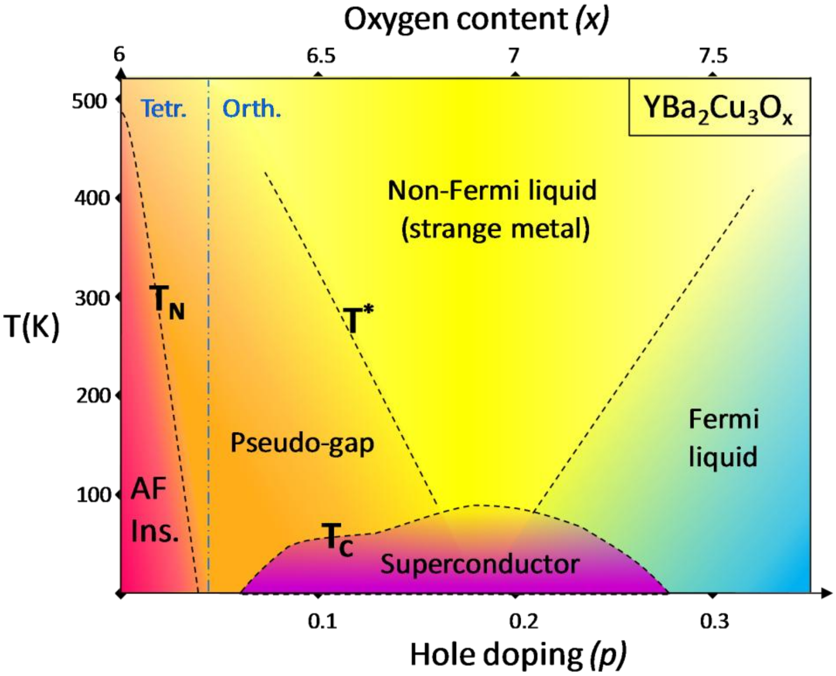

Fig.1.7 : Schematic temperature vs doping phase diagram of the YBCO adapted from references [53,54]

The Pseudogap

The metallic state above the superconducting T_C deviates from the Fermi liquid behavior and displays anomalous properties. Essentially, an energy gap appears in some properties and not others, what gives rise to the denomination of *pseudogap* state. The pseudogap is a normal state precursor of the superconducting gap due to local, dynamic pairing correlations in a state without long range phase coherence (some regions of the phase diagram contain effects similar to superconductivity like a partial suppression of electronic density of states) (see Fig.1.7). Indeed a large suppression of (but not strictly zero) low frequency spectral weight at $T > T_C$ was experimentally observed using different techniques (NMR, specific heat, μSR, etc) [55-57]. ARPES measurements revealed that the pseudogap phenomenon itself exhibits a *d*-wave symmetry which is smoothly connected to the *d*-wave superconducting gap [58-60]. Early theoretical works also demonstrated that antiferromagnetic spin fluctuations lead to pseudogap in the electronic spectrum [61].

1. 3. CMR manganites: the $La_{0.7}Ca_{0.3}MnO_3$

Manganites also belong to the family of strongly correlated transition metal oxides. In fact strong coupling between, charge, spin and lattice degrees of freedom produces a variety of phases in a chemically homogeneous material. In transition metal ions *d* electrons experience competing forces: Coulomb repulsion tends to localize individual electrons at atomic lattice sites, while hybridization with oxygen *p* electron states tends to delocalize electrons [63]. Their properties are strongly dependent on doping and disorder and the phase diagram of each compound often displays a great number of phase boundaries. Manganites can be represented by the general formula $A_{1-x}B_xMnO_3$ where A is a large rare earth trivalent cation and B is a divalent alkaline cation. The mixed valence oxides can be regarded as solid solutions between end members; the compound used in this work follows the formula $La_{0.7}Ca_{0.3}MnO_3$ (LCMO) with the formal end member valence states $La^{3+}Mn^{3+}O_3^{2-}$ and $Ca^{2+}Mn^{4+}O_3^{2-}$. The first intense study of the structural, electric and magnetic properties of manganite of the type $La_{0.7}B_{0.3}MnO_3$ was made by Jonker and van Santen in 1950 on polycrystalline samples [64,65]. In their work they captured some of the most important results about the intermixing of Mn^{3+} and Mn^{4+} and the effect on the magnetic/conducting state of the sample although interpreted on the basis of short range interactions. They also underlined the importance of the oxygen content and doping on the Mn valence measuring the Curie temperature (which coincide with the metal-insulator transition) and saturation magnetization of several compounds and finding a correlation between the conducting and ferromagnetic state of the manganites. In 1954 Volger first reported on the negative magnetoresistance of the $La_{0.8}Sr_{0.2}MnO_3$ [66]. This magnetoresistance showed a peak close to the Curie temperature which will be then recognized as a typical behavior in manganites.

Colossal magnetoresistance

The magnetoresistance (MR) is defined as the change in the resistance due to the application of a magnetic field: $MR = \frac{R_H - R_0}{R_0}$. The change observed by Volger was quite small (10%), probably due to the polycrystalline nature of the sample and the method of fabrication. Only in the '90s it was possible to improve the MR effect thanks to the development of growing techniques for high quality thin films. In 1994 Jin et al. [67] obtained 100000% value of MR at low temperature in a $La_{0.67}Ca_{0.33}MnO_3$ thin film grown on $LaAlO_3$, that they called *colossal magnetoresistance* (CMR). This fact, together with the renewed general interest on complex oxides, the possibility of making layered heterostructures and the advent of high T_C superconductivity concurred to renovate the interest in these materials.

The phase diagram of LCMO

A fundamental contribution in the understanding of the phase diagram of manganites was given by Wollan and Koehler in 1955 [68]. They presented and extended neutron diffraction analysis of the La,Ca manganite and showed the existence of unexpected complex phases (including charge and orbital order) and several different magnetic structures (for example the CE type) depending on the doping content. Fig.1.8 shows the temperature vs Ca content phase diagram for the $La_{1-x}Ca_xMnO_3$ series [69].

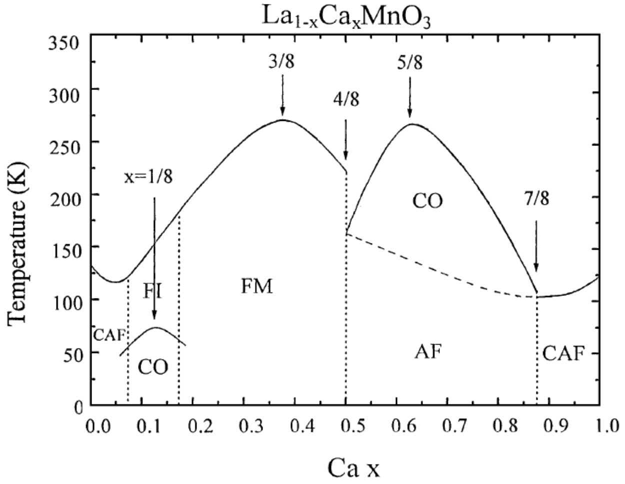

Fig.1.8 : Phase diagram of the $La_{1-x}Ca_xMnO_3$ [62]

The presence of so many phases is a consequence of the strong correlation between the crystal structure and the fraction of Mn^{4+} and Mn^{3+}. As we can see the specific compound $La_{0.7}Ca_{0.3}MnO_3$ becomes ferromagnetic at a relative high temperature (270ºK).

Structure of the LCMO

The crystal structure of the LCMO is a cubic perovskite: in Fig. 1.9 we show the undistorted structure where Mn atoms occupy the four corners of the cube while the central position is occupied either by La or Ca randomly distributed in the whole crystal according to the stoichiometry. Each Mn ion is placed at the center of an O octahedron forming a MnO_6 structure.

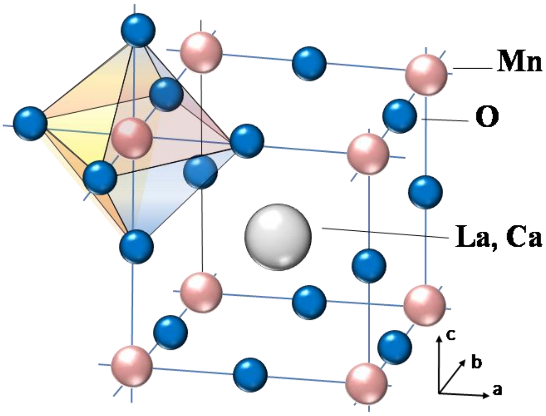

Fig. 1.9: Ideal crystal structure of the LCMO

A wide range of divalent cations can occupy the body-center position like Ca, Sr, Ba, Pb. This ideal cubic structure is distorted by cation size mismatch; the distortion may affect the oxygen octahedron itself (by deformation) or the relative orientation between adjacent octahedra (by cooperative tilting). This effect is called the Jahn-Teller distortion and yields to the splitting of the energy levels in order to lower the energy of the system. The JT effect in manganites arises from an electronic instability inherent to the Mn^{3+} ions in asymmetric MnO_6 octahedra. In the cubic lattice environment, the five-fold degenerate 3*d*-orbitals of an isolated atom or ion are split into a manifold of three lower energy levels, usually referred to as t_{2g}, once mixing with the surrounding oxygens is included, and two higher energy states called e_g .Fig.1.10 shows the orbitals resulting from the final energy split.

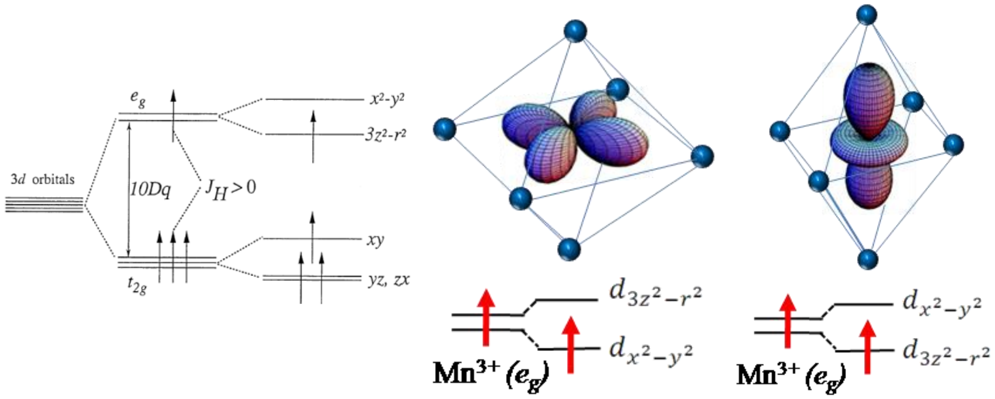

Fig.1.10 Field splitting of the five-fold degenerate atomic 3d levels into lower t_{2g} and higher e_g levels [70].

The distortion lifts the degeneracy of the e_g orbital and favors the occupation either of $d_{x^2-y^2}$ or $d_{3z^2-r^2}$. Since neighboring octahedra share one oxygen ion, the JT distortion can be cooperative. The cooperative rotation of MnO_6 octahedra leads to a change in lattice symmetry. This is usually accompanied by the shortening and stretching of the six Mn-O bonds. Consequently, the resulting various JT distortion modes lead to different electronic structures for the e_g states of Mn^{3+} ions (see Fig.1.11). The end-member compounds such as $LaMnO_3$ have a distorted perovskite structure where the Fermi level falls in a gap between the two Jahn-Teller split e_g bands.

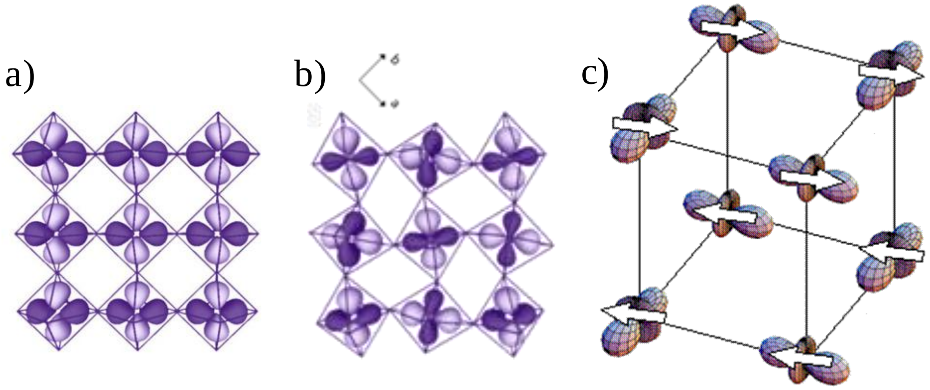

Fig.1.11 a) Undistorted perovskite structure, b) cooperative tilting of the octahedrons, c) prototypical e_g orbital ordering of $LaMnO_3$.

A local linear combination of those orbitals produces the stable states $d_{3y^2-y^2}$ $d_{3x^2-r^2}$ alternate on the Mn sites leading to orbital ordering on the *xy* plane and antiferromagnetic ordering in the z direction. By adding holes, that is equivalent to dope, for example, with Ca, a mixture of Mn^{4+} and Mn^{3+} is introduced in the sample. The number of electrons in the *d* band is altered as well as the interatomic distances and bond angles. This causes a strong reduction of the JT distortion which has dramatic consequences on the magnetic and metallic state of the compound. Moving towards a Ca content of x=0.5 the crystal structure approximates a stable cubic perovskite [64] and the material shows ferromagnetic-metallic behavior. In view of the strong intra-atomic Hund coupling, the metallic behavior found an explanation thanks to Zener's model of double exchange [71]. He considered the problem of the exchange between Mn^{3}+ and Mn^{4+} ions via an oxygen ion and introduced the concept of simultaneous transfer of an electron from the Mn^{3+} to the oxygen and from the oxygen to the neighbouring Mn^{4+}. The Hund coupling requires the spin of all the electrons involved in the simultaneous hopping to be parallel, what would explain the ferromagnetic interaction (see Fig. 1.12). The hopping intensity (or transfer integral) t is modulated by a factor that depends on the relative angle between the spins: $t = t_0 \cos(\theta/2)$, describing that for parallel spins the hopping is favored.

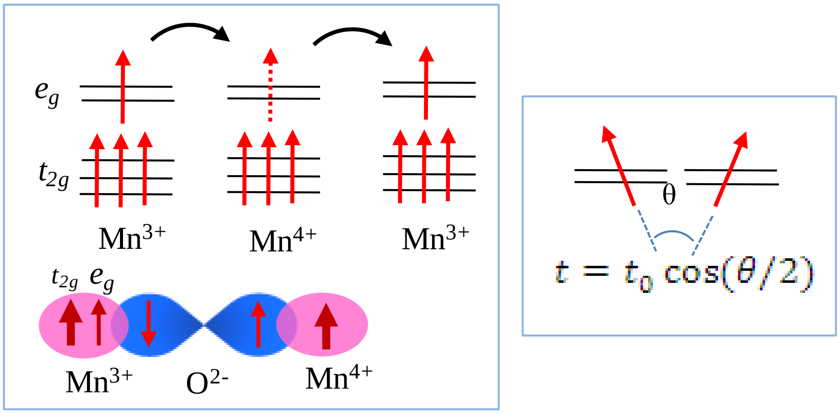

Fig. 1.12 : Left: schematic diagram illustrating the mechanism of the double exchange. Right: the hopping integral *t* depends on the relative angle between the spins.

If the localized spins in the one-orbital model for manganites are polarized, let`s say, up, then conduction electrons with up spins can move freely while conduction electrons with down spin cannot readily hop due to the large Hund coupling that prevents their movement. In other words the conduction electrons at the Fermi level are 100% polarized at low temperature. Among the manganites, $La_{1-x}Ca_xMnO_3$ and $La_{1-x}Sr_xMnO_3$ may have half-metallic character, although how close to 100% is the polarization is still under debate. Due to its ferromagnetic behavior at room temperature the $La_{1-x}Sr_xMnO_3$ has been largely used to probe the half metallicity of CMR manganites [72-74].

The hopping angle is then determined not only by the fraction of Mn^{4+} and Mn^{3+} in the sample but also by the temperature. Above the Curie temperature T_C spins are dynamically disordered and the paramagnetic insulator state emerges. Nevertheless below T_C but close to it, spins can be easily aligned by applying a magnetic field. This can be regarded as one of the concomitant agents for the occurrence of the colossal magnetoresistance. Another quantity affected by the JT distortion is the tight-binding bandwidth $W= 2zt$, where t is the transfer integral and z is the number of manganese nearest neighbors. The e_g bandwidth W is in fact sensitive to Mn-O distances and Mn-O-Mn bond angles [75]. The $La_{1-x}Ca_xMnO_3$ can be labeled as *intermediate-bandwidth* manganite to distinguish it from the truly low-bandwidth compound $Pr_{1-x}Ca_xMnO_3$ where a metallic ferromagnetic phase can only be stabilized by the application of magnetic fields and from the large bandwidth $La_{1-x}Sr_xMnO_3$ which shows robust ferromagnetism at room temperature but with reduced CMR effect.

Phase separation

A wide variety of experimental results and theoretical investigations have convincingly demonstrated that magnetic phases in mixed-valence manganites are not spatially homogeneous. These inhomogeneities are intrinsic features of single crystals, not related to grain boundary effects of policrystals. Theoretical investigations [69,76,77] show that, in a broad region of parameter space, the ground state is actually a nanoscale mixture of phases, particularly in the presence of quenched disorder. The two key competing states in manganites, ferromagnetic (FM) metallic and antiferromagnetic (AF) insulating (AFI), mix up in a temperature range between the Curie and the Neél temperature. In this regime, perturbations such

as small magnetic fields can have dramatic consequences, because they only need to align the randomly oriented magnetic moments of preformed nanosize FM clusters to render the system globally ferromagnetic (see 78 and references there in). This nanoscale phase separation is commonly regarded as the origin of the CMR effect and has been corroborated by several experimental results.
Some of the relevant experiments are listed below, for the case of La,Ca manganites:

- experiments with neutron diffraction showed anomalies below T_C [79] which might be explained by the two phase state.
- for the FM metalic phase (at $T<T_C$) hints exist for charge inhomogeneities; transport measurements were realized by Jaime et al. [80] including not only free electrons but also polarons.
- measurements of muon spin- relaxation and resistivity by Heffner et al. showed the effect of polarons on the spin and charge dynamics interpreted as spatially inhomogeneous Mn-ion correlation times [81] .
- for similar parameters and through magnetic resonance experiments, Allodi et al. [82] reported the coexistence of FM and AFM microdomains without spin canting.
- Lynn [83] and De Teresa et al. [84], observed at $T>T_C$ a short FM correlation length (magnetic polarons) through SANS measurements for a Ca concentration of x=1/3
- for a concentration of x=0.05 and 0.08 at low temperature, Hennion et al. [85] observed the existence of a disordered distribution of FM ’droplets’ by low angle neutron scattering experiment (SANS)
- through Raman spectroscopy, Yoon et al. [86] found localized states in the FM metallic phase at low T
- X-ray absorption by Booth et al.[67] shows evidence for localized and delocalized vacants at T<TC. [87].

Anisotropy of the LCMO

Magnetic anisotropy of LCMO has been discussed controversially in the literature since magnetic anisotropy, as many other properties in lanthanum manganites is strongly related to the thickness of the film, the doping and the degree of strain. Stoner and Wohlfarth modeled a mechanism of magnetic hysteresis for heterogeneous alloys based on the simplified problem of a single spheroidal particle

[88]. As it is shown in Fig.1.13 the remanence and the coercive field are smaller for a 45° loop in comparison to the 0° loop. This will be taken as a measure to identify the in-plane easy axis in thin films.

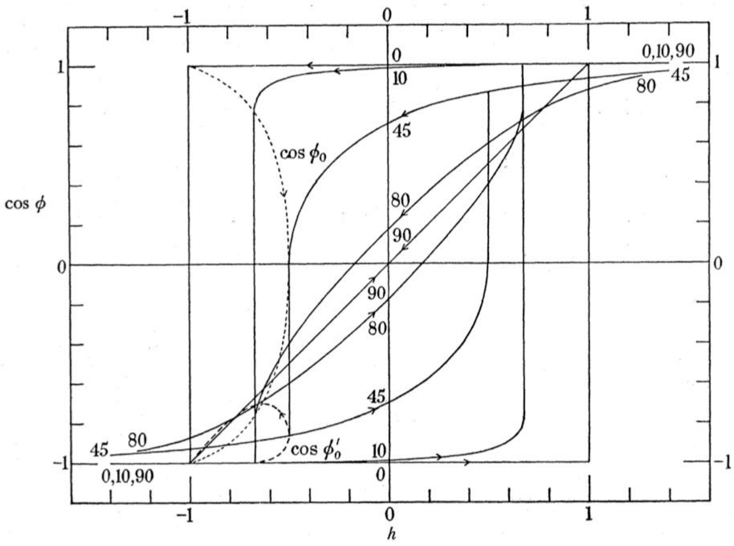

Fig.1.13 : Magnetization curves for a prolate spheriod for the Stoner-Wohlfarth model [88]. The hysteresis loops are shown for angles 0, 10, 45, 80 and 90° between the polar axis of the spheriod and the direction of the field.

It has been showed that in bulk LSMO magnetic anisotropy leads to the easy axis along the (111) direction and only when the thickness is reduced the easy axis would be projected along the [110] direction. For thin films the magnetic anisotropy can be strongly influenced by the lattice mismatch with the substrate. It is well known that ferromagnetic La manganites grown on $LaAlO_3$ display perpendicular anisotropy due to the in-plane compressive strain induced by the smaller lattice parameters of the LAO substrate. In the case of LCMO thin film grown on STO contradictory results have been found by different groups [89-93] yielding different directions for the easy axis. This fact can be justified by the use of different growth technique introducing different types of structural defects and by the extreme sensitivity of the crystal parameters to the oxygen and calcium content. Although the much better studied LSMO showed [110] easy axis, the majority of research studies involving magnetometry and field dependent transport properties of heterostructures and thin film containing LCMO has been carried out applying the magnetic field along the [100] substrate direction. LCMO effectively shows small changes in magnetization hysteresis loops which don't seem to affect certain kind of investigation like the study of CMR effect.

In thin films the anisotropy may be turned by artificial structures of the substrate. Magnetic domains may be orientated, for example, along steps on the substrate/film interface induced by the production miscuts in the substrate [94]. Uniaxial magnetization can be induced in $La_{0.67}Sr_{0.33}MnO_3$ films on STO at room temperature along the step edges but at low temperature a biaxial (crystalline) anisotropy appears with easy and hard axis along the [110] and [100] directions, respectively[95]. A study on $La_{0.7}Sr_{0.3}MnO_3$ on (110) STO shows that the in-plane easy axis lies in [001] and the strength can be tuned by varying film thickness [96] with the conclusion that relaxation with a resulting anisotropic stress determines the magnitude of the in-plane magnetic anisotropy in this case.

1. 4. Interplay between ferromagnetism and superconductivity at YBCO/LCMO interface.

Ferromagnetic (F) and superconducting (S) orders are antagonistic in the sense that ferromagnetism produces parallel and superconductivity antiparallel alignment of the spins. When a superconductor is placed in contact with a ferromagnet both long-range phenomena compete at the interface [97,98], giving rise to a variety of exotic phenomena like π junctions, spatially modulated order parameter, etc. [99-101]. There has been substantial activity in the past directed to study the F-S interplay in heterostructures containing transition metal superconductors (low T_c) and ferromagnets [102-109]. In many cases the F-S competition is obscured by interface disorder like roughness, interdiffusion, or interface alloying.

With the re-discovery of colossal magnetoresistance (CMR) materials there has been renewed activity in the field with heterostructures involving high-T_C superconductors (HTS) and CMR materials, [110-115]. As noticed earlier,,$YBa_2Cu_3O_{7-\delta}$ (YBCO) and $La_{0.7}Ca_{0.3}MnO_3$ (LCMO) incorporate a number of interesting new ingredients including similar crystalline structure, well-matching lattice parameters and good chemical compatibility which allows the growth of highly perfect interfaces, despite the larger complexity of these materials as compared to single-element or alloy transition metals. The short coherence length of the HTSs and the *d*-wave pairing symmetry, the high degree of spin polarization of the $La_{0.7}Ca_{0.3}MnO_3$ (LCMO) conduction band make this system an adequate candidate for the search for spin-dependent effects in transport.

The F-S interaction may be understood in two different scenarios: on the one hand the Cooper pairs of the superconductor may enter the ferromagnet (proximity effect) or spins of the ferromagnet may enter the superconductor. The latter situation will give rise to different physics depending on whether the electrons have energies larger (spin diffusion) or smaller (quasiparticle evanescent waves) than the superconducting gap.

The problem of the YBCO/LCMO interface will be introduced through a short description of the more general problems of the interface between a normal metal and a superconductor (N/S).

The N/S interface

It has been shown that near the *N/S* interface the superconductivity is suppressed over the correlation length ξ_S, meaning that the order parameter Δ is reduced at the interface in comparison with its bulk value. At the same time, the superconducting condensate penetrates the normal metal over the length ξ_N [116], which at low temperatures may be much larger than ξ_S; this is the so called *proximity effect* [117] Fig.1.14. The occurrence of the proximity effect depends on the intrinsic properties of the two materials and the quality of the interface. The problem of how the gap function $\mathit{\Delta}$ (the order parameter) propagates from the S to the N side has been well studied under a number of different circumstances that considered all these parameters [118,119]. The main theoretical result and experimental evidence is that if the thickness of the superconducting layer is less than a critical one the transition temperature will be reduced compared to that of a clean bulk superconductor. The length scale of the depression of the superconductivity (the penetration length) can be affected by basic properties of the interface, like the interface transparency. The interface transparency takes into account all the effects that cause electrons to be reflected rather than transmitted at the interface resulting in screening of the proximity effect. In principle the transparency can depend on both extrinsic and intrinsic factors such as, for example, interface imperfections, fabrication methods, Fermi velocities and band-structure mismatches. On the other hand the length of the condensate penetration into the *N* region ξ_N can be also restricted by decoherence processes (inelastic or spin-flip scattering) [120].

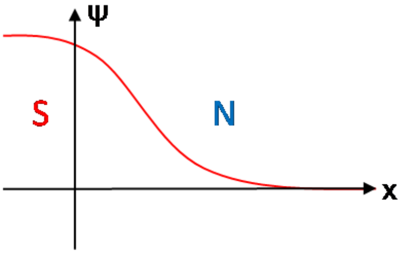

Fig.1.14: Schematic diagram of the superconducting proximity effect

For arbitrary transparency one has to consider also the “clean” or “dirty” limit, represented by the relation between l and ξ, the electron mean free path and the coherence length respectively. In the clean limit (that is for a pure metal or superconductor) $l>\xi$ and the electron or Cooper amplitude travels ballistically over the distance

$$\xi_C = \frac{\hbar v_F}{2\pi kT} . \qquad 1.15$$

In the dirty limit $l<\xi$ and at the N/S interface the leakage of the superconductivity is controlled by diffusion processes. So a diffusion coefficient, which is defined as $D = v_F l / 3$, has to be introduced. The coherence length in this case is given by

$$\xi_D = \sqrt{\frac{\hbar v_F l}{6\pi kT}} . \qquad 1.16$$

This expression is valid both for the normal metal and the superconductor assuming in the last case that T is the superconducting transition temperature. In the normal metal the distance covered by the diffusive electron’s motion is proportional to ξ_D.

The temperature-dependent form of the coherence length in the case of the superconductor is give by $\xi_S(T) = \frac{\pi}{2}\xi_D\sqrt{(1-T/T_C)}$ and it is often called the Ginzburg-Landau coherence length.

Under the hypothesis of a *dirty* type II superconductor, Usadel derived diffusion equations for an arbitrary value of the order parameter, taking advantage of the fact that a short mean free path leads to a nearly isotropic motion of the electrons [121]. Due to the great progress in the preparation of high-quality heterostructures, the observation of these interfacial effects reached an impressive level of precision.

The Andreev reflection

The process of Andreev reflection provides the microscopic mechanism of the proximity effect. The conduction of an N/S interface is determined by the processes that transform normal current into superconducting current. The microscopic mechanism that convert single-electron states of the normal metal into Cooper pairs have been described first by Andreev [122]. Andreev realized that an electron (or hole) of energy $E<\Delta$ approaching the N/S interface from the N side can be reflected as a hole (or electron), provided that the length scale over which Δ varies is much larger than the Fermi wavelength. The problem of a forbidden single electron penetration in the superconducting condensate is converted into a two-electron process. In fact the reflected hole possesses the same moment (retro-reflection) but opposite spin of the incident electron and it is associated to a missing electron; the corresponding charge $|2e|$ is transferred to the superconductor as a Cooper pair (see Fig. 1.15). This is the *Andreev reflection.* To account for arbitrary transparency the Blonder-Tinkham-Klapwijk (BTK) model [123] considers a barrier of strength Z ranging from 0 for a perfect metallic contact to ∞ for a low-transparency tunnel barrier. This not only yields to a generalization of the N/I/S tunnel problem but, since the sub-gap conductance results to be twice the normal state conductance, through the study of the I-V characteristics it allows calculating the *excess current* predicted by the Andreev reflection model. Upon the BTK approach the Andreev reflection appears as a low-barrier N/S tunneling limit.

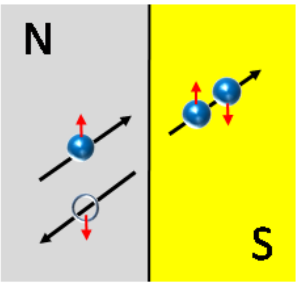

Fig. 1.15 : Diagram of the Andreev reflection

The F/S interface

While in the case of the N/S interface we were assuming that the electron-electron interaction was negligible inside the normal metal to allow a simplified discussion on the N/S proximity effect, in the case of the F/S interface we have to abandon every simplification on this aspect. In fact itinerant ferromagnetic metals represent an example of a system with strong electron-electron interaction leading to an order state of electron spins. The Andreev reflection picture is strongly modified because the incoming electron and the Andreev reflected hole occupy opposite spin bands. While in a classical Andreev reflection between a pure metal and a BCS superconductor the spin degree of freedom can be ignored, at the F/S interface the energy band splitting provoke a significant reduction of the proximity effect consisting in the reduced value of the excess current and a reduced propagation of the order parameter in the F side. The exchange interaction between the electrons and magnetic moments in a ferromagnet may be considered as an effective Zeeman field. This leads to an energy splitting ΔE_{ex} for spins parallel or antiparallel to the magnetization which causes the pairing amplitude to decay. If the degree of spin polarization increases, the distance over which superconductivity can penetrate is further shortened and becomes zero for a half metal since the injected current has only one of the spin orientations [124].

One of the most striking features of the F/S proximity effect is that the Cooper pair wave function extends from superconductor to ferromagnetic with damped oscillatory behavior (see Fig. 1.16). As a consequence of this effect, new effects have been predicted, such as oscillations in the electron density of states, non-monotonic dependence of the superconducting critical temperature in F/S multilayers on the ferromagnet layer thickness and the realization of ’π’ Josephson junctions in S/F/S systems [98] . The physical origin of the oscillations has been explained for a generic s-wave superconductor in terms of the cosine dependence of the pair wave function modulation factor in the ferromagnet [125], which takes into account the angle between the pair moment and the normal to the F/S interface. On the other hand, when electrons of the ferromagnet with energy larger than the superconducting gap enter the superconductor, superconductivity is depressed due to breaking of the time-reversal symmetry of the Cooper pairs.

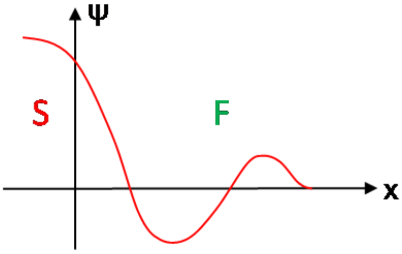

Fig. 1.16 : Schematic behavior of the superconducting wave function at the F/S interface.

The current injected from the ferromagnet is spin polarized and causes a non-equilibrium spin density to build up in the quasiparticle density of states of the superconductor, which causes the quasi Fermi levels for spin down and spin up to be displaced in opposite directions by $\delta\mu$ [98,124]. This non equilibrium spin density affects superconductivity in a similar way as an exchange field of Zeeman energy $2\delta\mu$ [128], and the energy $2\delta\mu$ plays the role of a pair-breaking energy [129] .Electrons of the ferromagnet with energies smaller than the superconducting gap will enter the superconductor as quasiparticle evanescent waves (see Fig.1.17 (left)). With respect to the penetration length of spin-polarized electrons, we have to distinguish between above-gap and below-gap energies. Electrons with energies larger than the superconducting gap will diffuse with the spin diffusion length, while electrons with energies below the gap have a characteristic penetration depth which is close to the dirty limit coherence length of the superconductor. The increased number of quasiparticles within this length scale results (self-consistently) in a suppression of the superconducting gap. This mechanism has been experimentally found to take place in permalloy/Nb heterostructures with transport measured perpendicular to the layers by Gu *et al.*[130]. In this way, the interaction between F and S has three characteristic length scales: the coherence length of the ferromagnetic metal (proximity effect), the spin diffusion length (spin injection), and the superconducting coherence length (subgap quasiparticle diffusion), which will all typically be in the nanometer range. In the diffusive limit the coherence length in the ferromagnetic side takes the form: $\xi_F = \sqrt{\frac{D}{h}}$

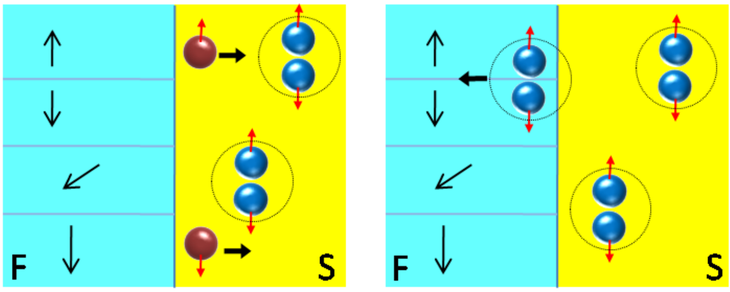

Fig.1.17 : Diffusion of spin-polarized quasiparticles (left), superconducting proximity effect (right).

The YBCO/LCMO interface

The problem of the F/S interface has been faced using all sorts of materials, starting with ferromagnetic/superconducting single transition metals or compound and passing through complex oxides. The interface between oxides with perovskite structure it's a subject of great interest in the recent scientific investigation due to the possibility of playing with the multiple phases offered by these complex systems. The present work is focused on the interplay between ferromagnetism and superconductivity in YBCO/LCMO hybrids. This kind of interface showed interesting physical phenomena arising from an effective coupling between the two competing orders.

YBCO and LCMO can be successfully grown in high quality layered heterostructures which, thanks to the reduced layer thickness, allows the study of interface effects. In addition high-T_C superconductors and CMR manganites are interesting candidate materials to the development of new spin-based electronics because the low carrier density of the HTS and the almost full spin polarization of the CMR oxides can be combined to yield high sensitivity, fast devices. A first signal of F/S coupling is in general given by the reduction of the critical current consistent with suppression of superconductivity by spin-polarized quasiparticle injection. This evidence has been reported by several groups in recent years [131-133], opening the door to practical devices based on complex oxides.

Interface properties are expected to play a dominant role in the physics of CMR/HTS F/S heterostructures, and extrinsic (interface alloying or roughness) or intrinsic factors (proximity effect) may deeply influence the performance of the devices . The presence of magnetism and superconductivity in these kinds of samples has been reported before [110-114]. It has been demonstrated that in YBCO/LCMO hybrids the systematic depression of the critical temperature when the YBCO thickness is reduced does not result of extrinsic factors like deoxygenation or roughness. A T_C depression results over relatively long-length scales in the superconductor, which has been theoretically addressed by Radovic *et al.*, [97,134] and experimentally observed in metallic superlattices by several groups [103]. In our system, due to the short YBCO coherence length (0.1–0.3 nm), *S* layers are expected to sustain superconductivity down to a much thinner thickness than in the case of conventional (low-temperature) superconductors. On the other hand, the *F* material LCMO shows a large exchange splitting (3 eV) and relatively small bandwidth, giving rise to a fully spin-polarized conduction band [135], which may suppress superconducting proximity effect into LCMO over very short length scales (small ξ_F). On the other hand, superconductivity induced within the *F* layer decays with a length scale $\xi_F = v_F / \mathrm{D}_{Eex}$. Given the large exchange splitting of the LCMO (3 eV) and a Fermi velocity for the majority band of 7.43×10^7 cm/s,[135] the former expression yields very small values for ξ_F of about 0.2 nm. Therefore, the large exchange splitting of the manganite strongly does not support the superconducting proximity effect. It has been speculate that the injection of spin-polarized carriers from LCMO into YBCO may add a new source of superconductivity depression: pair breaking by spin-polarized carriers.

This mechanism has been theoretically analyzed before [136]. In the recently observed depression of the critical current with the injected spin-polarized current in manganite/HTS junctions [131,133] the injection of spin-polarized carriers over the superconducting gap depresses the order parameter monotonically with the increasing quasiparticle density. At low temperatures where the thermally induced quasiparticle density is small, recombination of injected spin-polarized carriers requires spin flip scattering what considerably increases their diffusion time. This pair breaking effect extends over the spin diffusion length (l_S) into the superconductor which can be very long; for example, a value of the order of 1 cm has been reported for Al. An estimate of l_S in YBCO can be obtained following Ref. 133. A much shorter coherence length of YBCO compared to low-T_C superconductors allows superconductivity to exist down to quite small thicknesses in presence of magnetic layers.

In summary, due to the complexity of the YBCO/LCMO interface several different experiments are required to clearly understand the physical phenomena occurring. Although a multitude of experiments is reported in literature the picture is far from being complete due to the continuous emergence of new effects. The experiments presented in this thesis (see chapter 3) contribute to the understanding of the interplay between ferromagnetism and superconductivity at the YBCO/LCMO interface through the analysis of the effect of the magnetic anisotropy of the LCMO on the inverse superconducting spin switch, as the realization of the transport of spin-polarized quasiparticles at the F/S interface. Through the use of extremely precise depth sensitive techniques (XRR, PNR, XMCD) combined to magnetotransport, AFM and FMR measurements, we are able to weigh up the importance of the effects that may be present at the YBCO/LCMO interface (diffusion of spin-polarized quasi-particles, proximity effect, stray fields, vortex pinning, etc.).

References

1. M. Bibes and A. Barthelemy. Oxide spintronics. IEEE transactions on electron devices, 54,1003 (2007)
2. I. Zutic, J. Fabian, and S. Das Sarma. Spintronics: Fundamentals and applications. Rev. Mod. Phys., 76,323 (2004)
3. J. J. Hauser, H. C. Theuerer, and N. R. Werthamer. Phys. Rev., 136, 11 (1964). J. J. Hauser, H. C. Theuerer, and N. R. Werthamer. Phys. Rev., 142, 2 (1966)
4. P. G de Gennes. Effects of double exchange in magnetic crystals. Phys Rev, 118, 4 (1960) , P. G. De Gennes and E. Guyon. Phys. Lett., 3,168 (1963)
5. N. R. Werthamer. Phys. Rev., 132,2440 (1963)
6. A. A. Abrikosov and L. P. Gor’kov. Sov. Phys. JETP, 12,1243, (1961)
7. Z. Radovic, L. Dobrosavljevic-Grujic, A. I. Buzdin, and John R. Clem. . Phys. Rev. B, 38,2388 (1988).
8. Z. Radovic, M. Ledvij, L. Dobrosavljevic-Grujic, A. I. Buzdin, and John R. Phys.Rev. B, 44,759, (1991)
9. A. I. Buzdin, Rev. Mod. Phys. 77, 935 2005.
10. F. S. Bergeret, A. F. Volkov, and K. B. Efetov, Rev. Mod. Phys. 77, 1321 2005.
11. V. V. Ryazanov, V. A. Oboznov, A. Yu. Rusanov, A. V. Veretennikov, A. A.Golubov, and J. Aarts, Phys. Rev. Lett. 86, 2427 (2001).
12. T. Kontos, M. Aprili, J. Lesueur, F. Genêt, B. Stephanidis, and R. Boursier, Phys. Rev. Lett. 89, 137007 (2002).
13. A. Y. Rusanov, M. Hesselberth, J. Aarts, and A. I. Buzdin, Phys. Rev. Lett. 93, 057002 (2004).
14. Z. R. Yang, M. Lange, A. Volodin, R. Szymzak, and V. V. Moshchalkov, Nat. Mater. 3, 793 (2004).
15. L. R. Tagirov, Phys. Rev. Lett. 83, 2058 (1999).
16. J. Y. Gu, C.-Y. You, J. S. Jiang, J. Pearson, Ya. B. Bazaliy, and S.D. Bader, Phys. Rev. Lett. 89, 267001 (2002).
17. I. C. Moraru, W. P. Pratt, and N. O. Birge, Phys. Rev. Lett. 96, 037004 (2006).
18. G. Jakob, V. V. Moshchalkov, and Y. Bruynseraede, Appl. Phys.Lett. 66, 2564 (1995).

19. P. Przyslupski, S. Kolesnik, E. Dynovska, T. Skoskiewicz, and M.Sawicki, IEEE Trans. Appl. Supercond. 7, 2192 (1997).
20. C. A. R. Sá de Melo, Phys. Rev. Lett. 79, 1933 ,(1997); Phys.Rev. B 62, 12303 (2000)
21. P. Prieto, P. Vivas, G. Campillo, E. Baca, L. F. Castro, M. Varela,C. Ballesteros, J. E. Villegas, D. Arias, C. Leon, and J. Santamaria,J. Appl. Phys. 89, 8026 (2001)
22. H.-U. Habermeier, G. Cristiani, R. K. Kremer, O. I. Lebedev, and G. Van Tendeloo, Physica C 354, 298 (2001)
23. A. Pimenov, P. Przyslupski, A. Loidl, and B. Dabrowski, Phys.Rev. Lett. 95, 247009 (2005)
24. J. Chakhalian, J. W. Freeland, G. Strajer, J. Strempfer, G. Khaliullin,J. C. Cezar, T. Charlton, R. Dalgliesh, C. Bernhard, G.Christiani, H. U. Habermeier, and B. Keimer, Nat. Phys. 2, 244 (2006)
25. Z. Sefrioui, D. Arias, V. Peña, J. E. Villegas, M. Varela, P. Prieto, C. León, J. L. Martínez, and J. Santamaría, Phys. Rev. B 67, 214511 (2003)
26. M. Varela, Z. Sefrioui, J. Santamaria, and S. J. Pennycook, Solid-State Electron. 47, 2245 (2003)
27. A. Hoffmann, S. G. E. te Velthuis, Z. Sefrioui, J. Santamaría, M.R. Fitzsimmons, S. Park, and M. Varela, Phys. Rev. B **72**,140407 (2005)
28. V. Peña, Z. Sefrioui, D. Arias, C. Leon, J. Santamaria, J. L. Martinez,S. G. E. te Velthuis, and A. Hoffmann, Phys. Rev. Lett.**94**, 057002 (2005).
29. M. J. M. de Jong and C. W. J. Beenakker, Phys. Rev. Lett. **74**,1657 (1995).
30. A. Y. Rusanov, S. Habraken, and J. Aarts, Phys. Rev. B 73,060505R (2006)
31. A. Singh, C. Surgers, and H. v. Lohneysen, Phys. Rev. B 75,024513 (2007)
32. J. Aarts and A. Y. Rusanov, C. R. Phys. 7, 99 (2006)
33. R. Steiner and P. Ziemann, Phys. Rev. B 74, 094504 (2006)
34. D. Stamopoulos, E. Manios, and M. Pissas, Phys. Rev. B 75,014501 (2007)
35. C. Bell, S. Tursucu, and J. Aarts, Phys. Rev. B 74, 214520 (2006)
36. Z. H.Wang, G. Cristiani, and H. U. Habermeier, *Appl. Phys. Lett.*, vol.82, p. 3731, (2003)

37. M. Mathews, F. M. Postma, J. C. Lodder, R. Jansen, G. Rijnders, andD. H. A. Blank, *Appl. Phys. Lett.*, 87, 242507 (2005).
38. T. Taniuchi, H. Kumigashira, M. Oshima, T. Wakita, T. Yokoya, M.Kubota, K. Ono, H. Akinaga, M. Lippmaa, and M. Kawasaki *et al.,Appl. Phys. Lett.*, vol. 89, p. 112505, 2006.
39. I. C. Infante, J. O. Osso, F. Sanchez, and J. Fontcuberta, *Appl. Phys.Lett.*, 92, 012508 (2008).
40. M. K. Wu *et al.* , Phys. Rev. Lett. 58 , 908 (1987)
41. L. J. J.Bardeen, Phys. Rev. 108, 1175.(1957).
42. M. Tinkham. (2004). Introduction to superconductivity. Courier Dover Publications.
43. W. Meissner, R. (1933). Naturwissenschaften (21), 787.
44. V. L. Ginzburg, L. Zh.Eksp.Teor.Fiz. (20), 1064.(1950).
45. A. A. Abrikosov. Sov.Phys.JETP (5), 1174.(1957).
46. M. R. Eskildsen, M. S. Phys.Rev.Lett (89), 187003.(2002).
47. V. Moshchalkov, M. T. (2009). Phys.Rev.Lett. (102), 117001.
48. J. G. Bednorz, Z.Phys.B (64), 189.(1986).
49. D. R. Nelson. Phys.Rev:Lett. (60), 1973 (1988).
50. W. E. Pickett, Rev.Mod.Phys, 61, 433 (1989).
51. C. C.Tsuey, J. Rev. Mod.Phys. (72), 969 (2000).
52. J. R. Kirtley, C. C. Tsuei, Ariando, C. J. M. Verwijs, S. Harkema, H. Hilgenkamp. Nat.Phys. (2), 190 (2006).
53. M. A. Hossain et al.*Nat.Phys.*4, 527 (2008)
54. Y. Li, V. Balédent, N. Barii, Y. Cho, B. Fauqué, Y. Sidis, G.Yu, X. Zhao, P. Bourges, M. Greven. Nature (455), 372.(2008).
55. W. W. Warren et al, Phys. Rev. Lett. 62, 1193 (1989); H. Alloul et al, Phys. Rev. Lett. 70, 1071 (1993)
56. J. Loram et al, Phys. Rev. Lett. 71, 1740 (1993) and Physica C 235-240, 134 (1994)
57. Y. J. Uemura et al, Phys. Rev. Lett. 62, 2317 (1989)
58. T. Hotta, M. Mayr, Elbio Dagotto, Phys.Rev.B 60, 13085 (1999)
59. J. M. Harris, Z.-X. Shen, P. J. White, D. S. Marshall, M. C. Schabel, J. N. Eckstein, and I. Bozovic, Phys. Rev. B 54, 15 665 (1996)

60. H. Ding, T. Yokoya, J. C. Campuzano, T. Takahashi, M.Randeria, M. R. Norman, T. Mochiku, K. Kadowaki, and J.Giapintzakis, Nature 382, 51 (1996)
61. A. Kampf and J. R. Schrieffer , Phys.Rev.B 41, 6399 (1990)
62. B. Fauque, Y.Sidis, V.Hinkov, S. Pailhès, C.T.Lin, X.Chaud, P.Bourges. Phys.Rev.Lett. (96), 197001.(2006) H.A. Mook, Y.Sidis, B.Fauqué, V.Balédent, P.Bourges. Phys.Rev.B (78), 020506(R)(2008).
63. Y. Tokura. Phys.Today (7), 50.(2003)
64. G. Jonker, J.van Santen. Physica (16), 337. (1950)
65. J.van Santen, G.Jonker . Physica (16), 599.(1950)
66. J. Volger. Physica (20), 49.(1954).
67. S. Jin, T.H.Tiefel, M.Mc Cormack, R.A.Fastnacht, R.Ramesh, L.H.Chen. Science (264), 413.(1994).
68. E. Wollan, W.Koehler . Phys.Rev. (100), 545.(1955)
69. E. Dagotto, T.Hotta, A.Moreo. Phys.Rep. (344), 1-153.(2001)
70. Y. Tokura. (1999). *Fundamental Features of Colossal Magnetoresistive Manganese Oxides*. In Y.Tokura, Contribution to Colossal Magnetoresistance Oxides, Monographs in Condensed Matter Science. Gordon & Breach.
71. C. Zener. Phys.Rev. (2), 403 (1951).
72. J.-H. Park, C.T.Chen, S-W. Cheong, W. Bao, G. Meigs, V. Chakarian, Y.U. Idzerda. Phys.Rev.Lett. (76), 4215. (1996).
73. B. Nadgorny, I.I. Mazin, M. Osofsky, R. J. Soulen,Jr, P. Broussard, R. M. Stroud, D.J. Singh, V.G. Harris, A. Arsenov, Ya. Mukovskii. Phys.Rev.B (63), 184433.(2001).
74. G.M. Müller, J.Walowski, M. Djordjevic, G.-X. Miao, A. Gupta, A.V. Ramos, K. Gehrke, V. Moshnyaga, K. Samwer, J. Schmalhorst, A. Thomas, A. Hütten, G. Reiss, J.S. Moodera, M. Münzenberg. Nat.Mater. (8), 56.(2009).
75. J. L. García-Muñoz, J. Fontcuberta, M. Suaaidi, X. Obradors. J.Phys.:condens.Matter (8), L787.(1996).
76. S.Yunoki, J.Hu, A. L. Malvezzi, A. Moreo, N. Furukawa, E. Dagotto. Phys.Rev.Lett. (80), 845.(1998).
77. J. Burgy, A. Moreo, E. Dagotto. Phys.Rev.Lett. (92), 097202.(2004).

78. E. Dagotto. (2003). Nanoscale phase separation and colossal magnetoresistance: the physics of manganites and related compounds. Springer.
79. I. O. Troyanchuk. Sov.Phys. - JETP (75), 132.(1992).
80. M. Jaime, M. B. Salamon, M. Rubinstein, R. E. Treece, J. S. Horwitz, D. B. Chrisey. Phys.Rev.B (54), 11914. (1996).
81. R. H. Heffner, L.P.Le, M. F. Hundley, J. J. Neumeier, G. M. Luke, K. Kojima, B. Nachumi, Y. J. Uemura, D. E. MacLaughlin, S. W. Cheong. Phys.Rev.Lett. (77), 1869.(1996).
82. G. Allodi, R. De Renzi, G. Guidi, F. Licci, M. W.Pieper Phys.Rev.B (56), 6036.(1997).
83. J. W . Lynn, R.W.Erwin, J. A. Borchers, Q. Huang, A. Santoro, J-L. Peng, Z.Y.Li. Phys.Rev.Lett. (76), 4076.(1996).
84. J. M. DeTeresa, M. R. Ibarra, P. A. Algarabel, C. Ritter, C. Marquina, J. Blasco, J. Garcia, A. del Moral, Z. Arnold. Nature (386), 256.(1997).
85. M. Hennion, F. Moussa, G. Biotteau, J. Rodriguez-Carvajal, L. Pinsard, A. Revcolevschi. Phys.Rev.Lett. (81), 1957.(1998).
86. S. Yoon, H. L. Liu, G. Schollerer, S. L. Cooper, P. D. Han, D. A. Payne, S.-W. Cheong, Z. Fisk. Phys.Rev.B (58), 2795.(1998).
87. C. H. Booth, F. Bridges, G. H. Kwei, J. M. Lawrence, A. L. Cornelius, J. J. Neumeier. (1998). Phys.Rev.Lett. (80), 853.
88. E. C. Stoner and E. P. Wohlfarth. IEEE Transactions 27,3475, (1991).
89. Y. Suzuki *et al.* Appl. Phys.Lett. **71**, 140 (1997)
90. J. O’Donnel *et al.* Appl. Phys.Lett. **72**, 1775 (1998)
91. K. Steenbeck, and R. Hiergeist, Appl. Phys.Lett. **75**, 1778 (1999)
92. T. K. Nath *et al.* Appl. Phys.Lett. **74**, 1615 (1999)
93. M. Ziese, Phys. Rev. B **62**, 1044 (2000)
94. Zhi-Hong Wang, G. Cristiani, and H. U Habermeier. Appl Phys Lett, 82, 3733, (2003).
95. M. Mathews, F. M. Postma, J. C. Lodder, R. Jansen, G. Rijnders, and D. H. A. Blank. Appl. Phys.Lett., 87, 12 (2005)
96. I. C. Infante, J. O. Osso, F. Sanchez, and J. Fontcuberta. Appl Phys Lett, 92, (2008)
97. Z. Radovic, L. Dobrosavljevic-Grujic, A. I. Buzdin, and J. R. Clem, Phys.Rev. B **38**, 2388 (1988)

98. A.I.Buzdin. *Rev.Mod.Phys.* (77), 935. (2005).

99. V.V. Ryazanov, V. A. Oboznov, A. Y. Rusanov, A. V. Veretennikov,,A. A. Golubov, and J. Aarts, Phys. Rev. Lett. **86**, 2427(2001).

100. T. Kontos, M. Aprili, J. Lesueur, F. Genêt, B. Stephanidis, and R. Boursier, Phys. Rev. Lett. 89, 137007 (2002).

101. A. Buzdin and I. Baladié, Phys. Rev. B 67, 184519 (2003).

102. C. Uher, R. Clarke, G. G. Zheng, and I. K. Schuller, Phys. Rev. B 30, 453 (1984).

103. J. Aarts, J. M. E. Geers, E. Bru¨ck, A. A. Golubov, and R. Coehorn, Phys. Rev. B **56**, 2779 (1997)

104. Th. Mühge, N. N. Garif'yanov, Yu. V. Goryunov, G. G. Khaliullin, L. R. Tagirov, K. Westerholt, I. A. Garifullin, and H. Zabel, Phys. Rev. Lett. 77, 1857 (1996)

105. L. V. Mercaldo, C. Attanasio, C. Coccorese, L. Maritato, S. L. Prischepa, M. Salvato, Phys. Rev. B 53, 14040 (1996)

106. J. S. Jiang, Dragomir Davidovic, Daniel H. Reich, and C. L.Chien, Phys. Rev. B 54, 6119 (1996)

107. A. Yu. Rusanov, M. Hesselberth, J. Aarts, and A. I. Buzdin, Phys.Rev. Lett. 93, 057002 (2004)

108. G. Verbanck, C. D. Potter, V. Metlushko, R. Schad, V. V. Moshchalkov, Y. Bruinseraede, Phys. Rev. B 57, 6029 (1998)

109. L. Lazar, K. Westerholt, H. Zabel, L. R. Tagirov, Yu. V.Goryunov, N. N.Garifyanov, and I. A. Garifullin, Phys. Rev. B 61, 3711 (2000)

110. G. Jakob, V. V. Moshchalkov, and Y. Buynseraede, Appl. Phys. Lett. **66**, 2564 (1995)

111. P. Przyslupski, S. Kolesnik, E. Dynovska, T. Skoskiewicz, and M.Sawicki, IEEE Trans. Appl. Supercond. 7, 2192 (1997)

112. C. A. R. Sá de Melo, Phys. Rev. Lett. 79, 1933 (1997); Phys.Rev. B 62, 12303 (2000)

113. P. Prieto, P. Vivas, G. Campillo, E. Baca, L. F. Castro, M.Varela, C. Ballesteros, J. E. Villegas, D. Arias, C. Leon, and J. Santamaria, J. Appl. Phys. **89**, 8026 (2001)

114. H.-U. Habermeier, G. Cristiani, R. K.Kremer, O. I. Lebedev, and G. Van Tendeloo, Physica C **354**, 298 (2001)

115. Z. Sefrioui, M. Varela, V. Peña, D. Arias, C. Leon, J. Santamaria,J. E. Villegas, J. L. Martinez, W. Saldarriaga, and P. Prieto, Appl. Phys. Lett. 81, 4568 (2002)
116. H. Meissner. *Phys.Rev* (117), 672.(1960).
117. G. Deutsche, P. G. deGennes. Proximity effects. In R.D.Parks *Superconductivity* (Vol. 2, págs. 1005-1034) (1969).
118. N. R. Werthamer. *Phys.Rev* (132), 2440.(1963).
119. P. G. de Gennes. *Rev.Mod.Phys.* , 225.(1964).
120. C. Attanasio. Proximity Effect and Interface Transparency in Nb-based S/N and S/F Layered Structures. In A. L. R.Gross, *Nanoscale Devices - Fundamentals and Applications* (págs. 241-249). Springer.(2006).
121. K. D. Usadel. *Phys.Rev.Lett.* (25), 507.(1970).
122. A. F. Andreev.*Sov.Phys.-JETP* (19), 1228. (1964).
123. G. E. Blonder, M.Tinkham, T.M.Klapwijk. *Phys.Rev.B* (25), 4515. (1982).
124. M. J. M. De Jong, C.W.J.Beenakker. *Phys.Rev.Lett.* (74), 1657.(1995).
125. E. A. Demler,G.B.Arnold, M.R.Beasley.*Phys.Rev.B* (55), 15 174. (1997).
126. M. Johnson, R.H.Silsbee.*Phys.Rev.Lett.* (55), 1790. (1985).
127. M. Johnson. *Appl.Phys.Lett.* (65), 1460. (1994).
128. S.Takahashi, H.Imamura, S.Maekawa.*Phys.Rev.Lett.* (82), 3911. (1999).
129. G. Sarma. *J.Phys.Chem.Solids* (24), 1029.(1963).
130. J.Y.Gu, J.A.Caballero, R.D.Slater, R.Loloee, W.P.Pratt Jr. *Phys.Rev.B* (66), 140507R. (2002).
131. V.A. Vas’ko, V. A. Larkin, P. A. Kraus, K. R. Nikolaev, D. E. Grupp, C. A. Nordman, and A. M. Goldman, Phys. Rev. Lett. **78**, 1134 (1997).
132. A.M. Goldman, V. A. Vas’ko, P. Kraus, K. Nikolaev, and V. A. Larkin, J. Magn. Magn. Mater. **200**, 69 (1999)
133. N.C. Yeh, R. P. Vasquez, C. C. Fu, A. V. Samilov, Y. Li, and K. Vakili, Phys. Rev. B **60**, 10522 (1999)
134. Z. Radovic, M. Ledvij, L. Dobrosavljevic-Grujic, A. I. Buzdin, and J. R. Clem, Phys. Rev. B **44**, 759 (1991)
135. W. E. Pickett and D. J. Singh, Phys. Rev. B **53**, 1146 (1996)
136. A. G. Aronov, Zh. E ´ ksp. Teor. Fiz. **71**, 370 (1976)

2. Experimental Techniques

2. 1. Sample preparation

Samples are prepared by sputter deposition in high O_2 pressure. This method is based on the ballistic impact of atoms against a substrate after being removed from a material source. The sputtered ions come from targets made of the stoichiometric compound while the oxygen plays the role of the sputtering element. In our case the substrate is placed on a heater plate below the targets and the sputtering process is in general realized by applying a *dc* bias between substrate (anode) and target (cathode). The growth takes place inside a chamber in which a high vacuum of about 10^{-6} mbar is previously realized. The chamber, shown in Fig.2.1, is connected to a turbo-molecular pump supported by a membrane pump. A constant oxygen flow is injected and controlled by a system of needle valves. Since the sputter yield depends on the energy of the incoming O_2 ion and the source atom species, the material removed from the target will deposit on the substrate in a matter which strongly depends on several controllable parameters such as the temperature of the substrate, the applied bias, the pressure inside the chamber. In order to grow epitaxial oxide heterostructure high temperature and pressure are usually required in this technique. All the samples studied in this work have been grown on as-received $SrTiO_3$ substrate (100)-oriented. The high oxygen pressure (3.4mbar) applied during the deposition, favors a complete thermalization of the extracted species and at the same time prevents them from back-sputtering and loss of oxygen in the final crystal structure. The substrate temperature is kept constant at 900ºC. Under these conditions the deposition rate is slow (0.7nm/min) and ensures the epitaxial growth of the sample. To preserve the optimal oxygen content of the structure an *in-situ* annealing at 1000 mbar O_2 pressure is necessary. The procedure is slightly different for YBCO thin films and heterostructures containing LCMO. In the former case the chamber is oxygenated at 600ºC and the annealing is made at 550ºC during 5 minutes. In the latter case the chamber is oxygenated at 800ºC and the samples are annealed at the same temperature during 30 minutes.

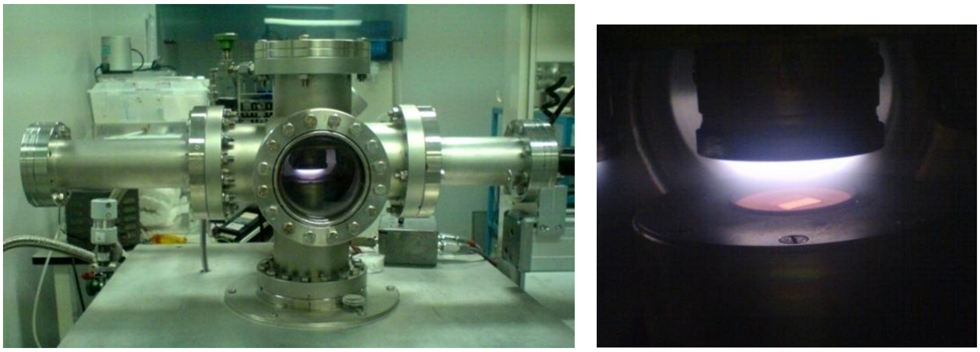

Fig.2.1 (left) View of the sputtering chamber. The targets are mounted on a remote controlled arm to switch between the different materials. (right) Enlarged view of the powered target on the substrate.

2. 2. Structural characterization: XRR, XRD

X-ray reflectivity (XRR) and diffraction (XRD) patterns allowed determining the thickness and the structural quality of our samples. XRR and XRD measurements have been carried out at CAI de Diffraccion de Rayos-X (UCM), with a Philips X'pert MRD diffractometer, using a Cu tube as X-ray source (λ_x= 1.5418Å) operating at 45kV an 40mA.

X ray Reflectivity

The coherent and collimated radiation coming from an X-ray source is reflected at the interface between layers with different electronic densities (the substrate, the film, the air). The different refractive indexes induce a change in the path length of the X-ray and consequently a constructive/destructive interference of the different reflected beams. In an analogous way, the interference resulting from a layered structure produces oscillation in the reflectivity pattern. This pattern is obtained by measuring the reflected intensity as a function of the incident angle (2θ) through a detector which is set in θ-2θ (Bragg) geometry with respect to the source (see Fig.2.2).

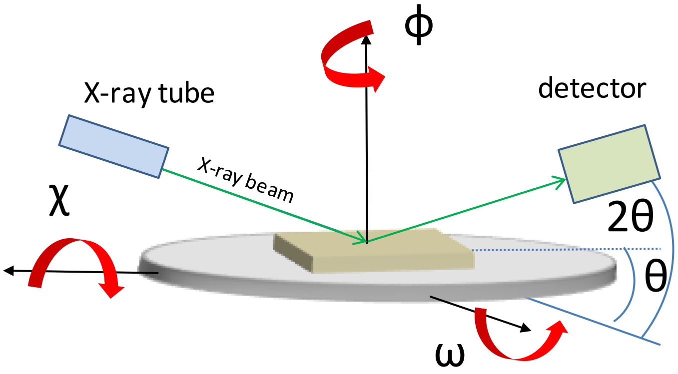

Fig.2.2: Schematic diagram of the θ-2θ geometry

Reflectivity scans showed in this work are usually taken up to an angle of 2θ~10 degrees. In this range of angle we are able to see finite size oscillations (2θ<7º),related to the total thickness of the sample, and the first order Bragg (diffraction) peak of the YBCO, centered around 2θ=7.5º , accompanied by satellite diffraction peaks, as shown in see Fig.2.3a. The period of the finite size oscillations is inversely related to the thickness *d* of the whole sample. By indexing the position of the maxima and minima (*n*=1,2..) we can calculate the total thickness using the formula:

$$(\sin\theta)^2 = \left[\frac{(n-k)\lambda_x}{2d}\right]^2 + 2\delta \qquad 2.1$$

where k=0 correspond to a minimum and k=1/2 to a maximum. δ is the real part of the refraction index:

$$n = 1 - \frac{\rho_n r_e \lambda_x}{2\pi}(f_0 + \Delta f' - i\Delta f'') = 1 - \delta + i\beta \qquad 2.2$$

where ρ_n is the electronic density, r_e is the electron radius, f_0 is the atomic dispersion factor, $\Delta f'$ and $\Delta f''$ are corrections due to the anomalous dispersion [1,2]. δ is approximately $1.54\cdot10^{-5}$ for LCMO thin films, $1.75\cdot10^{-5}$ for YBCO thin films and $3.5\cdot10^{-5}$ for heterostructures of these two materials. In Fig.2.3 we show some representative reflectivity curve of thin films and multilayers. The width of the YBCO diffraction peak is inversely proportional to its thickness, so thinner sample will show a wide less intense peak. The thickness can be calculated within a 10% error using the Scherrer's formula:

$$\xi = \frac{0.9\lambda_X}{b\cos\theta} \qquad 2.3$$

where λ_X is the X-ray wavelength, *b* is the peak width at half maximum(FWHM) and θ the corresponding angle.

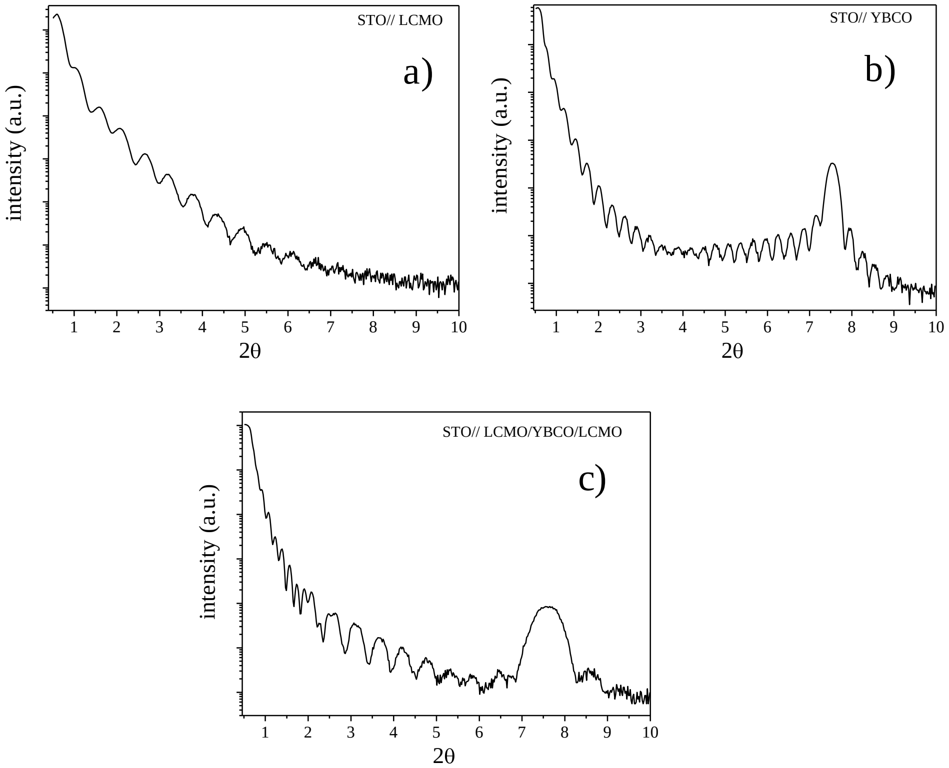

Fig.2.3: Reflectometry scans from (a) a 15nm- thick LCMO thin film, (b) a 29nm-thick YBCO thin film, (c) a LCMO(15nm)/YBCO(12nm)/LCMO(15nm) trilayer

X ray diffraction

Atomic layers in a crystal are separated by a distance *d*. Specular reflected X-rays will travel different distances due to this separation and will yield to constructive interference if the difference in path is an integer multiple of the X-ray wavelength. Thus the diffraction condition described by the Bragg law: $2d_{(hkl)}\sin\theta = n\lambda_x$ (where θ is the incidence angle of the X-ray beam) can be encountered in multilayers epitaxially grown on a monocrystalline substrate. For an epitaxial structure of different materials, a diffraction scan carried out in θ-2θ geometry, after optimizing around one of the (00*l*) diffraction peaks of the substrate will show only the Bragg peaks of the same family [3,4], In Fig.2.4 we can see a diffraction scan from a LCMO/YBCO/LCMO trilayer. LCMO and YBCO bulk lattice parameters slightly differ from those of the STO (see Table 2.1).

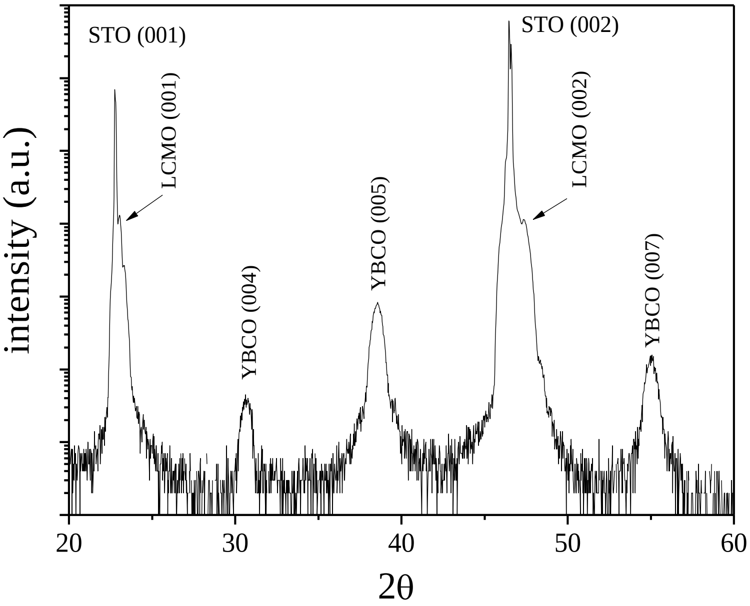

Fig.2.4 : diffraction scan of a LCMO(15nm)/YBCO(18nm)/LCMO(15nm) trilayers.

YBCO and LCMO thin films are then subject to an in-plane tensile strain which will cause a shortening of the *c*-parameter. The Bragg peak of the LCMO, for example, will be shifted to higher angles due to this change. The new c-parameter can be calculated using the Bragg formula:

$$c = \frac{\ell \lambda_x}{2 sin\theta} \qquad 2.4$$

where $\boldsymbol{\ell}$ is the order of the diffraction peak.

material	**Bulk lattice parameters**		
STO	a=3.905	b=3.905	c=3.905
YBCO	a=3.823	b=3.887	c=11.67
LCMO	a=3.87	b=3.87	c=3.87

Table 2.1: Bulk lattice parameter of STO (substrate), YBCO and LCMO.

2. 3. Magnetotransport measurements

Resistance measurements

For our low temperature resistance measurements we used a closed-cycle Cryophysics helium refrigerator which works with the expansion of highly-pure He-gas compressed in a Gifford McMahon cycle. The expansion through the capillaries undergoes two steps at 50K and at 8.5K. The sample is mounted onto a cooled copper piece in contact with the second cooling step. The system is evacuated by a rotary pump capable of a pressure down to 10mTorr, measured with a Pirani vacuum sensor. The best temperature was 9K. A silicon diode thermometer is in contact with the sample holder calibrated for measuring between 10 and 325K. The system is also equipped with a heater controlled by a Lake Shore 330-11 temperature controller which permits to control the sample’s temperature between room temperature and 9K with a 10-mK accuracy. Micro-coaxial wires connect the different parts for low noise measurements. For magnetoresistance measurements we used an electromagnet (with a 10cm separation between the magnetic cores) which provided a magnetic field in the range of ± 4000Oe.

The resistance was measured using the Van der Pauw four-point method [5] to eliminate any contribution given by the in-series contact resistance. Four electrical contacts were made on the surface of the sample by evaporation of silver and then connected to the low-noise wiring by indium. The instruments used were a Keithly 224 current source, capable of stabilizing a current supplied between 5nA and 100mA and a Keithly 2182 nanovoltimeter. For our low resistance measurements we used the conventional method of reversing the current sign and averaging the voltage measurements $V = [V(I+) - V(I-)] / 2$ to thermoelectric effect.

Magnetic measurements

SQUID magnetometry: The magnetometry data for this thesis have been taken using a Quantum Design Magnetic Property Measurement System (MPMS) SQUID magnetometer of the Magnetism and Transport Laboratory at ICMM (Madrid). The MPMS system comprises of two main sections: the dewar, probe and SQUID assembly, and the electronic control system. The probe contains a high precision temperature control system, allowing measurements between 1.9K and 400Kwith an accuracy of 0.01K, and superconducting electromagnet, giving a field of up to 50kG with an accuracy of up to 0.1G (Fig.2.5). The dewar consists of an inner liquid helium reservoir and outer liquid nitrogen jacket, to reduce excessive liquid helium boil off. The liquid helium is used both for maintaining the electromagnet in a superconducting state and for cooling the sample space. Samples are mounted within a plastic straw and connected to one end of a sample rod which is inserted into the dewar/probe. The other end is attached to a stepper motor which is used to position the sample within the center of the SQUID pickup coils. The measurement of the magnetic moment is done using the DC Josephson effect. In fact there are two Josephson junctions in parallel in a superconducting loop. To obtain DC measurements the sample is moved through the coils in discrete steps. The circulating current produced by a flux change is then detected by the use of a measuring current. The pickup coils are configured as highly balanced second-derivative coils, approximately 3cm long. The coils reject the applied field from the superconducting magnet to a resolution of 0.1%.

VSM magnetometry: We also performed magnetic measurements using a Vibrating Sample Magnetometer (VSM) of the Magnetism and Transport Laboratory at ICMM (Madrid). The VSM measures the difference in magnetic induction between region of space with and without the specimen. It therefore gives a direct and absolute measure of the magnetization. The magnetic moment of the sample is measured according to Faraday’s law. The sample oscillates sinusoidally inside a small pick-up coil with a frequency of about 40Hz. The induced voltage due to $E = -d\phi_B/dt$ is detected with the lock-in technique and converted to magnetic moment with an instrument specific calibration factor. It allows for the rapid measurement of MvsT and MvsH data with a useful sensitivity of approx. 10^{-6} emu. The sample is mounted on a diamagnetic stick fixed to a carbon rod (see Fig.2.5).

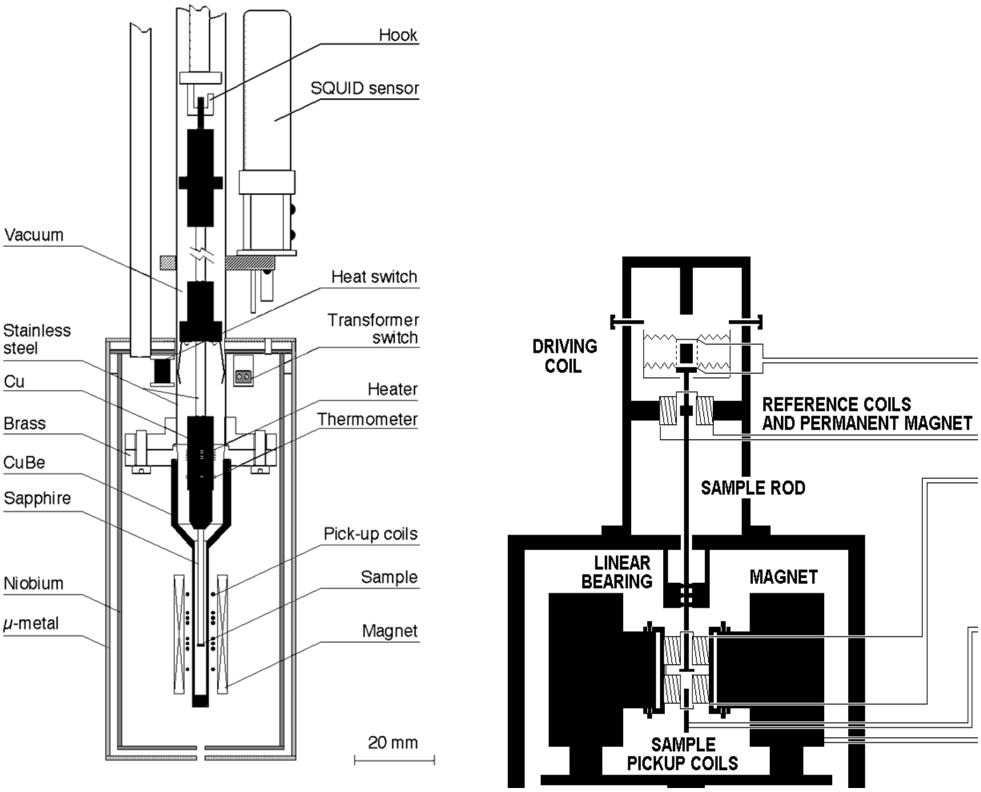

Fig.2.5 : Diagrams of SQUID (left) and VSM (right) magnetometers.

While SQUID magnetometry allows precise control of the magnetic field and high sensitivity measurements, VSM magnetometry provides very rapid measurements. The samples studied in this work showed quite high magnetic moment, allowing a comparable response from SQUID and VSM.

Ferromagnetic Resonance (FMR): Ferromagnetic resonance spectroscopy (FMR) can be used to measure the effective magnetic field within a sample, including the contributions of both magnetic anisotropy and magnetostatic interactions. If a magnetization vector is subject to a static field and a perpendicularly applied pump field, resonance will occur at a frequency more or less proportional to the strength of the static field. The microwave power absorbed by the magnetic sample as a function of frequency will typically be a Lorentzian centered at resonance. The FMR signal is measured by monitoring the microwave losses as a function of the applied dc-field. The data of this thesis have been taken using a 8.9 GHz JEOL ESR X-band electron spin resonance spectrometer, equipped with a liquid nitrogen cryostat, of the Dept. of Physics, University of Technology and Economics (Budapest). FMR is one of the best techniques to determine the magnetic anisotropy constants up to sixth order. Surface/interface and volume magnetic anisotropies in ultrathin films can be quantitatively determined with a resolution better than one μeV. One major advantage of this technique is the low excitation energy (microwave quanta) by which the magnetic ground state properties are probed. Also, the dynamic behavior i.e. the magnetic relaxation rate can be probed in a time window of typically few hundred picoseconds.

2. 4. Polarized Neutron reflectivity

Polarized neutron reflectivity (PNR) has been one of the main techniques used throughout this work. Similarly to the X-ray reflectivity, it consists of a measure of the intensity of the reflected neutron beam as a function of the perpendicular component of the wave vector transfer $Q_{\perp}$. Due to the fact that polarized neutrons are intrinsically sensitive to the difference of both magnetic and nuclear components of the refractive index across interfaces, PNR can provide detailed quantitative information about the magnetization depth profile and structural details of thin films and multilayers. Scattering techniques (diffraction, inelastic scattering) were developed soon after the discovery of the neutron but PNR is a relatively new technique [6,8]. Like X-rays and electrons, neutrons can be reflected on surfaces. In reflectivity geometry, the incidence angle θ_i is the same as the reflection angle θ_r and typically starts from a region of total reflection, in the range 0.5º-5º. The reflected radiation is related to the depth dependence of the index of refraction averaged over the lateral dimensions of the surface or interface. PNR is characterized by an extremely high depth resolution—a fraction of a nanometer even for films as thick as several hundred nanometers. For instance, in a multilayered stack consisting of ferromagnetic and non-ferromagnetic layers any parallel or antiparallel alignment of the ferromagnetic layers can be uniquely distinguished. The neutron is a very well suited probe for investigation of magnetic thin films. It is highly penetrating into the sample, without structural damages, due to its neutrality. At the same time, it interacts with the magnetic moments since it has spin $\frac{1}{2}$. Interactions can be represented by a scattering potential consisting of a nuclear contribution and a magnetic contribution: $V = V_n + V_m$.

Derivation of the neutron reflectivity

We can derive some important relations describing the mechanism of interaction of the scattering potential with the neutron [9,10,11] . Let's first consider the nuclear component of *V*. A derivation of the reflectivity arises by treating the neutron as a particle-wave. So a wave coming from the medium 0 (the vacuum) is scattered at the interface with the medium 1 (our sample) giving rise to a wave partly reflected and partly transmitted. By solving the Schrödinger wave equation, we can obtain an expression which connects the index of refraction with the wave vector in each medium. We should account for some conditions to simplify the problem, which however are effectively met in a reflectivity experiment. These conditions includes: a one-dimensional scattering potential, specular reflection (θ_i=θ_f) (see Fig. 2.6) and elastic scattering . The case we are going to treat first is equivalent to the problem of an unpolarized neutron beam reflected by a thick non-magnetic material that can be represented, for instance, by a $SrTiO_3$ (STO) substrate.

The scattering potential resulting from the interaction between neutron and nuclei in the material is given by:

$$V(y) = \frac{2\pi\hbar^2}{m}\rho(y) \qquad 2.5$$

where *y* is the direction perpendicular to the sample surface. The depth dependent quantity ρ is called the *scattering length density* (SLD) and is the sum of the atomic density of the nuclei in the material multiplied by their individual nuclear coherent scattering lengths b_i [6]:

$$\rho = \sum_i^J N_i b_i \qquad 2.6$$

In the case of $SrTiO_3$:

$$\rho_{STO} = \frac{\sum_i^J n_i b_i}{\mathrm{V_{STO}}} = \frac{1\cdot 7.02 + 1\cdot(-3.438) + 3\cdot 5.803}{(3.905)^3}\frac{10^{-15}m}{10^{-28}m^3} = 3.53\cdot 10^{-6}\text{Å}^{-2}$$

where the volume $\mathrm{V_{STO}}$ is the volume of the STO unit cell.

Given the equation:

$$\left[\frac{\hbar^2}{2m}\frac{\partial^2}{\partial y^2}+V(y)\right]\Psi(y)=E\Psi(y) \qquad 2.7$$

the wave functions for the incident and transmitted wave take the form:

$$\Psi_0(y)=e^{+ik_0y}+re^{-ik_0y} \qquad 2.8$$

$$\Psi_1(y)=te^{+ik_1y}$$

with *r* and *t* reflection and transmission amplitudes.

Elastic scattering imply conservation of momentum ($|\vec{k_\iota}|=|\vec{k_f}|=k_0$) and conservation of neutron intensity ($|\Psi|^2=1$) .

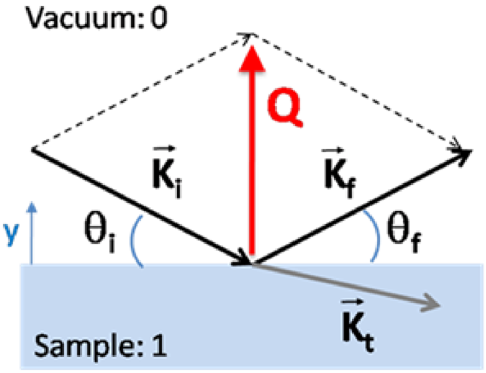

Fig. 2.6: Specular reflection and direction of the wave vector transfer Q.

The additional condition of continuity is required:

$$\Psi_0(0)=\Psi_1(0) \qquad \left.\frac{\partial\Psi_0}{\partial y}\right|_{y=0}=\left.\frac{\partial\Psi_1}{\partial y}\right|_{y=0} \qquad 2.9$$

that yields to the system of equations $\begin{cases}1+r=t\\ k_0(1-r)=k_1t\end{cases}$ and to the final form of the reflection amplitude:

$$r=\frac{k_0-k_1}{k_0+k_1} \qquad 2.10$$

The energy *E* and momentum k_0 of the incident neutron are given by:

$$\begin{cases} E = \frac{\hbar^2 k_0^2}{2m} \\ k_0 = \frac{2\pi \sin\theta_i}{\lambda} \end{cases} \qquad 2.11$$

with m and λ, neutron mass and wavelength respectively. An expression in the form of the Helmholtz equation arises:

$$\left[\frac{\partial^2}{\partial y^2} + 4\pi\rho(y) - k_0^2\right]\Psi(y) = 0 \qquad 2.12$$

which implies: $k = \frac{2m}{\hbar^2}(E - V)$

From general optical considerations: $nk_0 = k_1$ and $n^2 = 1 - \frac{V}{E}$

If we match these last two equations we obtain:

$$k_1 = \sqrt{1 - \frac{4\pi\rho(y)}{k_0^2}}\, k_0 \qquad 2.13$$

The observed quantity, the reflectivity, is defined as: $R = rr^* = |r|^2$ so that

$$R = \left|\frac{k_0 - k_1}{k_0 + k_1}\right|^2 \qquad 2.14$$

The accessible range of wave vector transfer:

$$Q = k_f - k_i = \frac{4\pi \sin\theta}{\lambda} \qquad 2.15$$

is inversely proportional to the resolution of a material distribution in real space; this allows connecting a R vs $Q_\perp$ pattern to the depth profile of the sample. When k_0 is sufficiently small, the beam is completely reflected (R=1); this leads to a critical value of the wave vector transfer (the *critical edge*), $Q_c = 2k_0 = 4\sqrt{\pi\rho(y)}$. This quantity is the starting point for the construction of a reflectivity curve. In Fig.2.7 the simulated intensity of the unpolarized neutron reflectivity from a STO substrate as a function of $Q_\perp$ is represented. For $Q_\perp$<0.013Å^{-1} (the STO critical edge), the intensity is maximum.

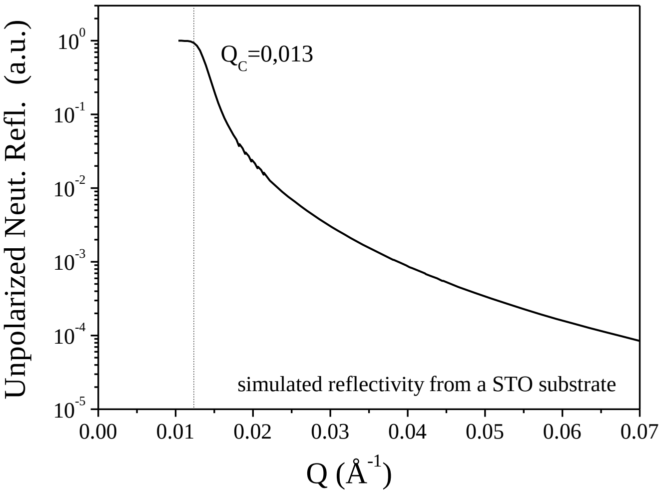

Fig.2.7: Simulated unpolarized neutron reflectivity from a $SrTiO_3$ substrate.

A similar concept can be applied to a system composed of a thin film of thickness d deposited on a substrate. In this case, two different wave vectors will be associated to the two different media. Since the path covered by the wave reflected between thin film and substrate is $2d$ longer than its analogous between vacuum and thin film, a phase factor has to be considered when calculating the reflectivity. Thus the reflection amplitude assumes a more complex form:

$$r = \frac{r_{01}+r_{12}e^{ik_1 2d}}{1+r_{01}r_{12}e^{ik_1 2d}} \qquad 2.16$$

where:

$$k_j = n_j k_0 = \sqrt{1-\frac{4\pi\rho_j}{k_0^2}}\,k_0 \qquad 2.17$$

Fig. 2.8 shows the simulated unpolarized reflectivity for a 400 Å thick YBCO thin film on STO, on the left, and for the same thickness of LCMO, on the right. Both reflectivity curves show the typical oscillating pattern in which the separation between two successive oscillations is approximately equal to $2\pi/d$. Since the amplitude of the oscillation is related to the contrast between the scattering length densities of the film and substrate, for the LCMO the oscillations are barely visible being ρ_{LCMO}=3.6 10^{-6} Å^{-2}, very similar to the STO value, while clearly visible in the case of YBCO being ρ_{YBCO}=4.73 10^{-6} Å^{-2}. It must be noted that the critical edge is still that of the STO, due to the fact that a few nanometers thick film is not opaque to the neutron beam.

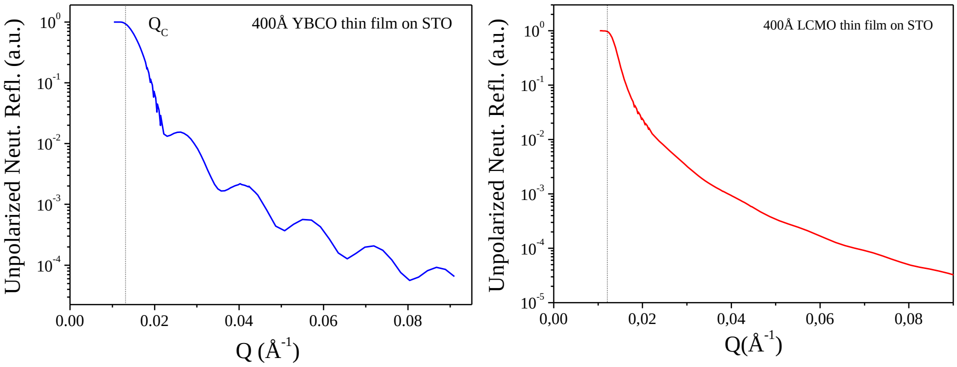

Fig. 2.8: Simulated unpolarized reflectivity from a thin film of YBCO (left) and LCMO (right).

In the study of superconductor/ferromagnet heterostructures much more information can be obtained by using polarized neutrons. As mentioned above, the neutron possesses spin $\frac{1}{2}$ and interacts with the atomic magnetism [12,13,14]. In a PNR experiment a magnetic field H is usually applied to the sample and represents the laboratory field of reference (see Fig.2.9). Given the relation $\vec{B} = \mu_0\vec{H} + \vec{M}$, since H is usually much smaller than M, the neutron spin will interact only with the magnetic induction inside the sample and then cannot distinguish between spin and orbital moment. The magnetic contribution to the scattering potential is given by $V_m = -\overrightarrow{\mu_n} \cdot \vec{B}$ where μ_n is the neutron magnetic moment. Neutrons can be polarized, by appropriate devices, to be parallel or antiparallel to the field applied to the sample.

In a PNR experiment, the guiding field, the polarization axis of the incident beam and the field used as a detector are usually collinear so the guiding magnetic field outside the sample provides a quantization axis for the neutron spin. If the magnetic induction ***B*** inside the sample makes an angle with the applied field H, the in-plane component of ***B*** perpendicular to H will lead to spin-flip scattering (the spin state of the reflected neutron may flip 180° depending upon the time the neutron spends in that region and the strength of the induction). This is a consequence of the precession of the neutron spin around B. As a convention, R^{++} and R^{--} indicate the non-spin-flip reflectivities (where the sign + and - indicates spin parallel or antiparallel to H respectively), while R^{+-} and R^{-+} indicates spin-flip reflectivities. Since neutrons are reflected by potential gradients across interfaces and since $\nabla \cdot B = 0$, perpendicular components of $\boldsymbol{B}$ are constant across a reflecting interface and therefore do not produce specularly reflected intensity [15] .

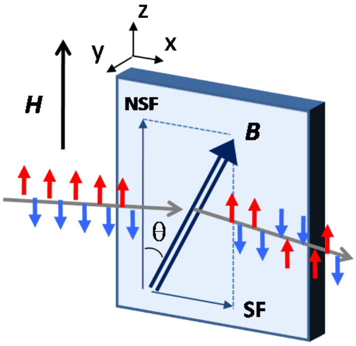

Fig.2.9 : Schematic representation of the magnetization components which induce spin flip (SF) and non-spin flip (NSF) scattering, relative to the neutron polarization.

If the magnetic induction is collinear with the guiding field and then with the direction of the incident neutron spin, the polarization of the neutron beam will remain the same after interacting with the magnetization of the sample. Reflectivity in this case depends on the relative orientation of the spin (parallel or antiparallel) of the incident neutron and the magnetization of the magnetic layer. As a result, the magnetic film acts as a birefringent medium and the scattering potential takes the form:

$$V^{\pm} = \frac{2\pi\hbar^2}{m}\rho \pm \mu B. \qquad 2.18$$

The solution to the Schrödinger equation now contains the spin dependence:

$$\Psi(y) = U_+ \begin{pmatrix}1\\0\end{pmatrix} \Psi_+ + U_- \begin{pmatrix}0\\1\end{pmatrix} \Psi_-$$

where:

$$\Psi_+(y) = e^{ik_+ y}$$
$$\Psi_-(y) = e^{ik_- y}$$

The refractive index is given by:

$$k_{\pm} = n_{\pm} k_0 = \sqrt{1 - \frac{4\pi(\rho_n \pm \rho_m)}{k_0^2}}\, k_0 \qquad 2.19$$

The neutron magnetic scattering length (mSLD) density ρ_m can be defined as:

$$\rho_m = \sum_i^J N_i p_i = C \sum_i^J N_i \mu_i = C'm \qquad 2.20$$

where p is the magnetic scattering length (in units of Å), μ is the magnetic moment per formula unit (in Bohr magnetons μ_B) and m is the volume magnetization density (in emu/cm^3), $C = 2.645 \cdot 10^{-5} \text{Å} \mu_B{}^{-1}$ and $C' = 2.853 \cdot 10^{-9} \text{Å}^{-2} cm^3/emu.$

In Fig.2.10 the simulated PNR curves for 400 Å of LCMO are represented. The magnetization is collinear with the external applied field and it is homogeneously distributed on the sample volume, with a value of 600 emu/cm^3.

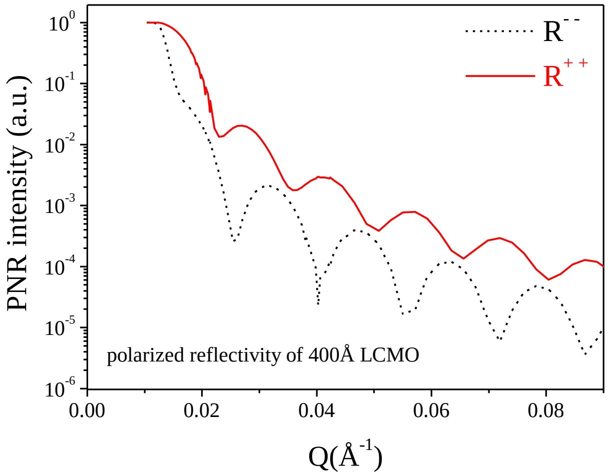

Fig.2.10: Simulated PNR curves for a LCMO thin film.

This is, ideally, the case of a LCMO thin film in a saturating field applied parallel to the sample surface. In the presence of a trilayer with a non-magnetic spacer the shape of the reflectivity curves assume a more complex appearance although with a suitable computer refinement the depth depending magnetic and structural characteristics can be described. In Fig.2.11 we represent the simulated PNR experiment for a representative LCMO/YBCO/LCMO sample under the hypothesis that the individual layers maintain the properties typical of the bulk materials. The resulting nuclear and magnetic SLD profiles are given.

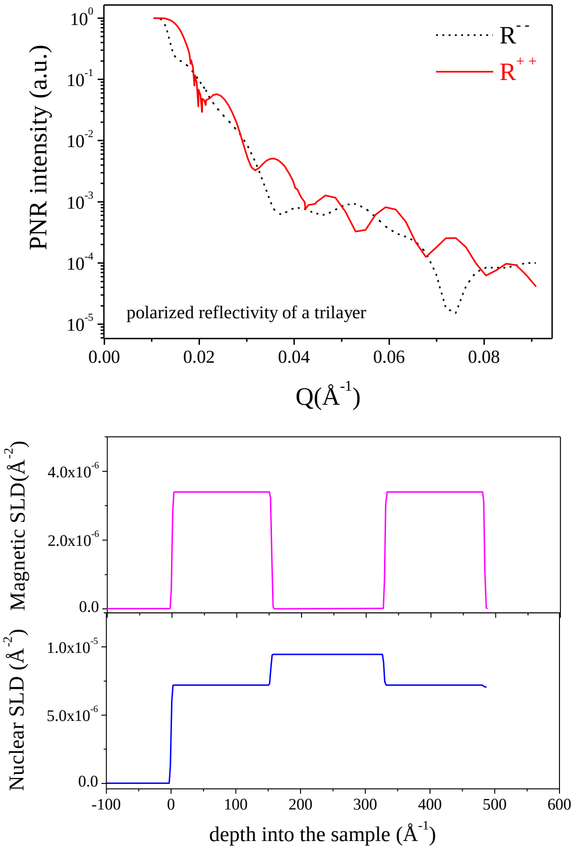

Fig.2.11 Top: simulated PNR curves for a LCMO/YBCO/LCMO trilayer. Bottom: magnetic and nuclear profile of the same trilayer.

If the magnetization inside the sample makes an angle θ with the guiding field, the sample is no more birefringent, since four different reflectivities arise. The magnetic scattering length density in this case is:

$$\vec{\boldsymbol{\rho}}_m = C'm(\cos(\theta)\hat{z} + \sin(\theta)\hat{x}) \tag{2.21}$$

The spin-flip reflectivity intensity is given by:

$$R^{SF} = \frac{R^{+-}+R^{-+}}{2}\ . \tag{2.22}$$

The R^{++}, R^{--} and R^{SF} curves can be analyzed simultaneously to obtain structural and magnetic information of the sample.

Fig.2.12 shows PNR curves for the same LCMO thin film of Fig.2.10, assuming this time that the magnetization is making an angle of 45° with the guiding field. As a result a quite intense R^{SF} curve is obtained. In the particular case of in-plane magnetization perpendicular to the guiding field (θ=90º), the R^{++} and R^{--}intensity would collapse to the same curve while R^{SF} would have the maximum intensity.

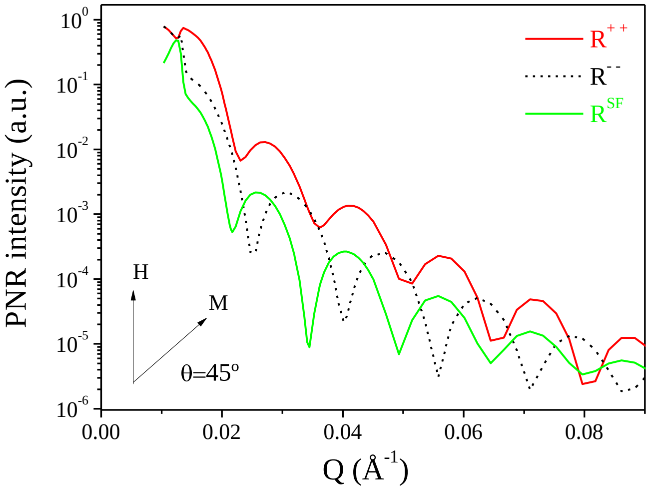

Fig.2.12: Simulated PNR curves for a LCMO thin film in which the in-plane magnetization lies at 45° with the applied field. Spin flip intensity is given by the green curve while the red and black curves represent the non-spin flip intensities.

Analysis of PNR data

The computer routine CO_REFINE, used in this work, has been developed by M.R. Fitzsimmons and C.F. Maykrzak [9]. It performs analysis of the R^{++} and R^{--} reflectivity curves by optimizing several parameters introduced by the user and initially set to describe an ideal model. The optimization is obtained by minimizing the χ^2 that is a measure of the error between the observed and the calculated reflectivity. The recursive calculation used to obtain the reflectivity curve is often referred to as the Parrat formalism [17]. The same routine to fit neutron data can be applied to fit x-rays reflectivity to get a preliminary structural model. This is in fact the procedure that has been carried out to analyze the neutron data shown in this thesis. X-ray reflectivity curves of the samples have been refined according to an initial ideal model in which the thickness of each layer, the real and imaginary part of the x-ray scattering length density (obtained from literature) and the surface and interface roughness are introduced. The best fit is obtained from the optimization of these parameters within a proper range of values. The resulting structural model is introduced in the routine for the neutron study. In this case different parameters are considered, such as the nuclear and magnetic scattering length densities for neutrons. To fit neutron data taken with polarization analysis the SPIN_FLIP software has been used which calculates both the non-spin-flip and spin-flip reflectivities in a way similar to that of CO_REFINE. Besides generating the magnetic SLD profile, SPIN_FLIP provides the angle between magnetization and guiding field of each layer. While generating the structural or magnetic profiles, both programs apply an error function $erf\left(\frac{y-\Delta}{\sigma\sqrt{2}}\right)$ that describes the variation of the SLD across the interface: y is the depth into the sample, Δ is the layer thickness and σ is the interface width. This variation is usually set as a parameter to be optimized in the analysis of neutron data and can be independent from the analogue value obtained for the structural (x-ray) profile. It is not unusual in fact to see a gradient in the magnetization where the structural profile shows a sharp interface. In Fig.2.13a the nuclear SLD profile for a YBCO thin film is represented; the case of rough interface and surface is compared to the case of ideally flat sample. The derivative of the error function leads to Gaussian peaks with standard deviation corresponding to the interface width. Fig.2.13d shows that the reflectivity intensity can be drastically affected by only 20Å of interface and surface roughness.

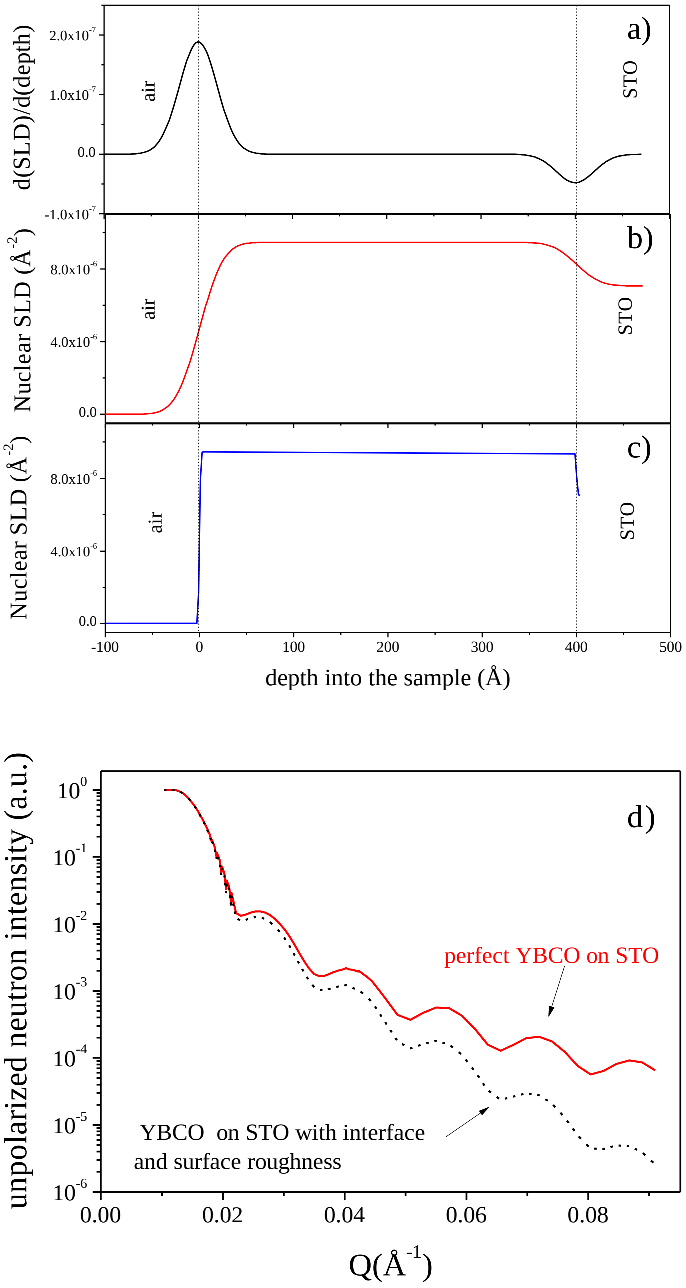

Fig.2.13 Nuclear SLD profile for a YBCO thin film in the case of flat b) and rough c) interface and surface; the roughness can be displayed as the derivative of the SLD profile (a). d): comparison between neutron reflectivity for a YBCO thin film with flat (red line) and rough (black dotted line) interface and surface.

Beamline configuration

The intensity of the reflected radiation is measured for selected values of the scattering wave vector k_0. This can be achieved in two ways: by changing the angle of incidence of the beam to the sample surface, and/or by changing the wavelength λ of the neutron beam (see Fig.2.14). In the latter case neutron wavelength is measured at pulsed neutron sources by recording the time-of-flight (TOF) of a neutron to travel a known distance. Sources of pulsed neutrons (e.g. LANSCE at Los Alamos National Laboratory) provide neutron pulses that are typically very short, on the order of 100-300 μs, and periodic—with periods ranging between $\tau \sim 10$ - 100 ms. The TOF method has been applied in the PNR experiments described below. The instrument used is the reflectometer/diffractometer ASTERIX of the Los Alamos Neutron Science Center (LANSCE). A schematic diagram of Asterix is represented in Fig.2.15. The sample is illuminated at a fixed incident angle, while a magnetic field is applied parallel to the sample surface.

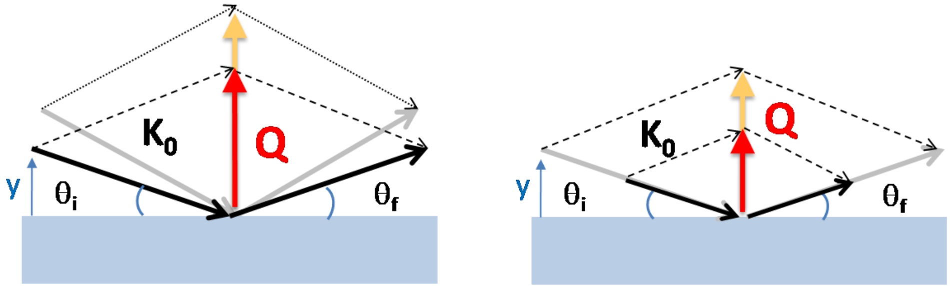

Fig.2.14: The wave vector transfer can be modulated by: changing the incidence angle of the beam (left), changing the neutron wavelength (right).

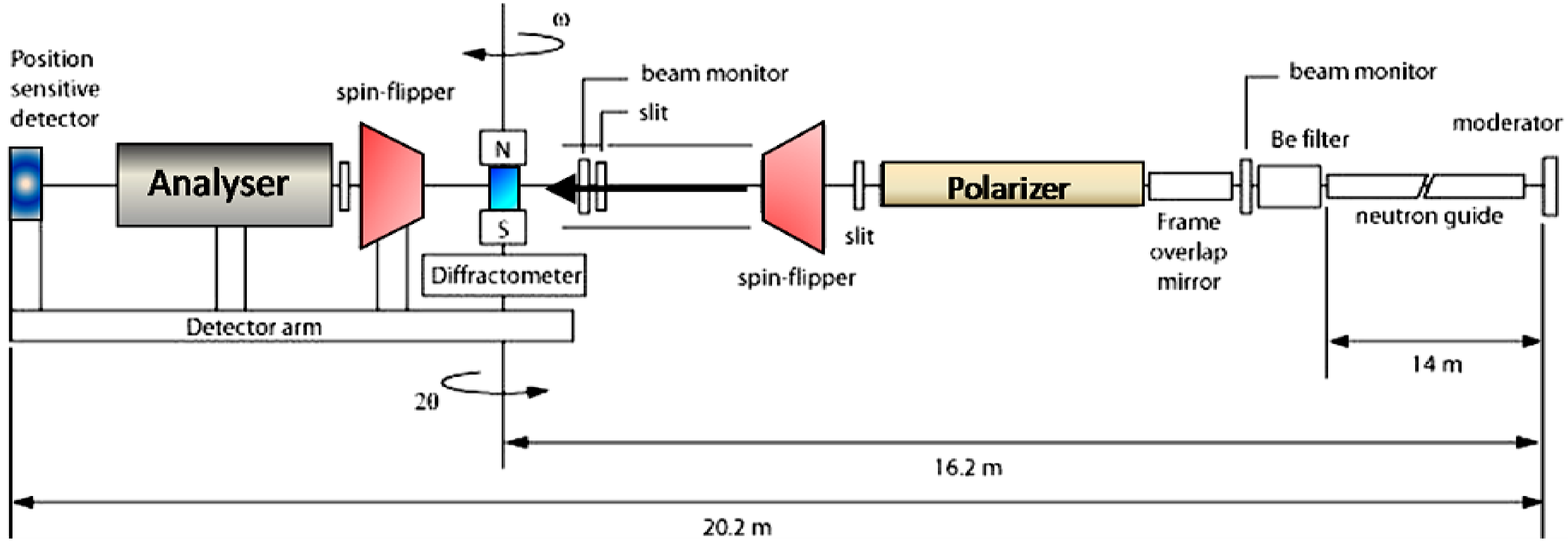

Fig.2.15: Schematic side view of the reflectometer Asterix at LANSCE [9]

Several devices, placed along the neutron beam, accomplish different tasks. Some of them play with the capability of the neutron spin to precess around *B*. One of them is the polarizer. It consists in a system of wedge-shaped supermirrors inside a cavity through which neutrons are transmitted (see Fig.2.16). The angle ε subtended by the supermirror is chosen such that only spin-down neutrons with wavelengths greater than a minimum value are transmitted through the cavity. The final part of the cavity is properly magnetized by a special arrangement of magnetic fields which make an angle φ with the axis of the beam and vary in time. Provided that the rate of change in φ with time, $| d\varphi/dt |$ is less than 1/4 of the Larmor precession frequency ω_L , the neutron beam polarization will follow the change in the direction of the magnetic field. Specifically, the neutron spin precesses on the surface of a cone with frequency equal to ω_L. The polarization direction changes from parallel to the beam axis to perpendicular and spin-down oriented.

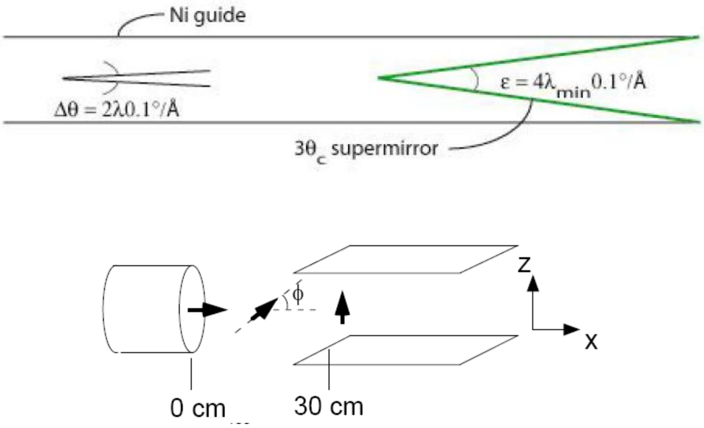

Fig.2.16: Schematic diagram of the polarization cavity [9]

The polarization of the beam can be switched from down to up using a radio-frequency gradient field spin-flipper, which consists of two orthogonal magnetic fields, one static and one rotating (see Fig.2.17). The static field is produced by a wedge shaped yoke, which generates a low field in the center of the flipper with a longitudinal gradient. The rotating field is produced by a radio-frequency solenoid. The frequency of this field is chosen so that a resonance occurs in the middle of the spin flipper every time the device is activated. The result is an adiabatic inversion of polarization of the beam.

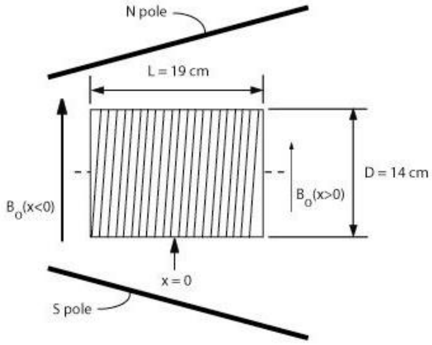

Fig.2.17: Schematic diagram of the radio-frequency gradient field spin-flipper [9]

The resolution of the reflectometer, δQ/Q is approximately given by:

$$\left(\frac{\delta Q}{Q}\right)^2 = \left(\frac{\delta\theta}{\theta}\right)^2 + \left(\frac{\delta\lambda}{\lambda}\right)^2 \qquad 2.23$$

The first term is determined by a combination of factors including sample size and the dimensions of slits that collimate the incoming neutron beam. For glancing angles of incidence (typically less than 5°), δθ/θ is of order 2% . The second term is determined by how well the wavelength of the incident neutron beam is measured. When the TOF technique is used δλ/λ is typically 0.2% .

2. 5. X-ray Magnetic Circular Dichroism (XMCD)

X-ray magnetic circular dichroism (XMCD) spectroscopy makes use of high energy X-rays to explore the structural and magnetic properties of matter. It was first suggested by Erskine and Stern [18] and pioneered by Schütz et al. [19]. It has several capabilities not afforded by traditional magnetic techniques. Its foremost strengths are the element-specific, quantitative determination of spin and orbital magnetic moments and their anisotropies [20]. Other strengths are its chemical sensitivity [21], its lateral resolution of at least 1 μm^2 [22], and its sub-monolayer sensitivity [23]. An XMCD experiment usually consists of illuminating the sample with intense circularly polarized X-rays produced in synchrotron sources and tuning the X-ray energy on the absorption edge of a specific element. The difference between left and right circularly polarized X-ray absorption cross section (the dichroism signal) of a ferromagnetic or a ferrimagnetic material is directly proportional to the mean value of the macroscopic magnetic moment.

XMCD technique has been applied to the samples studied in this work to analyze the Mn and Cu absorption edge. To describe the magnetism of the *d* orbitals in transition metal compounds (as well as the 4*f* orbitals in rare earth compounds), soft X-rays, with energy less than 3keV, have to be used. As a consequence of the absorption and reflection of X rays on the surface, different effects can be detected as the production of fluorescence, secondary electrons, and altered reflected intensity. Each of these effects yields information about the magnetic state of the sample and can be collected simultaneously by different detectors. The detection modes are usually referred to as fluorescence yield (FY), total electron yield (TEY) and reflectivity. [24,25]

X-ray absorption spectroscopy (XAS): chemical environment

X-ray absorption spectroscopy (XAS) studies the effect of photon absorption on the matter. It is not necessarily dependent on the incident photon spin. In X-ray absorption a photon is absorbed by an atom giving rise to a transition of an electron (a photoelectron) from a core state to an empty state above the Fermi level. The absorption cross-section depends on the energy and on the measured element. To excite an electron in a given core level, the photon energy has to be equal or higher than the energy of this core level which is characteristics of the element. [25] When this energy level is crossed, a sudden jump in the absorption intensity is observed (Fig 2.18). Excitation of photoelectrons gives rise to the creation of core holes which may decay by either radiative or non-radiative transitions. These vacancies present an unstable condition for the atom. As the atom returns to its stable condition, electrons from the outer shells are transferred to the inner shells giving off, during the process, a characteristic X-ray whose energy is the difference between the two binding energies of the corresponding shells. The emitted X-rays produced from this process can be detected in the FY mode. The secondary X-ray excitations can promote additional electronic transitions; in fact when a vacancy is created in the L-shell by the excitation an electron from the M or N shell “jumps in” to occupy the vacancy Fig 2.19a.

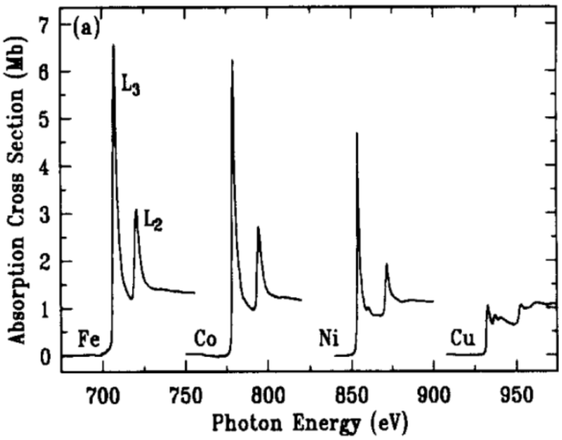

Fig 2.18: X-ray absorption spectra recorded by total electron yield detection near the L, and L1 edges for Fe, Co, Ni, and Cu metal, showing the existence of white lines for Fe. Co, and Ni and its near-absence for Cu, due to its nearly filled d shell. [20]

In this process, it emits X-rays and in turn, produces a vacancy in the M or N shell. In transition metals the *d*-orbitals are partially filled and close to the Fermi level. If an X-ray has just sufficient energy to excite a core level, then the resultant photoelectron will leap into unoccupied states above the Fermi level Fig 2.19b. On the other hand when the excitation energy from the inner atom is transferred to one of the outer electrons, this (Auger) electron is ejected from the atom. The energy spectrum of the emitted electrons consists of well defined lines due to photoelectrons and Auger electrons on top of a background due to secondary electrons. These low-energy secondary electrons resulting from inelastic collisions of initially excited photoelectrons or Auger electrons, give rise to a major portion of the electron emission, and the sample can be regarded as an effective electron multiplier. Monitoring the total electron yield (TEY), i.e. all electrons emitted from the sample, offers the simplest mode for detecting the photo-absorption process. It is often easier to measure not the emitted electrons directly but their complement given by the sample drain current flowing into the sample. The transitions are usually labeled according to the position of the exited electron; transition from the $p_{1/2}$ level would lead to the L_{II} line, while transition from $p_{3/2}$ would lead to the L_{III} line. Table 2.2Table reports the binding energies of the electrons involved in the transitions both for Mn and Cu where we highlighted the L_{II} and L_{III} edges studied in this work. Low energy secondary electrons have short excape depth (l_e= 2-4 nm) which limits the available information; all the electrons that excape must originate at the surface.

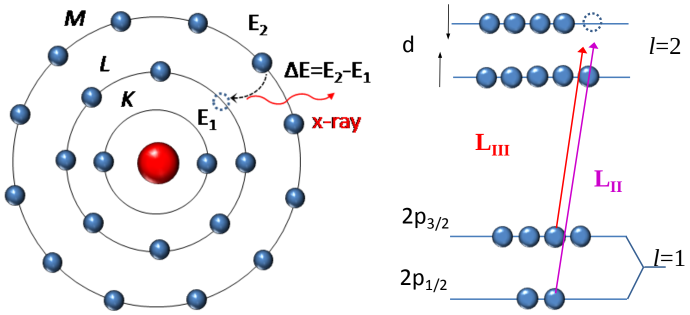

Fig 2.19: Schematic diagram of fluorescence process (left) and electronic transition (right).

The fluorescence signal escape depth l_f is much greater than l_e, in fact the photon created in the fluorescent decay has a mean free path of the same order of magnitude of the incoming X-ray, which exclude any surface effect [25] . In spite of the short inelastic mean free path of secondary electrons, it has been shown that by monitoring the X-ray induced TEY versus grazing incident angle at a fixed incoming photon energy one can obtain information about microstructures not only in the near-surface region but also about the buried interfaces [28-30]. This is due to the fact that electron emission from stratified medium is determined by the radiant energy losses in the near-surface region, which is the primary source of total electron yield, and this process is governed by the electromagnetic distribution in the entire stratified medium. Spectra taken from a single metal mainly show two broad peaks, reflecting the width of the empty *d*-bands Fig 2.18. In general the oxide spectra are more complicated exhibiting multiplet structure due to the electrostatic interactions between 2p core-hole and 3d valence electrons and 2p core-hole spin-orbit interactions, as well as by the local crystal fields and the hybridization with the O 2*p* ligands [31-33] .(see Fig.2.20).

ORBITAL	LABEL	ENERGY (eV)
1s	K	8979
2s	L_{I}	1096.7
$2p_{1/2}$	L_{II}	952.3
$2p_{3/2}$	L_{III}	932.7
3s	M_{I}	122.5
$3p_{1/2}$	M_{II}	77.3
$3p_{3/2}$	M_{III}	75.1

ORBITAL	LABEL	ENERGY (eV)
1s	K	6539
2s	L_{I}	769.1
$2p_{1/2}$	L_{II}	649.9
$2p_{3/2}$	L_{III}	638.7
3s	M_{I}	82.3
$3p_{1/2}$	M_{II}	47.2
$3p_{3/2}$	M_{III}	47.2

Table 2.2: Binding energies for Cu (left) and Mn (right) [26]

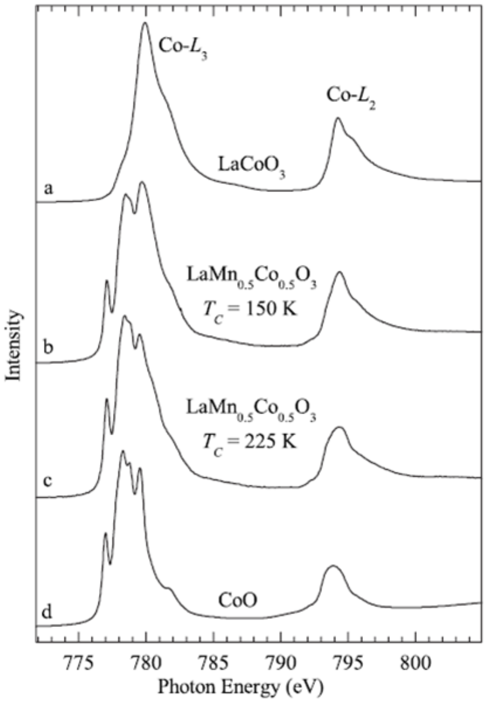

Fig.2.20: XAS spectra for different Co oxides [33].

XMCD: magnetic information

Constraints on the transition are represented by the selection rules. Because of the ΔJ=0,±1 dipole selection rule the 1/2→ 5/2 (or inverse) transition is forbidden (spin flips are forbidden in electric dipole transition), spin-up (spin-down) photoelectrons from the *p* core shell can only be excited into spin-up (spin-down) *d* hole states. Hence the spin-split valence shell acts as a detector for the spin of the excited photoelectron and the transition intensity is simply proportional to the number of empty *d*-states of a given spin. The quantization axis of the valence shell "detector" is given by the magnetization direction. When circular polarization is applied to the photon beam, the electromagnetic field vector turns around the direction of the propagation vector. The difference between the transition probability for left and right circularly polarized light gives the circular magnetic dichroism. Since the dipole selection rule is different for right (RCP) and left (LCP) circularly polarized light, the respective components may be absorbed differently, depending on the nature of the two magnetic band state (see Fig.2.21). The emitted radiation will reflect this imbalance and will be elliptically polarized with the major polarization axis rotated relative to that of the incident light. If a spin-orbit splitting is assumed both in the *p* and *d* state, the L_{III}/L_{II} line and dichroism can be dramatically affected. X-ray resonant magnetic reflectivity (XRMR) provides an alternative method for measuring the magnetic dichroism from the subsurface region. Resonant reflectivity measurements present some advantages if compared to other techniques. XRMR is a coherent elastic scattering process with no complex final state effect, and the presence of a core excitation makes it element selective [34] . It also presents some strictly experimental advantages: it is a photon-in/photon-out process, hence not affected by the presence of magnetic fields acting on the sample, and collecting the reflectivity at different angles gives a coarse way of tuning the probing depth [35-37]. XRMR and XMCD signals cannot be directly compared since the reflected intensity measured is a dynamically scattered beam that depends upon both the absorptive and dispersive parameters of the material. The most common way of measuring XMCD in the soft x-ray region is total electron yield (TEY), because of the easy experimental setup and high signal-to-noise ratio compared to fluorescence yield.

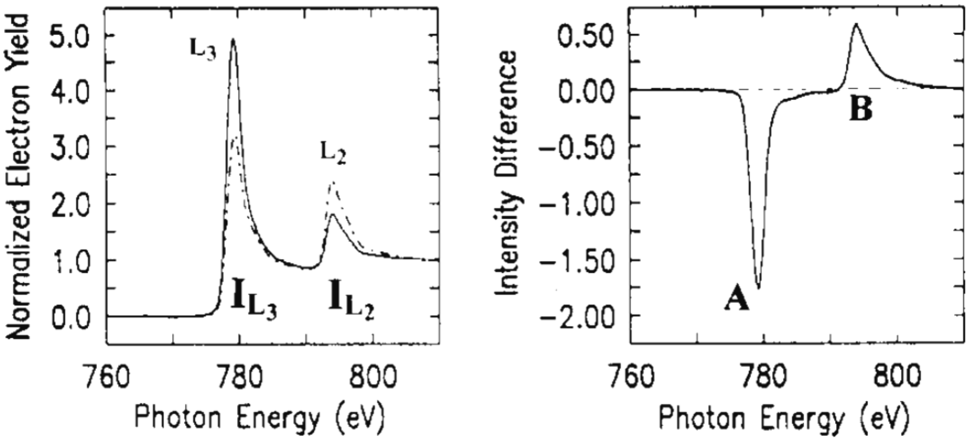

Fig.2.21: Left) Normalized X-ray magnetic circular dichroism spectra at the L_{III} and L_{II} edges for Co metal. The original spectra have white line intensities I_{L3} and I_{L2} which depend on the relative orientation of photon spin and magnetization direction, shown solid for parallel and dashed for antiparallel alignment. Right) The difference spectrum gives dichroism intensities ,$A < 0$ and $B > 0$ at the L_{III} and L_{II} edges, respectively.

After determining the energy position of the maximum magnetic signal, one can sweep the magnetic field to recreate a hysteresis loop. The determination of the intensity, shape, coercivity of a XMCD hysteresis loop can be very useful to distinguish between the magnetic behavior of the single layers in multilayers of alternating soft and hard ferromagnets [38] and as further information about induced ferromagnetic moment at interfaces [39] . Surprisingly TEY was used only marginally for magnetization curves in the past. The major problem using field dependent TEY is the complex current behavior as a function of applied magnetic fields, which directly results in corresponding normalization problems. [40]

Sum rules

XMCD measurements are connected to the ground-state value of the orbital and spin moment by the magneto-optical sum rules [41,42]. For example, the first sum rule says that, in a good approximation, the total transition intensity of the two (L_{II} and L_{III}) peaks is proportional to the number of *d* holes. So the spin and orbital moment can be determined from linear combinations of the dichroic difference intensities (A and B, see Fig.2.21). There are six sum rules which link polarization dependent $p \rightarrow d$ X-ray absorption intensities to ground state properties of the *d* shell. Three sum rules link angle and polarization dependent X-ray absorption intensities to anisotropic *d*-shell properties: the charge density, the spin density and the angle-dependent orbital moment. Three others allow the determination of angle-integrated d-shell properties: the number of *d* holes, the magnetic spin moment, and the orbital magnetic moment. Because of their important implications for magnetic materials and the fact that they were derived from a single-ion model which neglects several aspects of the band structure arising in real systems, there have been many attempts to verify the validity of XMCD sum rules in determining element-specific orbital and spin moments. Although the applicability of the sum rules has been confirmed to bulk-like Co and Fe and films [43], the applicability for low-symmetry systems (like strongly correlated electron systems) and their practical application is complicated by the spectral density weight spreading over a broad energy interval.[20]

Basic theory

Spin-dependent absorption of circularly polarized photons may be visualized as a two stage process (see Fig.2.22). First, a circularly polarized photon excites a photoelectron from a core level. In the second stage, the photoelectron is captured into an unoccupied valence state. The transition rate depends on the number of available final states with spin parallel to the photoelectron spin, and so differences in the spin polarized density of state lead to different transition probabilities for spin-up and spin-down photoelectrons.

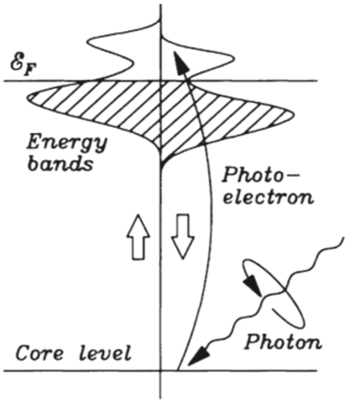

Fig.2.22 The two stage picture of spin-dependent photoabsorption [45]. A circularly polarized photon excites and polarizes a photoelectron which is subsequently absorbed into a vacant spin-polarized valence band.

Since the photoelectron spin is governed by the helicity of the absorbed photon, the transition rates become different for left- and right- handed photons.A correct description of the dichroism effect can be made by applying the principles of crystal-field theory. Here we will limit to describe the fundamental steps which explain the importance of the dichroism signal. In general the X-ray wave-length is much larger than the typical size of a light atom (for example, at the L_{III} edge $\lambda_{Mn}\approx 19.2$Å and $\lambda_{Cu}\approx 13.3$Å). This fact allows one to study the interaction between the atom and the polarized X-ray using the electron dipole approximation: $e^{\left(i\left(\frac{\omega}{c}\right)\boldsymbol{n}\cdot\boldsymbol{r}\right)} \cong 1$ (here $\boldsymbol{n}$ is a unit vector that specifies the propagation direction) [24,45]. As a consequence the electromagnetic wave (the perturbation) assumes a simplified form as well as the interaction Hamiltonian:

$$H_{int} = -\left[\sum_i \frac{q}{m}\boldsymbol{p_i}\cdot\boldsymbol{A}(\boldsymbol{r}_i) - \sum_i \frac{q^2}{2m}\boldsymbol{A}(\boldsymbol{r}_i)^2\right] - \left[\sum_i g_i \frac{q}{m}\boldsymbol{S}\cdot\boldsymbol{B}(\boldsymbol{r}_i)\right] \tag{2.24}$$

The photon electromagnetic field is described by the vector potential $\boldsymbol{A}$ which includes the electric field ***e***, and by ***B***. The second term is proportional to the electric quadrupole operator while the third term is proportional to the magnetic dipole operator. Magnetic dipole transitions and electric quadrupole transitions are respectively about 10^5 and 10^8 times more unlikely than similar electric dipole transitions. In a first order approximation the third term results to be zero. This means that the spin is conserved during the absorption: $\Delta m_s = 0$. (Spin dependence will result from spin-orbit interactions).

From the time-dependent perturbation theory we know that the transition probability between an initial state $|i\rangle$ to a final state $|f\rangle$, is given the Fermi Golden Rule:

$$T_{i,f} = \frac{2\pi}{\hbar}\sum_{i,f}|\langle f|\boldsymbol{e}\cdot\boldsymbol{r}|i\rangle|^2\ \delta\left(E_f - E_i - \hbar\omega\right) \tag{2.25}$$

where $\boldsymbol{e}$ characterize the direction of the X-ray electric field vector while $\boldsymbol{r}$ denotes the electron's position vector: $r = e_x x + e_y y + e_z z$

(the delta function takes care of the energy conservation and a transition takes place if the energy of the final state equals the energy of the initial state plus the X-ray energy).

Hence one should proceed with the calculation of the transition matrix elements$|\langle f|\boldsymbol{e}\cdot\boldsymbol{r}|i\rangle|^2$. A particularly simple case of photon absorption by an atom occurs when the photon is circularly polarized with the preferred axis parallel or antiparallel to the photon propagation (see Fig 2.23).

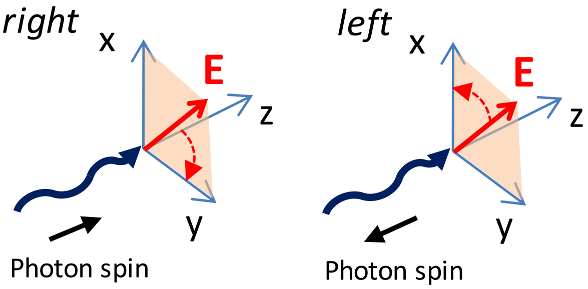

Fig 2.23: Schematic representation of the polarization of the incident photon and the spin direction

Since the electromagnetic field vector turns around the direction of propagation we will have:

$$e^- = \frac{1}{\sqrt{2}}\left(e_x - ie_y\right) \quad right \qquad 2.26$$

$$e^+ = \frac{1}{\sqrt{2}}\left(e_x + ie_y\right) \quad left$$

The transition is now described by polarization-dependent dipolar operators: $\boldsymbol{e}^+ \cdot \boldsymbol{r}$ and $\boldsymbol{e}^- \cdot \boldsymbol{r}$. The dipolar operators can be written in terms of the spherical harmonics $Y_l^{m_l}(\theta, \varphi)$ where l=1 and m_l=0,±1 , assuming the form $P_{m_l}^{(l)}$ which depicts the role of the orbital angular momentum l and its projection along the z direction m_l (m_l=0 would refers to linear polarization):

$$P_1^{(1)} = \frac{1}{\sqrt{2}}(x + iy) = -r\sqrt{\frac{4\pi}{3}}Y_1^1 \quad right$$

$$P_{-1}^{(1)} = \frac{1}{\sqrt{2}}(x - iy) = r\sqrt{\frac{4\pi}{3}}Y_1^{-1} \quad left \qquad 2.27$$

$$P_0^{(1)} = z = r\sqrt{\frac{4\pi}{3}}Y_1^0 \quad linear$$

The transition matrix element, a combination of spherical harmonics, is non-zero only if:

$$\Delta l = l_f - l_i = \pm 1$$

and

$$\Delta m_l = m_{lf} - m_{li} = +1 \quad left \qquad 2.28$$

$$\Delta m_l = m_{lf} - m_{li} = -1 \quad right$$

These are the selection rules for the electric dipole approximation.

The electric dipole approximation allows a transition from a *2p* state to a *1s* state, but disallows a transition from a *2s* to a *1s* state. To understand the consequences of the polarization dependence Sthör and Wu [45] make a further simplification to the problem considering $p \rightarrow d$ transitions only for a d^9 configuration band, where all the spin-up states are filled and there is a hole in the spin-down states. Only five spin-down functions have to be considered (with m_l=-2,-1,0,1,2). This procedure reduces the number of transition probabilities to be calculated without changing the final result and its underlying meaning (all the relevant one-electron wave functions for these transitions are reported in table xx2). They also consider another quantity: the strength of the transition, i.e. the X-ray absorption intensity per atom *I*. It is a dimensionless quantity (also called the *oscillator strength*) and is given by the expression:

$$I = \frac{2m}{\hbar^2}\frac{\left(E_f - E_i\right)^2}{\hbar\omega}|\langle f|\boldsymbol{e}\cdot\boldsymbol{r}|i\rangle|^2 \qquad 2.29$$

The polarization dependent form is given by:

$$I_{\pm} = \frac{m}{\hbar^2}\frac{\left(E_f - E_i\right)^2}{\hbar\omega}|\langle f|x \pm iy|i\rangle|^2 \qquad 2.30$$

Where + refers to *right* and – to *left.*

As before, *I* can be written using the spherical harmonics. The radial wave function *R* is explicitly introduced but it is assumed to be identical, as well as the radial matrix element, for the spin-orbit split states.

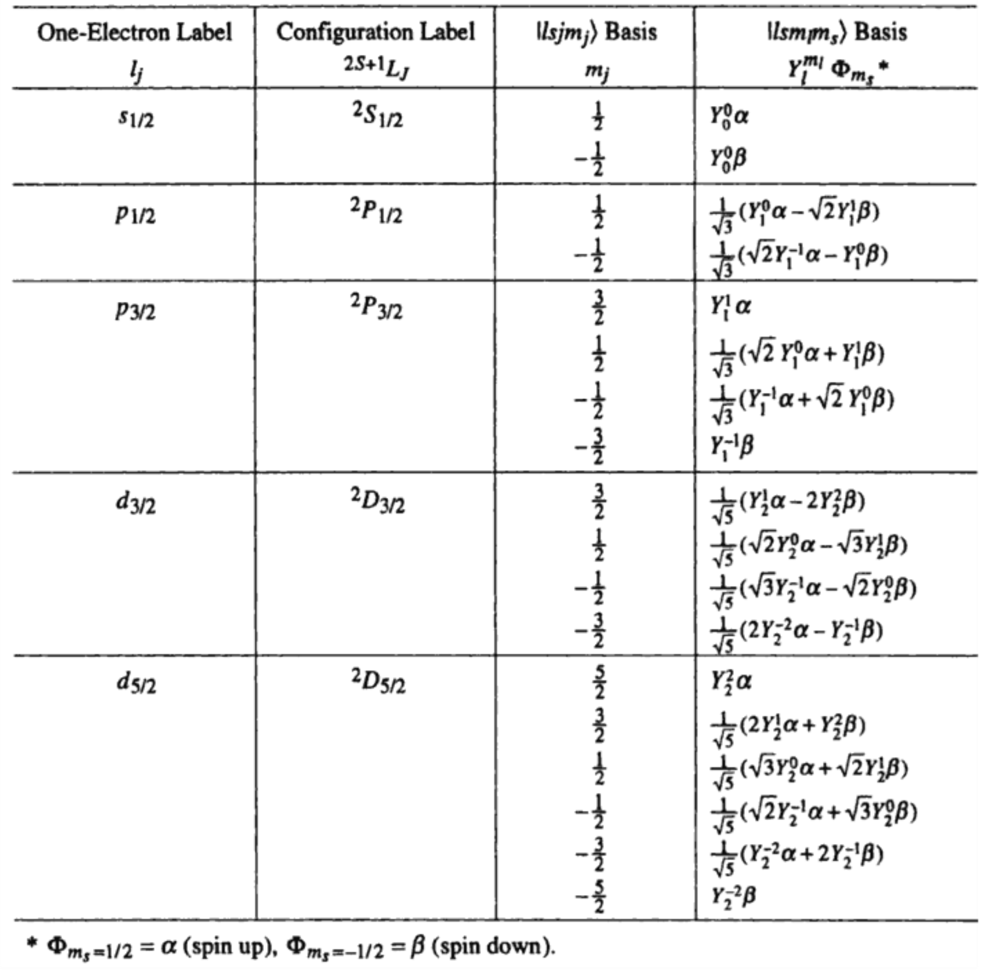

One-Electron Label l_j	Configuration Label $^{2S+1}L_J$	$\|lsjm_j\rangle$ Basis m_j	$\|lsm_lm_s\rangle$ Basis $Y_l^{m_l}\,\Phi_{m_s}$*
$s_{1/2}$	$^2S_{1/2}$	$\frac{1}{2}$ $-\frac{1}{2}$	$Y_0^0\alpha$ $Y_0^0\beta$
$p_{1/2}$	$^2P_{1/2}$	$\frac{1}{2}$ $-\frac{1}{2}$	$\frac{1}{\sqrt{3}}(Y_1^0\alpha-\sqrt{2}Y_1^1\beta)$ $\frac{1}{\sqrt{3}}(\sqrt{2}Y_1^{-1}\alpha-Y_1^0\beta)$
$p_{3/2}$	$^2P_{3/2}$	$\frac{3}{2}$ $\frac{1}{2}$ $-\frac{1}{2}$ $-\frac{3}{2}$	$Y_1^1\alpha$ $\frac{1}{\sqrt{3}}(\sqrt{2}\,Y_1^0\alpha+Y_1^1\beta)$ $\frac{1}{\sqrt{3}}(Y_1^{-1}\alpha+\sqrt{2}\,Y_1^0\beta)$ $Y_1^{-1}\beta$
$d_{3/2}$	$^2D_{3/2}$	$\frac{3}{2}$ $\frac{1}{2}$ $-\frac{1}{2}$ $-\frac{3}{2}$	$\frac{1}{\sqrt{5}}(Y_2^1\alpha-2Y_2^2\beta)$ $\frac{1}{\sqrt{5}}(\sqrt{2}Y_2^0\alpha-\sqrt{3}Y_2^1\beta)$ $\frac{1}{\sqrt{5}}(\sqrt{3}Y_2^{-1}\alpha-\sqrt{2}Y_2^0\beta)$ $\frac{1}{\sqrt{5}}(2Y_2^{-2}\alpha-Y_2^{-1}\beta)$
$d_{5/2}$	$^2D_{5/2}$	$\frac{5}{2}$ $\frac{3}{2}$ $\frac{1}{2}$ $-\frac{1}{2}$ $-\frac{3}{2}$ $-\frac{5}{2}$	$Y_2^2\alpha$ $\frac{1}{\sqrt{5}}(2Y_2^1\alpha+Y_2^2\beta)$ $\frac{1}{\sqrt{5}}(\sqrt{3}Y_2^0\alpha+\sqrt{2}Y_2^1\beta)$ $\frac{1}{\sqrt{5}}(\sqrt{2}Y_2^{-1}\alpha+\sqrt{3}Y_2^0\beta)$ $\frac{1}{\sqrt{5}}(Y_2^{-2}\alpha+2Y_2^{-1}\beta)$ $Y_2^{-2}\beta$

*** $\Phi_{m_s=1/2}=\alpha$ (spin up), $\Phi_{m_s=-1/2}=\beta$ (spin down).**

Table 2.3 : Relevant on-electron wave function for the transition between p$\frac{1}{2}$ and p$\frac{3}{2}$ state to the empty spin down state of the d band. [45]

Under these considerations for the L$_{III}$ edge we will have:

$$I_{L_{III}}^{+} = \textstyle\sum_{i,f} \left|\left\langle f \middle| P_1^{(1)} \middle| i \right\rangle\right|^2 = \frac{1}{3}R \qquad 2.31$$

$$I_{L_{III}}^{-} = \sum_{i,f} \left|\left\langle f \middle| P_{-1}^{(1)} \middle| i \right\rangle\right|^2 = \frac{5}{9}R$$

and for the L$_{II}$ edge:

$$I^{+}_{L_{II}} = \sum_{i,f} \left|\left\langle f\middle|P^{(1)}_{1}\middle|i\right\rangle\right|^{2} = \frac{1}{3}R \qquad 2.32$$

$$I^{-}_{L_{II}} = \sum_{i,f} \left|\left\langle f\middle|P^{(1)}_{1}\middle|i\right\rangle\right|^{2} = \frac{1}{9}R$$

This result shows that the dichroism signal is given by the difference $\Delta I = I^{+} - I^{-}$ and that the signals form L$_{III}$ and L$_{II}$ edges are opposite in sign.

Finally, the quantity which gives a measure of the probability of the transition process is the absorption cross-section and is defined as the ratio of the power absorbed by the atom to the incident power per unit area (cU) of the electromagnetic field:

$$\sigma_{abs} = \frac{\hbar\omega T_{i,f}}{cU} \qquad 2.33$$

In the electron dipole approximation is given by:

$$\sigma_{abs} = \frac{\pi e^{2}}{\varepsilon_0 m^{2}\omega c} \left|\langle i|\boldsymbol{e}\cdot\boldsymbol{r}|f\rangle\right|^{2} \delta\left(E_f - E_i - \hbar\omega\right) \qquad 2.34$$

which in the polarization-dependent form is written as:

$$\sigma_{\pm} = 4\pi^{2}\hbar\omega\alpha \sum_{i,f} \left|\left\langle i\middle|\mp\sqrt{\frac{4\pi}{3}}rY^{-1}_{1}\middle|f\right\rangle\right|^{2} \delta\left(E_f - E_i - \hbar\omega\right) \qquad 2.35$$

(α is the fine structure constant).

The experimental dichroism signal is then defined as the asymmetry ratio:

$$XMCD = \frac{\sigma_{+} - \sigma_{-}}{\sigma_{+} + \sigma_{-}} \qquad 2.36$$

Beamline configuration

Most of the XAS and XMCD data shown in this thesis have been taken at the 4-ID-C beamline of the Advanced Photon Source (Argonne National Laboratory). A schematic view of the beamline optics is shown in Fig 2.25. The X-ray source consists in a helical undulator which provides circularly polarized photons while a spherical grating monochromator allows operating in the region from 500eV to 3000eV. Vertical and horizontal focusing is realized by a set of plane and spherical mirrors. After having been collimated the final spot covers an area of about 100x100μm^2. The spectrometer is also capable to select between linear and circular polarization. The switching between RCP and LCP occurs at a frequency of 1Hz. The sample is placed in a UHV cryostat where the temperature can be controlled in the range from 30K to 400K; lower temperatures cannot be achieved due to the heating effect of the X-ray beam. Fig 2.24 shows a schematic view of the sample chamber. The magnetizing coils provide a magnetic field up to 0.1T that is always parallel to the sample surface. The total electron yield signal is measured amplifying the current which flows through the sample after connecting the sample surface (separated from the conducting sample holder by the insulating STO substrate) to the ground by means of silver paint. TEY, FY and reflectivity signal can be collected simultaneously through energy scans in which at every energy step the polarization is switched between RCP and LCP after applying a magnetic field. The experimental setup also allows to vary the incident angle of the beam. In our case we performed our measurements at grazing incidence angle, between 5º and 10º since we assume that the magnetization vector lies in the plane of the sample (for more detail see the experimental chapter).

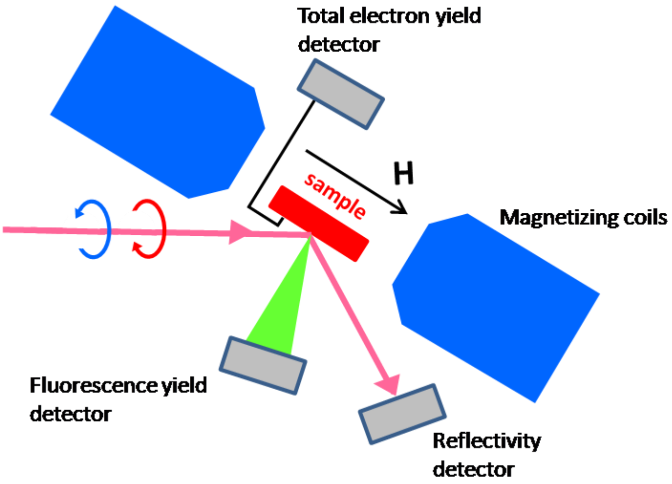

Fig 2.24: Schematic top view of the sample chamber.

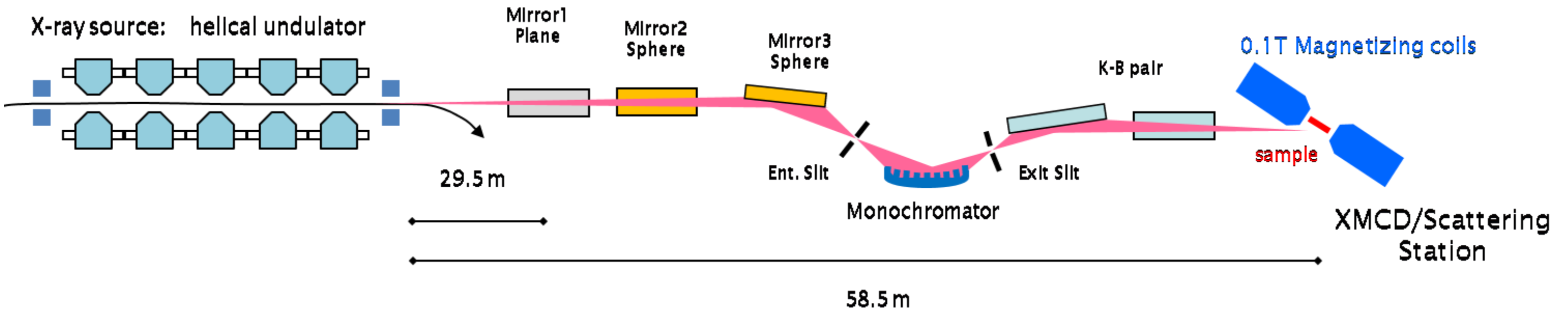

Fig 2.25: Schematic top-view of the 4-ID-C beamline at the Advanced Photon Source (Argonne National Lab).

References

1. O. Nakamura, E. Fullerton, J. Guimpel, I. K. Schuller. Appl.Phys.Lett. 60,120, (1992)
2. D. Kelly, E. Fullerton, J. Santamaría, I. K. Schuller. Scripta Metallurgica et Materiala 33, 1603 (1995)
3. A. Guinier. ”*X ray diffraction in crystals, imperfect crystals and amorphous bodies”*. Dover Publications (1994)
4. N. M. Aschroft and N. D. Mermin. “Solid State Physics”. HR International Editors, Hong Kong (1987)
5. L. J. van der Pauw. Philips Res. Rep., (13), (1958)
6. *Neutron News*, Vol. 3, No. 3, , pp. 29-37 (1992)
7. C. F. Maykrzak, J.W. Cable, J. Kwo, M. Hong, D.B. McWhan, Y.Yafet, J. Waszcak. *Phys.Rev.Lett.* (56), 2700 (1986).
8. G. P. Felcher, R. O. Hilleke, R. K. Crawford, J. Haumann, R. Kleb, and G. Ostrowski. Rev. Sci. Instrum. (58), 609 (1987)
9. M. R. Fitzsimmons, C. F.Majkrzak. In Y. Zhu, *Modern Techniques for Characterizing Magnetic Materials* (pp. 107-155). Springer (2005)
10. C. Fermont, F.Ott, A.Menelle. Neutron Reflectometry. In A. J. Daillant, *X-ray and Neutron Reflectivity* (p. 183). Springer(2009).
11. H. Ekstein. Phys.Rev. (76), 1328 (1949).
12. F. Bloch.. Phys.Rev. (50), 259 (1936)
13. D. J. Hughes, M.T.Burgy.. Phys.Rev (76), 1413 (1949)
14. D. J. Hughes, M.T.Burgy.. Phys.Rev. (81), 498 (1951)
15. J. F. Ankner,G.P.Felcher. J.Magn.Magn.Mater. (200), 741 (2000).
16. J. S. S. Schwinger. Phys.Rev (51), 544 (1937)
17. L. G. Parrat. Phys.Rev. (95), 359 (1954)
18. J. L. Erskine, Phys.Rev.B (12), 5016 (1975)
19. G. Schütz, W. Wagner, W. Wilhelm, P. Kienle, R. Zeller, R. Frahm, G. Materlik. . Phys.Rev.Lett. (58), 737 (1987)
20. J. Sthör. J.Elec.Spe.Rel.Phen. (75), 253 (1995).
21. F. Sette, C. T. Chen, Y. Ma, S. Modesti, N. V. Smith . In S. S. Hasnain, X-ray Absoption Fine Structure (p.96). Ellis Horwood. (1991)
22. J. Sthör, Y. B. . Science (259), 658 (1993)
23. L. H. Tjeng, I. U. Idzerda, P. Rudolf, F. Sette, C.T. Chen, J.Magn.Magn.Mater. (108), 288 (1992).

24. F. Baudelet.. X-ray Magnetic Circular Dichroism. In F. Hippert, *Neutron and X-ray Spectroscopy* (page 103). Springer. (2006)
25. F. deGroot, J. Vogel Fundamentals of X-ray absorption and dichroism: the multiplet approach. In E. J.-B. F.Hippert, *Neutron and X-ray spectroscopy* (p. 3). Springer. (2006).
26. J. C. Fuggle, N. Mårtensson. J. Electron Spectrosc.Relat.Phenom. (21), 275. (1980)
27. Y. Zhu, In *Modern techniques for characterizing magnetic materials* (page 159). Springer.(2005)
28. A. Krol, C.J.Sher, Y. H. Kao, Phys. Rev. B , 42, 3829 (1990)
29. V. Chakarian, Y. U. Idzerda, C. T. Chen. (1998). *Phys.Rev.B* (57), 5312.
30. H. Ebel, M. Mantler, R. Svagera, R. Kaitna. *Surf.Interface Anal.* (22), 602. (2004).
31. G. van der Laan, B. T. Thole. *Phys.Rev.B* (43), 13401 (1991).
32. M. Kobayashi,Y. Ishida,J. l. Hwang,T. Mizokawa, A. Fujimori, K. Mamiya, J. Okamoto, Y. Takeda, T. Okane,Y. Saitoh,Y. Muramatsu, A.Tanaka, H. Saeki, H.Tabata, T.Kawai.. Phys.Rev.B (72), 201201 (2005)
33. T. Burnus, Z. Hu, H.H Hsieh, V. L. J. Joly, P.A. Joy, M.W. Haverkort, Hua Wu, A. Tanaka, H.-J. Lin, C.T. Chen, L.H. Tjeng. Phys.Rev.B (77), 125124 (2008)
34. C. Kao, J. B. Hastings, E. D. Johnson, D. P. Siddons, G. C. Smith Phys.Rev.Lett. (65), 373 (1990).
35. M. Sacchi, J. Vogel, S. Iacobucci. J.Magn.Magn.Mater. (147), L11 (1995)
36. J. W. Freeland, K.E.Gray, L.Ozyuzer, P.Berghuis, E.Badica, J.Kavich, H.Zheng, J.F.Mitchell. Nat.Mater. (4), 62.(2004)
37. S. Valencia, A. Gaupp, W. Gudat, Ll. Abad, Ll. Balcells, B. Martinez. . J.Appl.Phys. (104), 023903. (2008)
38. M. Yu, J. Hattrick-Simpers, I. Takeuchi, J. Li, Z. L. Wang, J.P. Liu, S.E. Lofland, S. Tyagi, J.W. Freeland, D. Giubertoni, M. Bersani, M. Anderle. J.Appl.Phys. (98), 063908 (2005)
39. A. Baruth, D. J. Keavney, J. D. Burton, K. Janicka, E. Y. Tsymbal, L.Yuan, S. H. Liou, S. Adenwalla. . Phys.Rev.B (74), 054419 (2006)
40. A. Goering, A. Fuss, W. Weber, J. Will, G. Schütz. . J.Appl.Phys. (88), 5920 (2000)

41. B. T. Thole, P. Carra, F. Sette F, G. van der Laan. Phys.Rev.Lett. (68), 1943 (1992).
42. P. Carra, B. T. Thole, M. Altarelli, X. Wang. Phys.Rev.Lett. (70), 694 (1993)
43. C. T. Chen, Y. U. Idzerda,H-J. Lin, G. Meigs, A. Chaiken, G.A. Prinz, G. H. Ho. Phys.Rev B (48), 642 (1993).
44. S. W. Lovesey, S. P. Collins. *X ray Scattering and Absorption by Magnetic Materials.* Oxford University Press (1996)
45. J. Sthör, Y. Wu. (1994). X-ray magnetic circular dichroism: basic concepts and theory for 3d transition metal atoms. En F. A.S.Schlachter, *New directions in research with third-generation soft x-ray synchrotron radiation sources.* Springer.

3. Experiments

3.1 Introduction

Thin film heterostructures combining ferromagnets (F) and superconductors (S) are ideally suited to study the interplay between both long range orderings [1,2]. When a superconductor is placed in contact with a ferromagnet both long range phenomena may compete at the interface, which gives rise to a variety of exotic phenomena like π-junctions, a spatially modulated order parameter, etc. [3,4]. Interesting effects occur at the interface between a superconductor and a ferromagnet. Due to the F/S proximity effect the pairing amplitude penetrates into the F side and the order parameter is also depressed in the S material due to the effect of the exchange field [1,2]. When a thin superconductor is brought in contact with an inhomogeneous ferromagnet the cancellation of the exchange field over the coherent volume results in novel effects. Examples are domain wall superconductivity [5,6] or the F/S/F superconducting spin switch (see Fig. 3.1) [7-9]. In the first case, oppositely directed magnetizations at both sides of a domain wall promote nucleation of superconductivity if the coherence length is larger than the width of the domain wall. In the second case, antiferromagnetic alignment of the magnetizations of the F layers results in larger T_C values than does the ferromagnetic alignment, due to the averaging out of the exchange field over the coherent volume.

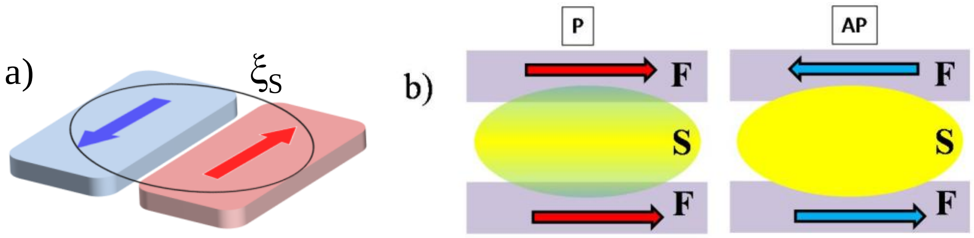

Fig.3.1 Schematic representation of a) the domain wall superconductivity, b) F/S/F superconducting spin switch.

In recent years there has been an increasing interest in structures combining oxide ferromagnets and oxide superconductors [10-14]. In particular, the combination of high- T_C superconductors (HTS) and colossal magnetoresistance manganites (CMR), gives rise to a number of new properties and behaviors, which considerably enrich the study of F/S interplay [15,16]. The unconventional pairing symmetry (*d*-wave) of the superconductor with an anisotropic gap exhibiting nodes in [110] directions, affords quasiparticles to be incorporated at zero energy cost. On the other hand, the highly spin polarized conduction band of the manganites will cause the suppression of Andreev reflection, and thus conventional proximity effect, at F/S interfaces. Thus *d*-wave superconductivity and half metallicity will conspire to enhance the relative importance of phenomena originating at the transfer of (spin polarized) quasiparticles. Perovskite HTS and CMR materials, chosen with good lattice matching, can be grown epitaxially one on top of the other with atomically flat interfaces exhibiting no interdiffusion [17,18]. F/S/F hybrids of the HTS superconductor $YBa_2Cu_3O_{7-\delta}$ (YBCO) and the CMR manganite $La_{0.7}Ca_{0.3}MnO_3$ (LCMO) display large values of magnetoresistance when magnetization of the ferromagnetic layers is antiparallel aligned. This effect can be denominated as *inverse superconducting spin switch* since in contrary to the (direct) spin switch superconductivity is promoted in the ferromagnetic alignment of the F layers. The origin of the magnetoresistance is quite controversial. Some reports have proposed spin dependent effects on transport: diffusion of spin polarized quasiparticles from one ferromagnetic layer to the other would be disfavored in the antiparallel alignment of the F layers resulting in the depression of the superconducting order parameter (see Fig.3.2a) [19-22]. Others favor the importance of stray fields due to the domain structure of the ferromagnet in depressing the critical temperature at the coercive field (see Fig.3.2b) [23,24]. This last scenario is justified by the fact that a well defined antiparallel alignment is difficult to establish due to the short distance between the coercive fields. The aim of the present chapter is to clarify the origin of the magnetoresistance through the study of the magnetic and transport properties of LCMO single films and LCMO/YBCO heterostructures. Several experiments have been performed using different techniques (VSM and SQUID magnetometry, FMR, AFM, PNR, XMCD) which addressed the origin of this magnetoresistance on spin dependent effects.

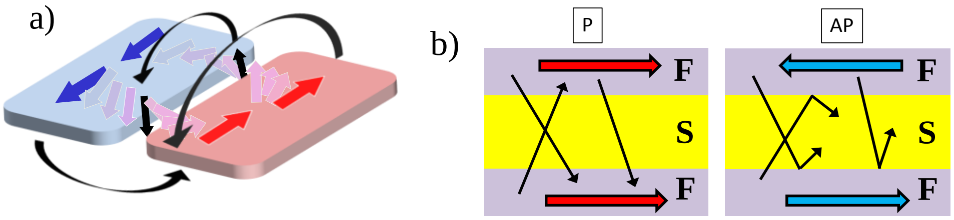

Fig.3.2 Schematic representation of a) the stray field effect, b) the diffusion of spin polarized quasiparticles, in F/S/F hybrids.

3.2 F/S interplay in bilayers

A detailed study of the domain structure of the ferromagnetic layers is of major importance. Magnetic anisotropy may depend on crystalline orientation and on thickness through the influence of strain, surface morphology, and roughness [25-28]. In the following sections we focus on the magnetic properties of epitaxial LCMO thin-films as the first and necessary step in gaining an understanding of the properties of F/S structures. We address this with resistivity, magnetization, and ferromagnetic resonance (FMR) experiments.

a) Thickness dependent magnetic anisotropy of ultrathin LCMO epitaxial thin films

We first used LCMO thin films with thickness ranging from 3nm to 39 nm, to study the structure (using X-ray reflectivity and diffraction) and magnetotransport properties. Magnetization was measured in a VSM (Quantum Design PPMS) magnetometer. Temperature dependent magnetization was recorded on warming in a field of 0.1 T after field-cooling in 1 T. The hysteresis loops were recorded at 77 and 10 K between either ±3 T or ±1 T. Magnetotransport was measured in a cryostat equipped with a 9 T magnet (Quantum Design PPMS-9 T).

Then we compared FMR measurements for a thin (4nm) and a thick (15nm) film. FMR was recorded in a modified JEOL ESR spectrometer operated at 8.9 GHz, in a cryostat filled with liquid nitrogen. The substrates were 10x5x1 mm^3 rectangles and were subsequently cut with a diamond wheel to smaller pieces as needed by the various techniques. X-ray scattering was measured on a 5x5 mm^2 piece and for resistivity measurements four silver contacts were evaporated in the corners. Magnetization experiments were done on 1.5x1.5 mm^2 squares to allow for measurements in orientation perpendicular to the magnetic field. For the FMR experiments, the 1.5 mm pieces were mounted on small, cylindrical, teflon holders either parallel or perpendicular to the cylindrical axis using vacuum grease and then sealed in 4-mm diameter quartz tubes after evacuating and backfilling them with 20 mbar He exchange gas. These ampoules were then directly placed in the liquid nitrogen.

We measured X-ray reflectivity (top panel) and diffraction (bottom panel) for several thin films, as shown in Fig.3.3 . The thickness was calculated using finite size oscillation of the reflectivity pattern (see chapter 2). An X-ray refinement technique, using the SUPREX 9.0 software, was used to obtain quantitative information about the interface roughness [29-32].Thin manganite films on STO suffer compressive strain along the *c*-axis, which is reflected by the position of the (002) diffraction peak (see Fig.3.3); this peak moves toward higher angle when the thickness is reduced indicating a shortening of the *c*-axis parameter. This strain relaxes relatively slowly; the *c* lattice parameter changes only by 0.5% between a 60 Å and a 390 Å LCMO film that in turn differs from the bulk by 1.2%. In Fig.3.4, we summarize the magnetization (top) and resistivity (bottom) results of LCMO thin films of various thicknesses. Manganite layers as thin as 3-nm exhibit clear ferromagnetic hysteresis loops. The saturation magnetization of the thinnest manganite films takes values close to the bulk indicating the absence of thick magnetic dead layers. The coercive field increases drastically in thinner films, suggesting a change in the domain structure. Nevertheless, the field of saturation is also larger in thinner films raising the possibility that the magnetization lies out of the film plane. Temperature dependent resistivity is shown in the bottom panel of Fig.3.4. Films thicker than 6 nm are metallic at low temperature with well defined metal insulator transition, although the thinnest films remain insulating in the whole temperature range.

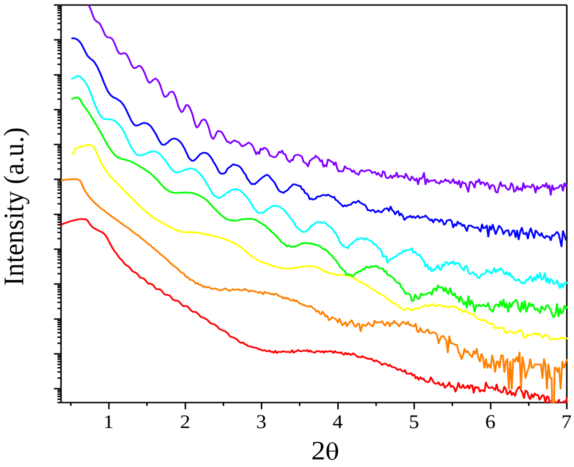

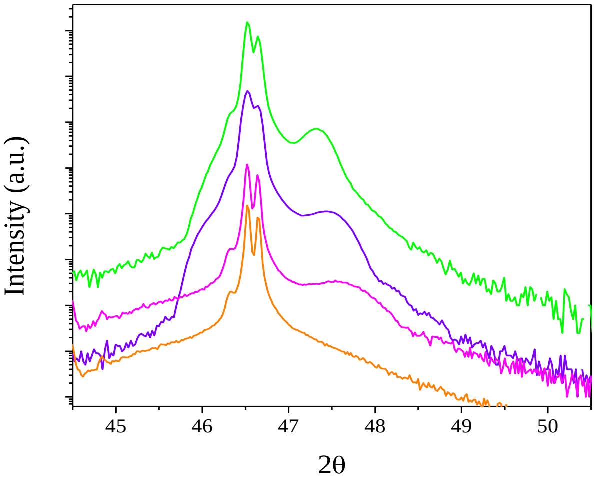

Fig.3.3(top) X-ray reflectivity of LCMO thin films with thickness: 3, 4, 6, 11, 15, 22, 39 nm, from bottom to top . (bottom) X-ray diffraction around the STO (002) Bragg peak of the LCMO thin films. Thicknesses are: 3, 6, 15, 39 nm, from bottom to top.

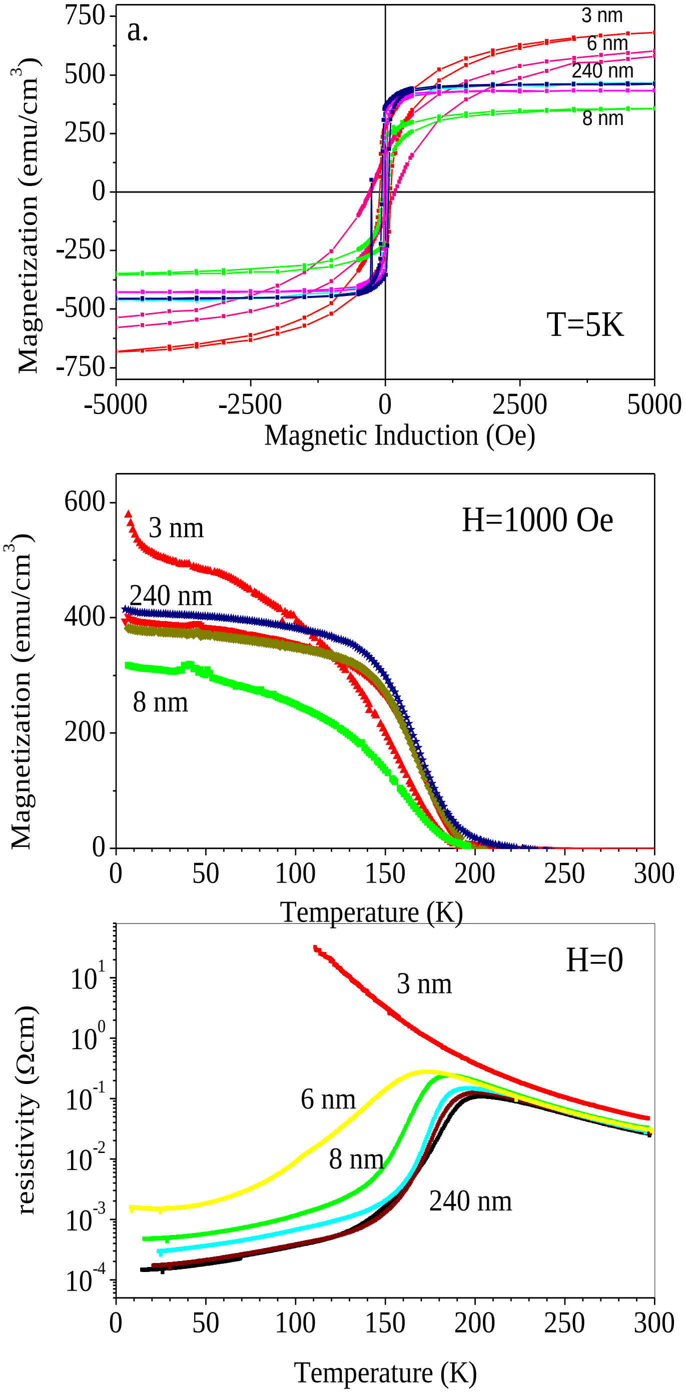

Fig.3.4 (a) Magnetization hysteresis loops, (b) temperature dependent magnetization, (c) and resistivity of LCMO thin films with various thicknesses between 3 and 240 nm.

Next, we investigate the direction of easy axes of magnetization in the individual F layers. Fig.3.5 shows the magnetization hysteresis loops of 4- (top) and 15-nm- (bottom) thick LCMO thin films. The hysteresis loops were recorded at 77 K, to match the temperature of the FMR experiments. Each sample was mounted three times, on a standard Plexiglas VSM sample-holder using kapton-tape, with the external magnetic field directed along the [100], [110], and [001] crystallographic directions of the cubic STO substrate, with the first two lying in the plane of the LCMO thin film, and the third being perpendicular. The magnetic field was swept by 50 Oe/s. The data appear quite noisy, but this is due only to the very small size of the samples; the typical saturation magnetization is1-2x10^{-5} emu, whereas the noise floor of the VSM is a few times 10^{-7} emu. The hysteresis loops of both LCMO recorded with the field perpendicular to the film plane exhibit a pronounced round shape and very large saturation field (~ 0.5 T and over 1 T for the 4 and the 15-nmthick LCMO, respectively), compared to the in-plane hysteresis loops (with saturation fields around 0.1 T). The coercive field is also appreciably larger for both samples with the field perpendicular. These observations indicate that the magnetization lies preferentially in-plane in both LCMO, irrespective of thickness [25-28]. Furthermore, similar differences can be discerned between the two in-plane hysteresis loops of the 15-nm-thick LCMO (Fig.3.5, lower panel). The lowest saturation field is seen when the magnetic field is oriented along a [110] direction of the cubic STO substrate, or practically, making 45 degrees with the edge of the sample. This indicates that the easy axes in these thicker LCMO films lie along the [110] axes. Similar conclusions cannot be drawn for the in-plane anisotropy of the thinner LCMO based on the magnetization hysteresis loops because of the relatively stronger noise of the data. The difference between the in-plane and out-of-plane hysteresis loops is less pronounced in the 4-nm-thick sample.

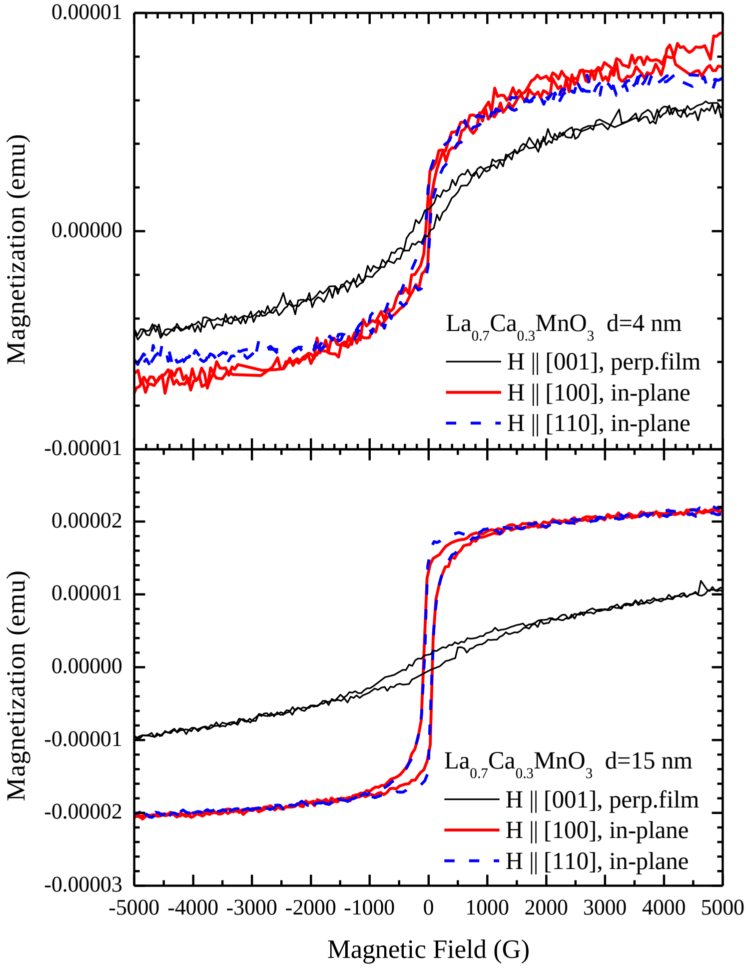

Fig.3.5. Magnetization hysteresis loops of d=4 nm (*top*) and d= 15 nm (*bottom*) LCMO thin films with the external magnetic field lying along [100] and [110] in-plane directions and along [001], perpendicular to the film-plane, at 77 K.

Fig.3.6 shows a series of FMR spectra for both the 4- (left) and the 15-nm-thick (right) LCMO thin films, as they are rotated in-plane with respect to the external magnetic field. 0, 90, 180 and 270 deg indicate directions when the field is parallel to the edge of the samples, and thus to crystal axes, [100] or [010], of the cubic STO substrate. Consequently, the field in these directions also coincides with pseudo-cubic crystal axes of the manganite. It is apparent from Fig.3.6 that the position of the FMR varies with this in-plane angle. In fact, it displays 4 maxima and minima. Furthermore, at angles when the FMR is at maximum in the 4-nm-thick LCMO, it is at minimum in the 15-nm-thick LCMO and vice versa. The small peaks around 3300

G are paramagnetic resonance lines of the STO substrate. In Fig.3.6 and Fig. 3.7 the y-axis position of the baseline denotes the angle of orientation in which the spectra were recorded, whereas the actual spectral intensity (the derivative of microwave absorption) is given in arbitrary units. The lower panel of Fig.3.6 shows the FMR field (indicated radially) extracted from the spectra on a polar plot, with the polar angle corresponding to the actual orientation of the sample in the spectrometer. Similarly, Fig. 3.7 depicts a series of FMR spectra as the film plane is rotated with respect to the external magnetic field. The lower panel shows the FMR field versus out-of-plane orientation. Using ferromagnetic resonance we mapped the direction of the in-plane easy axes in 4- and 15-nm-thick LCMO films and found that both exhibit biaxial symmetry, similar to (LSMO) thin films [25,26]. Nevertheless, the symmetry direction in the two films is rotated by 45 degrees with respect to the crystallographic directions. In the 4-nm film, the in-plane easy axes are the [100] and [010] while in the 15-nm film the easy axes are the [110] and [1–10], indicated by the minimum values of the FMR field. We have simulated the 15-nm data of Fig.3.6 and Fig. 3.7 on the following magnetic anisotropy model for the free energy density:

$$F=-M_S*\mathbf{B_0}.\mathbf{m}+(\mu_0/2*M_S^2+K_{2c})\,m_z^2+K_{4ab}\,(m_x^4+m_y^4). \qquad 3.1$$

Here, B_0 is the external magnetic field, M_S is the magnetization, while **m** is the unit-vector in its direction. The first term is the energy of a magnet in the external field. The second term is due to the demagnetization, and its effect could be merged into the out-of-plane uniaxial anisotropy (third term), since they give the same orientation dependence. Therefore, they cannot be obtained separately from FMR only, and we use M_S = 450 kA/m as given by magnetometry. The last term represents the in-plane, biaxial anisotropy. We found that the simulation in Fig.3.6 and Fig. 3.7 using K_{2c} = 88 kJ/m^3 and K_{4ab} = 0.23 kJ/m^3 for magnetic anisotropies, is the best fit.

This model is unable to describe the FMR results of the 4-nm-thick sample. The data in Fig.3.6 deviate slightly from the fourfold symmetry due to the inevitable misalignment of the film plane and the external magnetic field. As the sample is rotated, it may wobble to and from the field direction. The principal directions are also a few degrees off of the expected 0, 45, 90, etc., because of a similar uncertainty in the angular offset when the sample is mounted. Fig. 3.7 shows the position of the FMR as the external field is rotated out-of-plane and the corresponding model based on the above Hamiltonian.

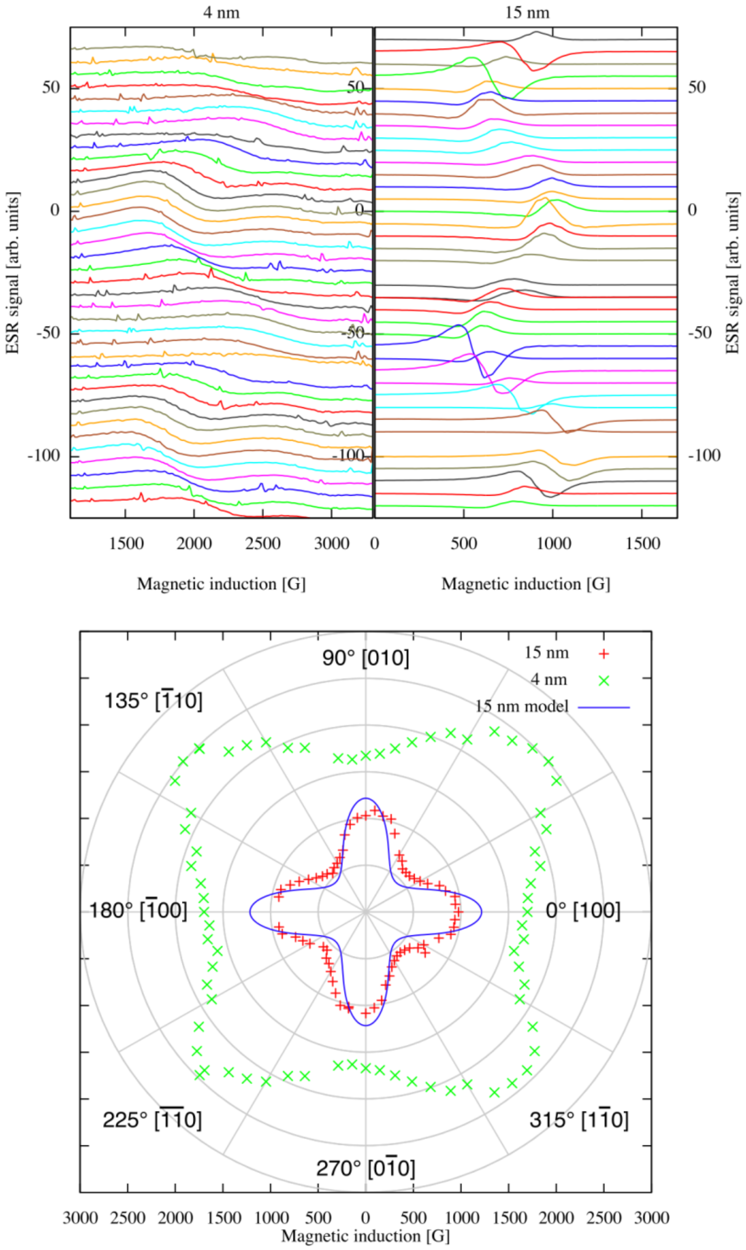

Fig.3.6 (Top) Ferromagnetic resonance spectra at *f*=8.88 GHz in d= 4 nm. (Left) d=15 nm. (Right) LCMO thin films at 77 K with the external magnetic field lying along various in-plane directions. The spectra were linearly displaced so that their baseline position indicates the in-plane angle. (Bottom) FMR positions shown in polar-plot for both 4- and 15-nm-thin films. The blue curve is a model for the 15-nm sample as described in the text. The radial axis corresponds to the magnetic field from 0 to 3000 G. Some of the 4-nm points are not independent data but mirrored from equivalent positions.

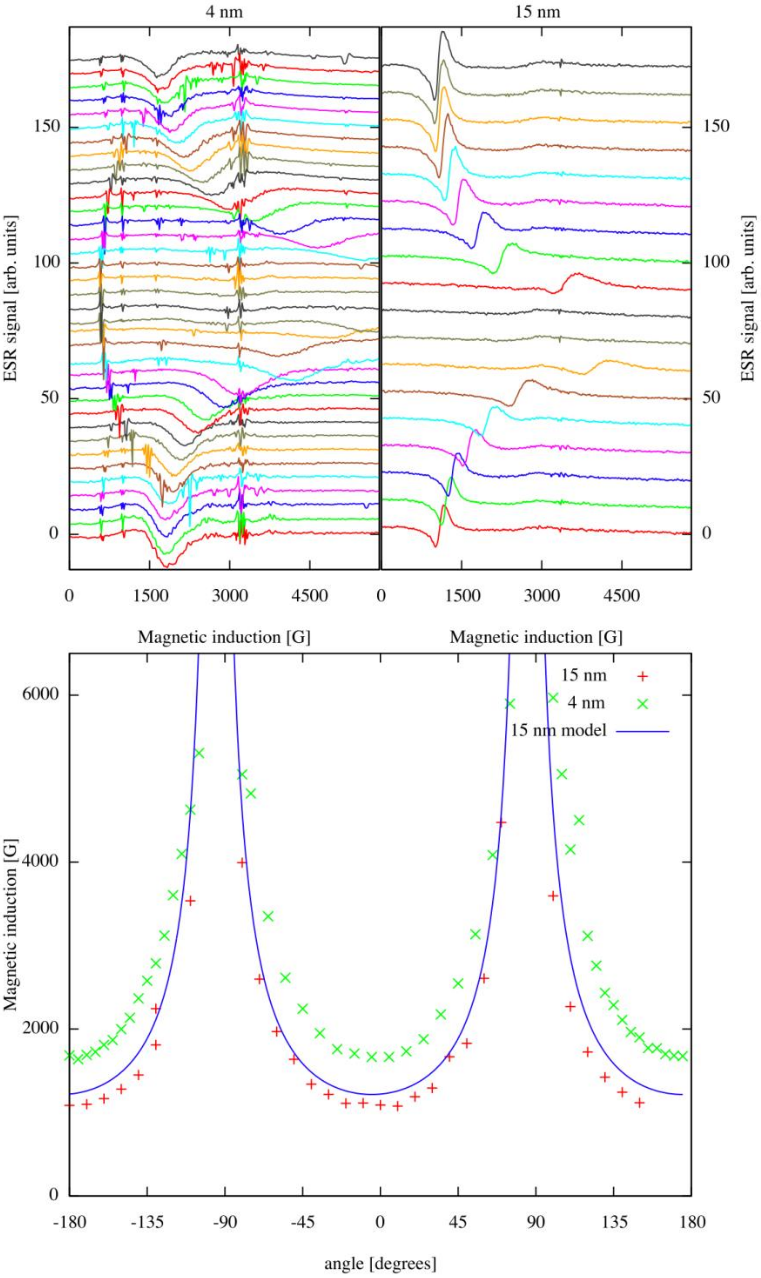

Fig. 3.7 (Top) Ferromagnetic resonance spectra at f=8.88 GHz in d= 4 nm. (Left) d=15 nm. (Right) LCMO thin films with the external magnetic field rotated out-of-plane. The spectra were linearly displaced so that their baseline position indicates the out-of-plane angle, 90 being the field perpendicular to plane configuration. (Bottom) FMR positions for both 4- and 15-nm-thin films.

The demonstration of biaxial in-plane magnetic anisotropy in LCMO is itself a new contribution of the present study. It agrees well with the similar finding in LSMO thin films and with recent reports in LCMO thin films [28]. However, the rotation of the biaxial anisotropy axes by 45 degrees with the change of the thickness of the LCMO is a new and unexpected finding. The direction of the easy axes in the thicker (15 nm) LCMO film agrees with that found in LSMO, that is, they lie along axes such as [110] and [1-10]. There are several reasons why the easy axes may move to the crystal axes [100] and [010]. Thinner LCMO is more strained. The STO substrate and bulk LCMO are not perfectly lattice matched (a_{LCMO}=3.87 Å, a_{STO}=3.905 Å) and tensile epitaxial strain may influence the orbital structure (favoring the occupation of the $d_{x^2-y^2}$ orbitals) and thus influence the magnetic anisotropy. Strain relaxation in thicker samples may thus generate a change in the magnetic anisotropy. Nevertheless, it is also possible that the magnetic anisotropy of very thin LCMO layers is influenced by extrinsic mechanisms such as steps and other correlated defects of the substrate. The STO single crystal substrates are cut along the [100] crystal planes within an approximately 0.5° uncertainty. Therefore, lattice steps are present on the polished surface. However, the direction of these terraces is completely random, being determined by the exact way the substrate is mounted during the polishing step. As the thickness of the manganite thin film is shown to be responsible for dramatic changes in the magnetic and metallic behavior of the ferromagnetic layer, it will be important to study the properties of manganite thin films when they form part of various LCMO/YBCO (F/S) hetero-structures.

In summary, ultrathin LCMO epitaxial films grown on STO remain ferromagnetic down to 3 nm. However, the metal-insulator transition is maintained only in films thicker than about 6 nm. The magnetic easy axis lies in the film plane independent of thickness, at liquid nitrogen temperature. However, there is a pronounced biaxial in-plane magnetic anisotropy, with two perpendicular, equivalent easy axes. The orientation of these easy axes changes with LCMO thickness. In thicker LCMO (~15 nm) the easy axes are the [110] and [1–10] pseudo-cubic directions. In thinner LCMO (~4 nm) the easy axes coincide with the in-plane crystal axes [100] and [010].

b) Bilayers with thin and ultrathin LCMO

As discussed previously, the high T_C superconductor YBCO and the half-metallic manganite LCMO have similar in-plane lattice parameters what allows the epitaxial growth of YBCO/LCMO heterostructures. The difference in the lattice parameters, though small, is such that one material grown on another will be affected by some degree of strain. In our case, both YBCO and LCMO would suffer in-plane tensile strain when grown directly on STO. The volume of a single unit cell must remain constant according to the Poisson law; as a consequence the *c*-axis parameter would shorten. In the previous section we showed that the LCMO (c_{bulk}=3.87 Å) is fully strained up to quite large thicknesses since the *c*-axis parameter ranges between 3.82Å and 3.84Å (30Å<d<390Å). The orthorhombic structure of YBCO is a fundamental component for the superconductivity. The in-plane large deformation suffered by the unit cell has strong consequences on the transport properties of thin films. Very few unit cells of YBCO on STO are superconducting but the T_C results much depressed. A way to restore the superconductivity is to introduce between the substrate and the thin film a very thin buffer layer of $PrBa_2Cu_3O_7$ (PBCO). This material is a paramagnetic semiconductor, isostructural to the YBCO, with in-plane lattice parameter 1% larger than those of YBCO. It has been shown that PBCO improve the growth of YBCO and its transport properties [33]. Almost all the samples used in this work are free of any PBCO buffer layer except for very particular cases in which a PBCO buffer layer has been used with the purpose of observing the effect of the structural changes on YBCO.

Previous results on the magnetic and transport properties of YBCO/LCMO bilayers showed that this kind of heterostructures can be grown in very thin epitaxial layers preserving the intrinsic characteristics of both materials (superconductivity and ferromagnetism) [33-35]. The depression of the superconductivity in bilayers with a systematic change of the YBCO thickness has been observed and interpreted as the pair breaking effect due to injection (diffusion) of spin-polarized quasi-particles from the LCMO to the YBCO. At the same time a long range proximity effect induces a depression of the interface magnetization in the LCMO layer.

In this section we will discuss some experiments focused on the effect of the magnetic structure of the LCMO on the superconductivity and vice versa.

Here we consider a set of bilayers in which thin (15nm) and ultra thin (4nm) LCMO is grown alternately on top of the YBCO (Y/L samples) or directly on the STO (L/Y samples), as summarized in the sketch of Fig. 3.8. The thickness of YBCO is 12nm

(10 u.c.) for all the bilayers. By changing the thickness of LCMO we are acting on the domain structure (and possibly on the anisotropy) of the ferromagnetic layer. On one hand, when the LCMO is grown directly on the substrate we don't expect the structural properties to be different from that of a single film. Any effect on the magnetic properties is then caused by the presence of the superconducting layer. On the other hand, when the LCMO is grown on top of the YBCO we expect to see changes in the magnetic properties due to the different strain condition. It has been previously reported that in YBCO/LCMO hybrids the depression of the superconducting critical temperature is accompanied by improved magnetic properties of the LCMO [33,36]. The effect scales with the thickness of both YBCO and LCMO. In bilayers the magnitude of the effect depends on the position occupied by the LCMO. It has been shown that for a 15nm-thick LCMO grown on top of the YBCO the effect is more pronounced, even when a PBCO buffer layers is introduced between YBCO and substrate. In the two configurations Y/L and L/Y the superconducting critical temperature recovers the bulk values when the YBCO is approximately 18nm thick. In the present experiment the superconducting layer is thick enough to be relaxed, so the LCMO layer grown on top of it has to adjust its lattice to the anisotropic *ab* plane of the YBCO. This may favor the formation of an inhomogeneous ferromagnetic phase although the LCMO structure is chemically homogeneous.

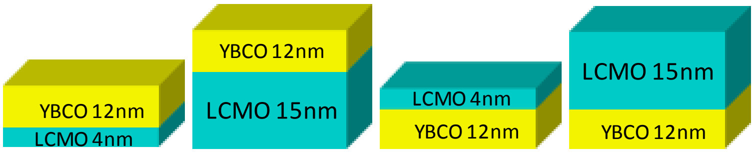

Fig. 3.8 Schematic arrangement of the bilayers as it will be used along this section.

In the previous section it has been showed that the magnetic easy axis of the LCMO changes from the [100] direction in ultra thin layers to [110] direction in thickest layers. Our purpose here is to study the magnetic anisotropy of the LCMO in bilayers to separate the contribution of the top and bottom LCMO in the LCMO/YBCO/LCMO trilayers studied in the next sections. We performed magnetization measurements in a VSM magnetometer applying the field along the [110] and [100] direction at several temperatures to observe the magnetic behavior of the samples when the superconducting state is established. The critical temperature was determined by resistance measurements in zero applied field (see Fig.3.9a). The onset of the superconducting transition will be denominated T_{C_onset} while the temperature at which the resistance becomes zero will be called T_{C_0}. Fig. 3.9b shows magnetization *vs* temperature measurements for the bilayers taken while heating the samples in H=100 Oe. The field was applied in the plane of the sample along the STO [100] crystal axis. We compare the measurements for Y/L samples taken after zero-field cooling with those for the L/Y samples taken after cooling in H=100 Oe to show that T_{C_0}, the onset of the vortex glass regime, is indicated in the first case (ZFC) by a decrease of the magnetic moment due to the diamagnetism of the YBCO and in the second case (FC) by an increase of the magnetization due to the paramagnetic Meissner effect [37,38]. The large value of the magnetic moment in the latter case has been explained as follows: due to the impossibility of getting a perfect parallel alignment between field and sample there will always be a small perpendicular component of the field responsible of the nucleation of superconducting vortices. Lateral magnetic inhomogeneities of the sample, as in the case of phase separation, act as strong pinning centers inducing flux trapping and vortex compression. This phenomenon has been already reported in YBCO/LCMO superlattices with thicknesses of the individual layers comparable to those used here [39].

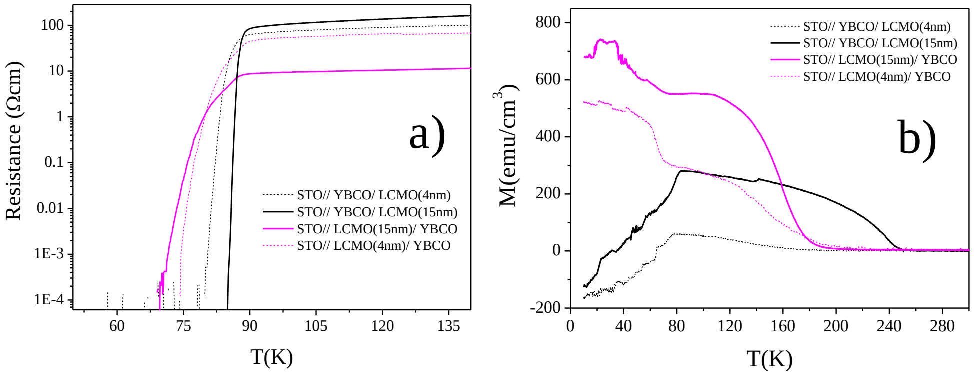

Fig. 3.9 a) Resistance vs temperature for the Y/L samples (black curves) and L/Y samples (pink curves) in zero applied field and b) Magnetization vs temperature measured with field applied along the [100] direction taken while heating up in H=100 Oe after FC in H=100 Oe for the L/Y samples and after ZFC for the Y/L samples.

The magnetic moment of the LCMO is close to the full moment in L/Y samples while it is quite depressed in Y/L samples due to different strain conditions. To see if the magnetic anisotropy was also affected by strain we measured magnetic hysteresis loops for all the samples applying the field along the [100] and [110] directions of the STO. In Fig. 3.10 we compare the L/Y bilayers with the 4nm-thick LCMO. The left panels show the behavior of the loops while approaching the saturation field, while the right panels show a smallest portion of the loop close to the coercive fields. Data were taken at 100K (well above the superconducting transition). FMR data on the LCMO ultra-thin film showed that the easy axis of magnetization lies along the [100] direction of the STO (the sample edge). From the hysteresis loops we cannot appreciate the different behavior when the field is applied along the easy or hard direction since the two measurements are almost identical. This is true also for the bilayer with the 4nm-LCMO on the bottom suggesting that the easy axis may be the [100] axis (see Fig. 3.10 b). For the 15nm L/Y sample the easy axis is clearly lying along the [110] direction as indicated by the higher remanence and the smaller saturation field of the [110] curve. The coercive field even for the thickest LCMO layer is always less than 100 Oe. This is in agreement with the FMR data for a 15nm-thick LCMO single film. While the results for the L/Y bilayers resemble those for the single films, the picture is quite different in the case of the Y/L samples as shown in Fig.3.11a. The bilayer with 4nm-thick LCMO grown on top of the YBCO clearly shows that the easy axis is directed along the [110] axis as stated by the shape of the curve, with a larger coercive field, of about 120 Oe, when the field is applied along the easy direction. This is in contrary to the case of the 4nm-L/Y bilayer and the 4nm-LCMO single film and shows that the anisotropic unit cell of the YBCO may play a role in determining the magnetic anisotropy of the LCMO on top. In the case of the 15nm-Y/L bilayer (see Fig.3.11b), the fact that the easy axis lies on the [110] direction, which can be an intrinsic property of relative thick LCMO films, is not a direct manifestation of the presence of the underlying YBCO. The large value (~300 Oe) of the coercive field indicates that the YBCO induces a different domain structure in the LCMO. Domain nucleation can be characterized by a larger number of domain walls and consequently a different size of the magnetic domains.

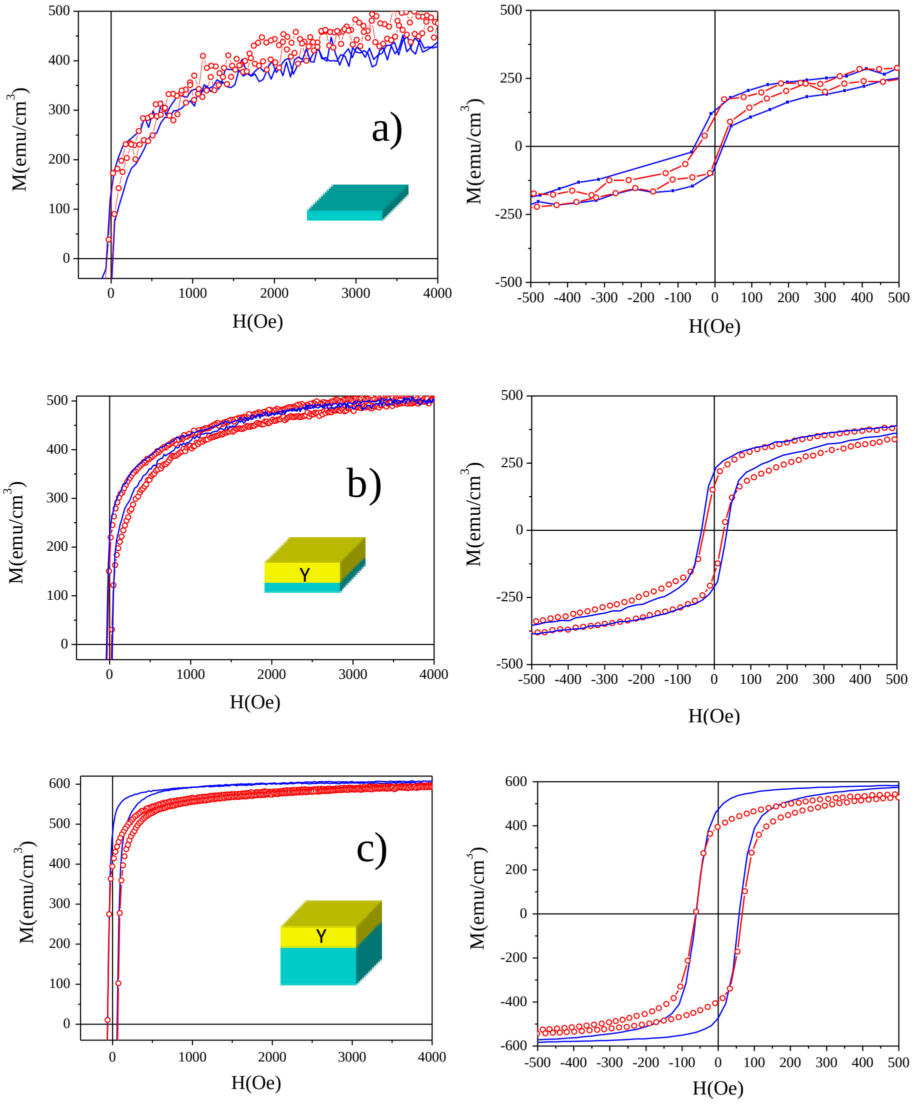

Fig. 3.10: Magnetic hysteresis loops taken at 100 K for a) a 4nm-thickLCMO thin film , b) the 4nm-L/Y bilayer c) the 15nm-L/Y bilayer, for field applied along the [100] direction (symbol) and [110] direction (line)Left panels show a broadened view in order to appreciate the saturation field. Right panels show en enlarged view of the areas close to the coercive fields.

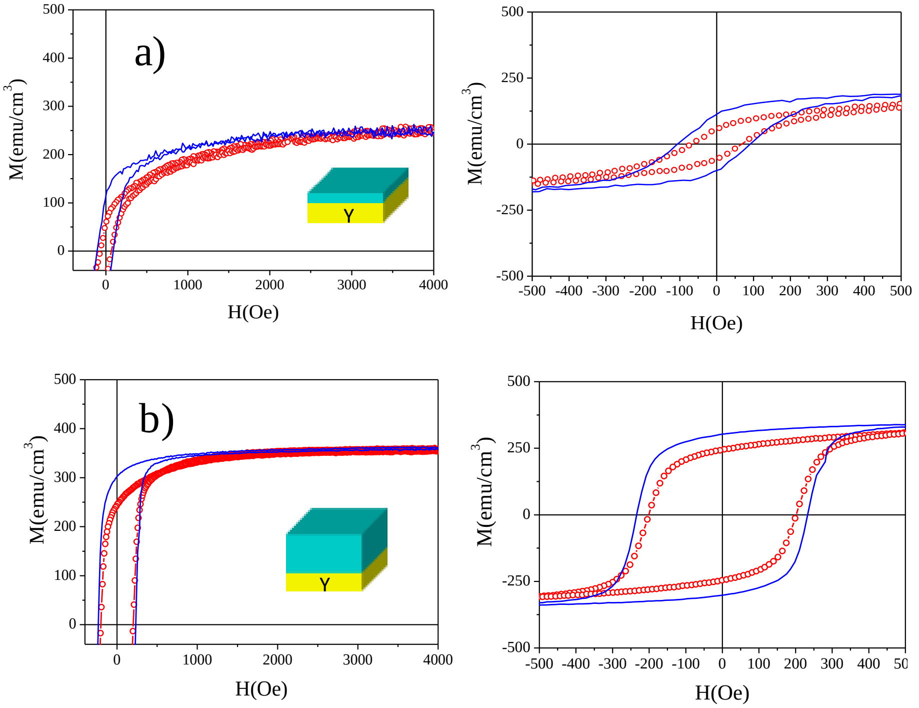

Fig.3.11 Magnetic hysteresis loops taken at 100 K for a) the 4nm-Y/L bilayer b) the 15nm-Y/L bilayer, for field applied along the [100] direction (symbol) and [110] direction (line)Left panels show a broadened view in order to appreciate the saturation field. Right panels show en enlarged view of the areas close to the coercive fields.

These considerations can be applied to LCMO/YBCO/LCMO trilayers. In fact it will be showed in the next sections that top and bottom LCMO have different coercive fields.

A YBCO thin film grown on LCMO preserves the same morphology as it was grown on STO. Here we compare atomic force microscope (AFM) images of the L/Y samples (Fig. 3.12*c* and *d*) with a YBCO single film (Fig. 3.12*b*). All the images were taken on samples grown on as-received STO (Fig. 3.12*a*). No treatment (chemical or thermal) was applied to the samples before the AFM analysis. The images are 1x1μm^2 size and were taken using a VEECO Multimode Scanning Probe Microscope equipped with a VEECO RTESP tip with radium between 10nm and 12.5 nm operating in tapping mode, at room temperature. Fig. 3.12*a* shows a STO substrate. The typical one unit cell steps with the edge oriented along one of the [100] crystal direction are clearly visible. The edge of each step is randomly shaped.

The margins can be removed by etching the substrates with a buffered HF solution which also causes the TiO_2 termination of the surface. Since in our case this treatment wasn't determinant to the magnetic and transport data we didn't perform any. Fig. 3.12*b* shows a 12nm-thick YBCO thin film. The image shows that the YBCO grows flat but there are particles consisting of element segregation spread over the surface. It is widely reported in the literature that it is almost inevitable to have precipitates on the film surface [40-42]. Nevertheless the underlying film is flat and homogeneous. The black line represents the position at which the AFM profile, displayed in Fig.*a*, was taken. The profile shows that the YBCO surface contains 0.4 nm-high steps, corresponding to 1 u.c. of STO, and 1.2 nm-high steps corresponding to an entire YBCO unit cell. Root mean square (RMS) roughness taken on an area free of particles gives a value RMS=0.4 nm, while if we consider the whole AFM scanned area we have RMS=0.8-1nm. We obtained similar results for the L/Y bilayers. Fig. 3.12*c* and *d* shows the AFM images for the 4nm-L/Y and the 15nm-LY samples respectively. The topology of the surface is not affected by the presence of the LCMO. The AFM profile (see Fig.*b* and *c*) in both cases shows steps as high as 1 u.c. of YBCO. As before, RMS measurements taken on an area free of particles give RMS_4=0.5nm and RMS_{15}=0.4nm for the 4nm-L/Y and the 15nm-LY samples respectively. If we consider the whole 1x1μm^2 scan the RMS in both cases is RMS=1nm. This result is important in the interpretation of the depth profiles obtained from depth sensitive measurements as XRR and PNR, shown in the next sections. Although each precipitate particle is about 10nm high, the relatively low density doesn't alter the physical properties of the YBCO/LCMO interface and the genuine effects arising from the F/S interplay. In a XRR or PNR experiment the sample is illuminated by a beam several μm wide. The resulting profile will average out the interfacial roughness. As we will see the structural roughness obtained using these techniques is comparable to the RMS obtained on the 1x1μm^2 AFM scan.

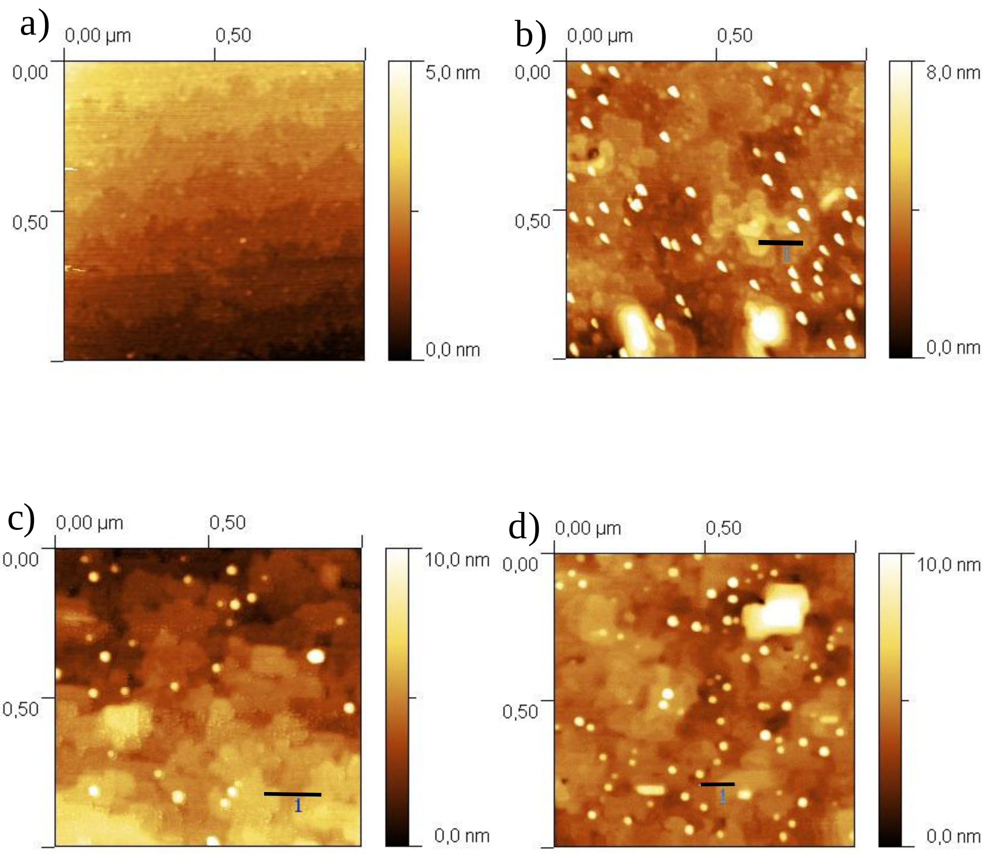

Fig. 3.12: AFM images of a) STO substrate, b) 12nm-thick YBCO on STO, c) 4nm-L/Y bilayer, d) 15nm-L/Y bilayer. The black lines indicate where the AFM profiles of Fig. have been taken.

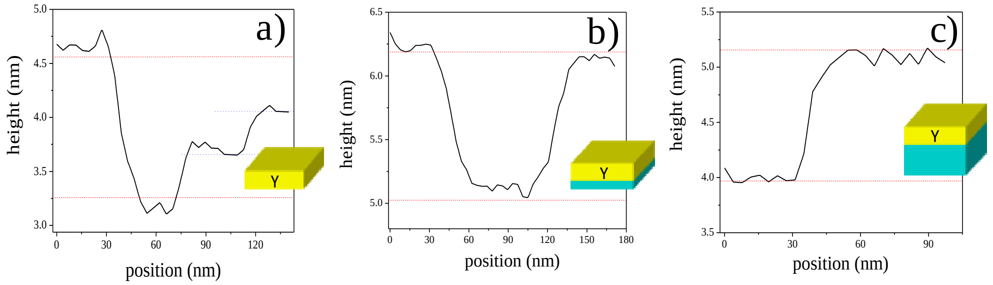

Fig.3.13: AFM profiles of a) 12nm-thick YBCO on STO, b) 4nm-L/Y bilayer, c) 15nm-L/Y bilayer. The red dotted lines represent the height of a YBCO unit cell while the blue lines a STO unit cell.

We then studied the evolution of the magnetization loop as a function of the temperature in our bilayers. Fig. 3.14*a* show magnetization loops for the 4nm-L/Y sample when the field is applied along the [100] direction, taken between 100K and 10K. We extracted the value of the remanent magnetization M_{REM} and the coercive field H_C from these curves as a function of temperature. In Fig. 3.14*b* and *c* we compare results obtained for field applied along the [100] with those obtained for field along [110] direction (hysteresis loops not shown). It is evident that when the full superconducting state is reached (indicated by T_{C_0} that is the temperature of the zero-resistant state) M_{REM} and H_C undergo a rapid increase due to the paramagnetic Meissner effect. Similar results are obtained for the 15nm –L/Y bilayer although the magnitude of the effect is reduced by the predominant ferromagnetic signal of the thicker LCMO layer. Magnetic hysteresis loops for field along the [100] direction are shown in Fig. 3.14*d*, while Fig. 3.14*e* and *f* display the values for M_{REM} and H_C in the two orientation of the magnetic field. A small change is observed in the remanent magnetization at T_{C_0} while the coercive field is essentially constant at all temperatures. We performed the same analysis on the Y/L samples. The result is given in Fig. 3.15. In contrast to the previous case, the M_{REM} (Fig. 3.15*e*) and H_C (Fig. 3.15*f*) reveal an unusual behavior when the field is applied along the [100] direction. At T_{C_0} the two quantities start to decrease reaching a minimum value at ~50K. This corresponds to a narrowing of the magnetization curve along the H and M axes. At this point the trend changes and both remanence and coercive field increase rapidly. A possible scenario to discuss this behavior is the *cryptoferromagnetic state*, a theoretical scenario predicted by Anderson and Suhl [43] to describe a change in the domain structure of a ferromagnetic superconductor, where domains are modified in the length scale of the Cooper pairs, and later adapted by Bulaevskii and Buzdin [44] to thin film hybrids. The number of walls (domains) increases in such a way that there is more than one domain in the scale of the coherence length. Consequently, the Cooper Pairs, instead of a ferromagnetic exchange field, 'feel' an antiferromagnet in which the exchange field over the coherence volume is cancelled. Given the small size of the coherence length of the cuprates this scenario would apply close to the critical temperature where the coherence length (the size of the Cooper pairs) is diverging. Bulaevskii and Buzdin theorized that a ferromagnetic layer on a superconductor would spontaneously form a domain structure on the length scale of ξ when it becomes thin enough.

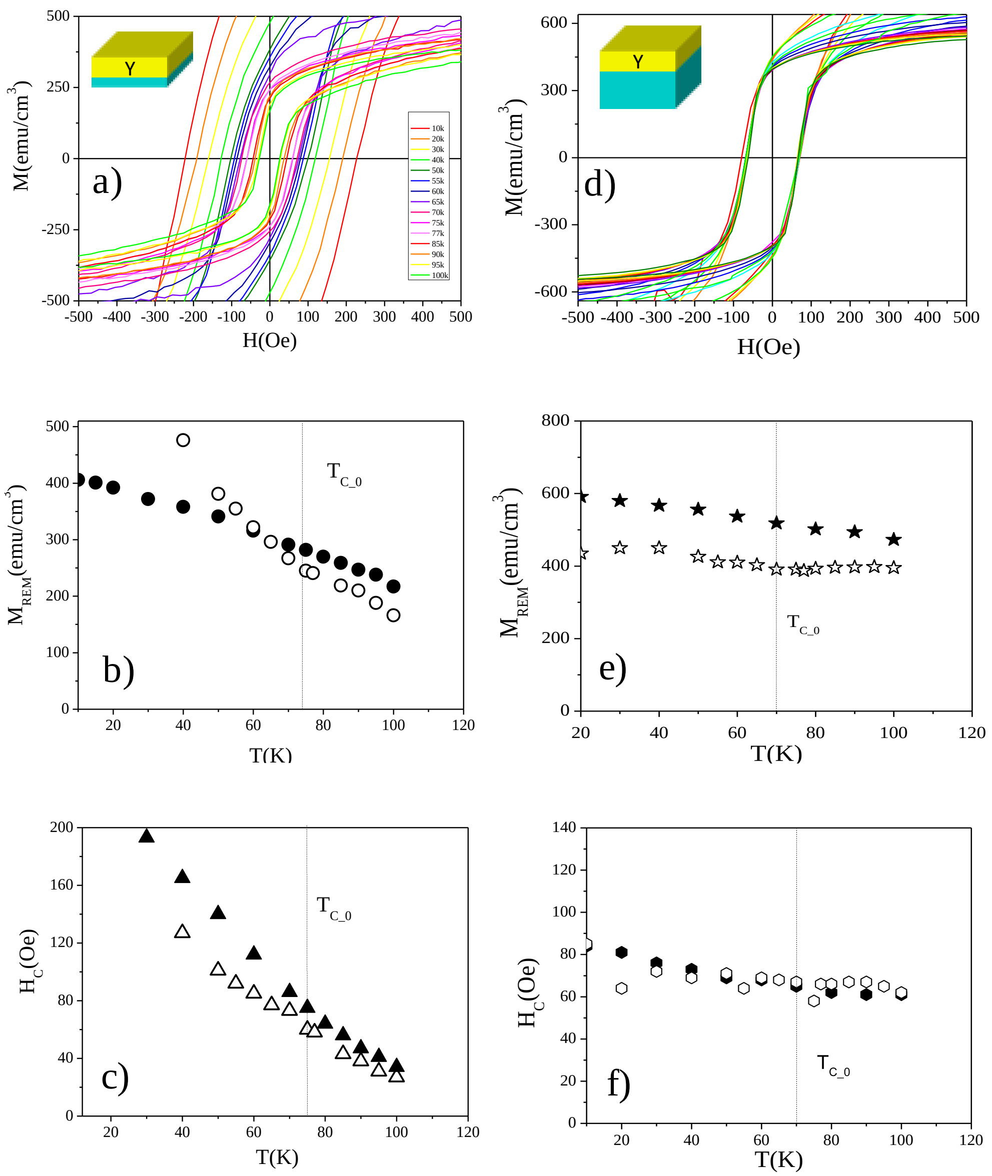

Fig. 3.14: Magnetization loops for a) the 4nm-L/Y bilayer and d) the 15nm-L/Y bilayer taken at several temperatures between 100K and 20K. Field is applied in the plane of the sample along the [100] direction. Panels b) and e) show the respective remanent magnetization while panels c) and f) the respective coercive field, extracted from the MvsH curves, for field along the [110] (solid symbol) and [100] (open symbol) axes.

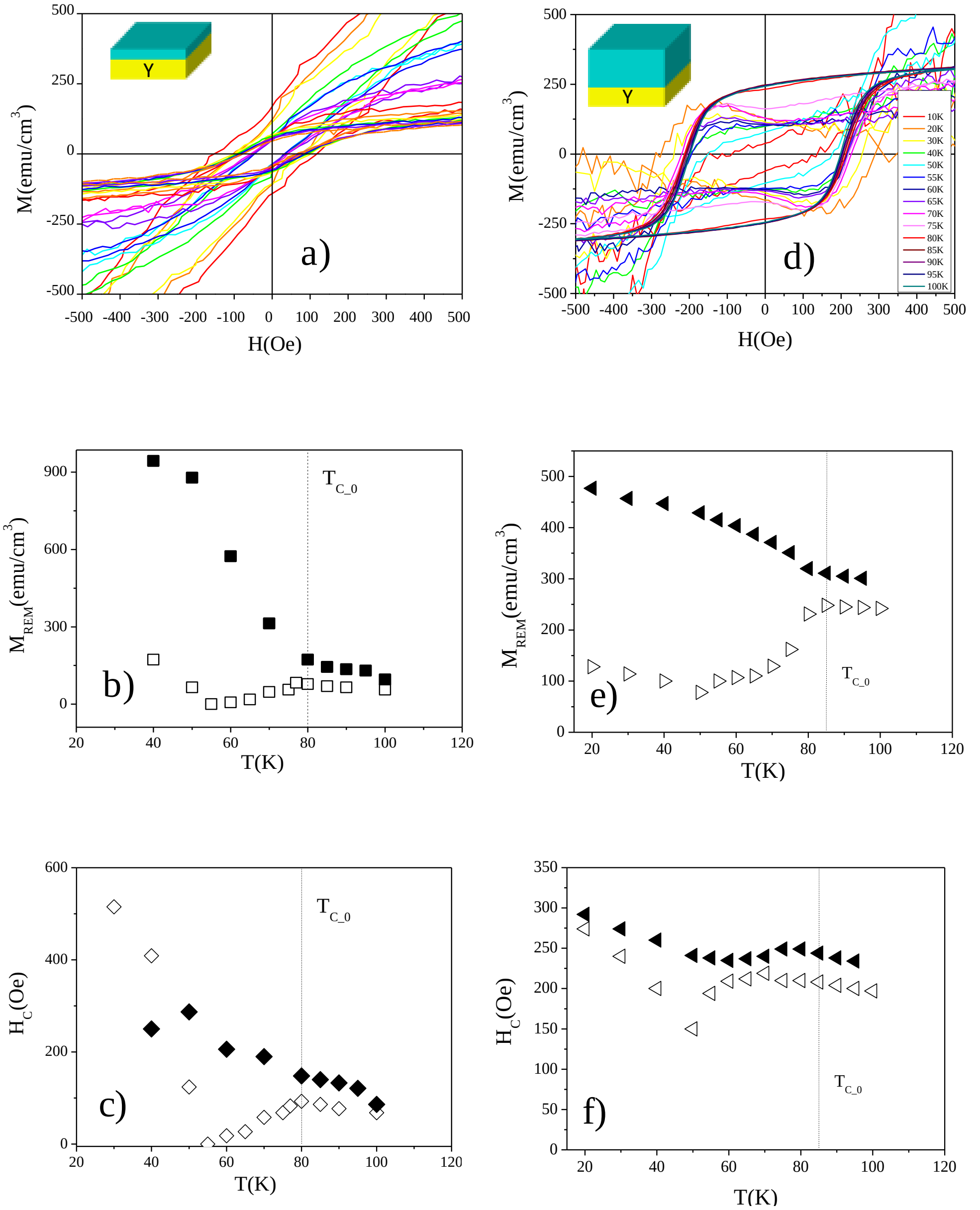

Fig. 3.15: Magnetization loops for a) the 4nm-L/Y bilayer and d) the 15nm-Y/L bilayer taken at several temperatures between 100K and 20K. Field is applied in the plane of the sample along the [100] direction. Panels b) and e) show the respective remanent magnetization while panels c) and f) the respective coercive field, extracted from the MvsH curves, for field along the [110] (solid symbol) and [100] (open symbol) axes.

The energy cost of forming the large number of domain walls would be compensated by the increased superconducting gap energy. They noted that the details of the transition between the normal ferromagnetic state and the fine domain structure would depend upon many system parameters: film homogeneity, the details of the superconductor/ferromagnet interface, the density of electronic states in both films and many others. They also calculated the maximum thickness of the ferromagnetic layer for the formation of the domain structure to be energetically favorable based upon the following simplifying assumptions:

- a perfect interface,
- a coherent modulation of the ferromagnetic order over the entire thickness of the ferromagnet,
- short electronic mean free paths (the dirty regime),
- a ferromagnetic easy direction parallel to the interface
- the ferromagnet thickness (d_F) is smaller than ξ and the transition into the fine domain structure takes place close to Tc.

Reducing the thickness of the manganite reduces also the anisotropy field and favors domain walls to be of the Neel type, where magnetization rotates in the plane of the layers. If the domain size becomes comparable or smaller than the width of the domain wall, we may come to a situation closely resembling the one described by the cryptoferromagnetic state.

The cryptoferromagnetism alone may explain the behavior observed for the thinnest 4nm-Y/L bilayer while it would not be applicable in the case of the 15nm-Y/L sample. It must be noticed that in our case the phenomenon is also related to the direction of the magnetic field with the in-plane crystal axes. Contrarily to any prediction it occurs when the field is applied along the hard axis where a reduced number of domain walls is expected during the magnetization reversal. This suggests the possibility that the anisotropic structure of the YBCO may be involved. It is well known that YBCO tends to form twins to accommodate the orthorhombic crystal on a cubic lattice. The twin boundaries are usually oriented at ~45 degrees with the [100] crystallographic direction [45]. It has been also shown that a strong coupling between twin boundaries and domain structure may occur in F/S bilayers

[46]. In some cases the magnetic domains can be effectively split by the presence of a twin creating a favorable condition for the cryptoferromagnetic effect to occur. Stripe-like magnetic domains have been observed by off-specular neutron reflectivity in LCMO/YBCO heterostructures, arising at a temperature few degrees below T_C [47]. In fact, at T_{C_0}, where the decrease of H_C and M_{REM} starts, the sample enters the vortex glass regime in which the vortex lattice presents long range correlations. A complex arrangement of the YBCO superconducting vortices combined with the anisotropic structure of the crystal and the magnetic anisotropy of the LCMO may establish a particular condition in which the break up into magnetic domains is enhanced at low magnetic field during the magnetization reversal. This also matches with the fact that the non-monotonic behavior of H_C and M_{REM} was not found in sample with the LCMO on the bottom, less affected by the structure of the YBCO. In this matter further investigation is needed to clarify in which way the superconductivity alter the magnetic structure of the top ferromagnetic layer.

c) XMCD of YBCO/LCMO bilayers

In spite of the well defined chemical interface structure the electronic and magnetic structure at the interface can be significantly more complex due to charge transfer or other interface processes. It has been reported that the antiferromagnetic interaction across the YBCO/LCMO interface competes with the antiferromagnetic superexchange coupling between nearest neighbor Cu spins within a copper oxide layer. As the latter interaction is large, Cu is ferromagnetically polarized due to spin canting (see Fig. 3.16). [47] The interface induce magnetic moment of Cu can be studied through XMCD measurement in which TEY and FY signals from the Mn and Cu absorption edge are measure in the same conditions of applied magnetic field.

Next we present an experiment performed on bilayers of the type STO//YBCO/LCMO in which we measured XMCD as a function of the temperature. The samples studied have the same thickness of LCMO (15nm) but different YBCO thickness: 9nm and 29nm. This implies a quite different structural condition for the top LCMO/YBCO interface given by larger roughness and reduced effect of strain in the case of the thickest YBCO. For 29nm-thick YBCO the bilayers presents the same critical temperature of the YBCO bulk (T_C=90K) while for the 9nm-thick YBCO sample the T_C is somewhat reduced do to the long range proximity effect at the YBCO/LCMO interface.

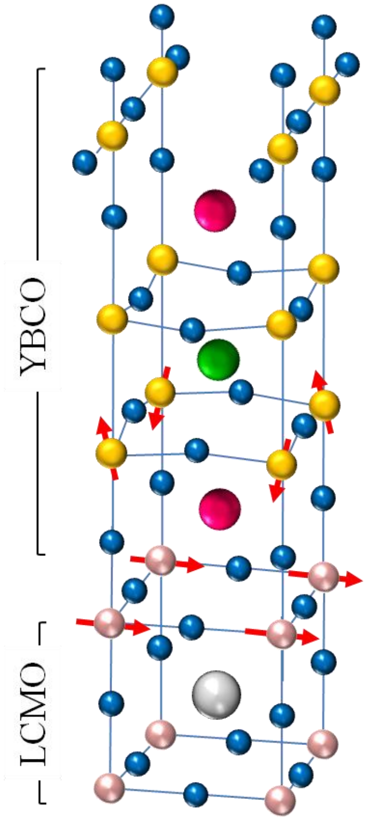

Fig. 3.16. Canting of the Cu spins at the YBCO/LCMO interface.

The critical temperature for this sample is around T_C=80K. All the measurements have been taken at the Spring 8 synchrotron radiation facility at Hyogo (Japan) at the BL25SU beamline. The beamline was equipped with twin helical ondulators to obtain left- and right-circularly polarized radiation with 1Hz-switching rate of the helicity. The beamline monochromator is a constant deviation type with varied line-spacing plane gratings covering an energy region of 0.22 ~ 2 keV. The sample chamber was a continuous liquid-He-flow-type cryostat which provided a lower stable temperature of 30K, in which the sample was mounted with the beam axis parallel to the [100] crystallographic direction of the STO, corresponding to the sample edge, and making an angle of 30º with the sample surface, as shown in Fig. 3.17

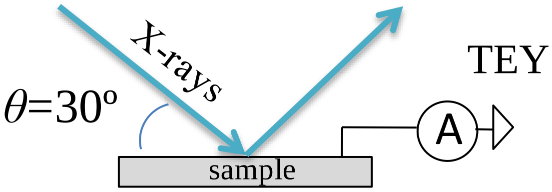

Fig. 3.17. Schematic diagram of the experimental set up.

All the measurements have been collected in the total electron yield (TEY) mode which measures the primary and secondary photoelectrons resulting from the photo-absorption process.

The XAS measurements have been obtained as the sum of the right- and left-circularly polarized TEY scans as function of the X-ray energy, while the XMCD curves have been obtained as the difference of the same X-ray scans. All the measurements have been taken applying a field H=-5000Oe in the plane of the sample.

Fig. 3.18 shows the XAS and XMCD data for the thin YBCO sample, in which we compare measurements taken at 150K, close to the Curie temperature of the LCMO, and at 50K, well below the superconducting transition. For clarity the tow curves are shifted. The absorption edges in Fig. 3.18a and Fig. 3.18c can be identified by the two peaks and are centered at 643eV and 654eV for Mn and at 931eV and 951eV for Cu, for the L_{III} and L_{II} edges respectively, in good agreement with the values found in the literature [48,49,50]. The profiles also show no trace of peaks deriving from a valence of the Mn or Cu different from that expected in LCMO and YBCO. As can be seen from the XMCD (Fig. 3.18b and Fig. 3.18d), the magnetic moment for Cu is coupled antiferromagnetic to that of Mn since the peak of the corresponding L edge is pointing in opposite direction. Fig. 3.19 shows analogous measurements for the thick-YBCO sample. By comparing the two samples it can be immediately seen from Fig. 3.18d and Fig. 3.19d that there's a large difference in the dichroism intensity at high temperature for the thin-YBCO sample, in which the Cu magnetic moment is still high, and the thick-YBCO sample in which it is almost absent.

We performed a set of measurements at several temperatures between 30 and 200K. We established a method for comparing the magnetic moment at the Cu and Mn edge based on the ratio between the integrated L_{II} and the L_{III} peaks. The result is shown in Fig. 3.20

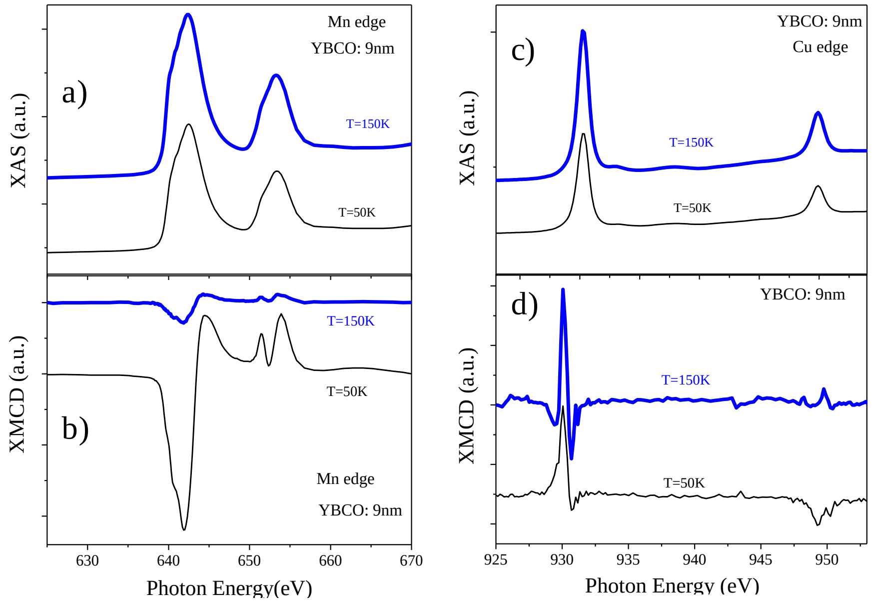

Fig. 3.18. XAS (a) and XMCD (b) for the STO//YBCO(9nm)/LCMO(15nm) bilayer at the Mn absorption edge. XAS (c) and XMCD (d) for the same sample at the Cu absorption edge. The thick blue line refers to data taken at 150K while the thin black line to data taken at 50K.

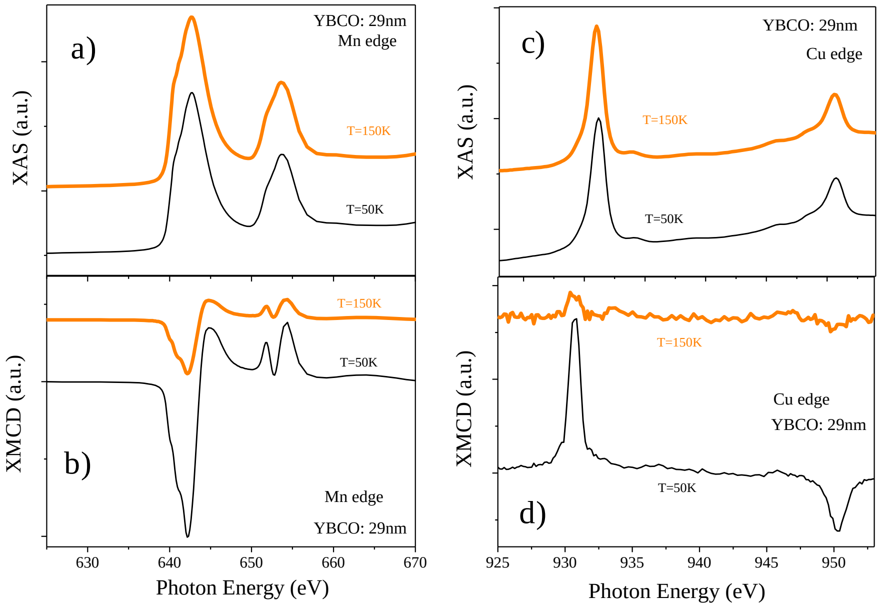

Fig. 3.19. XAS (a) and XMCD (b) for the STO//YBCO(29nm)/LCMO(15nm) bilayer at the Mn absorption edge. XAS (c) and XMCD (d) for the same sample at the Cu absorption edge. The thick orange line refers to data taken at 150K while the thin black line to data taken at 50K.

In the case of the bilayer with thin (9nm) YBCO layer (Fig. 3.20a), the Cu magnetic moment, decays at the same temperature of the Mn, corresponding to a Curie temperature of about 200K. This is in agreement with results reported in superlattices of the same materials [47]. In the case of the thick (29nm)-YBCO sample (Fig. 3.20b) the intensity of the dichroism signal is much weaker both at the Cu and Mn edge, due to the reduced magnetic moment of the LCMO. Nevertheless, the low temperature measurements show that the signal from Cu moment maintains the same proportion (6%) to that of Mn.

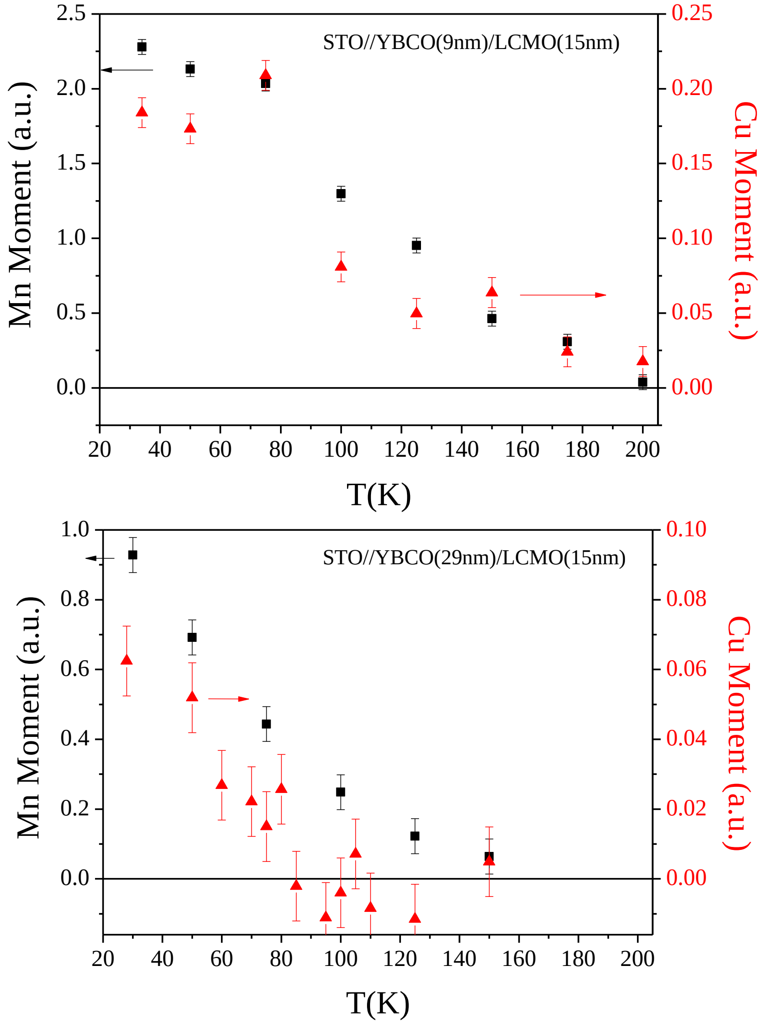

Fig. 3.20. Top: temperature dependence of the magnetic moment of Mn (left axis) and Cu (right axis) for the STO//YBCO(9nm)/LCMO(15nm) bilayer. Bottom: temperature dependence of the magnetic moment of Mn (left axis) and Cu (right axis) for the STO//YBCO(29nm)/LCMO(15nm) bilayer.

While the Mn magnetic moment disappears at high temperature (T_{Curie}=160K), though it is a little lower than the previous case, the Cu moment decays more rapidly and it is essentially zero at a temperature corresponding to the superconducting transition T_C.

This is a puzzling result suggesting that either the ordering of the manganese orbitals at the interface is different for the two thicknesses of YBCO (different strain) or the nature of the superexchange coupling at the interface (canting of Cu moment) depends on thickness of the superconducting layer. At the stage of writing this thesis we have not been able to provide a clear cut explanation. More experiments will be needed in the future.

3.3 The inverse superconducting spin switch

In conventional F/S/F junctions the critical temperature may be modulated by the relative orientation of the magnetization in the two ferromagnetic layers. This T_C modulation results from a compensation of the exchange field over the coherent volume in the antiferromagnetic configuration if the thickness of the superconductor is comparable to the coherence length.[7-9] Since at the interface between a half metal and a superconductor proximity effect is suppressed,[52] T_C is affected distinctly in F/S/F structures with highly spin polarized carriers. It has been previously reported that a very large magnetoresistance (MR) (in excess of 1000%) arises in F/S/F structures made of $La_{0.7}Ca_{0.3}MnO_3$ (LCMO) and $YBa_2Cu_3O_7$(YBCO) [19]. This MR originates from a larger resistance in the antiferromagnetic (AF) configuration of the F layers and it has been denominated inverse superconducting spin switch (ISS) because it is opposed to conventional (direct) superconducting spin switch of proximity coupled F/S/F structures, where the larger resistance occurs in the F alignment [7-9]. Here we explore different mechanisms as possible origins of this magnetoresistance. In particular we have analyzed the relative importance of vortex dissipation, anisotropic magnetoresistance (AMR) and giant magnetoresistance (GMR) like spin dependent effects related to the transmissions of (spin polarized) quasiparticles from the ferromagnet into the superconductor. We emphasize especially the current dependence since a markedly different current dependence is expected for each of the three proposed scenarios. In detail, vortex dissipation is zero when the current is applied parallel to the magnetic field, the

AMR is maximized when the current is applied parallel to the magnetic field, and spin dependent transport should be current independent.

a) Spin dependent magnetoresistance of LCMO/YBCO/LCMO trilayers

We show that magnetoresistance measurements are independent of the (in plane) orientation of the applied magnetic field with respect to current, and to the magnitude of the electrical current itself. Furthermore, we show that the MR is also independent of the sweep rate of the magnetic field. This rules out explanations in terms of vortex dissipation or anisotropic magnetoresistance and constitutes a strong indication that spin dependent transport of (spin polarized) quasiparticles diffusing from the ferromagnet plays a major role in the MR phenomenon. Scattering at both F/S interfaces in the AF configuration has a pair breaking effect and depresses the critical temperature compared to the F case where this scattering process is absent.

Samples were grown on [100] oriented $SrTiO_3$ single crystals. For this study we grew F/S/F trilayers keeping the thickness of the LCMO fixed at 40 unit cells (15 nm) and the thickness of the YBCO at 13 (15 nm) and 15 unit cells (18 nm). We have measured magnetoresistance at selected temperatures along the resistive transition with the magnetic field applied parallel to the layers. Fig. 3.21 shows $R(H)$ loops at various temperatures for a trilayer sample with a 13-unit cells thick YBCO layer. Current flows in the plane of the layers (current in plane geometry), perpendicular to the magnetic field direction. The magnetic field was swept between 0.5 and 0.5 T in a hysteresis loop sequence. Large MR peaks are observed whose relative height decreases when the temperature is increased (see Fig. 3.21*a*). In previous works it has been shown that these peaks occur in a magnetic field region where polarized neutron reflectometry and SQUID magnetometry show an AF alignment between the LCMO layers [19] (not shown here). AF alignment results from the top layer having a larger coercivity than the bottom layer due to the different epitaxial strain in each layer. Fig. 3.21*a* shows that the MR peaks are superimposed on a resistance background which increases with magnetic field. Most likely this background is due to vortex dissipation since it is known that vortex motion in the liquid state is thermally activated with activation energy depending on field as $1/H^{0.5}$. In fact, the line in Fig. 3.21*a* is a fit to a thermally activated resistance with the activation energy depending on field as $1/H^{0.5}$. It is worth mentioning that in samples with thicker YBCO (above 18nm) such a thermally activated description of the background is hampered by the appearance of glassy properties in the vortex system at low temperatures and low fields. Fig. 3.21*a* also shows that the MR peaks decrease when temperature is increased and they vanish abruptly at the superconducting onset. Fig. 3.21*b* displays a positive MR peak at 57 K just below the superconducting onset, while Fig. 3.21*c* shows a much smaller negative peak at 61 K, just above the super conducting onset. This proves that the superconductivity is an essential ingredient for the large MR seen in Fig. 3.21*a* (see the discussion below). Note also that the 61 K curve shows a decrease of the resistance when the magnetic field increases, which is characteristic of the colossal magnetoresistance of the manganite layers. We consider three different scenarios to explain this MR phenomenon at the superconducting transition: (a) Vortex dissipation (including vortices due to stray fields of domains or domain walls), (b) anisotropic magnetoresistance (AMR), which in manganites is known to be large due to strong spin orbit scattering, and finally (c) GMR like dissipation originating at spin dependent transport. Each of these mechanisms has a very characteristic current-field dependence. Vortex dissipation is zero when the current is parallel to the field, AMR is maximized when the current is parallel to the field, and GMR is independent of both the current value and of the relative orientation of current and field. Experiments changing the current values and the direction between current and field are thus useful to explore the origin of the magnetoresistance. Fig. 3.22. *a* shows the MR peaks of a trilayer sample with a YBCO thickness of 18nm measured at 54.5, 55.5, and 56.5 K (from bottom to top) with the current in the plane of the layers, and directed parallel (line) and perpendicular (open symbols) to the magnetic field. As for the background, the high field dissipation increases substantially when the current is perpendicular to the field. For current parallel to the field the Lorentz force density on vortex lines $J \times \phi_0$, where J is the current density and ϕ_0 is the flux quantum) vanishes and consequently the vortex dissipation due to vortices parallel to the external magnetic field vanishes as well. We cannot exclude additional vortices perpendicular to the layers due to a small misalignment of the magnetic field or spontaneous vortices due to the stray field of domains, responsible for the high field dissipation in this current-field configuration. Fig. 3.22. *b* shows an enlarged view of the MR peaks of the same sample as in Fig. 3.22. *a*, measured at 55.5 K with the current in the plane of the layers, and directed parallel (line) and perpendicular (open symbols) to the magnetic field.

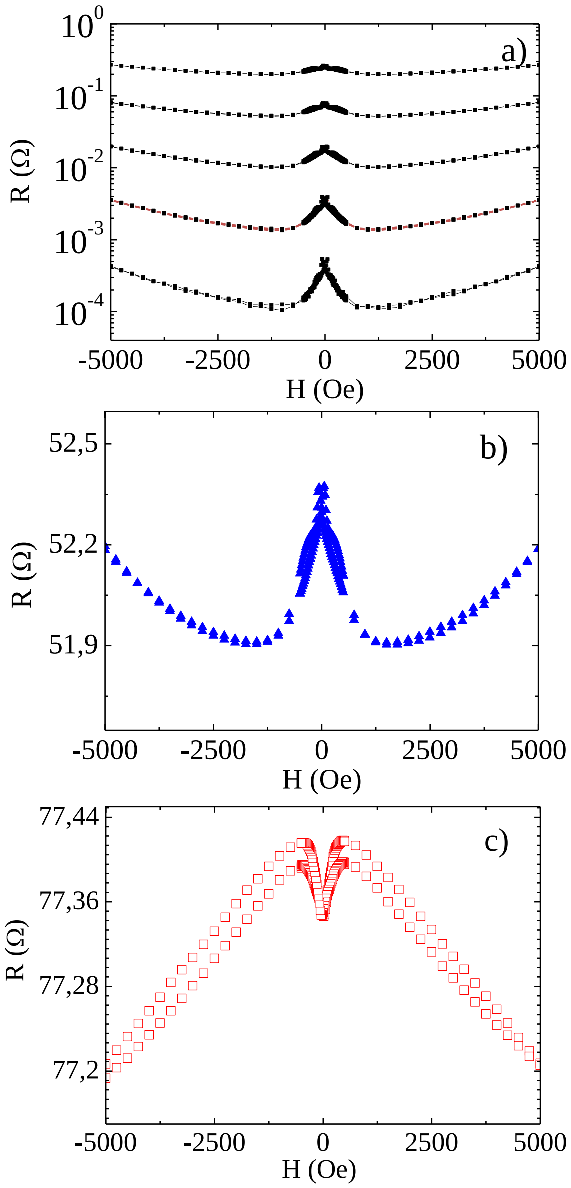

Fig. 3.21(a) Resistance as a function of magnetic field, *R*(*H*) loops, of a F/S/F trilayer LCMO (15nm) /YBCO (15nm.)/ LCMO (15nm) at different temperatures along the resistive transition. The magnetic field, applied parallel to the layers and perpendicular to electric current, was swept between −0.5 and 0.5 T fields in an hysteresis loop sequence. The temperatures are 49, 49.5, 50, 50.5, and 51 K from bottom to top. (b) *R*(*H*) loop of the same sample at 57 K (just below the superconducting onset). (c) *R*(*H*) loop of the same sample at 61 K (just above the superconducting onset).

We want to emphasize that the size and shape of the peaks do not depend on the angle between magnetic field and current, ruling out explanations in terms of vortices parallel to the layers. This also discards the contribution of the anisotropic magnetoresistance (AMR) of the individual ferromagnetic layers, known to be important in manganite single layer films. Nevertheless, the AMR shows up when the temperature is raised above the superconducting onset and it is in fact negative (larger dissipation when current is perpendicular to field) as previously found in manganite thin films (see Fig. 3.21*c*).

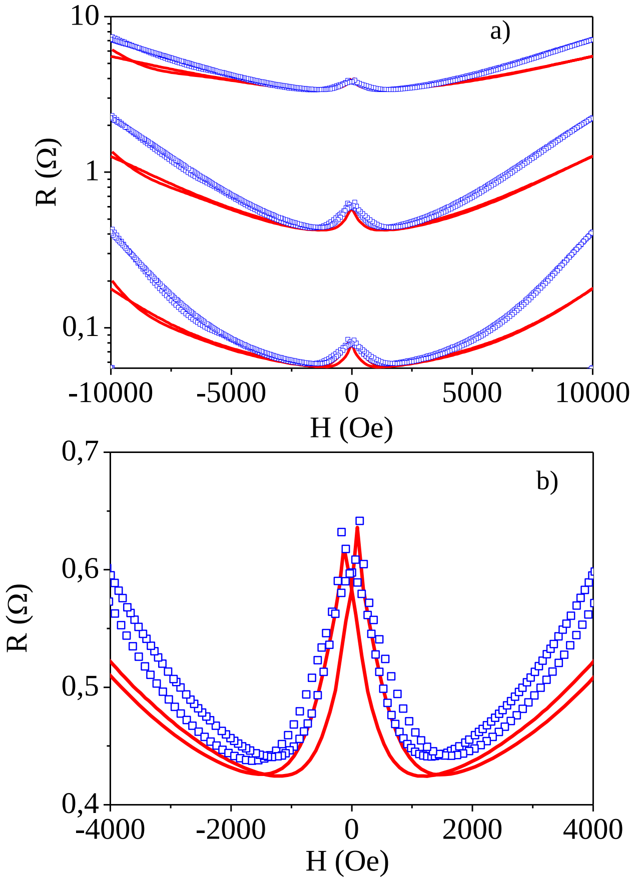

Fig. 3.22. (a) Resistance as a function of magnetic field, *R*(*H*) loops, of a F/S/F trilayer LCMO (15nm)/YBCO (15nm)/ LCMO (15nm) measured at 54.5, 55.5, and 56.5 K (from bottom to top) with the current in the plane of the layers and applied parallel (line) and perpendicular (open symbol) to the magnetic field. b) Enlarged view of the R(H) loop measured at 55.5 K with the current applied parallel (line) and perpendicular (open symbols) to the magnetic field.

We have also performed current-dependent measurements for currents directed perpendicular to magnetic field. Increasing the current the transition width increases even at zero magnetic field as shown in Fig. 3.23*a*. This occurs due to the increased vortex dissipation which adds a magnetic field dependent background to $R(H)$ curves. The magnetoresistance is calculated from resistance maxima and minima of the $R(H)$ loops as a resistance change relative to the background (R/R_b)where (R is the resistance value with respect to the background and R_b is the background resistance). An increasing current results trivially in smaller MR values as a result of dividing by the larger background resistance R_b as shown in Fig. 3.23*b*). However by looking at the temperature shift of the resistance curve at the corresponding resistance value, instead of looking at MR (resistance shift at a given temperature), when magnetic alignment changes from parallel to antiparallel, a completely different picture emerges. Fig. 3.23*c*) shows the temperature shift,)ΔT_w, for different current values as a function of resistance normalized to the onset values. The first observation is that there is a logarithmic dependence of the temperature shift as a function of resistance. Secondly, it is clear that the temperature shift is independent on current, evidencing that smaller magnetoresistance is caused solely by the increased background resistance. This provides further evidence for excluding vortex dissipation causing the MR peaks, and points strongly towards spin dependent effects on transport. Further information about the origin of MR can be obtained by measuring the dependence of the magnetoresistance on the sweep rate of the magnetic field. On one hand, spin valve effects have been shown to be sweep rate independent, while on the other hand spontaneous vortices (with a component perpendicular to the layers) induced in the superconductor due to the stray field of domains or domain walls may yield sweep rate dependent effects. Vortices created by domain walls would in principle also show a larger dissipation around the coercive field where the density of domains is maximized. One expects dissipation associated to the motion of domain walls, and thus a voltage should build up proportional to the domain wall velocity. To explore these possibilities we have done experiments changing the sweep rate of the magnetic field between 0.1 and 50 Oe/ s (Fig. 3.24) and did not see any measurable change in peak shape or height. The explored time scale in the range of seconds is too slow for the magnetic relaxation or switching of the LCMO electrodes, where the characteristic time scale is set by the ferromagnetic resonance frequency in the GHz range.

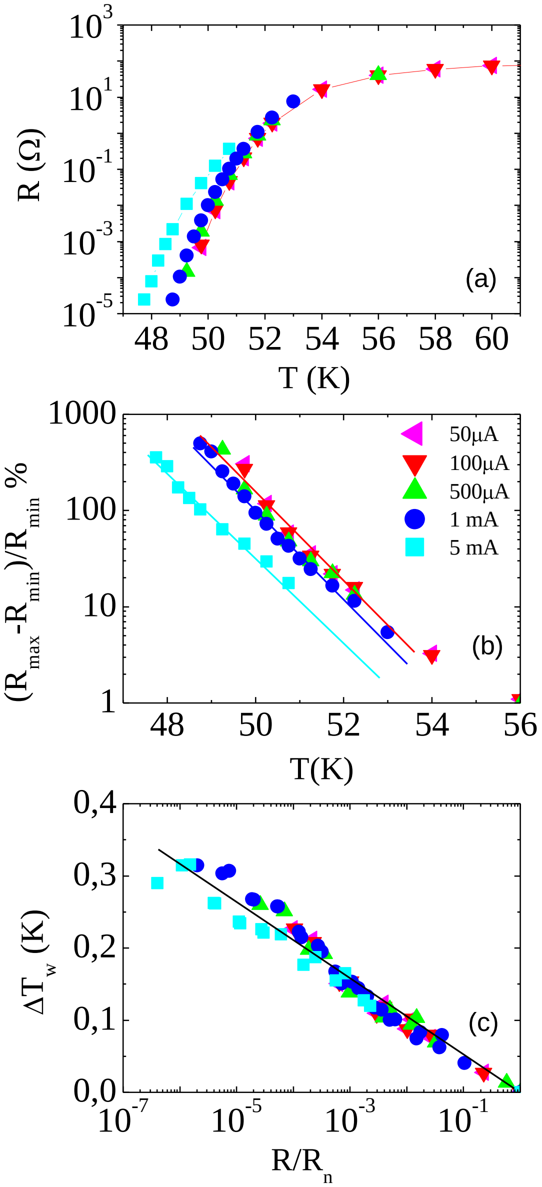

Fig. 3.23. (a) Resistance vs temperature curves for different current values J for a F/S/F trilayer [LCMO (15nm) /YBCO (15nm)/ LCMO (15nm)] at zero magnetic field [squares (5 mA), circles (1 mA), up triangles (0.5 mA), down triangles (0.1 mA), and left-facing triangles (0.05 mA)]. (b) Temperature dependence of the magnetoresistance extracted from the maxima and minima in the *R*(*H*) plots, using the same symbols as in (a). (c) Temperature shift of the resistance curves from parallel to antiparallel alignment of the magnetizations of the LCMO layers as a function of the resistance drop relative to the onset, using the same symbols as in (a). The solid lines are guides to the eye.

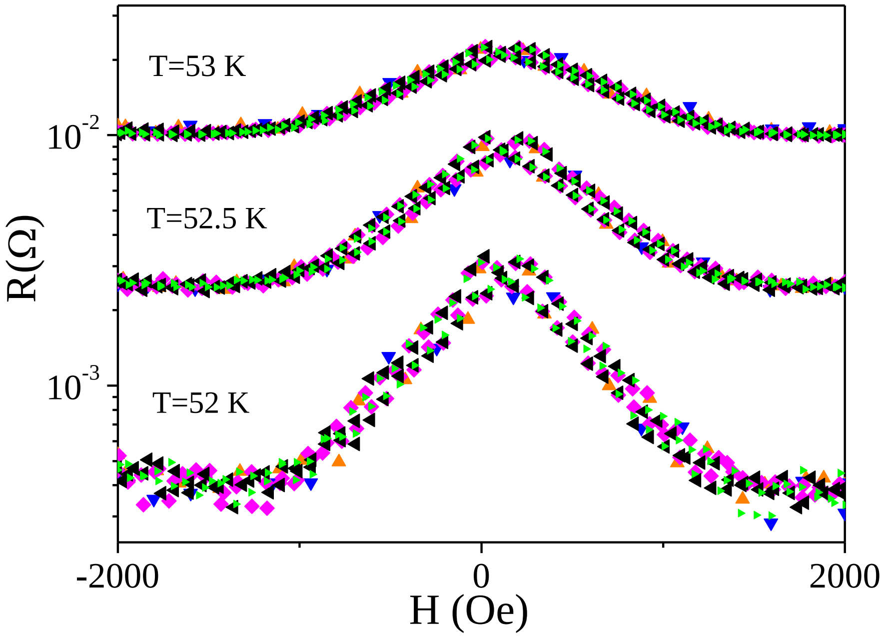

Fig. 3.24. Resistance as a function of magnetic field, $R(H)$ loops, of a F/S/F trilayer [LCMO (40 u.c.) /YBCO (15 u.c.)/LCMO (40 u.c.)] at 52, 52.5, and 53 K (from bottom to top) along the resistive transition. The sweep rates of the magnetic field are 50 Oe/ s (up triangles), 25 Oe/s (down triangles), 5 Oe/s (diamonds), 1 Oe/s (left-facing triangles), and 0.1 Oe/ s (right-facing triangles).

On the other hand it is a more realistic time scale for vortex relaxation phenomena (triggered by thermal activation over intersite barriers). HTS films are known to exhibit strong (logarithmic) relaxation, with a rate diverging at low temperatures. The independence of the MR peaks on the sweep rate excludes interpretations in terms of spontaneous vortices or anisotropic magnetoresistance of the ferromagnetic layers and supports the view that the magnetoresistance phenomenon originates at the spin dependent transport of quasiparticles transmitted from the ferromagnetic electrodes into the superconductor. In fact our MR phenomenon has many of the ingredients of the GMR in metallic superlattices in so far as it is independent of the current and of its direction relative to the field and depends solely on the orientation of the magnetization of the LCMO layers. Accordingly, we propose an explanation in terms of spin dependent scattering of spin polarized quasiparticles diffusing thermally from one ferromagnetic layer to the other. Although in our case the transport takes place parallel to the layers, normal electrons may diffuse from one ferromagnet to the other, keeping memory of their spin orientation if the superconductor is thin enough. In the AF configuration (for half metals) transport between the ferromagnets is not possible since there are no vacant states at the Fermi level with the right spin orientation [53]. Strong scattering occurs then at both interfaces under AF alignment, while it is absent when the magnetizations of the LCMO layers point to the same direction. The increased interface scattering in the AF configuration brings about an effective increase of the number of quasiparticles in the superconductor, which self-consistently reduces the critical temperature, thus providing a basis for the increased (magneto)resistance in the AP configuration. Recent reports have shown similar magnetoresistance on permalloy/Nb/permalloy trilayer structures, [54] suggesting that a high degree of spin polarization plays an important role in the occurrence of this phenomenon. For the YBCO thickness of this work the coupling of the F layers through normal electrons with subgap energy transmitted into the superconductor in the form of evanescent waves [55,56] is not possible. The length scale of this process is close to the Ginzburg Landau coherence length,[57] which is much shorter than the thickness of the superconducting spacer (16–18 nm) used in this work. Hopefully these results will open new theoretical avenues in the study of junctions between unconventional superconductors and spin polarized ferromagnets. [58-60]

In summary, we have described the large MR found in F/S heterostructures made of highly spin polarized LCMO and high-T_C superconducting YBCO. This MR is reminiscent of the GMR in metallic superlattices as it depends on the relative orientation of the magnetic layers and is independent of the relative direction of current and field. Neither does the MR peak depend on the current values or on the sweep rate of the magnetic field. These results rule out vortex dissipation or AMR as sources of our MR phenomenon and point to a spin dependent transport as its more probable origin. However, in contrast to traditional GMR, the MR vanishes in the normal state of the YBCO and only occurs in the superconducting state. Furthermore, the MR is opposite in sign to MR effects observed in F/S/F heterostructures (superconducting spin switch) based on low-T_C superconductors and transition metal ferromagnets. The possible origin of this MR is the depressed order parameter in the superconductor due to strong interface scattering at the F/S interface in the AF configuration.

b) *Origin of the inverse superconducting spin switch*

To check the validity of our interpretation which involves the transmission of spin polarized quasiparticles between both interfaces we now compare MR of trilayers with different YBCO thickness. The effect should disappear for sufficiently thick YBCO spacer since T_C is progressively suppressed and the transition width is increased in thinner YBCO films.

By examining the dependence on the thickness of the superconducting layer in LCMO/YBCO/LCMO trilayers, we obtain a measure of the spin-diffusion length in YBCO. Magnetization was measured with a 5 T superconducting quantum interference device (SQUID) magnetometer. Temperature-dependent magnetoresistance was measured using current in-plane (CIP) geometry. All samples presented here have 15-nm-thick (40 unit cells) ferromagnetic LCMO electrodes. The magnetic field was aligned within 0.05 degrees parallel to the substrate in the (010) direction of the substrate and perpendicular to the current.

Here we focus on how the magnetoresistance due to antiparallel alignment changes with the thickness of the superconducting spacer. To this end, it is of primary importance to examine if the antiparallel alignment over a magnetic-field range is maintained over the whole thickness range. Hysteresis [$M(H)$] loops measured below (T=5 K) and above the superconducting onset (T=100 K) display a clear plateau characteristic of antiparallel alignment as shown for a representative set of samples with varying YBCO spacer thickness in Fig.3.25 and Fig. 3.26. Polarized neutron reflectivity shows that the positions of the peaks of the derivative of the $M(H)$ loops correspond to the switching fields of the individual ferromagnetic layers (H_C^F) [19].

Thus the respective coercive fields can be obtained from the two peaks of the derivative (dM/dH) as displayed in Fig. 3.27. The region of antiparallel alignment shrinks rapidly with increasing YBCO spacer thickness. A weak shoulder on the main peak of dM/dH can be seen up to a thickness of 35 nm in the data at 100 K, while two distinct peaks are resolved for this sample at 5 K, showing that antiparallel alignment persists up to this limit, as demonstrated below. On the contrary, the 47-nm-thick sample displays a unique coercive field even at 5 K. Yet, the height of the magnetoresistance peak decreases apace with increasing spacer thickness.

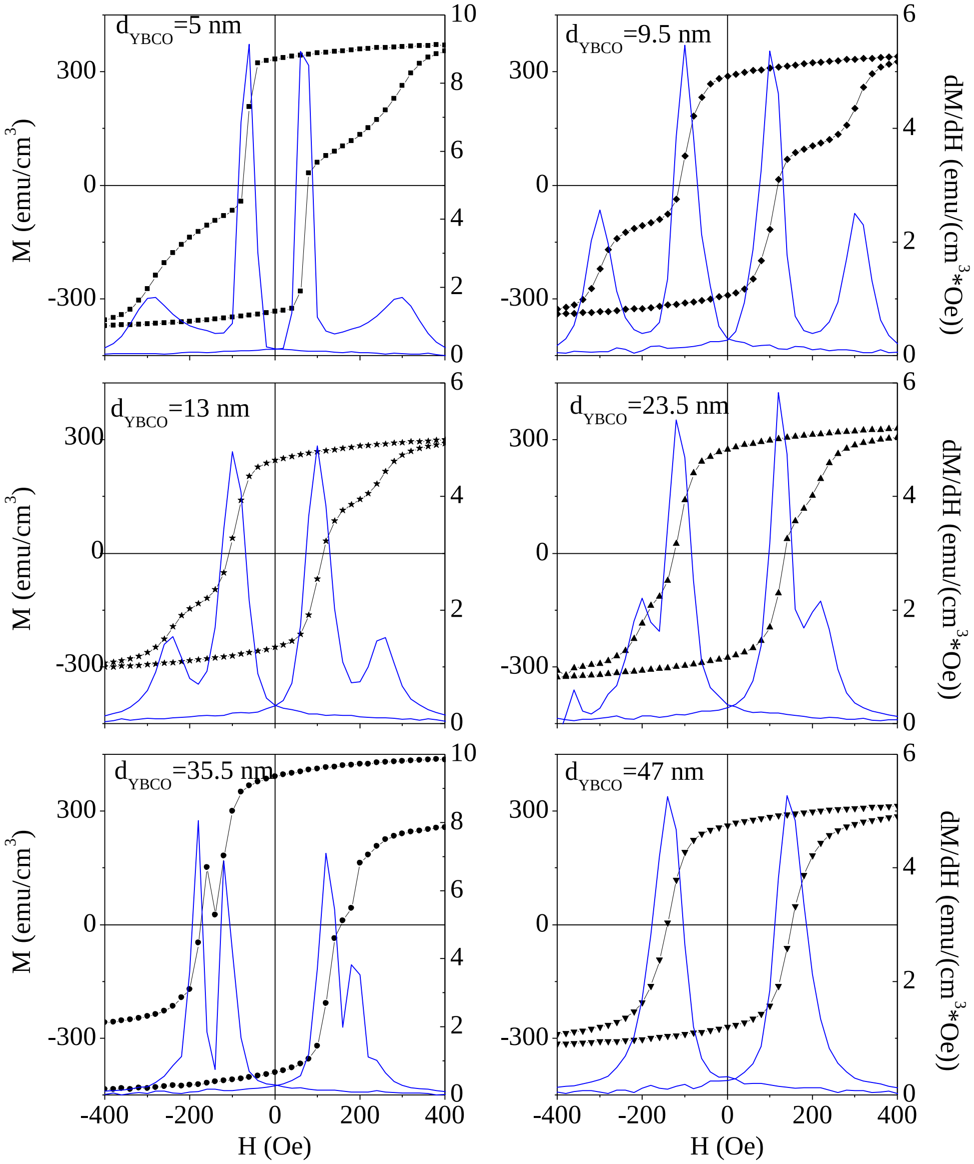

Fig.3.25 Magnetization hysteresis loops (symbols) and their derivatives (thin lines) for LCMO/YBCO/LCMO trilayers with varying YBCO thickness between 5 and 48 nm, below the superconducting transition, at *T*=5 K.

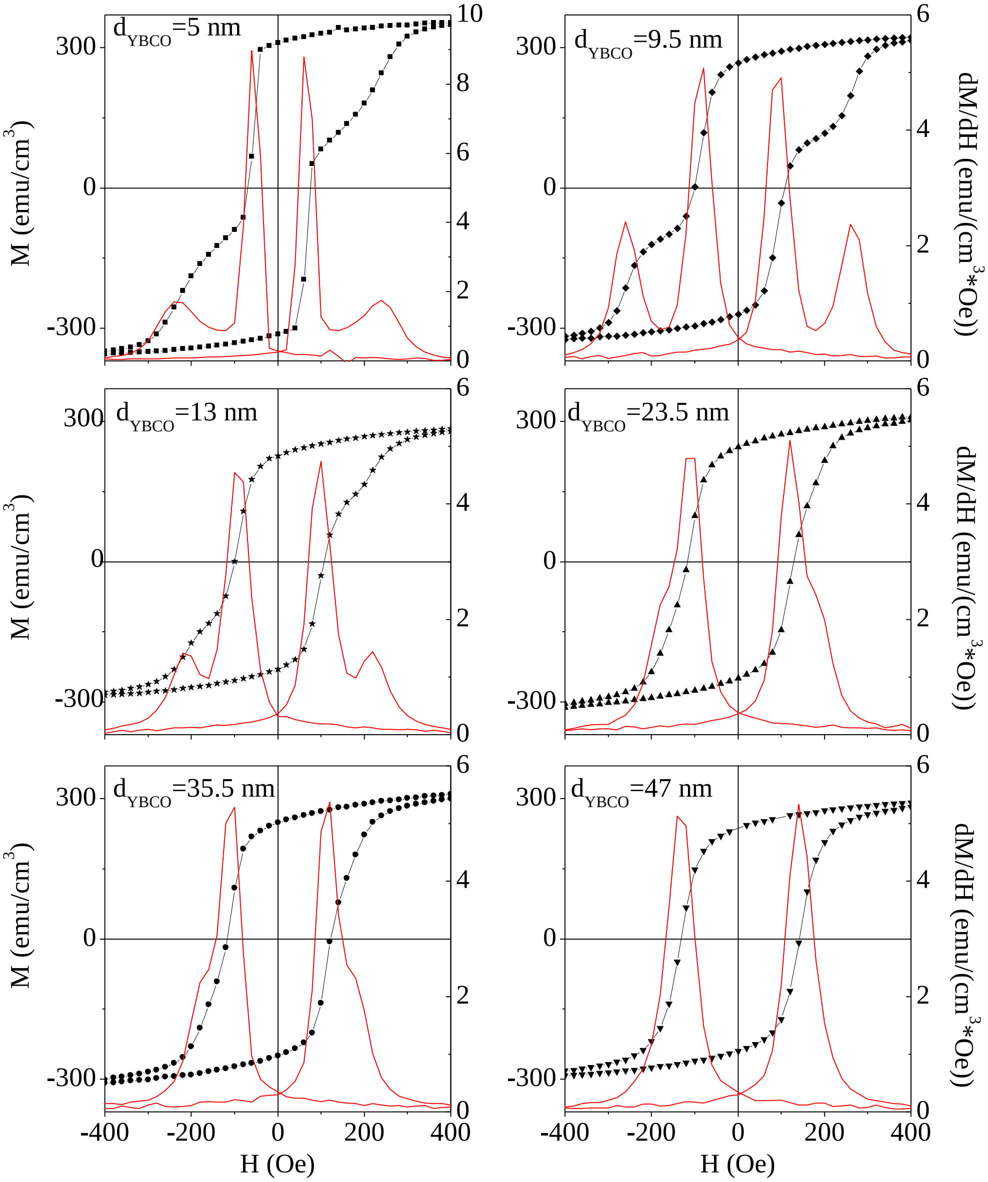

Fig. 3.26 Magnetization hysteresis loops (symbols) and their derivatives (thin lines) for LCMO/YBCO/LCMO trilayers with varying YBCO thickness between 5 and 48 nm, above the superconducting transition, at *T*=100 K.

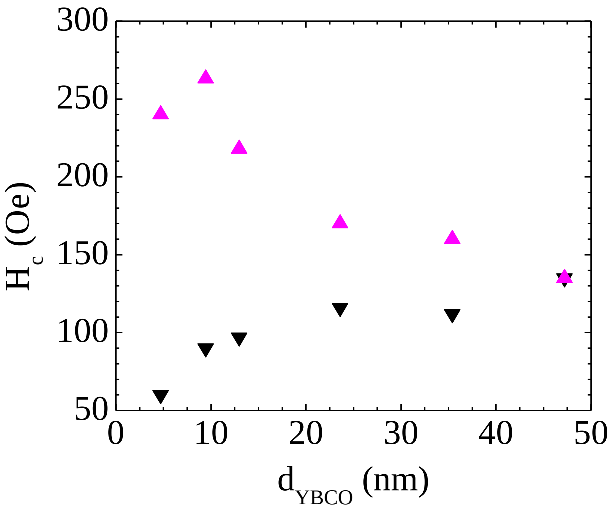

Fig. 3.27. Coercive field vs YBCO spacer thickness of the trilayers at T=100 K extracted from Fig. 3.26.

We have measured magnetoresistance at fixed temperatures along the superconducting transition while sweeping a magnetic field (between −1 and +1 T) applied parallel to the layers. The lower panel of Fig. 3.28 shows a typical $R(H)$ curve on a trilayer with 8-nm (7 unit cells)-thick YBCO measured at a resistance drop $R_{\mathrm{min}/}R_n$=10^{-4} relative to the normal state R_n. Large magnetoresistance peaks can be seen far be- low the onset and centered on a field interval where, owing to different coercivities, the magnetic moments of the ferromagnetic layers are antiparallel as determined by polarized neutron reflectivity. Increasing temperature results in a decrease in the magnetoresistance. Near the onset, as depicted by the upper panel of Fig. 3.28 at transition midpoint, there appears a negative magnetoresistance peak centered at H_c^F of the top LCMO in this particular trilayer.

To examine whether magnetoresistance is related to stray fields from domain walls in the ferromagnet, which has been proposed as an explanation for positive magnetoresistance peaks, we have investigated related bilayer samples. Two examples are shown in Fig. 3.28. In the bilayer with a 12 nm-thick YBCO bottom electrode there is no magnetoresistance feature at low field. The slowly rising background at higher fields, present in all superconducting films and strongly dependent on the alignment of film plane and magnetic field, is due to vortices (green dashed line).

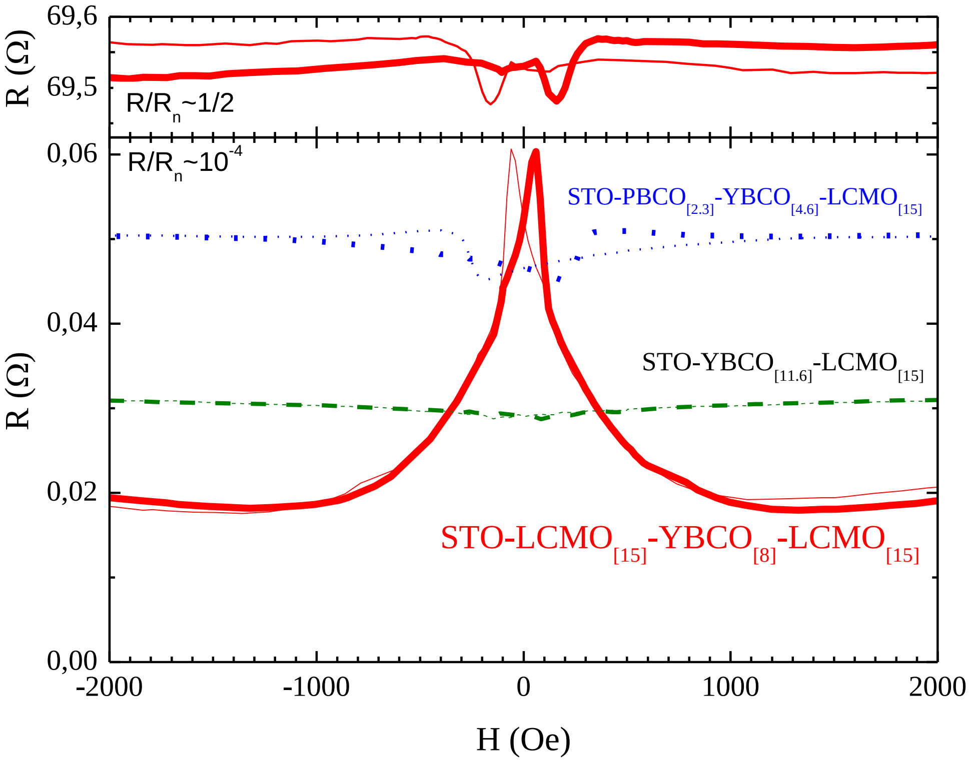

Fig. 3.28.Upper panel: Magnetoresistance of a trilayer with 8 nm YBCO measured at R_{min}/R_n=0.5. Note the negative magnetoresistance peak. Lower panel: Magnetoresistance measured at a resistance drop R_{min}/R_n=10^{-4}. Continuous red line: trilayer with 8 nm YBCO. Note the large positive magnetoresistance peak. Dashed green line: bilayer with 12 nm YBCO. Note the lack of magnetoresistance features at low field. Blue dotted line: bilayer with 5 nm YBCO. Note the negative magnetoresistance peak. Data are shown with thick lines for increasing fields with thin lines for decreasing fields.

In the much thinner bilayer (with 5-nm-thick YBCO) a 2-nm-thick $PrBa_2Cu_3O_7$ buffer was used to further improve the YBCO growth and thus the YBCO/LCMO interface quality (blue dotted line). This bilayer shows a well-defined *negative* magnetoresistance peak centered at H_c^F of the LCMO. It is important to remark that while trilayers show positive and very large magnetoresistance peaks, bilayers show no or very small negative or positive peaks. These observations rule out the effect of stray fields as an origin of the observed magnetoresistance in this trilayer system, because trilayers and bilayers with equally thick YBCO and LCMO and having similar interface quality shall have comparable stray fields. It is clear that although there may be an effect of stray fields associated to domain walls in bilayers their strength seems to be modulated by roughness and thickness of the YBCO. Clearly this cannot be the origin of the much larger MR peaks observed in trilayers. We calculated the increase in the width of the superconducting transition $\Delta T_C^{P\rightarrow AP}$ caused by the change in the relative orientation of the magnetization of the two ferromagnetic layers. The measured resistance was normalized by the normal state resistance R_n just at the onset, which is a good proxy to scaling by the YBCO thickness as the samples have identical LCMO layers and lateral dimensions. Resistance values at the maxima (R_{max}) and minima (R_{min}) were used to construct resistance vs temperature curves, $T^{\mathrm{AP}}(R)$ and $T^{\mathrm{P}}(R)$, in the antiparallel and parallel configurations of the F layers (Fig.3.29).

Magnetoresistance at a given temperature is related, through the slope of $R(T)$, to the local increase in the superconducting transition width defined as $\Delta T_C^{P\rightarrow AP}(R) = T^P(R) - T^{AP}(R)$. Thus, we converted our T-dependent magnetoresistance sweeps into R-dependent $\Delta T_C^{P\rightarrow AP}$, indicated by the horizontal black arrows in Fig.3.29, which is the chosen quantity in many of the studies of conventional superconducting spin switches. Samples with different YBCO thickness may be compared by picking the value of $\Delta T_C^{P\rightarrow AP}$ at a given $R_{\mathrm{min}/}R_n$. We chose $R_{\mathrm{min}/}R_n$=10^{-4}, as shown by the gray bar in the upper panel of Fig. 3.30.

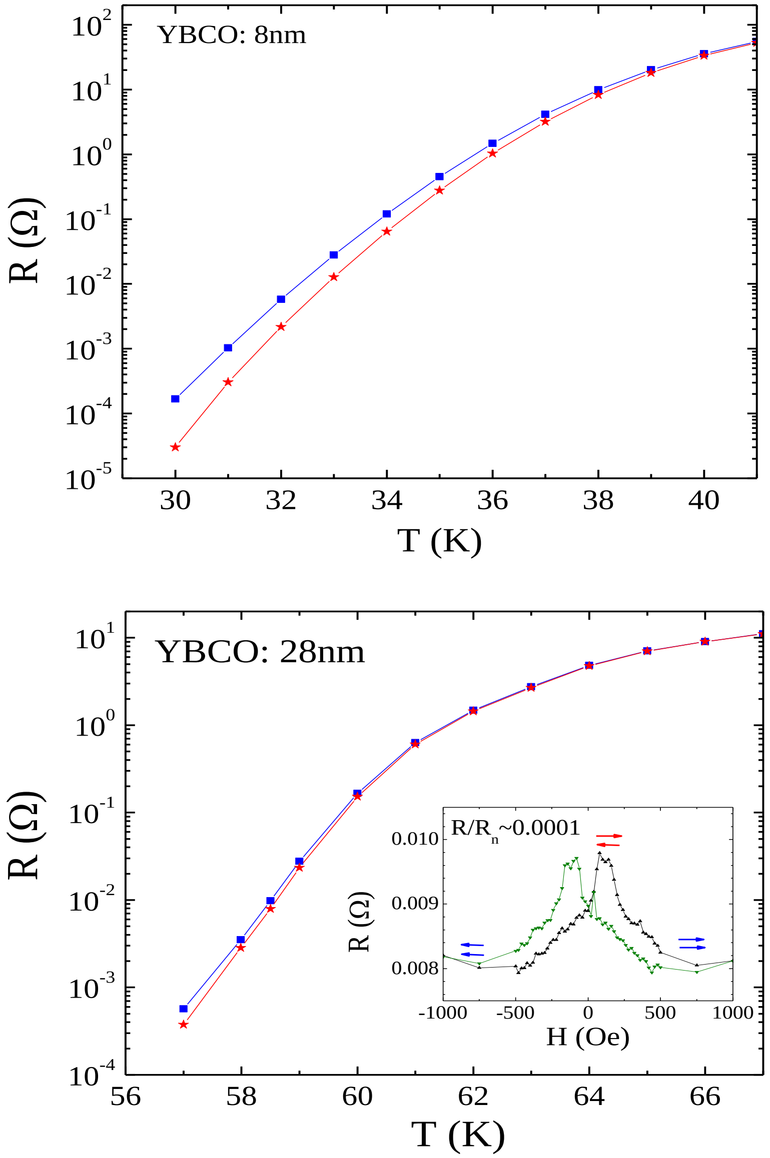

Fig.3.29. Trilayers with (upper panel) thin (8 nm) YBCO and (lower panel) thick (28 nm) YBCO. Modulation of the transition temperature, indicated by the arrow, obtained from the maximum (antiparallel, red squares) and minimum (parallel, blue circles) resistances. Inset of lower panel: Typical magnetoresistance in increasing (thick) and decreasing (thin) fields at $R_{min/}R_n$=10^{-4}. Magnetoresistance corresponding to the upper panel is shown in Fig. 3.28.

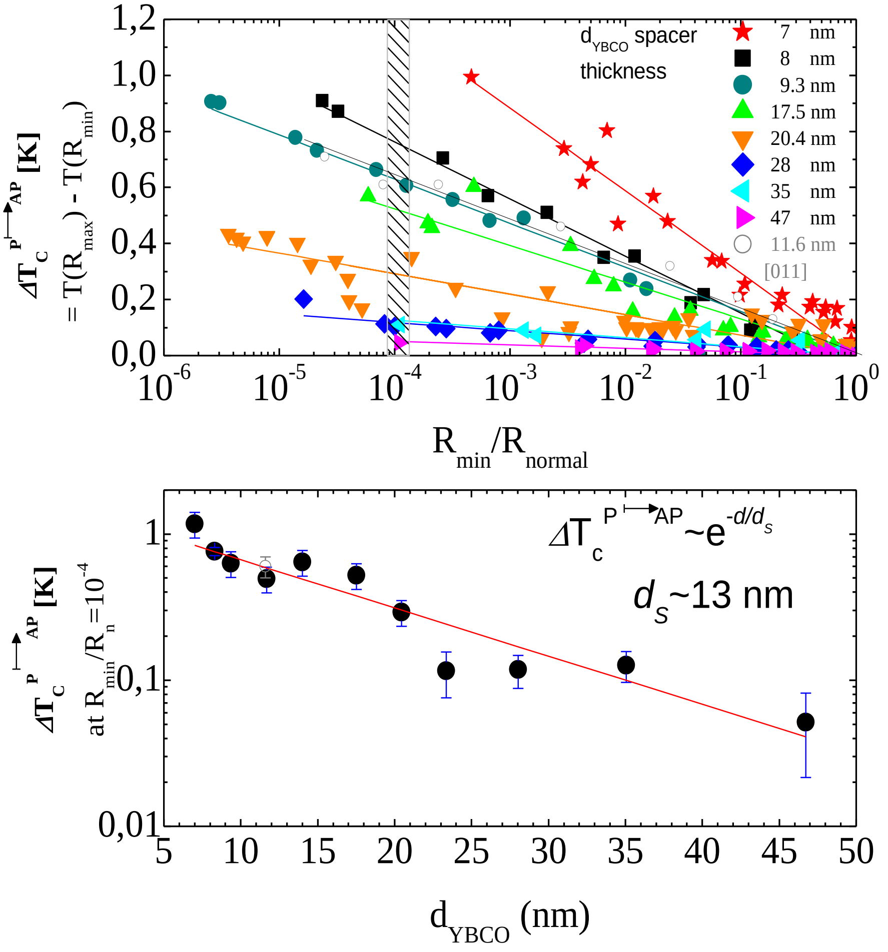

Fig. 3.30 Upper panel: $\Delta T_C^{P\to AP}$1:, as defined in Fig.3.29, decreases linearly with the logarithm of the resistance of the superconductor below T_c. The lines are logarithmic linear fits. The YBCO spacer thicknesses are given on the left. Lower panel: Decreasing pair-breaking effect with increasing YBCO thickness quantified by taking $\Delta T_C^{P\to AP}(R_{\text{min}}/R_n{=}10^{-4})$. The line is an exponential fit.

The effect is large. For the thinnest samples parallel and antiparallel resistance curves are separated by more than 1 K. This is in contrast to recent reports on proximity-coupled structures where T_C shifts by anywhere between 2 and 40 mK. [8,9,23,54,61] We observed an exponential decay of $\Delta T_C^{P\to AP}$ with increasing thickness of the superconducting spacer (Fig. 3.30, lower panel). The slope indicates a characteristic length scale of 13 nm, which can be related to the spin-diffusion length in YBCO. A different $R_{\min}/R_n$ choice would simply shift the data in the lower panel of Fig. 3.30, with no effect on its slope on a logarithmic scale.

To understand the magnetoresistance we propose a mechanism involving a different effective density of quasiparticles, which depends on the relative orientation of the magnetization in the ferromagnetic layers. Let us consider a normal/superconducting interface with no applied voltage; then a dynamical equilibrium exists in which particles approaching the interface from the normal side may diffuse into the superconductor and quasiparticles of the superconductor are transmitted into the normal metal at the same rate. In F/S/F double junctions, with thin superconducting layers, the simultaneous equilibrium of the two interfaces requires that quasiparticles thermally excited above the gap and transmitted through one interface may escape through the other and vice versa, since at equilibrium there should be no net charge transport. There will be a sizeable fraction $K_B/\Delta(T)$ of quasiparticles with energies larger than the gap $\Delta(T)$ that may be transmitted into the superconductor since close to T_C the gap approaches zero. A mechanism of F/S/F transport of subgap energy spins based on Andreev reflection [55] can be ruled out in the present case since Andreev reflection will be suppressed at the interface given the high spin polarization of LCMO. In particular, for highly spin-polarized ferromagnets, the situation depends on the relative alignment of the magnetization in the F layers. For parallel alignment, electrons transmitted from one electrode can escape through the opposed interface provided the superconductor is thinner than the spin-diffusion length. However, in the antiparallel configuration, electrons transmitted from one ferromagnetic electrode will be reflected if the superconducting spacer is thinner than the spin-diffusion length, as there are no states available at the Fermi level with the right spin orientation in a half metal [53]. This causes an effective increase in the number of quasiparticles that self-consistently reduces T_C due to a nonequilibrium process in the quasiparticle excitation spectrum. The excess quasiparticles may persist over large distances from the interface before they relax into Cooper pairs in the current to supercurrent conversion process, since the quasiparticle relaxation time diverges as $\tau_Q \sim 10^{-10} s/[\Delta(T)/\Delta(0)]$ close to T_C [62]. In addition, the *d*-wave pairing symmetry of YBCO allows introducing spin-polarized quasiparticle excitations at zero energy cost along nodal regions, thus increasing the importance of transmitted quasiparticles. This process involves an increased quasiparticle density due to mirror-like interfaces for the antiparallel alignment, yet it does not involve net spin or charge transport between the electrodes (CIP transport). When the thickness of the superconductor is larger than the spin-diffusion length, electrons transmitted from one electrode lose memory of their spin orientation and behave identically at the other interface irrespective of the magnetic configurations. This is consistent with the much smaller T_C shift for 28-nm-thick YBCO as compared to 8-nm-thick YBCO (see Fig.3.29). Furthermore, within this picture we may interpret the slope of the thickness dependence of $\Delta T_C^{P\rightarrow AP}$ as a measure of the spin diffusion length. A logarithmic linear fit (lower panel of Fig. 3.30) yields for the spin-diffusion length d_s=13 nm in YBCO. This value is in good agreement with previous estimates based on the thickness dependence of T_C for YBCO in bilayer samples. Therefore, inverse and conventional superconducting spin switches in F/S/F junctions result from different mechanisms, namely, proximity effect and quasiparticle diffusion. These may be present simultaneously and compete to some extent in the same sample. Large spin polarization of the ferromagnetic electrodes or increasing the thickness of the superconductor beyond ξ_{GL} reduces proximity coupling and favors the observation of quasiparticle scattering at the F/S interface responsible for the inverse superconducting spin switch behavior. Finally, an important issue is the interface transparency and the strength of the interface barrier. These determine the ratio of particles being transmitted versus those being Andreev reflected. In turn, this determines the operation of the F/S/F junction as conventional or inverse superconducting spin switch. This should be the reason why apparently similar structures with different interface properties yield opposite behaviors.

In summary, we have shown that F/S/F structures based on cuprates and manganites exhibit an inverse superconducting spin-switch behavior, where superconductivity is favored for parallel magnetizations of the two ferromagnetic layers. The inverse superconducting spin switch is controlled by scattering (reflection) of spin-polarized quasiparticles at the F/S interface, which is strongly enhanced for antiparallel alignment of the F layers. The high spin polarization of the manganite and the *d*-wave superconductivity of the YBCO are crucial for observing this effect. This is a unique form of coupling between the superconducting properties and the magnetic state of the ferromagnetic electrodes that occurs when the thickness of the superconducting layer is shorter than the spin-diffusion length, and it may form the basis of novel device concepts for spintronics.

c) *Critical current of a LCMO/YBCO/LCMO trilayer: the vortex pinning effect*

In many existing microstructured devices based on type II (typically high T_C) superconductors the motion of vortices results in a parasite resistance and a consequently reduced performance. Therefore there's a general trend in the scientific research in finding all sort of possible source of flux pinning to maximize the critical current density J_C supported by the superconductor. Vortices are known to pin at intrinsic structural defects of the crystal (interstitial defects, twin boundaries, etc.); this fact suggested the possibility of inducing pinning points in several ways, for example, ion induced columnar defects, nanopatterned structures facing the superconductor or controlled introduction of non-coherent interfaces acting as a constraint to the flux motion [63-65]. On the other hand the vortex pinning effect opened the possibility of developing devices based on a tunable pinning force. This can be achieved for example by introducing a periodic asymmetric pinning potential [66-68]. Alternatively, the control over the vortex state of the superconductor can be achieved by a pinning source of non-morphological nature. In F-S hybrids, in which the magnetostatic field of the magnetic domains can couple with the vortex cores, the magnetic state of the ferromagnet can be used as a probe of the vortex state of the superconductor and vice versa [69-71].

When an external current density J is applied to a vortex system the flux lines start to move under the action of the Lorentz force:

$$\overrightarrow{f_t} = \vec{J} \times \vec{B} \qquad 3.2$$

As a consequence of the flux motion, a finite electric field E will appear:

$$\overrightarrow{E_{eff}} = \overrightarrow{v_{fl}} \times \vec{B} \qquad 3.3$$

where E_{eff} is an effective electric field induced by the vortices travelling through the superconductor with velocity v_{fl}. In order to recover the desired property of dissipation-free current flow, the flux lines have to be pinned such that v=0 in spite of $\overrightarrow{f_L} \neq 0$.

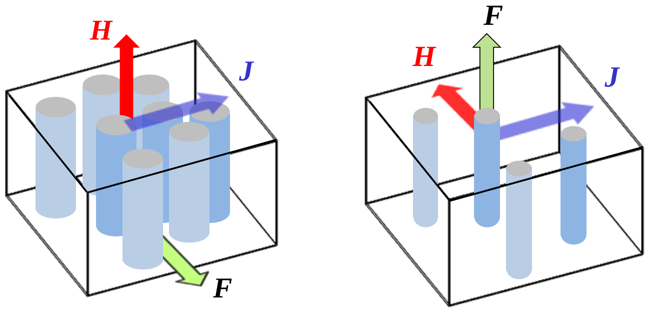

Fig.3.31 Schematic diagram of the vortex system under the action of an external magnetic field and current.

We know that the interplay between ferromagnetism and superconductivity can be realized in different ways: by proximity effect (in which electrons with energy below the superconducting gap enter the superconductor from the normal-metal side), by diffusion of electrons with energies larger that the superconducting gap, and the stray field effect (in which the superconductor is affected by the domain structure of the ferromagnet). We propose that, in our LCMO/YBCO/LCMO hybrids, another possible scenario is provided by the pinning of superconducting vortices in contact with the ferromagnetic layer. A possible source of pinning can be given by structural inhomogeneities of the superconductor induced by magnetic inhomogeneities of the ferromagnet. As shown in previous sections, we have measured the effect caused by the diffusion of spin polarized quasiparticles in the superconductor as the magnetoresistance of LCMO/YBCO/LCMO trilayers, observed along the transition in the antiparallel alignment of the ferromagnetic layers, In this section we will analyze the possibility of vortex pinning. This situation is encountered in a Bloch-type domain wall in which the magnetization rotates out of plane.

Magnetoresistance: a LCMO/YBCO/LCMO trilayer with 15nm-thick LCMO and 18nm-thick YBCO have been used for this experiment. The superconducting transition spans between 45K and 55K as shown in Fig. 3.32. Due to the fact that the most pinning phenomena occur in the vortex glass state, we expect this effect to be enhanced when the sample enters deeper into the glass state that is at temperature lower than the onset of the superconducting transition. This is the case shown in Fig. 3.33. The intensity of the dips, corresponding to the coercive field of the bottom LCMO, decreases when raising temperature that is approaching the mixed state in which the vortex liquid dominates overt the vortex glass. In the normal state (above T=55K) only the anisotropy magnetoresistance of the LCMO is visible.

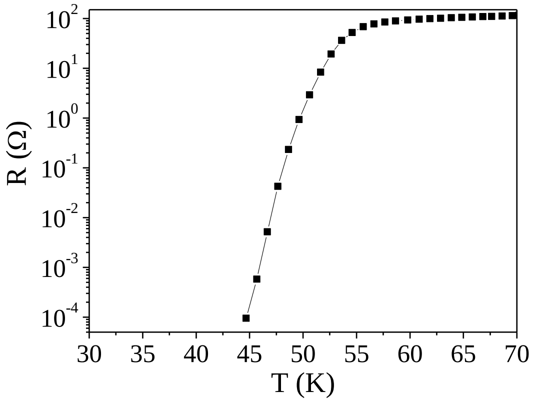

Fig. 3.32 Resistance vs temperature for the STO/YBCO/LCMO sample, in semilog and linear (inset) scale.

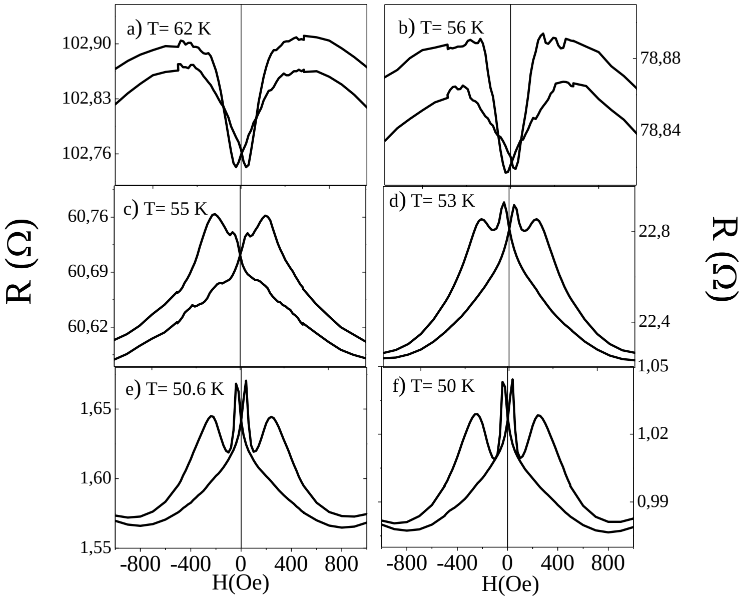

Fig. 3.33 left: Resistance vs magnetic field, measured at a) 62K, b)56K, c) 55K,d)53K, E)50.6K, 50K.

To study the extent of this effect in the glass state we performed an analysis of the critical current. Samples were patterned by photolithography to obtain the current density values necessary to measure the glassy response. The critical current is an intrinsic property of the superconductor being $\overrightarrow{J_C} \propto |\psi|^2$. Thin micro-bridge structures of 250x20 μm^2 size, were produced by ion-milling. An image of the structure is given in Fig. 3.34.The long axis of the micro-bridge lies on the [100] axis of the substrate. Due to the very different ratio of the lateral dimensions of the bridge compared to a large sample, the magnetic anisotropy is dominated by the shape anisotropy. It is well known that the superconducting properties of ultrathin YBCO layers are very sensitive to the lithography process, sometimes resulting in quite reduced critical current. We measured the superconducting transition of the patterned sample and we found that the critical temperature was reduced of a 10%. Nevertheless the width of the transition was the same as before the lithography process, spanning between 42K and 52K (see Fig. 3.35). The shape of the bridge also allows differentiating the effects caused by applying the field parallel or perpendicular to the current.

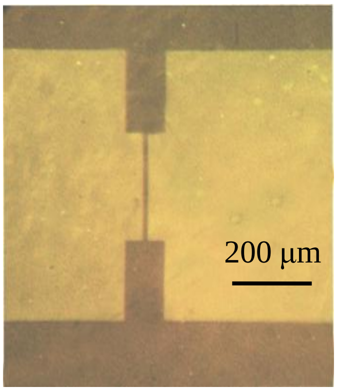

Fig. 3.34 Picture of the micro-bridge structure.

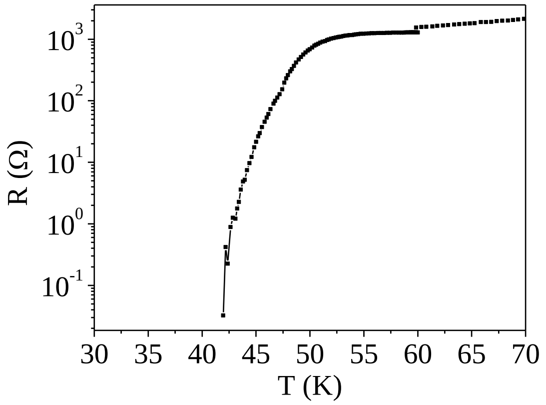

Fig. 3.35 Resistance vs temperature of the patterned sample.

Fig. 3.36 shows R vs H curves of the micro-bridge, taken in the superconducting transition (T=50K), applying the field perpendicular and parallel to the current. The value for the current was I=1μA. The qualitative behavior is similar in the two cases even though a more pronounced dip (four times deeper) is detected for field applied perpendicular to the current. MR effect has broadened and the position of the dip has moved towards higher field and the range. Under these conditions it is difficult to say what LCMO layer is responsible of the decrease in the resistance; we know from the results of the previous chapters that both layers are capable of this effect. Here we should also consider the possibility that both the LCMO layers are involved.

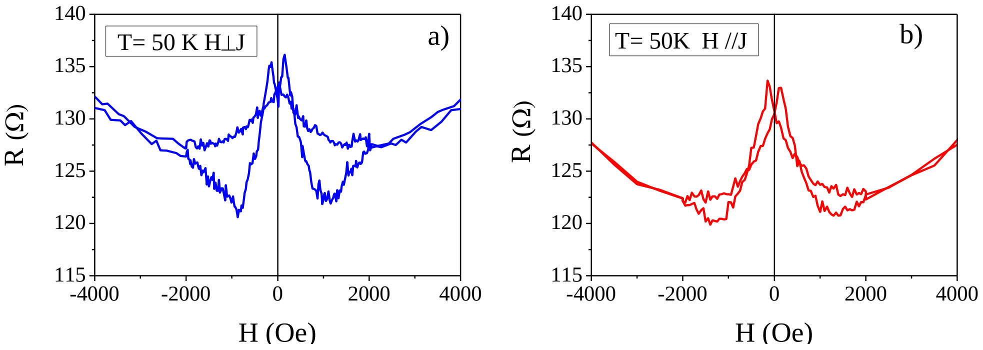

Fig. 3.36 Resistance vs magnetic field, at 50K, for field applied in the plane of the sample a) perpendicular and b) parallel to the current.

Since we were interested in the larger changes in the current value we performed the rest of the in-plane measurements with the field perpendicular to the current. To get a magnetoresistance curve in the vortex glass regime we used a current I=100μA to recover the resistive state of the YBCO. We can see from Fig. 3.37 that any positive component of magnetoresistance disappears and that the dip gets more intense at lower temperature, theorizing that peaks are a property of the liquid state while dips are related to vortex response.

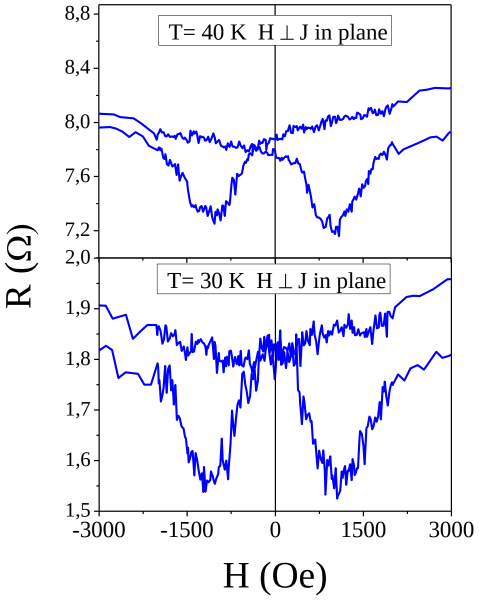

Fig. 3.37 Resistance vs magnetic field, at 40K (top) and 30K (bottom), using a current I=100μA.

Critical current: we now discuss the measurements of the critical current. The critical current is defined as $J_C=I_C/S$ where $S=2.4x10^{-9}cm^2$ is the microbridge cross section. A preliminary V-I measurement at T=10K allowed us identifying three different regimes: thermally activated (below $9x10^4A/cm^2$); flux creep, where we find the critical current (between $9x10^4A/cm^2$ and $1x10^5A/cm^2$), free vortex flow (above $1x10^5A/cm^2$).

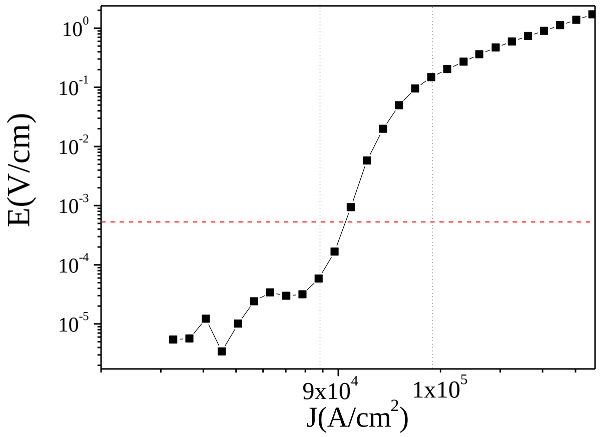

Fig. 3.38 V-I curve at 10K. The vertical lines separate the three vortex regimes. The horizontal line indicates the voltage value taken as reference for the calculation of the critical current.

The critical current for each curve will be taken using the voltage criterion E=4x10^{-4} V/cm (corresponding to V=10^{-5}V). We analyzed the behavior of the V-I curves as a function of temperature and magnetic field. Fig. 3.39 shows V-I curves taken at several temperature from 10K to 54K. For a fixed value of the voltage the corresponding current decreases when the increasing temperature because we are approaching the region of the phase diagram from the vortex glass (non-linear regime) to the vortex liquid regime (liner response). We then repeated the sequence of V-I curves this time applying a field H=1T perpendicular to the surface of the sample. In Fig. 3.40 we can see that the effect of the perpendicular field is to move all the V-I curves towards the linear regime. The drift is quite large because the in plane penetration depth is small such that many vortices can easily nucleate in the area covered by the micro-bridge. Consequently the distance between each vortex is reduced favoring the vortex-vortex interaction, i.e. the vortex liquid regime, at lower temperature.

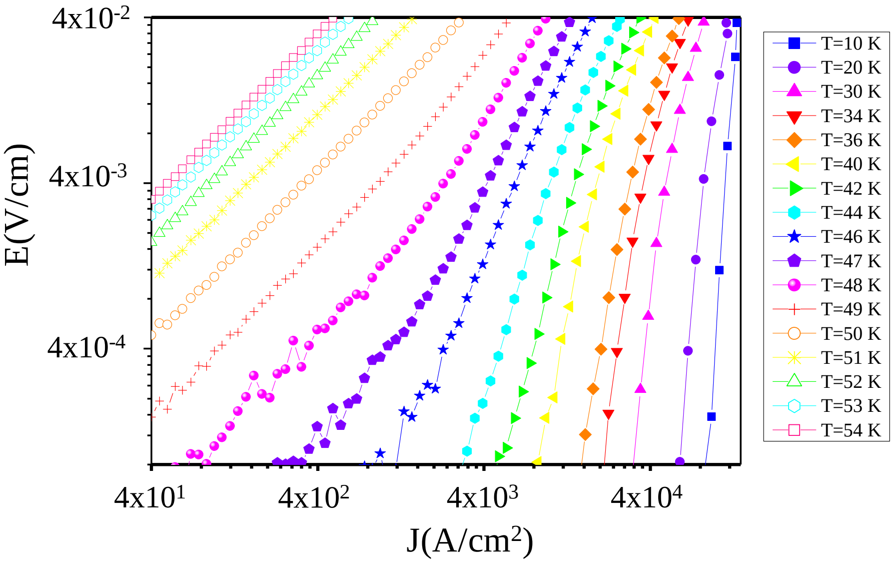

Fig. 3.39 V-I curve measured at several temperature without magnetic field. Temperature goes from 10K to 54K, as indicated in the figure, from right to left.

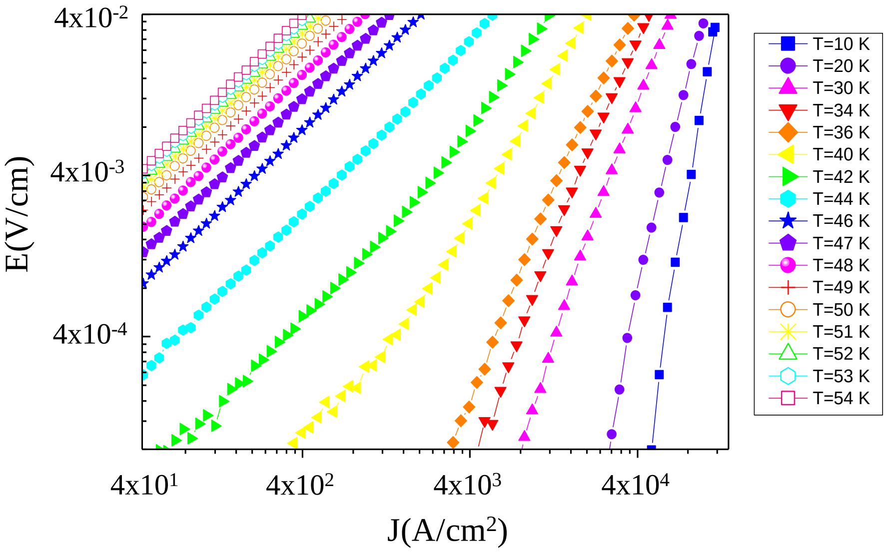

Fig. 3.40 V-I curve measured at several temperature in a magnetic field H=1T applied perpendicular to the sample surface. Temperature goes from 10K to 54K, as indicated in the figure, from right to left. The color-symbol code is the same of Fig. 3.39.

We repeated the measurement with the field applied in the plane of the sample, perpendicular to the current. In Fig. 3.41 we compare the two sets of measurements (with and without field). The drift is much weaker due to the fact that the penetration depth in the c direction is to large (~900Å) compared to the thickness of the YBCO layer (180Å) to allow the formation of vortices in the plane of the sample. Without vortices the magnetic field is expelled from the sample (the Meissner effect). However, due to the impossibility to get the sample perfectly aligned, a small perpendicular component of the magnetic field is the source of vortices and thus of the observed dissipation. We swept the field at fixed temperature to follow a $J_C$vsH hysteresis loop. The set of V-I curves taken for the field perpendicular to the sample surface is shown in Fig. 3.42. More than a hundred V-Is were measured for different values of magnetic field using a short step at low field range; notice the accumulation of curves on the right. The calculated critical current is given in Fig. 3.43.

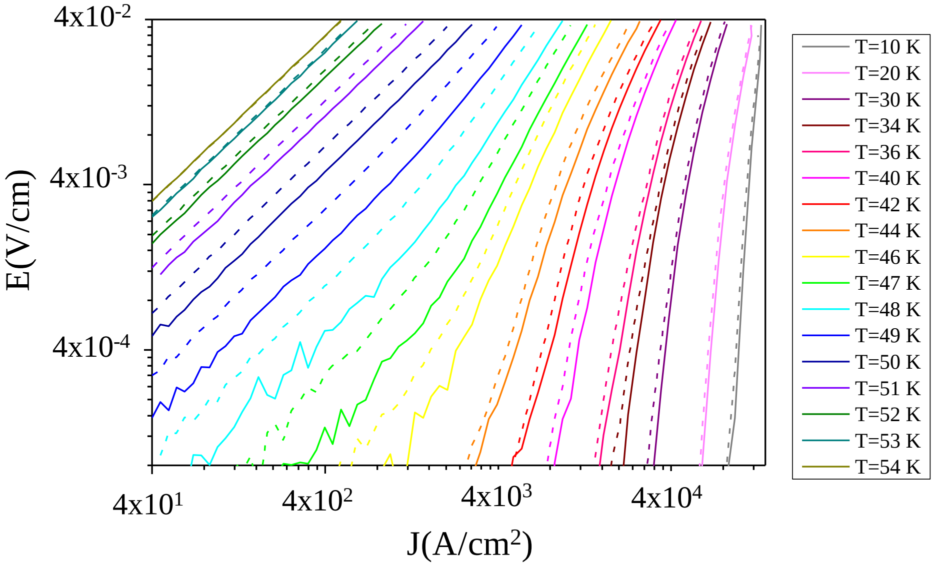

Fig. 3.41 V-I curve measured at several temperature without magnetic field (continuous line) and with a field H=1T applied in the plane of the sample. Temperature goes from 10K to 54K, as indicated in the figure, from right to left.

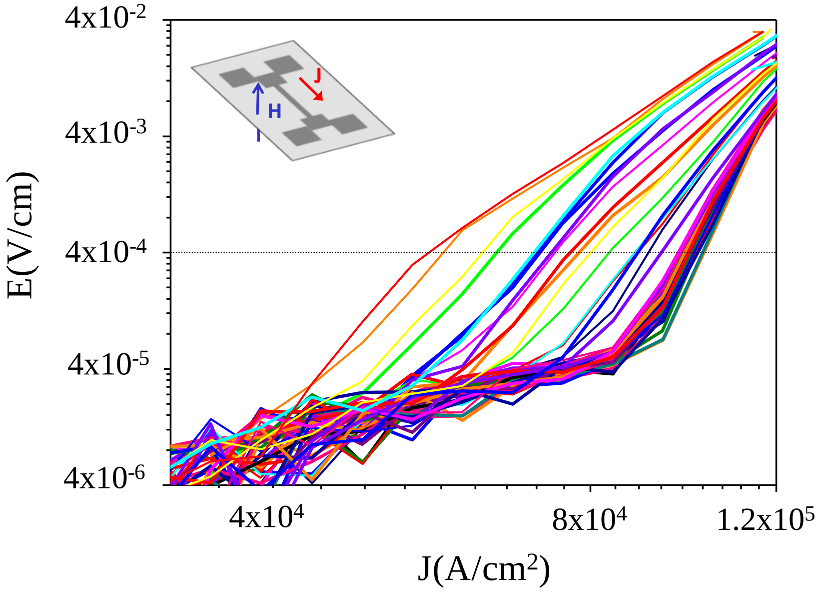

Fig. 3.42 V-I curve measured at 10K for several values of the magnetic field. The field interval was H=±1T and the field was applied perpendicular to the sample surface

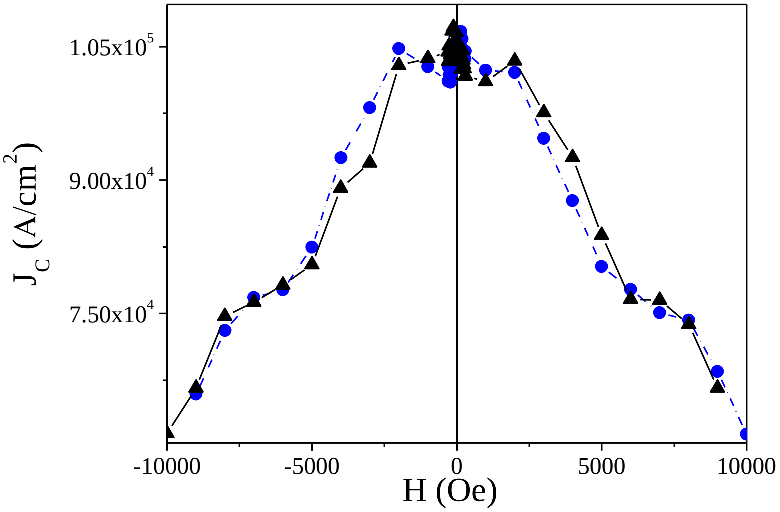

Fig. 3.43 Critical current as a function of the field, extracted from Fig. 3.42.

The J_C hysteresis loop displays a strong dependence with the field exhibiting a maximum at H=0. The same kind of analysis has been done for field applied in the plane of the sample, perpendicular to the current. Results are displayed in Fig. 3.44 and Fig. 3.45.In contrast to the previous case, the maximum contribution to the effect is given by the small perpendicular component of magnetic field which causes a small dissipation. However the J_C hysteresis loop is not centered at H=0 but clearly shows broad peaks corresponding to the field range of the domain nucleation. This is an unambiguous proof of the pinning of vortices to the domain walls of the ferromagnetic layers.

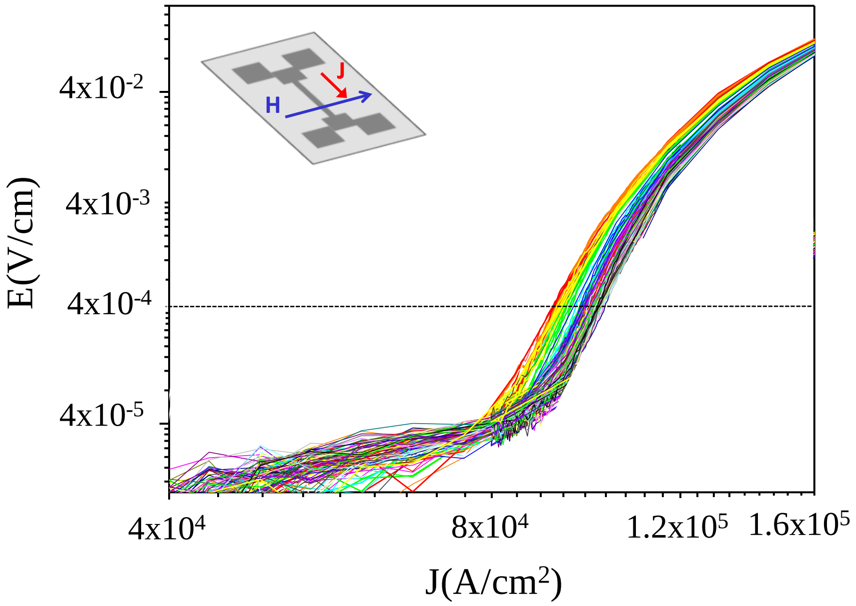

Fig. 3.44 V-I curve measured at 10K for several values of the magnetic field. The field interval was H=±1T and the field was applied in the plane of the sample, perpendicular to the current.

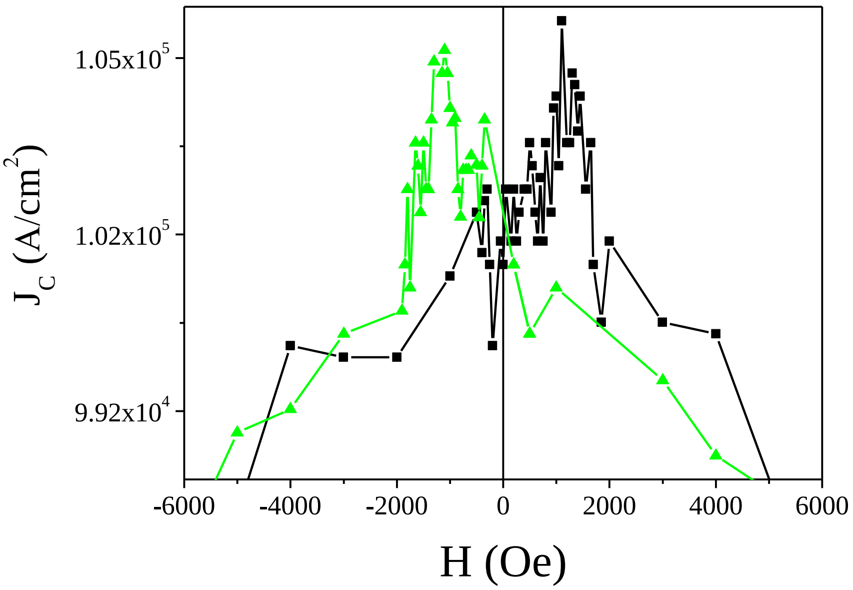

Fig. 3.45 Critical current as a function of the field, extracted from Fig. 3.44.

In conclusion we demonstrated that the increase in the critical current observed in the vortex glass regime (very low temperature) is due to the pinning of the superconducting vortices to the stray field generated by the domains. We also showed that in some cases the decrease in the dissipation dominates over the pair breaking effect caused by the stray field itself and that the effect can be projected at higher temperature by negative magnetoresistance peaks.

3.4 Directionally controlled superconductivity in LCMO/YBCO/LCMO spin switches

In the previous section we provided evidence for an ISS effect, with superconductivity favored when the F layers are parallel aligned, with an origin different from stray fields, in $La_{0.7}Ca_{0.3}MnO_3$ (LCMO) / $YBa_2Cu_3O_7$ (YBCO) / $La_{0.7}Ca_{0.3}MnO_3$ (LCMO) trilayers. This mechanism is determined exclusively by the magnetic alignment of the ferromagnetic layers and therefore has a spin dependent origin. Now we explore how the F/S interplay in F/S/F structures is modulated by the biaxial in plane magnetic anisotropy of the ferromagnets. The angle between applied magnetic field and easy axis controls magnetization switching and determines the magnetic alignment of the ferromagnetic layers, and this influences the superconductivity of S layer. We find a well defined positive MR plateau between the coercive fields when the field is applied along an easy axis. The (magneto) resistance closely follows the AP alignment with a high resistance state in the AP configuration and a low resistance state under P alignment (as opposed to the DSS).

We grew F/S/F trilayers with fixed 15-nm thick top and bottom LCMO layers while the YBCO thicknesses are between 9 and 46 nm. Within this range of YBCO thickness all the samples exhibit similar magnetic and magnetoresistive behavior (see section 3.2*b*). The samples were grown on as received [100] oriented $SrTiO_3$ (STO). Resistivity measurements were performed by using a four-probe method, with a *dc* current injected in plane. Resistance vs. field and angle was measured after zero-field cooling and a subsequent sweep from a positive to a negative saturating field of -10 kOe. Magnetic field was applied in the plane of the sample, at a variable angle (θ) with the substrates edges, which coincide with the magnetic hard axes, as shown below.

To get an insight into the magnetic anisotropies in the hybrids, we studied the ferromagnetic resonance by rotating the direction of the (large) external field within the film plane, on a sample with 12 nm thick (10 unit cells) YBCO. FMR was recorded while changing the direction of the external field (swept between 0 and 10 kOe) within the plane, above the superconducting onset. Data were taken at 77 K, which is above the superconducting transition temperature. The results of the angular dependence of the field of FMR of the bottom LCMO layer are shown in Fig.3.46 The four minima of the FMR field (the radial value of the polar plot) along the [110] directions indicate the magnetic easy axes. The simulated FMR position of Fig.3.46 is based on the same magnetic anisotropy model used in section 3.2*a* (pag.91). In this case we used M_S = 400 kA/m for the magnetization, K_{2c} = 180 kJ/m^3 and K_{4ab} = 3.1 kJ/m^3 for magnetic anisotropies.

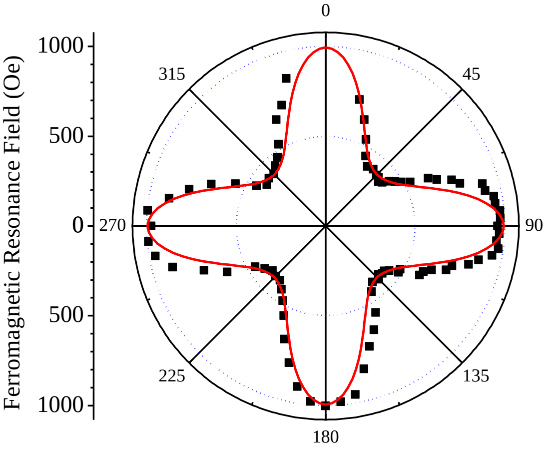

Fig.3.46 Angular dependence of the ferromagnetic resonance field (black squares), indicates a biaxial symmetry with magnetic easy axes along the [110] directions of the STO substrate. The continuous line is a fit as explained in the main text.

This corroborates that the four [110] directions of the STO substrate are magnetic easy axes, as also found in 15 nm-thick single LCMO films grown on STO [100]. This last issue has been discussed controversially in the literature since magnetic anisotropy, as many other properties in lanthanum manganites is strongly related to the thickness of the film, the doping and the degree of strain [72-76].

a) The PNR experiment

Polarized neutron reflectometry (PNR) measurements were performed at the polarized neutron reflectometer ASTERIX at the Los Alamos Neutron Science Center (Los Alamos National Laboratory) to get the magnetic depth profile of the trilayers. We applied PNR to trilayers with different YBCO thickness: 18nm (15 u.c) in the first case and 46nm (40 u.c.) in the second case. All the measurements have been performed applying the field in the plane of the sample and along the [100] direction. As shown in section 3.2*b*, trilayers with thin YBCO spacer show the biggest magnetoresistance effect, while trilayers with thick YBCO (>30nm) show almost no magnetoresistance. Our purpose is to track the effect played by the alignment of the magnetization of the LCMO electrodes using PNR as depth-sensitive probe.

LCMO/ YBCO (18nm)/ LCMO: we first obtained a structural model of the sample from the analysis of the X-ray reflectivity pattern. Fig.3.47 shows the whole scan (a), which includes the first order Bragg peak of the YBCO, and the refinement of the initial part (the finite size oscillations) which gives information about the thickness and the structural quality of the hole sample (b).This model, shown in Fig.3.49 (top) has been applied to the subsequent PNR refinement to compare the structural and the magnetic profile (see below). The real part of the X-ray scattering length density gives information about the distribution of the electronic densities of each material as a function of the depth into the sample while the imaginary part is a quantity related to the X-ray absorption. The value is almost constant inside each layer except for a gradient of about 20Å at the surface caused by roughness. The YBCO/LCMO bottom interface (at the right side of the profile) appears to be very sharp while the top YBCO/LCMO interface presents some roughness of the order of 1 YBCO unit cell. One of the most striking features is the presence of a thin layer of about 13Å just above the substrate with SLD values not corresponding to those of the LCMO. The best fit to the data (in particular the long period oscillation in the q range 0.15-3 $Å^{-1}$) with the CO_REFINE program required values most likely corresponding to those of $CaMnO_3$ (*Re* X-ray SLD: $3.16x10^{-5}$, *Im* X ray SLD:$1.92x10^{-6}$). It has been reported that strain induced chemical segregation can arise at the interface between LCMO and STO [77,78] resulting in reduced ferromagnetic and metallic properties. For thin layer of thickness <20nm it has been found that Ca segregates at the interface with the substrate while the free surface is enriched in La. However in our case this segregation does not affect the two YBCO/LCMO interfaces which show correct values of SLD for the LCMO. Lanthanum migration at the free surface would lead to large values of SLD which is not our case. The contrast between the LCMO and the Ca rich bottom layer allows identifying the thickness of the first LCMO given by the long period oscillations. We know that these oscillations are due only to the bottom LCMO layer through the analysis of X-ray reflectivity of trilayers in which we changed the thickness of only the bottom LCMO, keeping the rest fixed. The period of the oscillations was changing coherently (data not shown in this work). The calculated LCMO thickness is 15nm, taking into account that the base layer thickness is within in the uncertainty associated to this method (~10%).

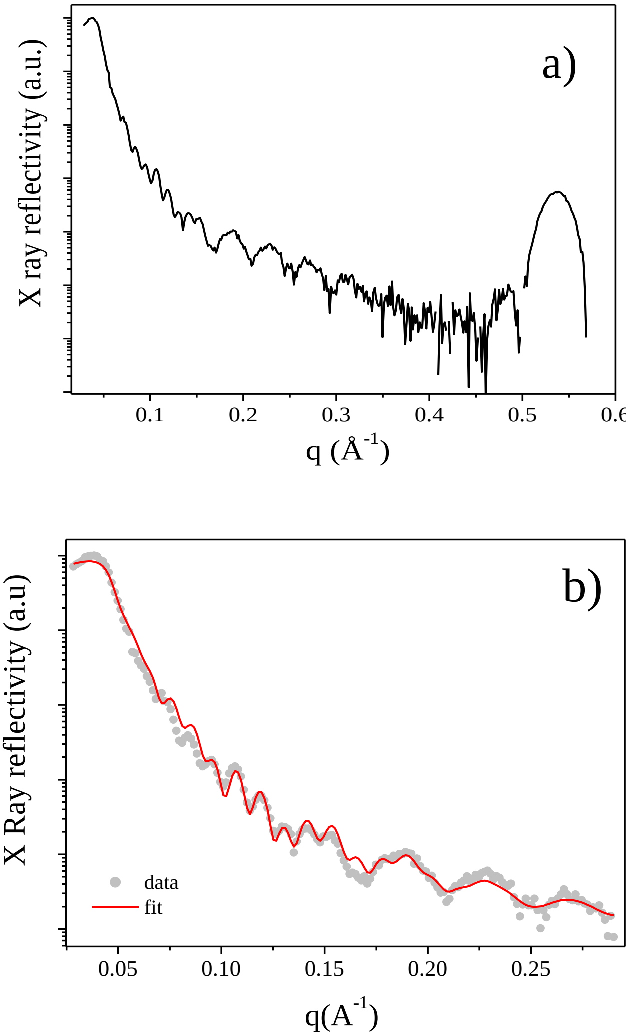

Fig.3.47 X ray reflectivity (a) and refinement (b) for the trilayer: 15nm LCMO/18nm/YBCO/15nmLCMO. The fit to the data is represented by the line.

Now we discuss the PNR data. The first PNR measurement was made at a saturating field of H= 5500 Oe and at a temperature of 10K (well below T_C), applying the field in plane along the [100] axis (with an accuracy of approx. 5 degrees). In this case polarization analysis was not necessary. Fig.3.48 shows the R^{++} and R^{--}curves. For clarity the two curves have been shifted. The analysis of these data produced the profile shown in Fig.3.49 (bottom panel).

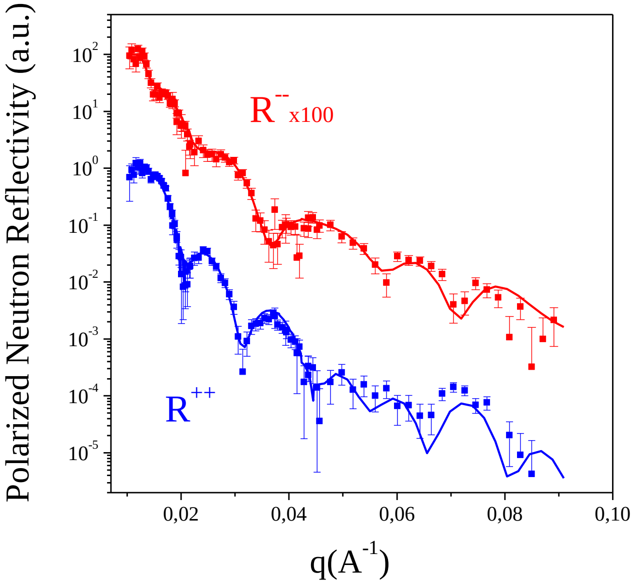

Fig.3.48 PNR data taken at saturation (H=5500 Oe) for the trilayer with 18nm-thick YBCO. The fit to the data is represented by a line.

As it has been already reported [33], top and bottom LCMO have different magnetization probably due to the different in-plane strain of the LCMO: tensile on the STO, compressive on the YBCO. The magnetic profile evidences a thin non-magnetic (*dead*) layer of the same thickness of that seen in the X-ray structural profile. This is consistent with the non-ferromagnetic nature of the $CaMnO_3$. Strain may be also partly responsible of the gradient close to the substrate (unrelated to roughness). The depression of the magnetization close to the surface may be caused by roughness but the extension into the sample is larger than that displayed by the X-ray data, thus not produced by chemical inhomogeneities. Without further evidence, we speculate that phase separation, triggered by the strain, may play a role in this matter. We also observe a depression of the magnetization at the interface which may be due to charge transfer from YBCO to LCMO (change of the Mn valence towards Mn^{2+}) [51]. We effectively observe a slow change in the interface magnetization, more pronounced for the top YBCO/LCMO interface. Again, this change propagates into the LCMO over the distance affected by the structural roughness.

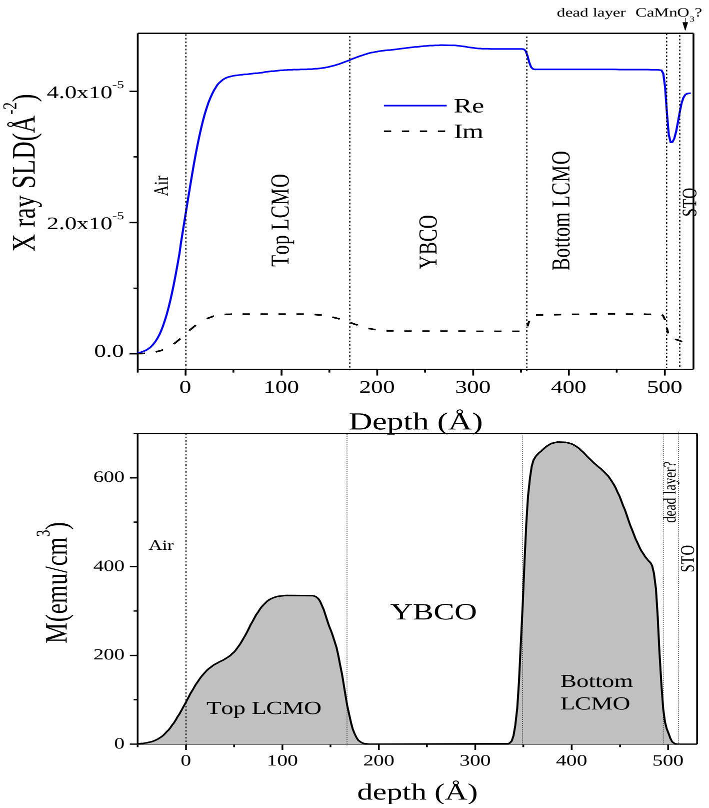

Fig.3.49 Top: structural profile given by the X-ray fit as a function of the depth into the sample. Bottom: magnetic profile given by the PNR fit at saturation.

In Fig.3.50 we show polarized neutron reflectivity data, taken in a magnetic a field of 82 Oe, after saturating in H=-5500 Oe. This field value is just after the first coercivity at this temperature. The right panel of Fig.3.51 shows the position in the magnetization loop. Magnetic field was applied along the hard axis in order to obtain a comprehensive picture of the magnetization reversal mechanism. PNR experiments were conducted with polarization analysis which allowed us to quantify the in-plane vector magnetization of each layer as a function of applied field. For the sake of simplicity we refer to the magnetization of the top and bottom LCMO as M_T and M_B, respectively. In addition to the intensity collected for the R^{++} (neutron beam polarization parallel to the applied field before and after reflection) and R^{--} (neutron beam polarization antiparallel to the applied field before and after reflection) spin state, a third curve $R^{spin\text{-}flip} = (R^{+-}+R^{-+})/2$ is shown. $R^{spin\text{-}flip}$ is the reflectivity of the portion of the neutron beam whose polarization flipped relative to the incident beam polarization after reflection. $R^{spin\text{-}flip}$ is related to the component of the magnetization that is perpendicular to the applied field. Simultaneous analysis of the R^{++}, $R^{--}$and $R^{spin\text{-}flip}$ curves gives detailed information not only on the magnetic depth profile but also on the angle the magnetization makes with the applied field. The fit to the data, carried out using the spin_flip software [79], indicates that the angle between magnetization and applied field is 77 degrees for M_B and 160 degrees for M_T, consistent with the magnetization switching by coherent rotation due to the magnetic field being applied in a different direction than the easy axis. The different equilibrium angles of the magnetizations of top and bottom layers show that the anisotropy field is larger for the top layer which aside from a small rotation, remains pointing in the direction of the saturating field. In addition a small uniaxial anisotropy keeps memory of the direction of the saturating field moves the magnetization out of the true easy direction.

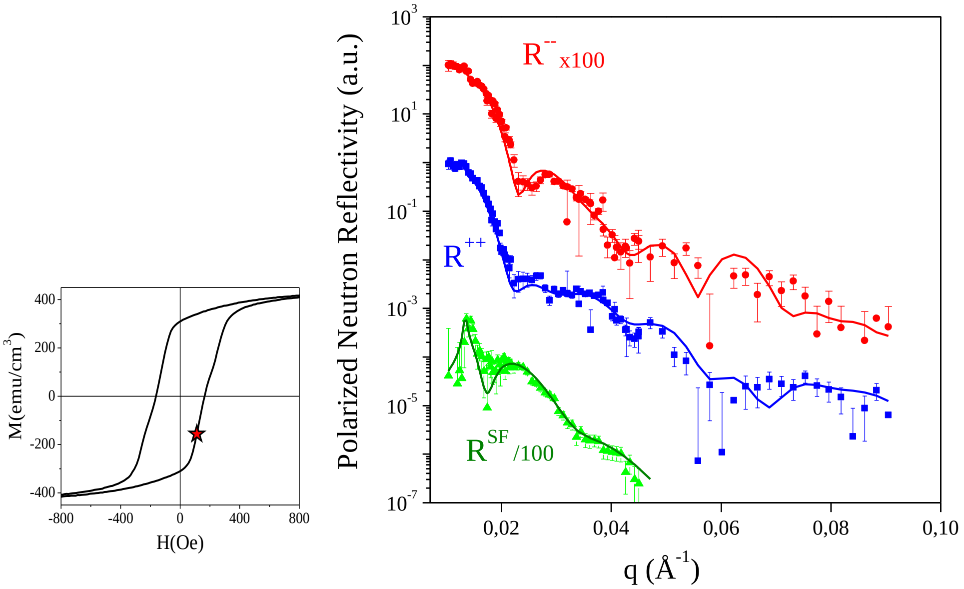

Fig.3.50 Left: magnetic hysteresis loop of the sample; the star indicates the field of the PNR measurement. Right: Polarized neutron reflectivity taken at 10 K applying a field of 82 Oe in-plane along the [100] axis. Data (symbols) are taken with polarization analysis. The fit to the data is represented by a line.

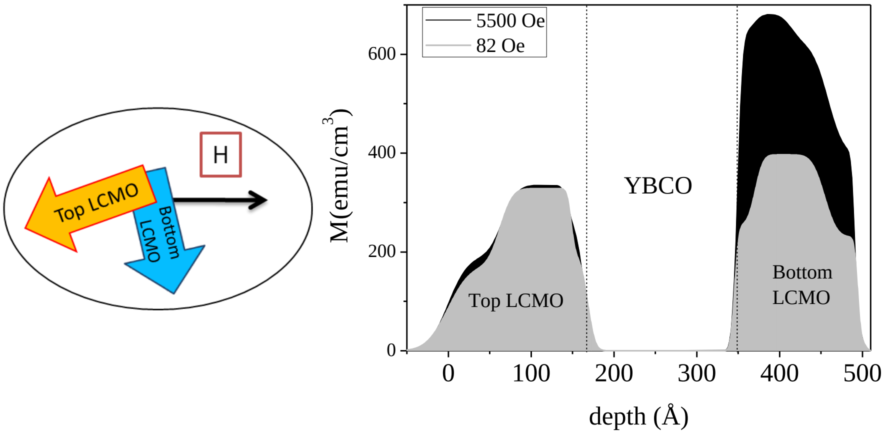

Fig.3.51. Right: magnetic depth profile at 82 Oe (grey), compared to the profile at saturation (black). Left: schematic orientation of the magnetization in the individual LCMO layers.

The magnetic profile is represented in Fig.3.51 compared to the one for saturation; the right side of Fig.3.51 shows a schematic diagram of the orientation of M_T and M_B with respect to the applied field. The magnetic moment of the top layer is essentially the same as in saturation (i.e. it rotates), whereas that of the bottom layer exhibits a significant reduction showing that there is substantial domain nucleation. In this measurement we can better appreciate the depression of the interface magnetization, at both side of YBCO. In conclusion we can see that the bottom layers switches first and that M_T and M_B are capable of a large angular misalignment at low field. Due to the limited beam-time we could not measure PNR at different magnetic fields.

LCMO/ YBCO (46nm)/ LCMO: we performed an experiment similar to the previous on a sample with a 46nm-thick YBCO spacer. The structural profile obtained from the X-ray analysis is compared with the magnetic profile supplied by the PNR measurements at saturation, as we did before. We collected data taken at different values of the applied field but in a shorter range of *q*. In doing so, we have been able to explore the behavior of the magnetic layer in a wider range of the magnetic hysteresis loop. Fig.3.52a. shows X-ray reflectivity of the sample. The first order Bragg peak is much more intense and surrounded by several satellites peaks. The fit shown in Fig.3.52*b* tells us that the long period oscillations correspond to the bottom LCMO layer and are due to the contrast between this and the buffer *(dead)* layer which naturally form at the interface with STO. The thickness is nearly the same as before (15Å).The quality of the upper and lower YBCO/LCMO interface reproduce the previous result: interface is sharp at the bottom and somewhat rough at the top, indicating that it is an intrinsic property of these heterostructures, not affected by the large thickness of YBCO. Although, we do not discard that the top LCMO is subject to a different amount of strain.

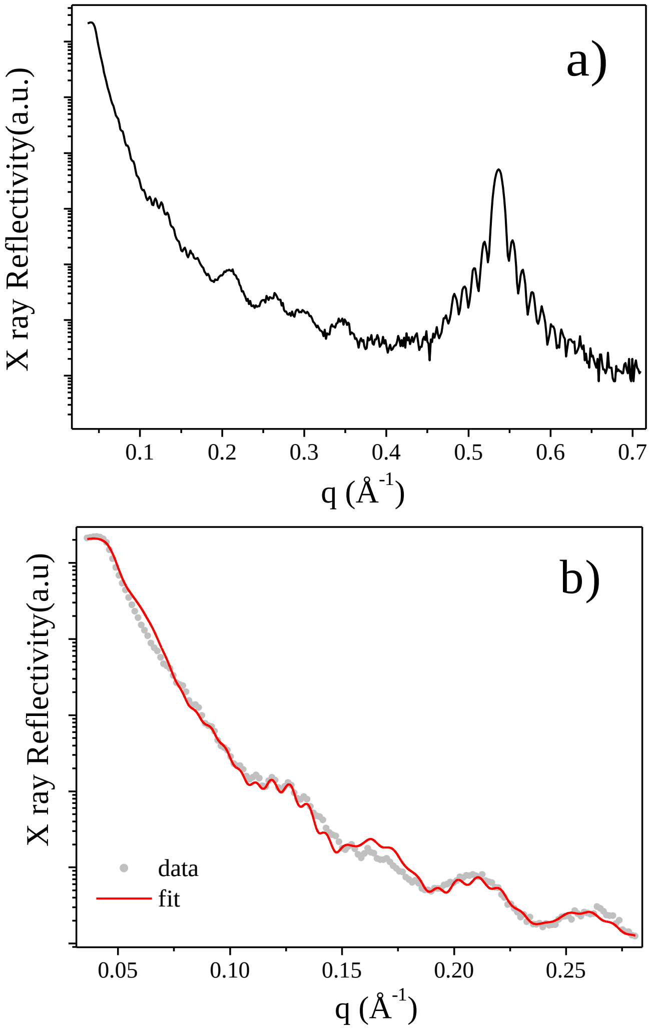

Fig.3.52 X ray reflectivity (a) and refinement (b) for the trilayer: 15nm LCMO/46nm/YBCO/15nmLCMO. The fit to the data is represented by the line.

Fig.3.53 show PNR curves at saturation (H=5500Oe); the magnetic profile obtained from the fit is shown in Fig. 3.54. In this case a large gradient is observed at both YBCO/LCMO interfaces, extending over 60Å inside the LCMO . This result strongly suggests the possibility of charge transfer at the YBCO/LCMO interface.

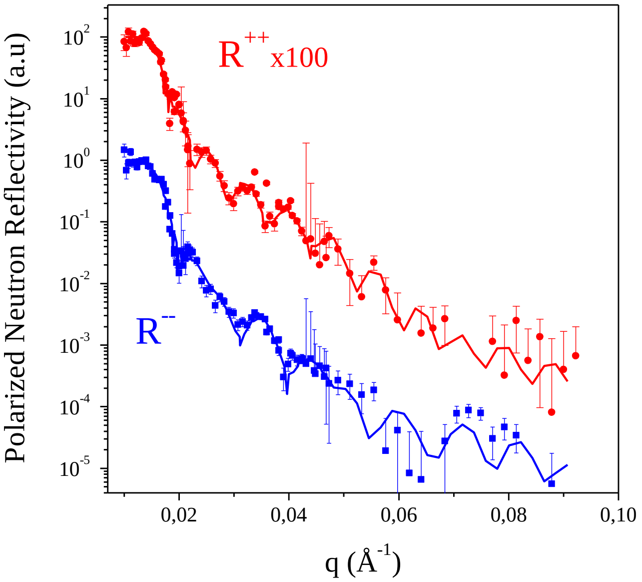

Fig.3.53 PNR data take at H=5500 Oe for the trilayer with 46nm-thick YBCO.

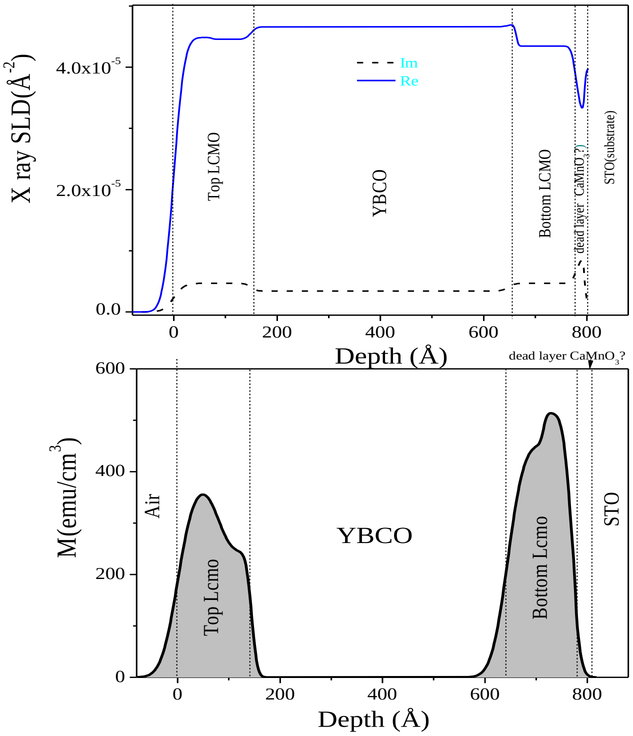

Fig. 3.54. Top: structural profile obtained from the X-ray fit as a function of the depth into the sample. Bottom: magnetic profile obtained from the PNR fit at saturation, for the sample with 46nm-thick YBCO

Several measurements have been carried out at different magnetic fields, retracing the increasing field branch of the hysteresis loop around the coercive field H_C. We first saturated the sample in H=-5500 Oe and then we collected PNR data at: 84, 100, 115, 130,145,160 Oe. The R^{++}, R^{--} and R^{SF} curves at each value of the field are represented, together with the fit, in Fig. 3.55. An overview of the result is summarized by the schematic representation of Fig. 3.56. In contrast to the previous case (thin YBCO spacer) first M_T starts the switches partially up to an angle of 103 degrees, where it remains pinned for a wide part of the hysteresis loop preceding the coercive field. At the same time M_B rotates, curiously *reducing* the misalignment while approaching the coercive field. Once H_C is crossed, both magnetizations undergo a sudden flip in a field range of only 15 Oe. This result clearly shows that a magnetic coupling between M_T and M_B exists, which tends to parallel align the LCMO magnetizations for thick YBCO spacer.

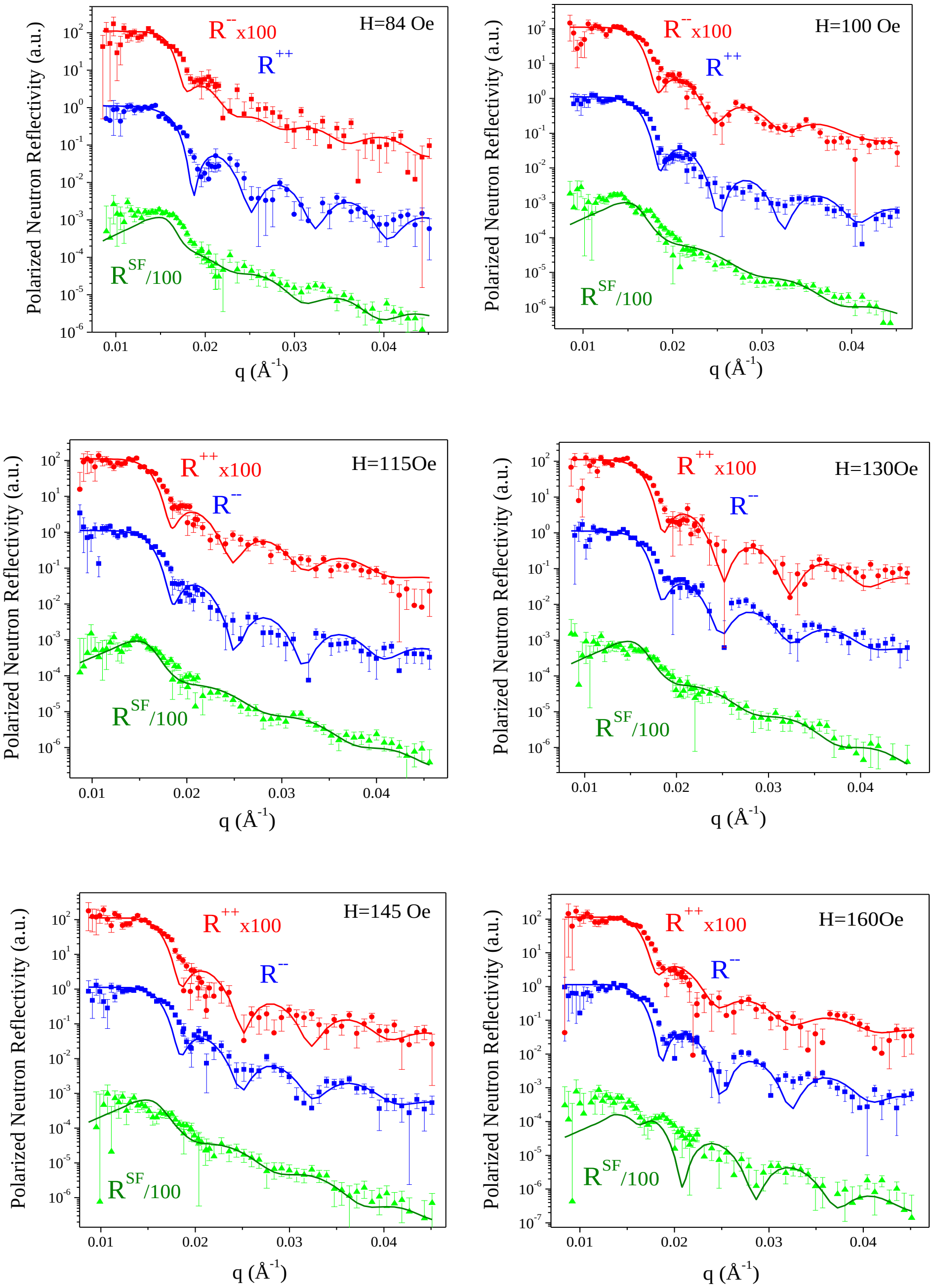

Fig. 3.55. PNR data taken at H=84, 100, 115, 130, 143, 160 Oe. The lines represent the fit to the data.

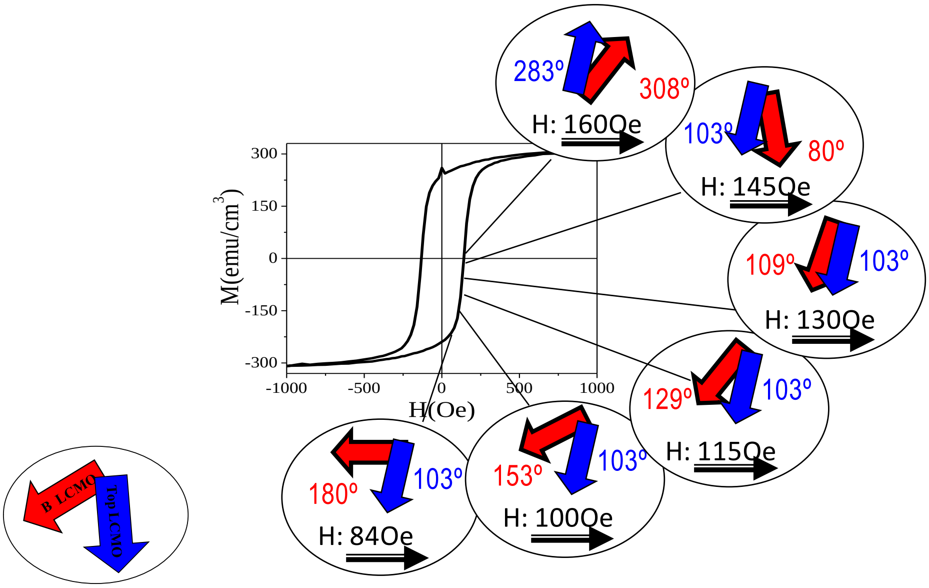

Fig. 3.56. Schematic behavior of the magnetization of each LCMO layer when changing the value of the in-plane magnetic field. The red arrow represents the bottom magnetization while the blue arrow represents the top magnetization.

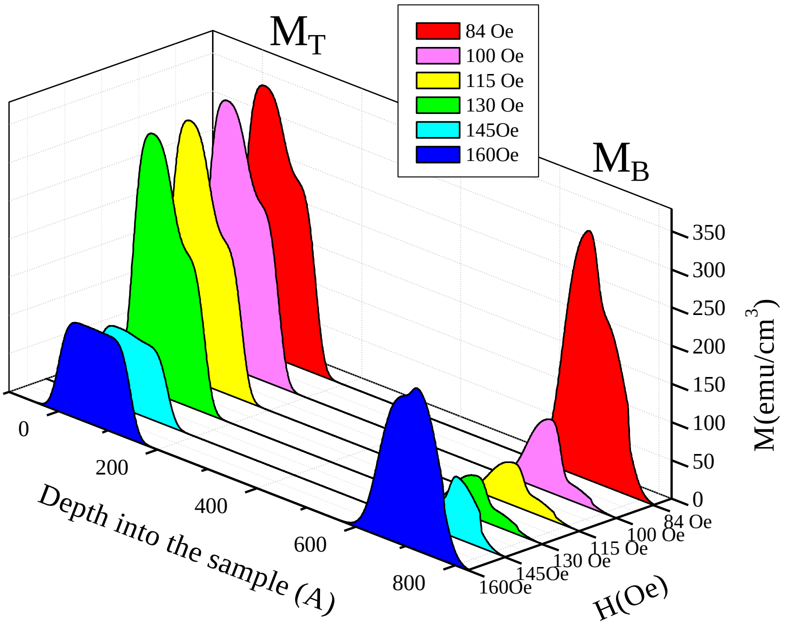

Fig. 3.57. Magnetic depth profile at H=84, 100, 115, 130, 145, 160Oe. The angle of the magnetization is not considered her.

In fact, as shown by magnetometry in section 3.3*b*, bottom and top layer have the same coercivity values. If we look at the magnetic profile (Fig. 3.57), we can see that the field H=84Oe marks the limit of the coherent rotation of the whole M_B. From H=100Oe magnetic domains nucleate considerably reducing the mean magnetic moment of the bottom LCMO; the remaining magnetization rotates coherently. The magnetization of the top layer M_T remains almost unchanged during the field sweep. Magnetic domains nucleate just before the coercivity (which we establish around H=145Oe). Note the strong tendency of M_T and M_B to align parallel during magnetization reversal. This points to the possibility of a magnetostatic (ferromagnetic) coupling triggered by domain structure. This is a very important result because it shows that the magnetostatic coupling between the magnetic domains can be realized in our sample and most important, it is uncorrelated to the magnetoresistance effect since this sample shows the weakest effect.

b) The XMCD experiment

Further evidence of the angular dependence of the magnetization is given by the analysis of hysteresis loops obtained from X-ray magnetic circular dichroism (XMCD) as a function of the applied field. By tuning the X-ray polarization at the resonance energy of a specific electronic transition one can obtain information on the chemical and magnetic state of a particular element. Soft X rays in the energy range of Mn and Cu L-absorption edge, have been used to get element specific hysteresis loops where magnetic reflectivity given by the difference between right and left circularly polarized signal was measured as a function of the applied field. During a dichroism experiment TEY, FY and reflectivity are collected simultaneously. In Fig.3.58 and Fig.3.59 we show XAS and XMCD data as a function of the photon energy taken at the Mn and Cu absorption edge for a trilayer with 18nm-thick YBCO, applying a field H=-500Oe in the plane of the sample along the [100] direction. For all detection modes the XAS data clearly shows the L_{III} and L_{II} edges. The position and shape of the FY and TEY signals agree with those reported in the literature for LCMO and YBCO [49-48], while the reflectivity is strongly dependent on our experimental conditions.

The TEY XMCD data at the right side of Fig.3.59 clearly show a small magnetic moment, reflected by the peak, at the Cu edge. The dichroic signal coming from the Cu L_3-edge has been demonstrated to originate at canted Cu spins of the interfacial CuO_2 layer in the YBCO, antiferromagnetically coupled with the nearest Mn moments of the LCMO [48]. In fact by comparing the XMCD TEY we can see that the peaks in Cu and Mn point to opposite directions. The three different modes appear to be suitable for measuring hysteresis loops, at least at the Mn edge. Nevertheless there are two main reasons for using reflectivity instead of TEY or FY in this kind of experiment. The first is that sweeping a magnetic field has a strong influence on the secondary electrons which are free to move into the sample. These electrons would move on spirals with H-dependent radii, resulting in an odd shape of the TEY hysteresis loop, which makes the identification of the coercive fields almost impossible [49]. The second reason is the much stronger, free of noise, signal obtained from reflectivity with respect to FY at the Mn edge. To get an adequate reflectivity signal from the Cu edge we summed over a large number of subsequent reflectivity loops (up to 80) after setting the energy to the peak position observed in TEY mode.

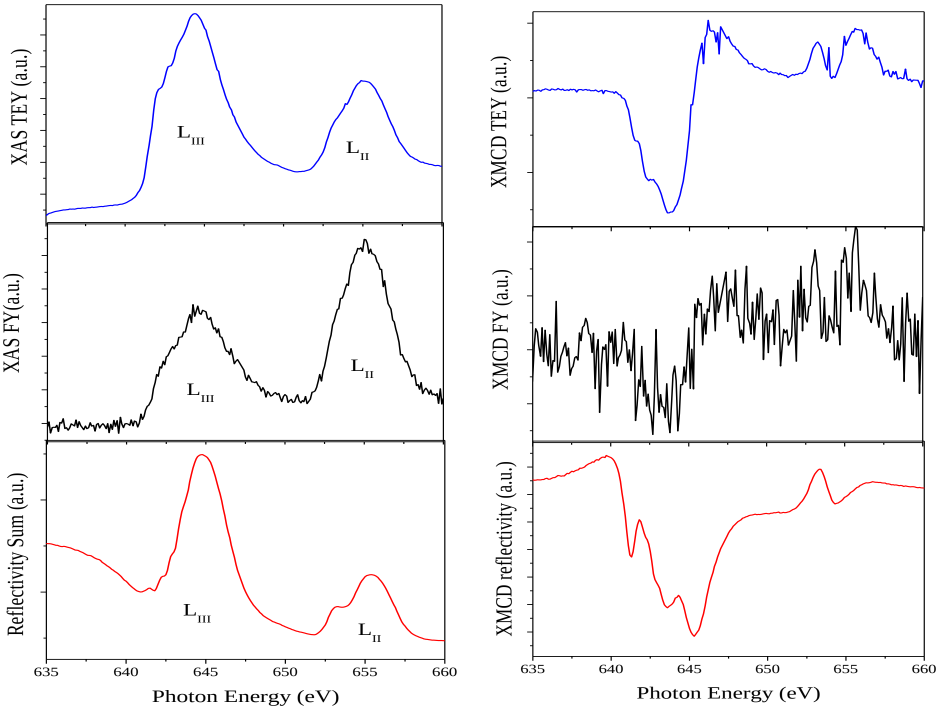

Fig.3.58 XAS (left) and XMCD (left) data, as a function of energy taken in the TEY,FY and reflectivity mode at the L_{III} and L_{II} Mn absorption edge. Experiment was done in a magnetic field H=-500Oe.

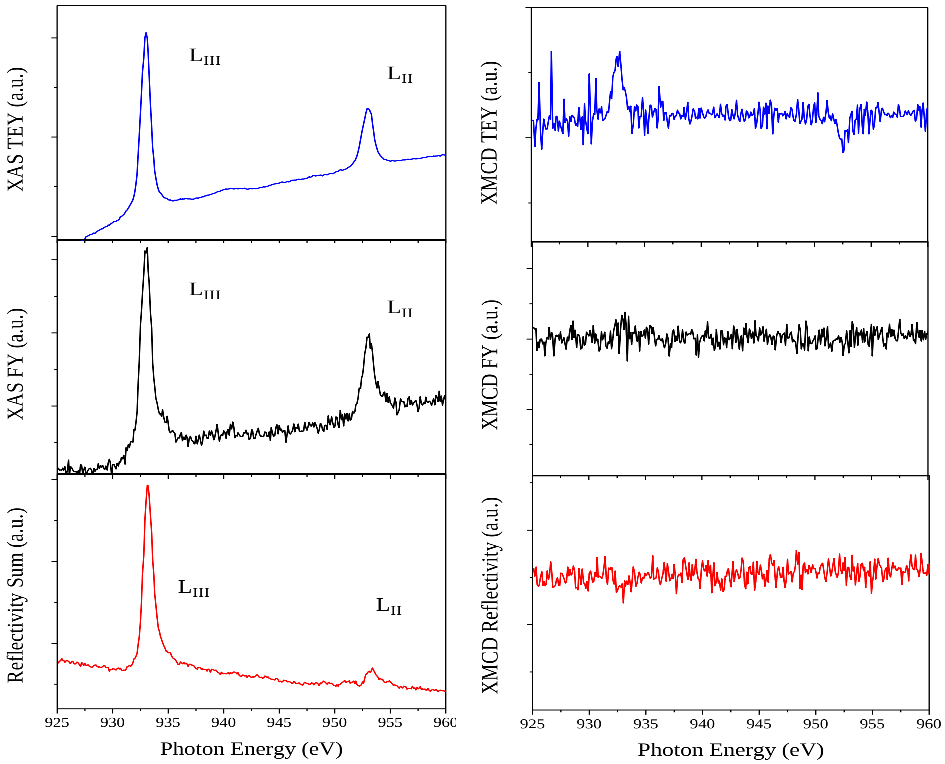

Fig.3.59 XAS (left) and XMCD (left) data, as a function of energy taken in the TEY, FY and reflectivity mode at the L_{III} and L_{II} Cu absorption edge. Experiment was done in a magnetic field H=-500Oe.

Next we discuss the magnetic hysteresis loop obtained in reflectivity mode. In our experiment the energy of the X rays was set at 645.5 eV for the Mn L_3-edge and at 932.5 eV for the Cu L_3-edge with the beam oriented always parallel to the external field and making an angle of 5-10 degrees with the sample surface to ensure deep penetration of the x-ray beam. In Fig.3.60we show hysteresis loops of a trilayer with 7 nm-thick YBCO. We performed two different sets of measurements, with the field applied along [100] and [110] axes, at a temperature of 30K, in the upper part of the superconducting transition. According to the Stoner-Wohlfarth model of magnetization reversal [81], larger coercivity and remanent magnetization (M_R) are in general a signature for magnetic field aligned with the easy axis. This sample represents an extreme limit in the range of YBCO thickness in our experiment, since it shows the largest superconducting spin-switch effect (see section 3.3*b*). Hysteresis loops taken at the Mn L_3-edge [Fig.3.60 top panel] show that magnetization reversal starts at very different fields for the lower and upper interface with YBCO. The bottom LCMO layer switches first and faster probably due to different strain which may lead to different magnitude of anisotropy and/or domain size and distribution.

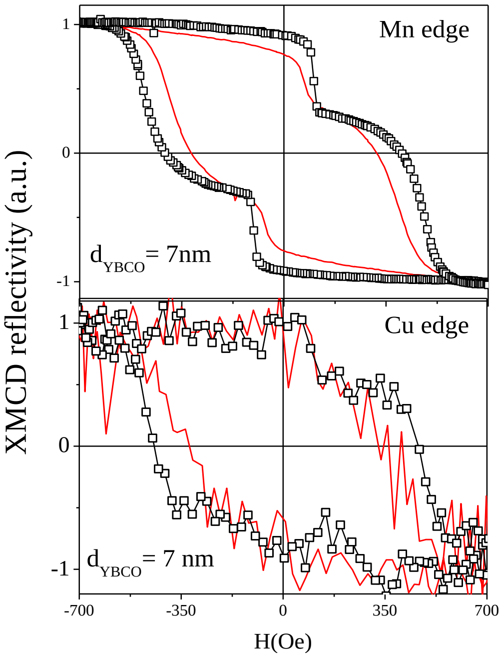

Fig.3.60 Top: X-ray magnetic reflectivity loops taken at the Mn absorption edge for the 7nmYBCO sample. Bottom: magnetic reflectivity loops taken at the Cu absorption edge for the same sample. All the data are taken at 30K applying the field along [100] (line) and [110] (symbols).

The hysteretic behavior of the Cu magnetic moments closely follows the Mn signal. This provides direct evidence that despite the magnetization depression at the interface showed above, the interface remains magnetic. In addition at the interface the magnetic anisotropy is the same as in the bulk sample (easy axis along [110]). We show that the induced magnetic moment in the Cu is present in all the trilayers even for the sample with the thickest YBCO spacing layer (46nm). Here we want to stress that only a qualitative analysis can be made on these kind of measurements since the absolute value of reflectivity does not provide a value for the magnetic moment upon varying the photon energy (around the same absorption edge), the applied field or the incidence angle of the beam. In contrast to the absorption (XAS) spectroscopy, the reflectivity signal is also sensitive to dispersive parameters.

As a result the loops may appear reversed. Nevertheless the relative change of the intensity along the same field sweep is associated to changes in the magnetization orientation giving a qualitative picture of the magnetization reversal process. In some cases it has been observed (see below) that down- and up-sweep branches may cross. The crossing is perfectly symmetric with respect to the sign of the applied field, allowing the identification of the coercive fields. In Fig.3.61 we compare the XMCD hysteresis loops taken at the Mn and Cu edge, for YBCO thickness of 12, 18 and 46 nm. Field was applied along the [100] direction. For clarity, the arrows in every picture indicate the direction of the field sweep.

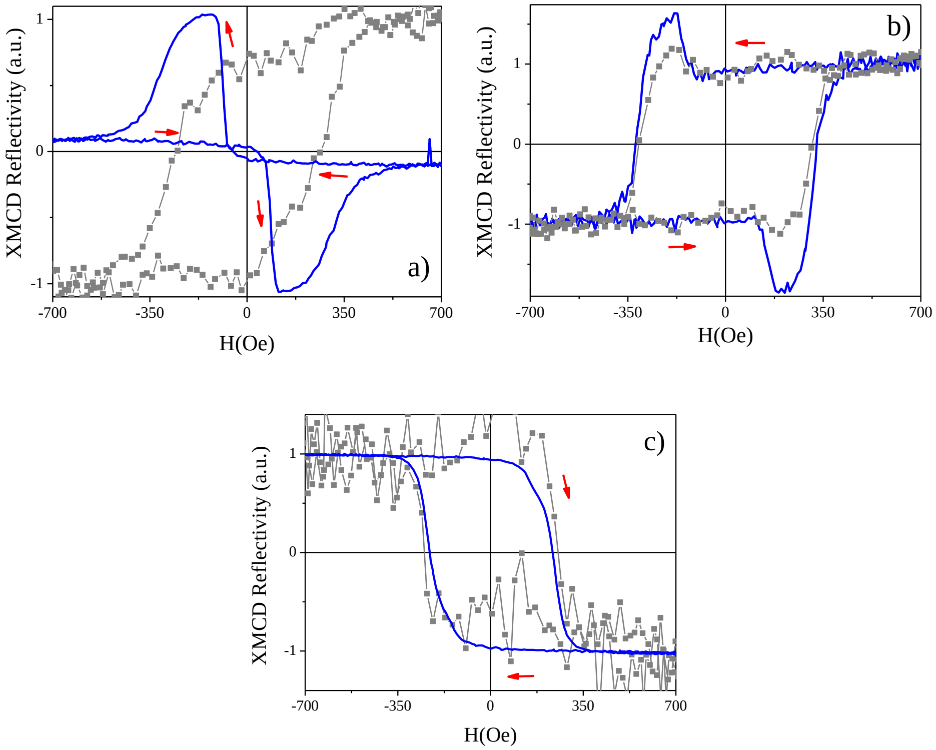

Fig.3.61 Normalized XMCD hysteresis loop taken at the Mn edge (line) and at the Cu edge (symbol) for trilayers with YBCO thickness of a) 12nm, b) 18nm, c) 46nm. The arrows indicated the direction of the field-sweep. The field was applied along the [100] direction. Temperature was T=30K.

Fig.3.62. shows the coercive field for top and bottom LCMO layer extracted by the loops for Mn as a function of the YBCO thickness, assuming that the smaller of the two coercive fields belongs to the bottom LCMO. This picture resembles that one

obtained by conventional magnetometry (see section 3.3*b*) showing that the coercivities merge into the same value when the YBCO spacer is thick enough.

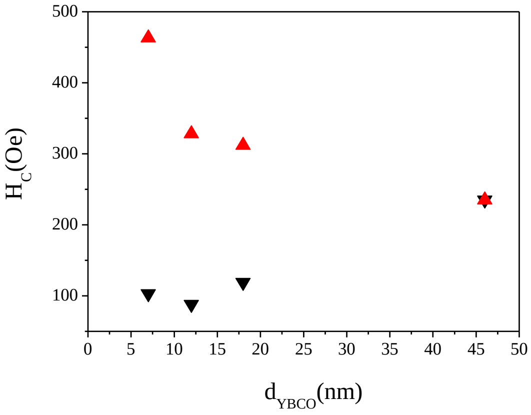

Fig.3.62 Coercive field for top (upward triangle) and bottom (downward triangle) LCMO extracted from the XMCD hysteresis loops as a function of the YBCO thickness.

c) The rotation experiment

The effect of magnetic alignment on superconductivity can be closely tracked by ensuing magnetoresistance signals. Applying magnetic field along the easy axis enables obtaining a wider (magnetic field interval) and better defined AP state. In Fig. 3.63*a* we compare a magnetoresistance curve (blue squares) with the corresponding magnetic hysteresis loop (red circles) of a trilayer with 12-nm-thick (10 unit cells) YBCO. Both resistance and magnetic measurements were acquired at a temperature of 48 K (the zero resistance critical temperature being T_C=47 K) and a resistance drop of R_{min}/R_n~10^{-4}. The different coercivities of top and bottom layers (100 Oe and 300 Oe for bottom and top layers, respectively) allow controlling magnetic alignment of the F layers: the two F layers switch independently and form the AP aligned state over a wide magnetic field range. For magnetic field applied along [110] a clear positive *plateau* can be identified between the two distinct coercive fields of the electrodes (marked dashed lines) where the AP alignment is maintained, clearly pointing to the importance of alignment in the MR phenomenon. When the field is applied along [100] hard axis (Fig. 3.63*b*), the magnetization switches by coherent rotation. This limits the AP alignment to a narrow field range resulting in a single peak located in an intermediate position between the coercive fields. However notice that the MR takes the largest values. Furthermore, small departures of 1-5 degrees of the applied field from the direction of the hard axes result in dips (*not peaks*!) at the coercive field of the bottom layer.

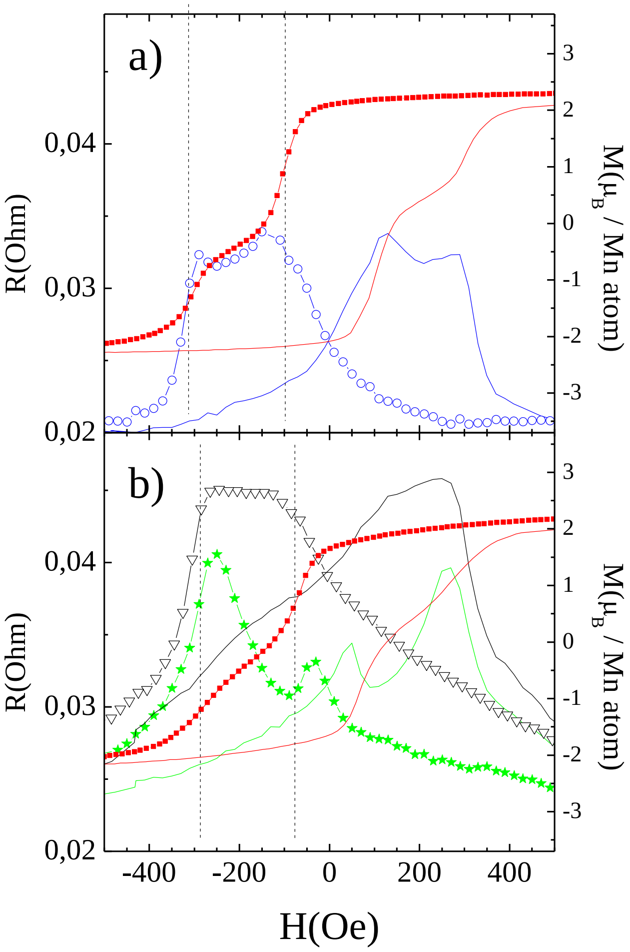

Fig. 3.63 Magnetization hysteresis loops (red squares) and resistivity vs. field (blue circles) for field H applied along (a) [110], and (b) [100] (black triangles) and 3 degrees away, in plane, from [100] (green stars).

This is the experimental situation of the PNR experiment of F where significant domain nucleation was observed in the bottom layer (as the measurement was not done exactly along [100]) while the top layer retained its full magnetic moment. This new feature outlines the different behavior of our oxide system as compared to any previously reported trilayer F/S/F system based on transition metals where, typically, positive MR peaks are observed at coercivity. These positive peaks have been attributed to stray fields generated by P aligned magnetostatically coupled domains. On the other hand, negative MR peaks (dips) at coercivity in systems with perpendicular anisotropy such as Co/Pd/Nb/CoPd, or [Co/Pt](n)/Nb/[Co/Pt](n), have been interpreted in terms of domain wall induced superconductivity[83,84].We propose a new mechanism to explain the MR dips at the coercive field: ferromagnetic coupling between face to face domains in neighboring layers occurs in our samples, as show in the previous section, but the P re-alignment *reduces* MR; positive MR values are determined solely by the extent of the misalignment of the local magnetization of the two F layers. (see below**)**. Fig. 3.64 shows the evolution of the magnetoresistance as a function of the angle between the magnetic field and the [110] axis. Each curve was measured at a fixed angle, continuously changing the in plane direction of the magnetic field every 5 deg. Notice that the shape evolves gradually from a plateau (H at 45 degrees) to an intermediate stage with a dip at the first lowest coercive field and finally to a peak through an abrupt change from 85 to 90 degrees. Fig. 3.65 shows that the plateau found for magnetic field applied along the easy axis is independent on the current-field geometry. We changed the position of the electric contact on the sample to inject the current parallel or perpendicular to the field even when H is applied along [110].

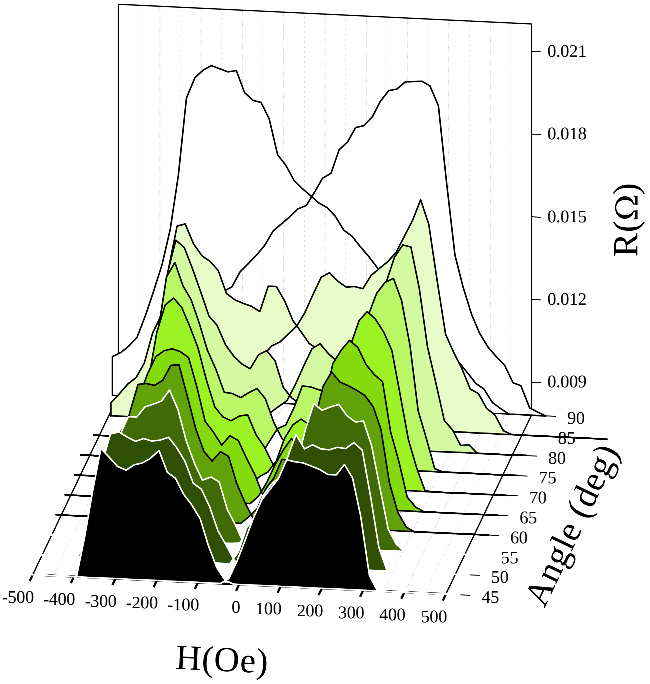

Fig. 3.64 Evolution of the magnetoresistance as a function of the angle between the magnetic field and the [100] crystal axis of the STO.

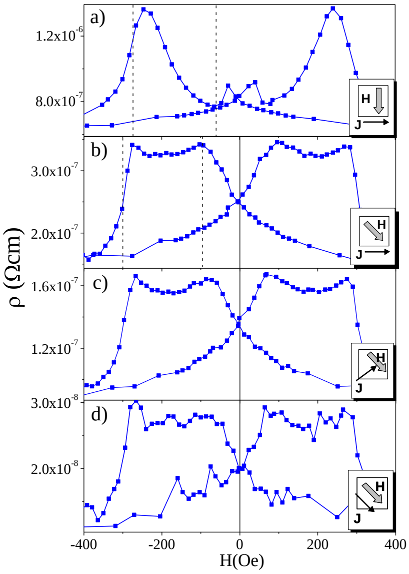

Fig. 3.65 Resistivity vs. field for field H applied along a) [100] 3 degrees away, in plane, b),c),d) along [110] with different current-field geometries.

Fig. 3.66 displays MR measurements for trilayers with 7, 10 and 18 u.c.-thick YBCO. It is worthy pointing out that the plateau found when the field was applied along the [110] direction is clearly present in all the trilayers. Its width and height scales with the thickness of YBCO. In the sample with 7 u.c. of YBCO a minor contribution from stray fields can be the origin of the small peaks at the coercive fields overlapped to the large (over 1000%) plateau of magnetoresistance.

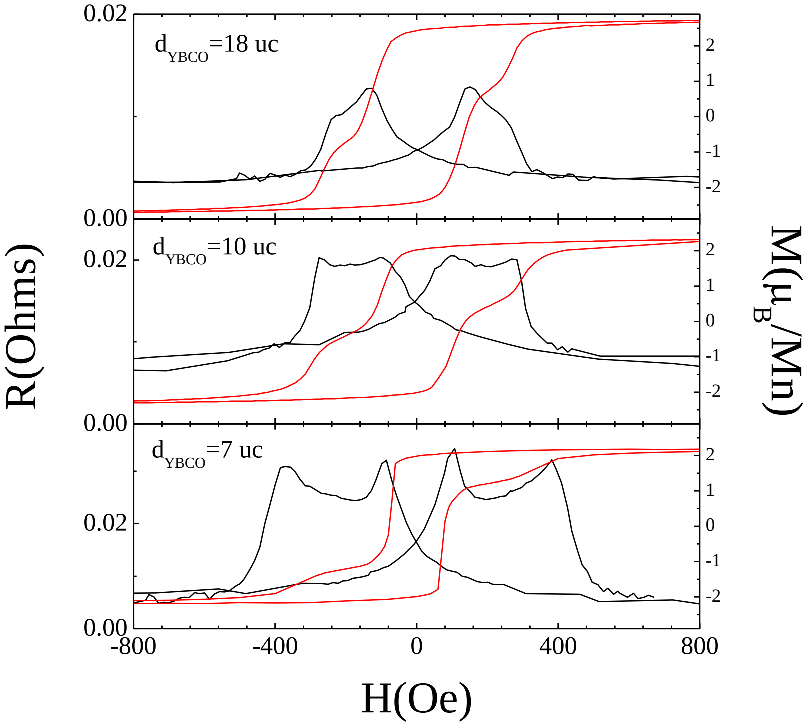

Fig. 3.66 Magnetoresistance measured with field applied along the [110] axis for trilayers with 7, 10 and 18 u.c.-thick YBCO.

Further information about the importance of AP alignment in the MR phenomenon is obtained from an experiment rotating the magnetic field in-plane. Magnetization switching is described in reference to the polar plot of the Stoner-Wohlfarth critical switching curve (CSC) or magnetic astroid [84]. In films with biaxial anisotropy the CSC is an astroid of eight cusps. An example is given in Fig. 3.67. When a magnetic field of magnitude less than the anisotropy field of the film under investigation is applied to the film along its easy axis and then rotated, the magnetization of the film will lag progressively further behind the applied field direction (Fig. 3.67*a*) until the tip of the applied field vector intersects a point on the CSC at the hard axis. At this time the angle of magnetization with field will undergo a large jump and will preceed the magnetic field vector until the astroid is intersected again at the next easy axis (Fig. 3.67*b*). If the sense of rotation is reversed, jumps will be observed when the applied field angle reaches mirror points to the previous in the astroid displaying hysteretic rotation. This is useful to highlight the influence of magnetic alignment on the magnetoresistance.

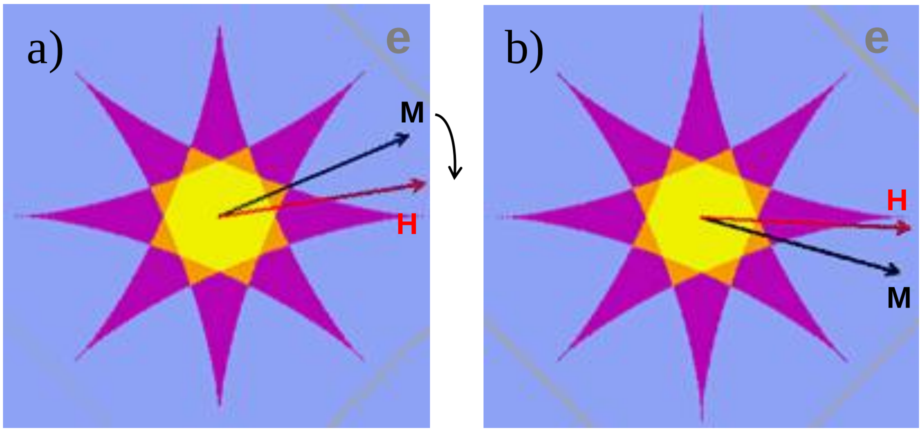

Fig. 3.67 Stoner-Wohlfarth astroids adapted from [84]. The black arrow represents the magnetization direction obtained when the magnetic field (red arrow) approaches a hard axis (a) or has just passed it (b).

The rotation experiment (using a trilayer with 9 nm thick YBCO) was done in a small field: 30 Oe in Fig. 3.68*a*, *b* and *c*, or 150 Oe in Fig. 3.68*d*, either after saturating at a large -10 kOe field, applied at an angle θ (Figs 4 a and b) or after zero field cooling (Fig. 3.68*c* and *d*). The 30 Oe field is well below the anisotropy field of the top layer, so that its magnetization M_T remains in the direction of the saturating field (as shown by neutron reflectivity data) over the whole rotation sequence. On the other hand, the magnetization of the bottom layer M_B of smaller coercivity is more sensitive to the effect of a rotation of the external field. This was shown by the PNR displaying a component of M_B effectively pointing in a direction antiparallel to M_T after applying a small field opposite to saturation. Fig. 3.69 shows a schematic diagram that illustrates this mechanism.

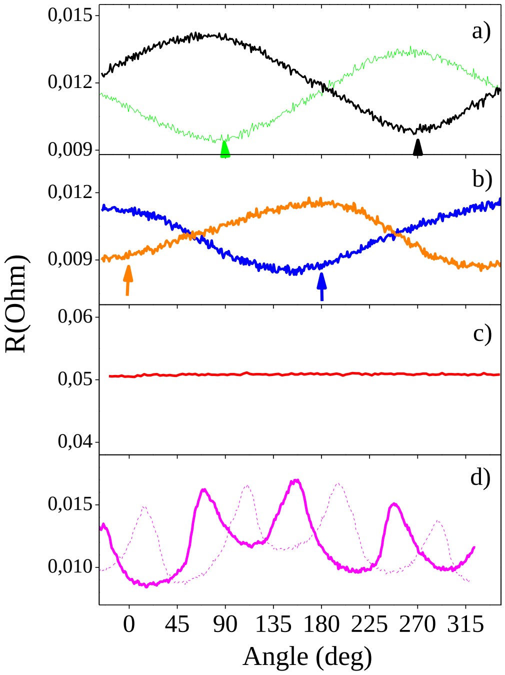

Fig. 3.68 Resistance vs. angle between applied field (+30 Oe) and sample edge after saturating the sample in -10 kOe at an angle of (a) 90 and 270 deg (green and black lines) and (b) 0 and 180 deg (red and blue lines). Resistance vs. angle in applied field of (c): +30 Oe and (d) +150 Oe after zero field cooling. The thick lines are rotations from high angle to low angle; the thin, dashed lines show the reversal.

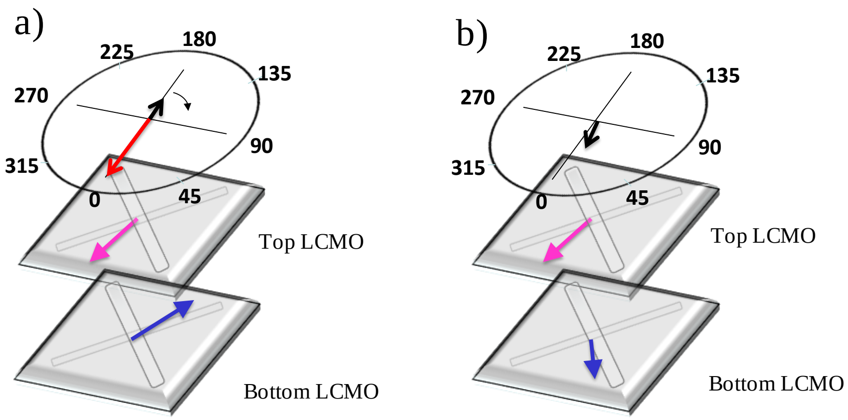

Fig. 3.69 Schematic diagram of the rotation experiment. The situation for H=30Oe is represented a) before starting the rotation and b) after a 180 deg rotation The red arrow represent the saturation field while the black arrow represents the rotating field.

Fig. 3.68*a*. and b. show the results of rotations obtained after saturating at angles θ=0, 90, 180, 270 degrees, indicated with an arrow. Notice that at the angle of saturation MR is at a minimum since the top and bottom layers both point to the direction of the saturating field that establishes the P state. Rotation yields a cosine like MR curve with a 360 degrees rotation angle period. I.e., for a 180º field rotation, the bottom layer has switched to a great extent following the field, while the top layer with a larger anisotropy field keeps pointing to the direction of the saturation field. This indicates that the AP state of the magnetizations of top and bottom ferromagnetic layers is essential in the mechanism of the magnetoresistance. Enhanced stray fields due to magnetic flux closure through the S layer have been proposed to result from magnetostatically coupled domains in the two F layers and have been observed to yield positive MR peaks [85]. However, this mechanism requires similar coercivities of the two F layers and ferromagnetically coupled face to face domains. This possibility can be ruled out in our system, since, as shown by magnetization and PNR, the top layer is not in a domain state at the small 30 Oe field. Moreover, 30 Oe rotation experiments in a sample cooled in zero magnetic field (when both layers end up in the domain state) show no angular modulation of the magnetoresistance (see Fig. 3.68c). This constitutes additional evidence that the angle dependent MR is not caused by stray fields but is due to the magnetic alignment of the domain state in the top and bottom layers. In addition its 360º period shows that also the domain state of the bottom layer is not at the origin of the MR, which according to the biaxial anisotropy would have 4-fold symmetry features in the angular sweeps. Fig. 3.68d, shows the effect of rotation of a 150 Oe field after cooling the sample in zero field. This field modulates the domain state of the top layer (notice that the rotation is hysteretic in up and down field sweeps) and is larger than the saturation field of the bottom layer which can rotate freely. The angle dependent MR tracks the misalignment between magnetizations when the rotating field vector crosses the hard axes, i.e. magnetizations of top and bottom layers are never anti aligned [84]. These results constitute solid evidence of the importance of spin dependent effects as opposed to stray fields in yielding the magnetoresistance phenomena. The P state is established in the direction of saturation and the system keeps memory of it. MR has a maximum at an angle 180 degrees away (opposite direction) independent of the angle of saturation. The system behaves as an angle sensitive magnetic memory with a (fast and low dissipation) sensitive superconducting sensor that can be operated with a small magnetic field. Operation is determined by P or AP magnetization states as in ordinary F/N/F memory elements, but the high resistance state occurs in the AP configuration contrary to ordinary spin switches. What is new here is that biaxial anisotropy yields stable magnetization states in two perpendicular directions (see Fig. 3.68), allowing the design of more complex logic operations.

In summary, we have made use of the modulation of the F/S interplay of by the biaxial magnetic anisotropies to examine the inverse superconducting spin-switch effect found in $YBa_2Cu_3O_7$ / $La_{0.7}Ca_{0.3}MnO_3$. When magnetic field is applied along the easy axes we have found a *plateau*-like (giant) magnetoresistance closely following the field interval over which antiparallel alignment takes place. Resistance measurements along the superconducting transition under a rotating magnetic field show that the response is purely caused by the alignment of the magnetization of the two LCMO electrodes. We have proven that the ISS in this system is exclusively determined by magnetic alignment and is not influenced by the stray fields generated at the domain state of the manganite layers.

3.1 Exchange bias modulated inverse superconducting spin switch in CoO/Co/YBCO/LCMO hybrids

Proximity coupled structures superconductivity is promoted for antiparallel (AP) orientation as a result of the cancellation of the effect of the exchange field over the coherent volume [8,9,86-89]. Resistance decreases when the magnetic configuration is changed from parallel (P) to antiparallel (AP), at temperatures fixed along the resistive transition. On the other hand, a number of reports show a resistance increase when going to the AP alignment, suggesting that superconductivity might be favored in the P state [19,21,54]. The term ”inverse” superconducting spin switch (SSS) has been coined to describe this behavior. A competing interpretation outlines the importance of stray fields, generated in the domain state of the ferromagnet, depressing superconductivity [23,61]. Spin dependent effects are expected to show up as a difference between transport properties of AP and P configurations. On the contrary, ferromagnetic domains at the interface influence superconductivity primarily at coercivity [23,90,91]. For Bloch type domain walls, magnetization rotates out of plane between neighboring domains, generating perpendicular stray fields, which may strongly depress superconductivity. Positive magnetoresistance (MR) peaks are thus expected at coercivity in resistance vs. field, R(H), sweeps. Quite frequently, the AP state is established in a narrow field interval between the different coercivities of top and bottom ferromagnetic layers, often due to different growth properties, thus it becomes a difficult task to distinguish between the two mechanisms. A key step to separate spin dependent transport from the effect of stray fields is to tailor well defined AP states that extend over wide magnetic field intervals, preferably together with sharp magnetization switching. In structures combining transition metal ferromagnets and low-T_c superconductors, this has been accomplished by means of pinning the magnetization of one of the layers via exchange bias in exchange spring structures [61,92]. In these cases, the antiferromagnet (AF) of the AF/F exchange bias structures was produced by *in situ* oxidation of one of the F layers. In this way Steiner and Ziemann [61] and also Stamopoulos *et al* [23] have shown magnetoresistance peaks at the coercive fields originating at stray fields. In heterostructures based on oxide (colossal magnetoresistance) ferromagnets and high-T_c superconductors (cuprates) the situation is more complicated. Such is the case of $La_{0.7}Ca_{0.3}MnO_3$ (LCMO) / $YBa_2Cu_3O_{7-\delta}$ (YBCO) / $La_{0.7}Ca_{0.3}MnO_3$ (LCMO) trilayers. The YBCO/LCMO interface displays interesting F/S interplay phenomena [23,35,47,93-95,96]. Natural oxidation cannot be used to produce an AF layer. Nevertheless, extrapolating the results obtained for transition metal ferromagnets and low-T_C superconductors to this system should be taken carefully. This is because the high spin polarization of the manganites, along with the *d*-wave pairing symmetry of cuprates, point to a stronger weight of spin dependent effects in transport compared to transition metal structures.

Here we examine a Co/YBCO/LCMO inverse superconducting spin switch. We exploit the natural oxidation of cobalt (Co) films to produce CoO/Co AF/F double layers that exhibit pronounced exchange bias, modifying the coercive field of the Co by several thousand oersteds. The CoO/Co layer also has a pronounced training effect, whereby the first magnetic hysteresis loop, after cooling from room temperature in a high magnetic field, has much higher coercive fields and sharper magnetization switching, and so differs considerably from the subsequent ones [98-102]. Measuring resistance vs. field sweeps at fixed temperatures along the superconducting transition, we find two distinct features. Positive MR peaks at the coercive fields of both the Co and the manganite can be ascribed to the effect of stray fields in all samples, whereas in samples with freshly deposited Co we observe a well defined MR plateau extending between the coercive fields of the LCMO and Co, determined by the AP alignment and probably related to spin dependent transport. After Co deposition, the cuprate at the interface shows a progressive deterioration (most likely a de-oxygenation) until superconductivity completely disappears after a few weeks of exposure to the ambient. Nevertheless, in an intermediate stage, after a few days of depositing the Co, we can still observe a superconducting transition, and the characteristic magnetoresistance peaks at the coercive fields of the Co and LCMO, but without the magnetoresistance plateau between them. We argue that the process deteriorating superconductivity also breaks the electronic coupling between ferromagnetic and superconducting layers at their interface. Consequently also the spin dependent scattering process at the interface is impeded that would give rise to the magnetoresistance plateau.

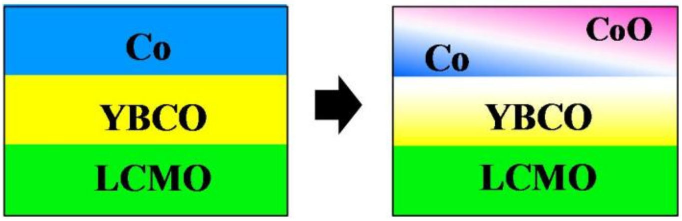

Fig.3.70. The LCMO/YBCO/Co trilayer reacts both with the oxygen of the atmosphere and the YBCO.

We extract the conclusion that while stray fields certainly cause positive magnetoresistance peaks in inverse superconducting spin switches, an additional spin dependent mechanism is also present, causing an MR plateau in fresh samples. In the experimental section we give details of sample preparation and measurement conditions. Then we present results on the growth of Co on YBCO and describe a deterioration of the superconducting YBCO in contact with the Co layer, manifested by structural and transport properties shown by combined x-ray diffraction, temperature dependent resistivity and magnetization measurements. Then we present magnetoresistance data on LCMO/YBCO and YBCO/Co bilayers, which exhibit MR peaks at coercivity. Next we describe the LCMO/YBCO/Co trilayer that shows an MR plateau between coercivities, along with the corresponding magnetization hysteresis loops showing exchange bias and training effects. Then we study the MR of the same trilayer, recorded over time, showing a deterioration of the YBCO layer. We discuss the results, focusing on the possible mechanisms giving rise to the magnetoresistance, in terms of stray fields (MR peaks) and spin dependent transport (MR plateau).

Experimental set up: Samples of LCMO and YBCO thin films were grown on [100] cut, polished SrTiO3 (STO) substrates. Temperature dependent magnetoresistance was measured in the current in plane (CIP) geometry, with four contact pads in the four corners of the 5 $x5mm^2$ square samples. The samples presented here have 15 nm thick (40 u.c.) ferromagnetic LCMO electrodes. The plane of the film was aligned, utilizing the sensitive field dependence of the resistivity in the superconducting state, parallel to the applied 10 kOe magnetic field to approx. 0.05 degrees with the help of a rotator. The magnetic field, perpendicular to the current, was swept between ±10 kOe at fixed temperatures along the resistive transition, above and below the superconducting onset temperature. When MR is expressed in terms of a per cent, it is calculated as $MR\% = (R_{max} - R_{min})/R_{min}\ x100$, where R_{max} is the maximum resistance value while R_{min} is the minimum value, between the MR peak and the high field vortex background, reached typically at a few thousand Oe. For heterostructures containing Co, 12 nm thick Co films were deposited in a different vacuum chamber using DC magnetron sputtering in argon. Typically, no more than 4 hours elapsed, with the sample in air, between terminating the oxide thin film deposition and commencing the metal deposition. After Co deposition, the chamber was backfilled with one atmosphere of O_2 to ensure a uniform growth of naturally oxidized CoO thin film on top of the Co. Immediately after Co deposition, the samples were transferred to the magnetoresistance setup, typically with delays not exceeding 2 hours between terminating the Co deposition and cooling the sample below 100 K. After the magnetoresistance measurements, the magnetization was measured, again with as little delay as possible (2 hours, typically). Finally, samples were characterized by X-ray reflectometry and diffraction. To this purpose, θ-2θ scans were performed on a 4-circle Bruker D8 diffractometer using Cu Kα radiation. Throughout the manuscript, fresh stage refers to the Co-containing samples and corresponding measurements taken after Co deposition (within 2 days), intermediate stage refers to measurements taken after approx. two weeks, whereas reacted stage refers to measurements taken after at least two months have elapsed.

The main focus of this study is the magnetoresistance of the LCMO/YBCO/Co trilayer. We first present structural and magnetic characterization of the trilayer, highlighting the notable changes over time. Then we show the magnetoresistance of various bilayers, as they can be considered the constituent parts of a trilayer, although with the caveat that in a trilayer the two F electrodes might be coupled magnetostatically. Finally, we return to the trilayer and present its magnetoresistance and magnetization both immediately after deposition and after two weeks of aging.

a) Growth of Co on YBCO

We studied a STO/LCMO/YBCO/Co trilayer structure (where the STO indicates the substrate). X-ray diffraction and low angle reflectivity provide structural information of the films, presented in Fig.3.71. The top panel shows the low angle X-ray reflectivity signal with the characteristic low angle oscillations of thin films. At 2θ ~7.5 deg, the YBCO (001) reflection is clearly seen in the fresh stage (thick, black), but is absent in the reacted stage (thin, red). In the bottom panel, between 45 and 49 degrees in 2θ the substrate STO (002) and the LCMO *Pnma* (040) reflections are well identified, and do not show appreciable change over time. At 2*θ* ~37 deg, for the fresh stage the YBCO (005) peak is well identified, but in the reacted stage it is missing. Co deposited directly upon YBCO apparently reacts slowly at the interface. Our structural data indicate that the YBCO structure is completely destroyed by in situ reaction with the Co. Probably, the Co extracts oxygen from the YBCO to form CoO on the YBCO side as well, similar to the other side of the Co film open to air.

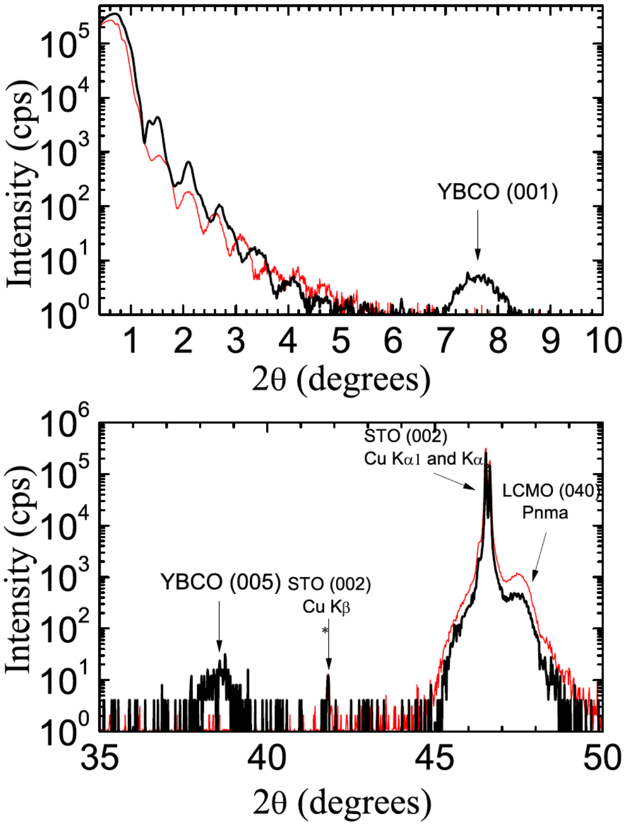

Fig.3.71. STO//LCMO/YBCO/Co sample in the fresh stage (thick, black line), and reacted stage (thin, red line). (Top): low angle reflectivity, the YBCO (001) diffraction is indicated, present only in the fresh stage. (Bottom): Bragg diffraction peaks, the YBCO (005) peak is indicated, present only in the fresh stage.

Magnetization provides a measure of the changes of the amount of metallic Co over time. Magnetization vs. temperature of the STO/YBCO/Co sample is presented in the top panel of Fig. 3.72 . The fresh stage (thick black curve) exhibits an upturn of the magnetization below *Tc*~50 K, characteristic of these ferromagnetic-superconducting thin film samples in the superconducting state, referred to as paramagnetic Meissner-effect [39]. The Curie temperature of the LCMO is ~200 K. Above 200 K the high magnetization is due to the Co layer; as Co has a much higher Curie-temperature, its contribution to the M(T) of the sample is largely constant in the temperature window of the figure. In the reacted stage (thin red curve) the contribution from the LCMO is unchanged. However, the low temperature upturn, related to superconducting YBCO, is missing and the magnetization of the Co is reduced by ~15%. This indicates that approx. 15% of the Co turned into CoO during the two months between the two measurements, with the necessary oxygen taken both from the air and the YBCO.

Temperature dependent resistance (Fig. 3.72 bottom panel) provides an indication of the quality of the YBCO sample, via the overall resistance value and the superconducting tran- sition temperature, T_{onset}. The latter indicates a progressive deterioration of the YBCO, it becomes lower with time, and is finally completely suppressed. Simultaneously, the normal state resistance also increases with time. The zero field R(T) in the fresh stage (thick, black curve) shows a high T_{onset} ~76 K and low normal state resistance that increases linearly with temperature, typical of high quality YBCO thin films. The onset temperature is reduced due to proximity to two F layers [17,105]. In the intermediate stage (thick, blue, dashed curve) T_{onset} is suppressed to 55 K, the transition is broadened, completed only at 10 K, with a large step in mid-transition. The normal state resistance is also increased, compared to the fresh stage, but still varies linearly with temperature. Finally, in the reacted stage (thin, red curve) the R(T) shows only the characteristic metal-insulator transition behavior of LCMO, with a peak at T_{Curie} ~220 K. The normal state resistance also increases drastically, as both the effective Co and YBCO conductance channel widths decrease or disappear.

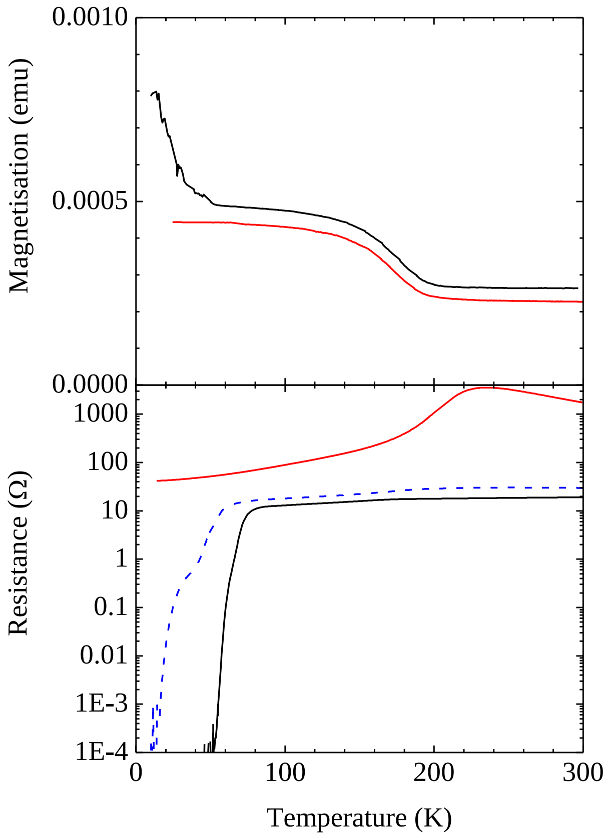

Fig. 3.72. (Top) Magnetization vs. temperature of the STO/LCMO/YBCO/Co trilayer sample in the fresh (thick, black line) and reacted stage (thin, red line). (Bottom) Resistance vs. temperature without applied field in the fresh (thick, black line), intermediate stage (thick, dashed, blue line) and reacted stage (red line).

b) Bilayers

Bilayers did not exhibit the large positive magnetoresistance peaks shown by trilayers with the same YBCO thickness, with either layer sequence STO/YBCO/LCMO, such that the YBCO was grown below the LCMO, or with layer sequence STO/LCMO/YBCO, such that the YBCO was grown on top of the LCMO, nor with layer sequence STO/YBCO/Co. In Fig. 3.73 we present the magnetoresistance of three different manganite-cuprate bilayers (panels on the left), exhibiting representative magnetoresistance behavior. The panels on the right show the corresponding temperature dependent zero field resistance curves for each sample, illustrating that for YBCO thickness greater than approx. 10 nm the critical temperature is not suppressed by the presence of the ferromagnetic layer. The panels on the top present transport data of a bilayer with the LCMO beneath the YBCO (STO/LCMO[15nm]/YBCO[12nm]). This is the bilayer structure (not the SAME bilayer though) that forms the basis of the trilayer structure studied in the preceding and next sections. The R(H) was recorded at T=56 K, a temperature where the resistance is reduced compared to the normal state value just above the T_{onset} as R_{min}/R_n~ 10^{-4}. The zero field resistance shows that T_{onset}~89 K is close to the bulk value. At the coercive field ($H^F{}_C$ ~60 Oe) a small MR peak of approx. 10-20% is seen. Both the height of the MR peak and the coercive field are temperature dependent, though. The coercive field of manganite thin films increases at low temperature slowly, whereas the MR peak increases from 0 at T_{onset} to the 20% seen at the lowest temperature with measurable non-zero resistance. It is worth emphasizing that these magnetoresistance values are much smaller than the values found in STO/LCMO/YBCO/LCMO trilayers with similar thickness of the individual layers, for which MR may take values in excess of 1000%. This small magnetoresistance is probably due to the effect of stray fields generated at the domain state of the ferromagnet. Domain structure in this sample geometry may be different than in bilayers with the YBCO underneath the LCMO and this is probably related to a small interface disorder. The smooth increase of the resistance at high magnetic field results from vortex dissipation. These vortices are perpendicular to the layers and are due to a small misalignment of the applied field out of the plane of the film. The middle panels show data of a bilayer with the LCMO on top of the YBCO (STO/YBCO[5nm]/LCMO[15nm]) at T=30 K, below T_{onset}~67 K, with R_{min}/R_n~10^{-4} . It exhibits a small MR peak, at most 20%, at $H^F{}_C$~340 Oe. The bottom panels show data of a bilayer with the LCMO on top of thicker YBCO (STO/ YBCO[12nm]/LCMO[15nm]) at T=69 K, below T_{onset}~86 K, with R_{min}/R_n~ 10^{-4}. The salient feature of this data is the lack of positive MR peaks at the coercive field of the LCMO, at $H^F{}_C$ ~200 Oe. The absence of positive MR peaks points to a limited effect of stray fields for this layer sequence. This is most likely related to the atomically flat interfaces shown by electron microscopy observations and low angle X-ray refinement in previous reports [105,106].

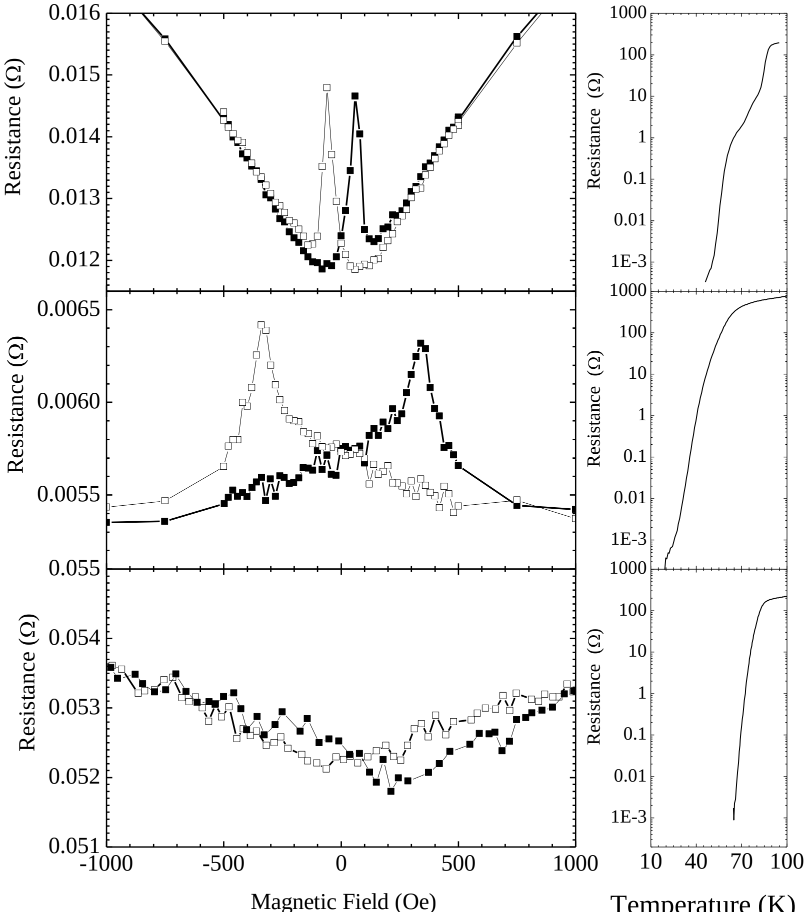

Fig. 3.73: Temperature dependent resistance around the superconducting onset transition in H=0 (panels on the right) and magnetoresistance below the onset, with R_{min}/R_n~ 10−4; the magnetic field is swept up (full symbols) and down (open symbols) (panels on left). (Top) bilayer (T=56 K): STO/LCMO[15nm]/YBCO[12nm] with positive MR peaks at H^F_C~ ±60 Oe. (Middle) bilayer (T=30 K): STO/YBCO[5nm]/LCMO[15nm] with positive MR peaks at H^F_C ~ ±340 Oe. (Bottom) bilayer (T=69 K): STO/YBCO[12nm]/LCMO[15nm] with no MR peaks at H^F_C ~ ±200 Oe.

We next present the magnetoresistance of a YBCO/Co bilayer (STO/YBCO[12nm]/Co[12nm]), at T=79 K, with R_{min}/R_n~ 10^{-3}, cooled in H=+40 kOe, in Fig. 3.74. The Co thin film has rather high coercive field, increasing with lower temperature. The magnetoresistance exhibits sharp positive peaks, up to 50% at the lowest temperatures, at the coercive field of the Co. As the Co film is exposed to air, it develops an intentional antiferromagnetic CoO oxide layer. This layer has been shown to be 2-3 nm thick from x-ray reflectivity experiments [98].

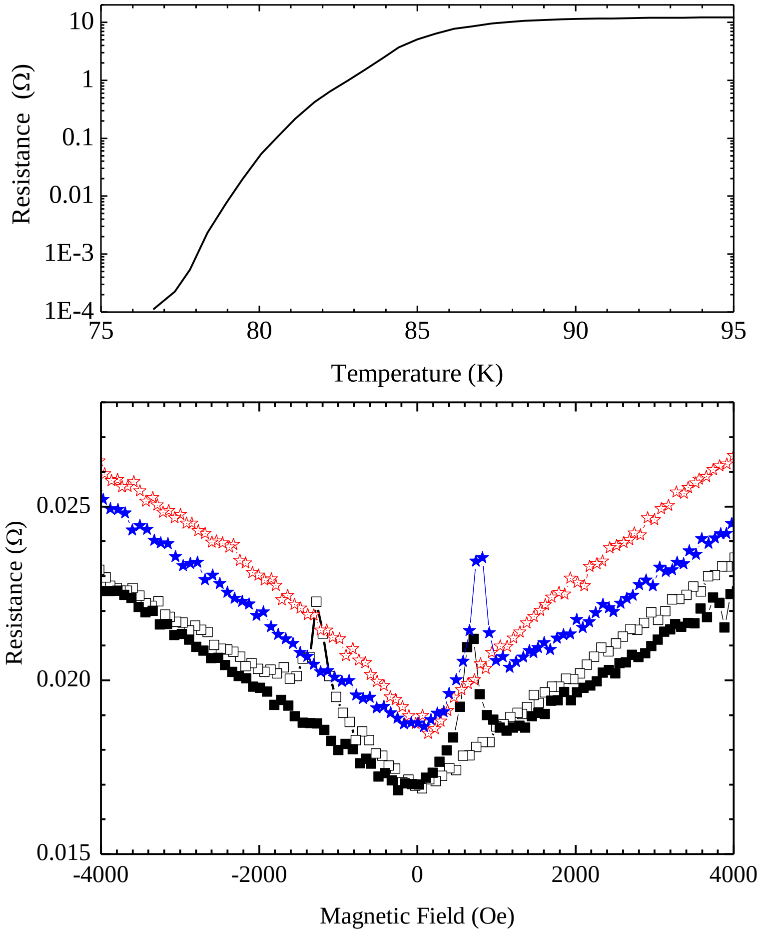

Fig. 3.74. Co coated YBCO film, STO/YBCO[12nm]/Co[12nm], (Top) temperature dependent resistance around the superconducting onset transition in H=0 and (Bottom) magnetoresistance below T_{onset}=79 K with R_{min}/R_n~10^{-3}, cooled in H=+40 kOe. The magnetic field was first swept down from +40 kOe to -10 kOe (red, open stars), then up to +10 kOe (blue, full stars). After several training cycles between ±10 kOe, the field was swept up (black, full squares) and down (black, open squares).

We studied the typical temperature dependent coercive field, exchange bias and training effect on samples of Co deposited on STO, (not shown). CoO is an antiferromagnet and the Co/CoO bilayer is exchange biased [98]. The Co/CoO bilayer also exhibits a pronounced training effect, whereby after cooling from room temperature the first magnetic field sweep has a very high coercive field, with sharp magnetization switching [101,107]. For the YBCO/Co sample, this untrained field sweep down from +40 kOe to -10 kOe gives a barely visible positive MR peak at

H^F_C ~2300 Oe (red, open stars). This is probably related to a domain nucleation process with all in plane magnetization components (see below). The subsequent field sweep from -10 kOe to +10 kOe has a pronounced positive MR peak at H^F_C ~780 Oe (blue stars). After several training cycles between ±10 kOe, the field was swept up (black, full squares) and down (black, open squares) with positive MR peaks at reduced coercive fields: H^F_C ~-1300 Oe and H^F_C ~690 Oe. The top panel of Fig. 3.74 shows the temperature dependent resistance of the YBCO/Co bilayer, in zero external magnetic field. This measurement was performed within 1 day of depositing the Co. T_{onset}~86 K of the YBCO is practically not affected by the subsequent ferromagnetic Co layer.

c) Trilayers

The main focus of this paper is the magnetoresistance of a LCMO/YBCO/Co trilayer immediately after Co deposition: in the fresh stage. We also present magnetization and magnetoresistance of the same sample after two weeks in air: in the intermediate stage. The temperature dependence of the superconducting transition in both fresh and intermediate stages are shown in Fig. 3.72.

The top panel of Fig.3.75 shows the magnetization hysteresis loops of the trilayer (STO/LCMO[15nm]/YBCO[12nm]/Co[12nm]), at T=55 K in the fresh stage. The red, open stars represent, after cooling in H=+10 kOe, the first sweep of the magnetic field to H=-10 kOe (untrained), while the subsequent sweep back up to H=+10 kOe is shown by the blue, full stars. The black squares show a hysteresis loop at the same temperature after many cycles (trained). The sharp switching of the Co in the untrained loop at a high coercive field, H^F_C~-2600 Oe is notable. Similarly on the next up-sweep, the switching is still sharp at a somewhat elevated coercive field H^F_C~+750 Oe, compared to the fully trained hysteresis loop with coercive fields of approx. -1200 Oe and +600 Oe and more rounded switching of the Co magnetization. The magnetization of the LCMO layer switches at H^F_C~±45 Oe, independent of the training of the Co. This asymmetry of the Co switching has been reported to result from different magnetization reversal mechanisms in the first and subsequent switches [99]. The first abrupt reversal is controlled by domain nucleation, while the more rounded subsequent reversals are due to magnetization rotation [101,102,107]. Magnetic Force Microscopy (MFM) observations show the micron size domain structure appearing after the first magnetization reversal. Once formed, the ferromagnetic domains survive even at very large fields and cannot be erased by the application of a magnetic field in the direction of the cooling field. The origin of the large exchange bias is the coupling of the ferromagnetic domains to a large number of uncompensated moments at the boundaries between ten nanometer size antiferromagnetic domains, given their difference in size [108].

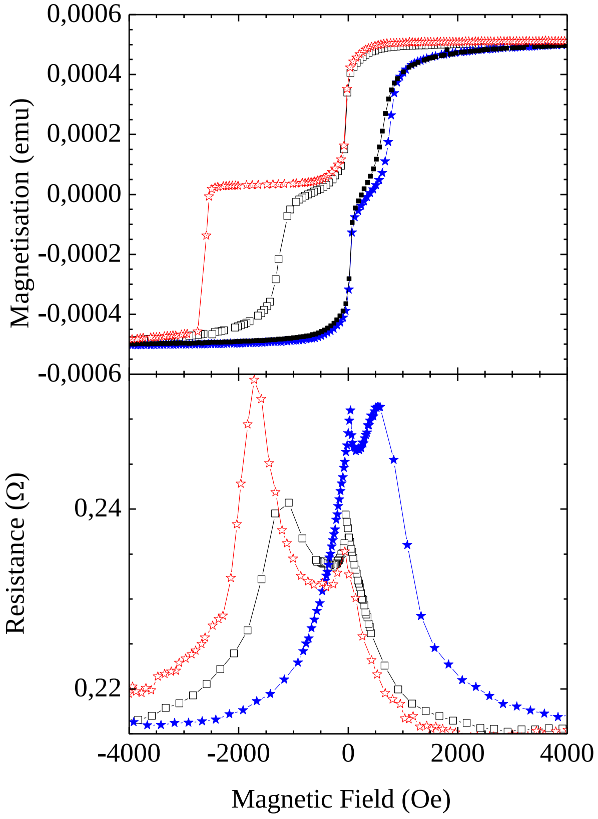

Fig.3.75. (Top) Magnetization hysteresis loops of the trilayer (STO/LCMO[15nm]/YBCO [12nm]/Co[12nm]) in the fresh stage, at T=55 K. The red, open stars show the first sweep down to -10 kOe after cooling in +10 kOe (untrained), the blue, full stars show the subsequent up sweep. The black squares show a hysteresis loop at the same temperature after many cycles (trained). (Bottom) Magnetoresistance of the same trilayer at T=52 K, $R_{min}/R_n \sim 10^{-2}$. The red open stars show the very first sweep, with magnetic field decreasing from +50 kOe. The blue full, stars show the subsequent sweep of the magnetic field up, from -10 kOe to +10 kOe. The black squares show the second sweep down of the magnetic field.

When the magnetization of the ferromagnet is reversed, some of the interfacial uncompensated moments will change their orientation, depending on their size and orientation with respect to the AF easy axis. I.e., not all magnetization vectors rotate back to their initial position so that the average AF interfacial magnetization is directed away from the cooling field at an angle that may be as large as 21º. This creates a torque on ferromagnetic spins and triggers the magnetization rotation mechanism. For the thickness of the LCMO (15nm) and Co (12 nm) chosen and their saturation magnetizations (3.6 and 3.8 μ_B per magnetic atom, respectively) their total magnetic moments are rather similar as indicated by the level of the plateau near M=0. The magnetic moments of the two ferromagnets are aligned antiparallel in the field range between the coercive fields of the LCMO and Co, that is, in the region of the plateau. In this field range, neither the LCMO, nor the Co magnetization changes, there are no domain wall movements. The very first hysteresis loop after cooling in a large field provides a very broad plateau. This offers us an experimental situation where any effects related to the magnetization switching at the coercive field can be decoupled from effects due to AP alignment of the magnetization. The bottom panel of Fig.3.75 displays the magnetoresistance of the trilayer at T=52 K and a resistance drop of R_{min}/R_n» 10^{-2} in the fresh stage. The red, open stars show the very first sweep, with magnetic field decreasing from +50 kOe (the field in which the sample was cooled down to 52 K). The untrained hysteresis loop has a reduced coercive field compared to the magnetic hysteresis loop at comparable temperature. In this experiment, the sample had to be realigned at 52 K again to make it parallel to the field, as the rotator may move approximately half a degree on temperature cycling. The realignment involves rotating the sample in the H=50 kOe field by as much as 10*o*, a process that is detrimental to the above described mechanism of F-AF domain coupling. There are two large positive MR peaks corresponding to the switching of the LCMO and Co at approx. -40 Oe and -1750 Oe, respectively. The blue, full stars represent the subsequent sweep of the magnetic field up, with the MR peaks at approx. +40 Oe and +550 Oe. Finally, the black squares show the second sweep down of the magnetic field. The Co is now trained, with the MR peaks at approx. -40 Oe for LCMO and at a reduced coercive field of approx. -1100 Oe for the Co. The LCMO has a coercive field of approx. ±40 Oe, independent of the training and exchange bias of the Co. The coercive fields of the Co (LCMO) are marked by broad (sharp) peaks in the magnetoresistance. Crucially, between the two coercive fields of the respective ferromagnetic layers, the resistance remains considerably higher than the background level, even in the case of the black curve, where the Co and the LCMO MR peaks are farthest separated. This is the sough after AP plateau! The size of the MR plateau presented in Fig.3.75 is only approx. 30% because the data was taken closer to the resistive onset, at R_{min}/R_n~ 10^{-2}. When the temperature is reduced to R_{min}/R_n~ 10^{-4}, the MR increases to above 100% exponentially with decreasing R_{min}/R_n, similar to LCMO/YBCO/LCMO trilayers [109] (not shown). Next, we contrast the magnetoresistance of the fresh and intermediate stages of the LCMO/YBCO/Co trilayer. We observed drastic changes, related to the deterioration of the YBCO, detailed in the first section. As Fig. 3.76 shows, the magnetoresistance displays sharp peaks at the coercive fields of the ferromagnetic layers. However, the elevated resistance between them, the AP plateau, seen in the fresh stage of Fig.3.75, is completely absent.

As Fig. 3.72 demonstrates, in the intermediate stage the superconducting onset is drastically reduced and even displays a step around 35 K. The bottom panel of Fig. 3.76 shows the magnetoresistance of the intermediate stage trilayer sample at 25 K with R_{min}/R_n~ 10^{-3}. At the coercive fields of Co and LCMO, the magnetoresistance has peaks of approx. 10% that are sharper than in the fresh stage. The red, open stars represent the untrained sweep, recorded after cooling with +50 kOe parallel to the film, here the Co peak is at H^F_C~- 4000 Oe. The coercive field of the untrained sweep is much larger than in the other figures due to the reduced temperature. In fact, we observed that at 10 K this coercive field can increase up to the surprisingly large value of -8000 Oe. The data of the blue, full stars were recorded afterwards, with the Co peak at H^F_C ~900 Oe, whereas the data of the black, open squares were recorded after training the Co, with the Co peak at H^F_C~-2200 Oe. Note that the height of the MR peaks at the Co coercive field is considerably weaker in the first field down sweep than in subsequent sweeps. On the contrary, the LCMO peak, at approx. ±130 Oe at this low temperature, is not modified substantially from up to down field sweeps, independent of the Co training. This can be explained in view of the change of the Co magnetization reversal mechanism after the first field switch from domain nucleation to magnetization rotation in large domains. It is reasonable that magnetization rotation may in fact change the intensity of the stray fields and thus the height of MR peaks. Importantly, between the coercive fields of Co and LCMO, there is no MR plateau, certainly in the case of sweeping the field down, when the peaks are well separated.

The top panel of Fig. 3.76 shows the magnetoresistance of the same trilayer in the intermediate stage above the step of the resistive transition at 47 K (see Fig. 3.72), with $R_{min}/R_n \sim 10^{-1}$. The color-coding of the sweeps is the same as in the bottom panel, showing the Co peak at different coercivities, reflecting the progressive training and exchange bias of the CoO/Co. The LCMO coercive fields are approx. ±50 Oe. The Co coercive fields are approx. -1700 Oe, -1400 Oe and +700 Oe for the untrained and trained down- and up-sweeps, respectively. Importantly, there is no hint of a plateau between the LCMO and Co coercive fields. As the MR peaks are approx. 10% high at both 47 K and 25 K, they do not display the exponential growth with decreasing R_{min}/R_n , contrary to the behavior seen in the fresh stage or in LCMO/YBCO/LCMO trilayers in Refs.19,109. Finally, in Fig. 3.77 the MR in the fresh (thick blue line) and intermediate (thin red line) stages in the top panel are contrasted to each other and to the derivative (thick black line) of the magnetization hysteresis curve (thin dashed purple line) in the bottom panel. Only the down sweeps with decreasing field are shown for simplicity.

All data were recorded at 48 K, in order to obtain the same coercive field of the trained Co layer, although this way the overall resistance in the intermediate stage remains quite high. In the fresh stage there is a well defined plateau between, and relatively small peaks at, the coercive fields of the LCMO and Co. In contrast, in the intermediate stage there are well defined peaks at each coercive field. Furthermore, the peak width of the intermediate stage corresponds well to the width of the derivative of the magnetization hysteresis curve at both the LCMO and Co coercive fields.

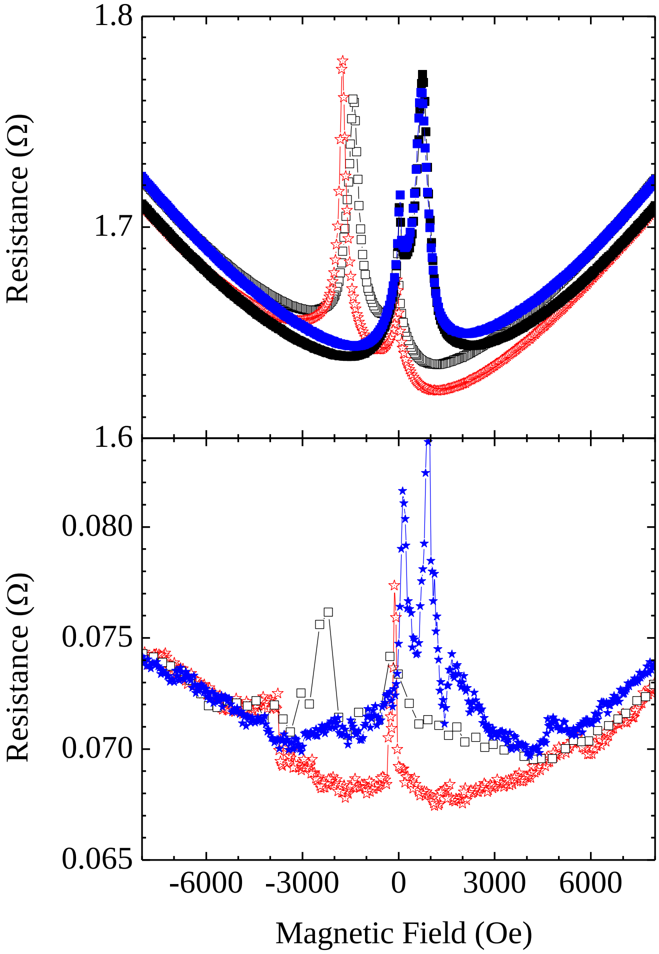

Fig. 3.76. Magnetoresistance of the trilayer sample in the intermediate stage, at 47 K with $R_{min}/R_n \sim 10^{-1}$ (top) and at 25 K with $R_{min}/R_n \sim 10^{-3}$ (bottom). The red, open stars show the first sweep down to -10 kOe after cooling in +50 kOe (untrained), the blue, full stars show the subsequent up sweep. The black squares show a hysteresis loop at the same temperature after many cycles (trained).

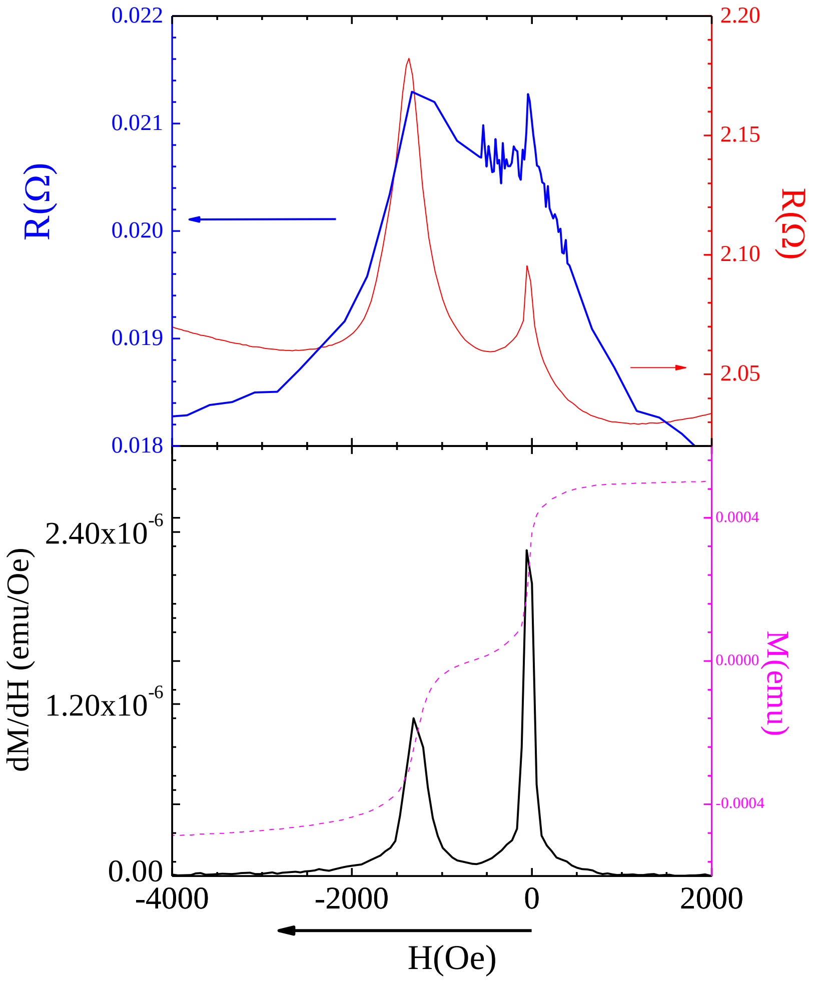

Fig. 3.77. Top Magnetoresistance of the trilayer in the fresh (thick blue line) and intermediate (thin red line) stages. (Bottom) Magnetization vs. field (thin dashed purple line) and its derivative (thick solid black line) in the fresh stage. All data were recorded at 48 K on sweeping down the magnetic field.

Discussion: We have shown that magnetization switching is accompanied by MR peaks pointing to an effect of stray fields on the superconductivity of the YBCO layer. It is clear, also, that specific domain configurations create magnetic fields affecting superconductivity differently as shown by the different behavior exhibited by magnetoresistance with untrained vs. trained Co in the intermediate stage. However, samples in the fresh stage have an additional, well defined MR plateau between the two coercive fields, which we attribute to a spin dependent effect related to the antiparallel orientation of the ferromagnetic layers. We have previously proposed that spin dependent quasiparticle scattering at the F/S interface of LCMO/YBCO/LCMO samples that is enhanced in the AP configuration may modulate the superconductivity giving rise to the large MR peaks [19,109]. The smaller magnetoresistance values at the plateau (30%-100%) in LCMO/YBCO/Co as compared to the large values found in symmetric LCMO/YBCO/LCMO trilayers in excess of 300% at similar R_{min}/R_n may be related to the smaller degree of spin polarization of the conduction band of the Co (34%) contrary to the high spin polarization of LCMO [110,111]. The effect of stray fields on the superconducting state has been extensively discussed by Steiner and Ziemann and by Stamopoulos *et al* [61,92]. Steiner and Ziemann studied F/S bilayers (Nb/Fe), F/S/F trilayers (Co/Nb/Fe) and EB-F/S/F exchange biased trilayers (CoO/Co/Nb/Fe). They found positive MR peaks (or equivalently depressions of T_c) at the coercive field(s) of the ferromagnet(s) in bilayers and trilayers and proposed that they originate in the micromagnetic stray fields of the ferromagnetic layers. Stray fields generated at coercivity emerge all over the surface of the ferromagnet (and should not be confused by stray fields appearing at the edges of a homogenously magnetized ferromagnet). It has been proposed that these stray fields mediate a magnetic (magnetostatic) coupling mechanism in which transverse field lines pierce the superconductor giving rise to resistive dissipation13. According to Stamopoulos *et al* [92] this mechanism should be maximal when the coercive fields of the two ferromagnets are very similar, coupling domains that emerge simultaneously in both ferromagnets. In contrast, when the coercive fields are different, the stray field mediated coupling is less pronounced. This, again according to Stamopoulos [92] would explain the smaller MR values observed in NiFe/Nb/NiFe samples with one of the layers pinned by exchange bias. Exchange bias maintains an in-plane magnetization, thus it restricts the out of plane magnetization rotation (necessary for the occurrence of broad dissipation peaks) to a small magnetic field range around coercivity. Therefore, in view of the large exchange bias and very different values of the coercivities found in LCMO/YBCO/Co samples, it is hard to conceive of a magnetostatic coupling between domain states of top and bottom ferromagnets that might be effective. Stamopoulos *et al [*92] predict strong magnetostatic coupling and intensive MR peaks in F/S/F trilayers when the coercive fields of the two F electrodes are comparable. It is clear however, that magnetization rotation in the trained state is an important ingredient for the occurrence of magnetoresistance peaks at coercivity also in our samples. In this regard it is worthwhile to recall that in the intermediate stage the MR in the very first (untrained) field sweep showed essentially no or very small magnetoresistance peaks. The first domain state in untrained samples is known to occur by domain nucleation with magnetization components only parallel and antiparallel to field. This conclusion has been reported to follow from very small or absent anomalous magnetoresitance peaks (AMR) at coercivity found in single-layer CoO/Co samples for current injected perpendicular to field [98,100,101]. Since AMR scales with $1 - \cos^2(\theta)$, with θ being the angle between current and magnetization, domain nucleation with magnetizations exactly parallel or antiparallel to field would yield $\cos^2(\theta) = 1$ and thus no measurable change in AMR at coercivity. Subsequent sweeps yield comparable AMR peaks, in CoO/Co, at both coercive fields reflecting that reversal now occurs by magnetization rotation, as also indicated by the more rounded hysteresis loops. The MR peaks associated with Co are considerably sharper in the intermediate stage than in the fresh stage, and this is especially pronounced in the more trained sweep. This is a remarkable result if one takes into account that training is accompanied by larger participation of rotation in magnetization switching, which would widen the MR peaks. Since an oxide barrier layer forms between Co and YBCO with aging, closure of field lines within the oxide layer might be the cause of the sharper MR peaks because the weak magnetic flux from the incipient domain state is effectively damped by the oxide. The diamagnetic screening by the superconductor of the component of the stray field perpendicular to the layers can also be ruled out since this effect is expected to be larger in the fresh sample. The change in MR peak width may thus be a reflection of an additional mechanism in the fresh stage originating at the alignment state of the magnetization of the F electrodes. The plateau exhibited in the fresh stage (see Fig.3.75 and Fig. 3.77) of the LCMO/YBCO/Co trilayer is then characterized as having an intrinsic spin dependent transport origin. For this mechanism, rather transparent and smooth interfaces are required between the ferromagnets and the superconductor. This point is shown up by the observation of the lack of plateau in the intermediate stage (see Fig. 3.76 and Fig. 3.77), where an oxide barrier is assumed to form between superconducting YBCO and ferromagnetic Co. As the chemical reaction between Co and YBCO slowly progresses, the interface necessarily deteriorates, and in the MR only the small, positive MR peaks at coercivity remain, again characterized according to Steiner and Ziemann as having an extrinsic origin, such as stray fields12. Interface roughness is an additional source of stray fields and thus of MR peaks. In flat layers with in plane magnetization the field induced in the superconductor would be very small and only due to finite size effects which may be enhanced in the domain state. This is the reason why in very smooth bilayers, with LCMO on top, switching effects are absent. Small MR peaks appear, however, in bilayers with LCMO on the bottom. Zalk *et al* have shown recently, by using finite element simulations, that at rough F/S interfaces substantial magnetic field penetrates into the superconductor40. The induced field due to the rough surface of the ferromagnet (”orange peel” effect) will be directed opposite to the magnetization and may thus be parallel or antiparallel to the applied field depending on the stage of the sweep, essentially causing a decreased effective field at saturation and an enhanced field after crossing zero field, but still before switching. At large field the resistance will be lower than in bare YBCO films due to roughness, as stray fields become AP to the applied field. A resistance increase occurs when external and stray fields point in the same direction. Thus at coercivity there is a down shift of the resistance curve due to a partial cancellation of the external field by the antiparallel stray fields making magnetoresistance change at coercivity to resemble more a step than a peak. Note however, that in our case MR peaks at coercivity are quite sharp pointing to magnetization rotation at coercivity as the dominant source of the stray fields.

In summary, we have examined the inverse superconducting spin switch behavior of Co/YBCO/LCMO structure. We have used the naturally forming CoO/Co AF/F double layers to magnetically pin the Co layer by exchange bias allowing the modification of the coercive field of the Co by several thousand oersteds. Measuring resistance vs. field sweeps at fixed temperatures along the superconducting transition, we found positive magnetoresistance peaks occurring at the coercive fields of both the Co and the LCMO which can be unambiguously ascribed to the effect of stray fields generated at the domain state of the ferromagnet. The pronounced training effect of the CoO/Co layer, originating in a larger participation of magnetization rotation within domains in magnetization switching, also has a strong effect on magnetoresistance peaks, showing that specific domain configurations create stray fields affecting superconductivity differently. In samples with freshly deposited Co we observe an additional, well defined, magnetoresistance plateau extending between the coercive fields of the LCMO and Co, determined by the AP alignment. This plateau disappears with time due to the formation of a non-superconducting oxide layer at the YBCO/Co interface that breaks the electronic coupling between the ferromagnet and the superconductor. We extract the conclusion that while stray fields certainly cause positive magnetoresistance peaks in inverse superconducting spin switches, an additional mechanism is also present possibly related to the spin dependent quasiparticle scattering at the F/S interface proposed for LCMO/YBCO/LCMO samples that is enhanced in the AP configuration.

References

1. A. I. Buzdin, Rev. Mod. Phys. 77, 935 (2005).
2. F. S. Bergeret, A. F. Volkov, and K. B. Efetov, Rev. Mod. Phys.77, 1321 (2005).
3. V. V. Ryazanov, V. A. Oboznov, A. Yu. Rusanov, A. V. Veretennikov,A. A. Golubov, and J. Aarts, Phys. Rev. Lett. 86, 2427(2001).
4. T. Kontos, M. Aprili, J. Lesueur, F. Genêt, B. Stephanidis, and R.Boursier, Phys. Rev. Lett. 89, 137007 (2002).
5. A.Y. Rusanov, M. Hesselberth, J. Aarts, and A. I. Buzdin, Phys.Rev. Lett. 93, 057002 (2004).
6. Z. R. Yang, M. Lange, A. Volodin, R. Szymzak, and V. V. Moshchalkov, Nat. Mater. 3, 793 (2004).
7. L. R. Tagirov, Phys. Rev. Lett. 83, 2058 (1999).
8. J. Y. Gu, C.-Y. You, J. S. Jiang, J. Pearson, Ya. B. Bazaliy, and S.D. Bader, Phys. Rev. Lett. 89, 267001 (2002).
9. I. C. Moraru, W. P. Pratt, and N. O. Birge, Phys. Rev. Lett. 96,037004 (2006).
10. G. Jakob, V. V. Moshchalkov, and Y. Bruynseraede, Appl. Phys.Lett. 66, 2564 (1995).
11. P. Przyslupski, S. Kolesnik, E. Dynovska, T. Skoskiewicz, and M.Sawicki, IEEE Trans.Appl. Supercond. 7, 2192 (1997).
12. C. A. R. Sá de Melo, Phys. Rev. Lett. 79, 1933 (1997); Phys.Rev. B 62, 12303 (2000).
13. P. Prieto, P. Vivas, G. Campillo, E. Baca, L. F. Castro, M. Varela,C. Ballesteros, J. E. Villegas, D. Arias, C. Leon, and J. Santamaria,J. Appl. Phys. 89, 8026 (2001).
14. H.-U. Habermeier, G. Cristiani, R. K. Kremer, O. I. Lebedev, and G. Van Tendeloo, Physica C 354, 298 (2001).
15. A. Pimenov, P. Przyslupski, A. Loidl, and B. Dabrowski, Phys.Rev. Lett. 95, 247009 (2005).
16. J. Chakhalian, J. W. Freeland, G. Strajer, J. Strempfer, G. Khaliullin, J. C. Cezar, T. Charlton, R. Dalgliesh, C. Bernhard, G.Christiani, H. U. Habermeier, and B. Keimer, Nat. Phys. 2, 244(2006).

17. Z. Sefrioui, D. Arias, V. Peña, J. E. Villegas, M. Varela, P. Prieto,C. León, J. L. Martínez, and J. Santamaría, Phys. Rev. B 67, 214511 (2003).
18. M. Varela, Z. Sefrioui, J. Santamaria, and S. J. Pennycook, Solid-State Electron. 47, 2245 (2003).
19. V. Peña, , Z. Sefrioui, D.Arias, C. Leon, J. Santamaría, J. L. Martinez, S. G. E. teVelthuis, and A. Hoffmann, Phys. Rev. Lett., vol. 94, p. 057002, 2005.
20. C. Visani, V. Peña, J. Garcia-Barriocanal, D. Arias, Z. Sefrioui, C. Leon, J. Santamaría, N. M. Nemes, M. Garcia-Hernandez, J. L. Martinez, S. G. E. te Velthuis, and A. Hoffman, Phys. Rev. B, vol. 75, p. 054501, 2007.
21. A. Singh, C. Surgers, and H. von Lohneysen, Phys. Rev. B, vol. 75, p.024513, 2007.
22. J. Aarts, A. Y. Rusanov, and C. R. , Physique, vol. 7, p. 99, 2006.
23. D. Stamopoulos, E. Manios, and M. Pissas, Phys. Rev. B, vol. 75, p.014501, 2007.
24. R. Steiner and P. Ziemann, Phys. Rev. B, vol. 74, p. 094504, 2006.
25. Z. H. Wang, G. Cristiani, and H. U. Habermeier, Appl. Phys. Lett., vol.82, p. 3731, 2003.
26. M. Mathews, F. M. Postma, J. C. Lodder, R. Jansen, G. Rijnders, and D. H. A. Blank, Appl. Phys. Lett., vol. 87, p. 242507, 2005.
27. T. Taniuchi, H. Kumigashira, M. Oshima, T. Wakita, T. Yokoya, M. Kubota, K. Ono, H. Akinaga, M. Lippmaa, and M. Kawasaki et al.,Appl. Phys. Lett., vol. 89, p. 112505, 2006.
28. I. C. Infante, J. O. Osso, F. Sanchez, and J. Fontcuberta, Appl. Phys.Lett., vol. 92, p. 012508, 2008.
29. I. K. Schuller, Phys. Rev. Lett., vol. 44, p. 1597, 1980.
30. W. Sevenhans, M. Gijs, Y. Bruynseraede, H. Homma, and I. K.Schuller, Phys. Rev. B, vol. 34, p. 5955,1986.
31. E. E. Fullerton, I. K. Schuller, H. Vanderstraeten, and Y. Bruynseraede,Phys. Rev. B, vol. 45, p. 9292, 1992.
32. D. M. Kelly, E. E. Fullerton, J. Santamaria, and I. K. Schuller, Scr.Metall. Mater., vol. 33, p. 1603, 1995.
33. V. Peña, C. Visani, J. Garcia-Barriocanal, D. Arias, Z. Sefrioui, C. Leon, and J. Santamaria, Carmen A. Almasan Phys.Rev.B 73, 104513 (2006)

34. N. C. Yeh, R.P. Vasquez, C.C. Fu, A.V. Samilov, Y. Li, K.Vakili, Phys. Rev. B 60, 10522 (1999)
35. S. Soltan, J. Albrecht, H.-U. Habermeier, Phs .Rev.B, 70,144517, (2004)
36. V. Pena, Z. Sefrioui, D. Arias, C. Leon, J. Santamaria, M.Varela, S.J. Pennycook, J.L.Martinez, Phys. Rev. B. 69, 224502 (2005)
37. A. K. Geim. et al., Nature, 396,144 (1998)
38. K. H. Han. et al., Nature 428, 4041 (2004)
39. M. A. López de la Torre, et. Al., Phys.Rev.B 73,052503 (2006)
40. J. P. Gong, M. Kavasaki, K. Fushito, R. Tsuchiya, M. Yoshimoto, H.Koinuma. Phys.Rev.B 50, 328 (1994)
41. N. Kanda, M. Kavasaki, T. Kitashima, H. Koinuma. Phys.Rev.B 56, 8419 (1997).
42. R. I. Chakalova, T. J. Jackson, G. Passerieux, I. P. Jones, P. Mikheenko, C. M. Muirhead, C. N. W. Darlington, Phys.Rev.B 70, 214504 (2004)
43. P. W. Anderson and H. Suhl. Phys. Rev.,116,898, (1959)
44. L. N Bulaevskii, A. I Buzdin, M. L Kuli´c, and S. V Panjukov. Adv. In Phys., 34,175–261, (1985).
45. C. L. Johnson, J. K. Bording, Y. Zhu, Phys.Rev.B 78, 014517 (2008)
46. F. Laviano, L. Gozzelino, E. Mezzetti, P. Przyslupski, A. Tsarev, and A. Wisniewski, Appl.Phys.Lett. 86, 152501 (2005)
47. J. Chakhalian, J. W. Freeland, G. Srajer, J. Strempfer, G. Khaliullin, J. C. Cezar, T. Charlton, R. Dalgliesh, C. Bernhard, G. Cristiani, et al., Nat. Phys. 2, 244 (2006).
48. J. Chakhalian, J. W. Freeland, H.-U. Habermeier, G. Cristiani , G. Khaliullin, M. van Veenendaal, B. Keimer, Science 318, 1114 (2007)
49. E. Goering A. Fuss, W. Weber, J. Will, and G. Schütz, J.Appl.Phys. 88, 5922 (2000)
50. S. Valencia A. Gaupp, W. Gudat, Ll. Abad, Ll. Balcells, and B. Martínez Phys.Rev.B, 75, 184431 (2007)
51. A. Hoffmann, S. G. E. te Velthuis, Z. Sefrioui, J. Santamaría, M.R. Fitzsimmons, S. Park, and M. Varela, Phys. Rev. B 72,140407 (2005).
52. M. J. M. de Jong and C. W. J. Beenakker, Phys. Rev. Lett. 74,1657 (1995).
53. S. Takahashi, H. Imamura, and S. Maekawa, Phys. Rev. Lett. 82,3911 (1999).
54. Y. Rusanov, S. Habraken, and J. Aarts, Phys. Rev. B 73,060505(R) (2006).

55. J. Y. Gu, J. A. Caballero, R. D. Slater, R. Loloee, and W. P. Pratt,Jr., Phys. Rev. B 66, 140507(R) (2002).
56. T. Yamashita, H. Imamura, S. Takahashi, and S. Maekawa, Phys.Rev. B 67, 094515 (2003).
57. G. E. Blonder, M. Tinkham, and T. M. Klapwijk, Phys. Rev. B25, 4515 (1982).
58. I. Zutic and O. T. Valls, Phys. Rev. B 60, 6320 (1999).
59. N. Stefanakis, Phys. Rev. B 64, 224502 (2001).
60. T. Hirai, Y. Tanaka, N. Yoshida, Y. Asano, J. Inoue, and S. Kashiwaya,Phys. Rev. B 67, 174501 (2003)
61. R. Steiner and P. Ziemann, Phys. Rev. B **74**, 094504 (2006).
62. M. Tinkham and J. Clarke, Phys. Rev. Lett. 28, 1366 1972.
63. S. R. Foltyn, L. Civale, J. L. Macmanus-Driscoll, Q. X. Jia, B. Maiorov, H. Wang, M. Maley, Mat.Mater, 6, 631 (2007)
64. J. Gutiérrez, A. Lordés, J. Gázquez, M. Gibert, N. Romà, S. Ricart, A. Pomar, F. Sandiumenge, N. Mestres, T. Puig, X. Obradords, Nat. Mater. 6, 367 (2007)
65. T. G. Holesinger, L. Civale, B. Maiorov, D. M. Feldmann, J. Y. Coulter, D. J. Miller, V. A. Maroni, Z. Chen, D. C. Larbalestier, R. Feenstra , X. Li, Y. Huang, T. Kodenkandath, W. Zhang, M. W. Rupich , A. P. Malozemoff, Adv.Mater. 20,391 (2008)
66. J. E. Villegas , S. Savel'ev , F. Nori , E. M. Gonzalez , J. V. Anguita , R. Garcia , J. L. Vicent, Science, 302, 1188 (2003)
67. C. C. D.Silva , J. V.de Vondel , M. Morelle , V. V. Moshchalkov ,Nature, 40, 651 (2006)
68. D. Cole D, S. Bending, S. Savel'ev , A. Grigorenko , T. Tamegai , F. Nori, Nat.Mater., 5, 305 (2006)
69. L. N. Bulaevskii , E. M. Chudnovsky , M. P. Maley, Appl.Phys.Lett.76, 2594 (2000)
70. F. Laviano, L. Gozzelino, R. Gerbaldo, G. Ghigo, E. Mezzetti, P. Przyslupski, A. Tsarou, A. Wisniewski, Phys.Rev.B, 76, 214501 (2007)
71. V. Vlasko-Vlasov, U. Welp, G. Karapetrov, V. Novosad, D. Rosenmann, M. Iavarone, A. Belkin, W.-K. Kwok, Phys.Rev.B, 77, 134518 (2008)
72. Y. Suzuki H. Y. Hwang, S-W. Cheong, R. B. van Dover. Appl. Phys.Lett. 71, 140 (1997)

73. J. O’Donnel M. S. Rzchowski, J. N. Eckstein, I. Bozovic. Appl. Phys.Lett. 72, 1775 (1998)
74. K. Steenbeck, and R. Hiergeist, Appl. Phys.Lett. 75, 1778 (1999)
75. T. K. Nath R. A. Rao, D. Lavric, C. B. Eom, L. Wu, F. Tsui Appl. Phys.Lett. 74, 1615 (1999)
76. M. Ziese, Phys. Rev. B 62, 1044 (2000)
77. M. Bibes, S. Valencia, Ll. Balcells, B. Martínez1 J. Fontcuberta, M. Wojcik, S. Nadolski, and E. Jedryka. Phys.Rev.B 66, 134416 (2002)
78. S. Estradé.J. M. Rebled, J. Arbiol, F. Peiró, I. C. Infante, G. Herranz, F. Sánchez, J. Fontcuberta, R. Córdoba, B. G. Mendis, A. L. Bleloch, Appl.Phys.Lett., 95,072507 (2009)
79. M. R. Fitzsimmons and C. F. Majkrzak, in Modern Techniques for Characterizing Magnetic Materials, edited by Y. Zhu (Springer, New York, 2005), Chap. 3, pp. 107-155.
80. N. Nüker , E. Pellegrin, P. Shweiss, J. Fink,S. L. Molodtsov, C. T. Simmons, G. Kaindl, W. Frentrup, A. Erb, G. Müller-Vogt, Phys.Rev.B 51, 8529 (1995)
81. E. C. Stoner, and E. P. Wohlfarth, Phil. Trans. R. Soc. London A 240 (826), 599 (1948)
82. K. Dybko, K. Werner-Malento, M. Sawicki, P. Przyslupski, EuroPhys. Lett.V85 57010 (2009) .
83. W. Gillijns, A. Y. Aladyshkin, M. Lange, M. J. Van Bael, V. V. Moshchalkov, Phys. Rev. Lett. V95 227003 (2005).
84. M. Vogel and T. Mewes, Stoner-Wohlfarth astroid applet, http://www.bama.ua.edu/~tmewes/Java/Astroid/StonerAstroid.shtmlChien 2009
85. J. Zhu, X. Cheng, C. Boone, I. N. Krivorotov, Phys. Rev. Lett. V103 027004 (2009)
86. A. Potenza and C. Marrows, Phys. Rev. B 71, 180503 (2005).
87. F. Giazotto, F. Taddei, F. Beltram, and R. Fazio, Phys. Rev. Lett.S 97, 087001 (2006).
88. G.X. Miao, K. Yoon, T. S. Santos, and J. S. Moodera, Phys. Rev. Lett. 98, 267001 (2007).
89. G.-X. Miao, A. V. Ramos, and J. S. Moodera, Phys. Rev. Lett.S 101, 137001 (2008).

90. L.Y. Zhu, T. Y. Chen, and C. L. Chien, Phys. Rev. Lett.S 101, 017004 (2008).
91. A. Y. Aladyshkin, A. V. Silhanek, W. Gillijns, and V. V. Moshchalkov, Supercond. Sci. & Techn. p. 053001 (2009).
92. D. Stamopoulos, E. Manios, and M. Pissas, Supercond. Sci. & Techn. 20, 1205 (2007).
93. P. Przyslupski, A. Tsarou, P. Dluzewski, W. Paszkowicz, R. Minikayev, K. Dybko, M. Sawicki, B. Dabrowski, and C. Kimaball, Supercond. Sci. & Techn. 19, S38 (2006).
94. K. Senapati and R. Budhani, Phys. Rev. B 71, 224507 (2005).
95. J. Hoppler, J. Stahn, C. Niedermayer, V. K. Malik, H. Bouyanfif, A. J. Drew, M. Roessle, A. Buzdin, G. Cristiani, H. U. Habermeier, et al., Nat. Mater. 8 , 315 (2009).
96. H. Habermeier, G. Cristiani, R. Kremer, O. Lebedev, and G. van Tendeloo, Physica C 364 , 298 (2001).
97. C. Visani and J. Santamaria, unpublished (2009).
98. F. Radu, M. Etzkorn, R. Siebrecht, T. Schmitte, K. Westerholt, and H. Zabel, Phys. Rev. B 67, 134409 (2003).
99. M. Gruyters and D. Riegel, Phys. Rev. B 63, 052401 (2001).
100. T. Gredig, I. Krivorotov, and E. Dahlberg, J. Appl. Phys. 91, 7760 (2002).
101. S. Brems, K. Temst, and C. Van Haesendonck, Phys. Rev. Lett.S 99, 067201 (2007).
102. A. Hoffmann, .Phys. Rev. Lett 93 , 097203 (2004).
103. M.de la Torre, V. Pena, Z. Sefrioui, D. Arias, C. Leon, J. Santamaria, and J. Martinez, Phys. Rev. B 73, 052503 (2006).
104. Z. Sefrioui, D. Arias, V. Pena, J. E. Villegas, M. Varela, P. Prieto, C. Leon, J. L. Martinez, and J. Santamaria, Phys. Rev. B 67, 214511 (2003).
105. V. Pena, Z. Sefrioui, D. Arias, C. Leon, J. Martinez, and J. Santamaria, Eur. Phys. Journ. B 40, 479 (2004).
106. M. Varela, A. Lupini, S. Pennycook, Z. Sefrioui, and J. Santamaria, Solid State Electr. 47, 2245 (2003).
107. S. Brems, A. Volodin, C. Van Haesendonck, and K. Temst, J. Appl. Phys. 103, 113912 (2008).
108. J. Nogues and I. K. Schuller, J. Magn. Magn. Mater. 192, 203 (1999).

109. N. M. Nemes, M. Garcia-Hernandez, S. G. E. te Velthuis, A. Hoffmann, C. Visani, J. Garcia- Barriocanal, V. Pena, D. Arias, Z. Sefrioui, C. Leon, et al., Phys. Rev. B 78, 094515 (2008).
110. M. H. Jo, N. D. Mathur, N. K. Todd, and M. G. Blamire, Phys. Rev. B 61 , 14905 (2000).
111. Z. Sefrioui, V. Cros, A. Barthelemy, V. Pena, C. Leon, J. Santamaria, M. Varela, and S. J. Pennycook, Appl. Phys. Lett. 88, 022512 (2006).

4. Conclusions

The main findings of this dissertation are summarized here. We performed an analysis of the interplay between ferromagnetism, F, and superconductivity, S, in epitaxial heterostructures of the high T_C superconductor $YBa_2Cu_3O_{7-\delta}$ (YBCO) and the ferromagnetic manganite $La_{0.7}Ca_{0.3}MnO_3$ (LCMO). We found large values of magnetoresistance in LCMO/YBCO/LCMO trilayers, arising along the superconducting transition, when the magnetizations of the LCMO layers are aligned antiparallel. This anomalous behavior is called *inverse superconducting spin switch*. The origin of this phenomenon is the subject of a recent controversial debate, in which the mechanism of enhanced pair breaking by spin-polarized quasiparticles is set against the effect of stray fields in depressing the superconductivity during the magnetization switching. For a clear understanding of the origin of the magnetoresistance, several experimental techniques applied to our samples provided fundamental results which can be summarized as follows:

- the magnetoresistance found in our oxide system, displays much larger values compared to the giant magnetoresistance in metallic superlattices or to F/S heterostructures in which the role of stray fields is demonstrated to be predominant.
- we found that the shape and height of the magnetoresistance peaks are not modified when the relative orientation of current and magnetic field is changed from parallel to perpendicular. Furthermore, we find that the temperature shift of the resistance curves is independent of the current value and of the sweep rate of the magnetic field. These observations rule out interpretations in terms of spontaneous vortices or anisotropic magnetoresistance of the ferromagnetic layers.
- a comparison of trilayers and bilayers (showing negative magnetoresistance o no magnetoresistance at all depending on the character of the LCMO/YBCO interface) allows ruling out the effect of the stray fields of the domain structure of the ferromagnet as the source of the inverse superconducting spin switch.
- combined ferromagnetic resonance, polarized neutron reflectometry, and magnetometry measurements shows that the magnetic anisotropy is biaxial

with easy axes along the [110] substrate directions. The orientation of the magnetic field with respect to the [110] biaxial easy axes showed a pronounced effect on superconductivity. We identify a well defined plateau of the magnetoresistance when the magnetic field is directed along the easy axes whereas peaks are observed for other field directions. The magnetoresistance closely follows the magnetic field interval over which magnetic moments of the manganite layers are aligned antiparallel to each other. Resistance measurements as a function of a continuous change of the in-plane direction of the applied field show that the response is purely caused by a misalignment of the magnetization of the two LCMO electrodes controlled by the biaxial in plane anisotropy.

- a not yet reported effect is found that yields a *positive MR plateau* for antiparallel alignment of the magnetizations of the F layers and *negative* MR peak at the coercive field. This evidences the importance of spin dependent interfacial scattering effects (as opposed to stray fields) in the MR behaviour of oxide inverse spin switches.
- we propose an explanation in terms of spin dependent scattering of polarized quasiparticles at the ferromagnet / superconductor interface. According to this scenario, the thickness dependence of the magnetoresistance yields an estimate of the spin-diffusion length (of spin polarized quasiparticles) in YBCO of 13 nm.
- Finally, our LCMO/YBCO/LCMO trilayer is effectively an inverse superconducting spin-valve which behaves as an angle sensitive magnetic memory; this memory concept exploits the advantages of the superconductor detection element (fast response and low dissipation) and has a number of peculiarities which differentiates it from GMR based memories, like the possibility of using writing fields applied at different directions and then reading with really small (10 mT) fields.

These results constitute direct evidence to the spin-dependent-transport origin of the inverse spin valve effect in this system and may form the basis of novel device concepts for spintronics.